Extended Low Density Ionized Gas in the inner Galaxy

A Study Using Recombination Lines

by

Raju R Baddi

A Thesis submitted to the
Jawaharlal Nehru University
for the Degree of
Doctor of Philosophy

2010

Raman Research Institute
Bangalore 560 080
India

Certificate:

This is to certify that the thesis entitled " **Extended Low Density Ionized Gas in the inner Galaxy: A Study using Recombination Lines** " submitted by Raju R Baddi for the award of the degree of Doctor of Philosophy of Jawaharlal Nehru University is his original work. This has not been published or submitted to any other University for any other Degree or Diploma.

D.Anish Roshi
(Thesis Supervisor)

Prof. Ravi Subramanyan
(Center Chairperson)
Director
Raman Research Insitute
Bangalore 560 080
INDIA

Declaration:

I hereby declare that the work reported in this thesis is entirely original. This thesis was composed independtly by me at Raman Research Insitute under the supervision of D.Anish Roshi. I further declare that the subject matter presented in this thesis has not previously formed the basis for the award of any degree, diploma, membership, associateship, fellowship or any other similar title of any university or institution.

(D. Anish Roshi) (Raju R Baddi)

Astronomy & Astrophysics Group
Raman Research Institute
Bangalore 560 080
INDIA

Acknowledgement:

We thank the staff of RAC who have made the observations with Ooty Radio Telescope(ORT) possible. RAC is run by National Centre for Radio Astrophysics of the Tata Institute of Fundamental Research.

We thank the staff of Westerbrock Radio Telescope(WSRT) who have made these observations possible.

This work has made use of data from NASA/IPAC Extragalactic Database(NED) which is operated by the Jet Propulsion Laboratory, California Institute of Technology, under contract with the National Aeronautics and Space Administration.

This work has made use of NASA's Astrophysics Data System.

We thank the staff of GMRT who allowed to do test observations in the initial phase of the project. GMRT is operated by the National Centre for Radio Astrophyscics of the Tata Institute of Fundamental Research.

Contents

1 Introduction

1.1 What are Radio Recombination Lines ? 1-1

1.2 A Brief History of RRL observations 1-2

1.3 The Interstellar Medium 1-3
  1.3.1 The components of Interstellar medium 1-4
  1.3.2 Extended Low Density Warm Ionized Medium & the present work 1-5

2 Understanding Recombination Lines

2.1 Physics of RRL 2-1
  2.1.1 Radiation Transfer 2-2
  2.1.2 Thermal Continuum radiation and its Optical Depth 2-5
  2.1.3 RRL Frequencies 2-8
  2.1.4 The Line Radiation: Coefficients and Optical depth 2-8

2.2 Line Broadening Mechanisms 2-11
  2.2.1 Lorentz Broadening 2-11
  2.2.2 Doppler Broadening 2-13
  2.2.3 Pressure Broadening 2-16
  2.2.4 The Voigt Profile 2-18

2.3 Non Local Thermodynamic Equilibrium 2-20
  2.3.1 Departures for LTE and the departure coefficients 2-20
  2.3.2 The non-LTE optical depth 2-21
  2.3.3 Non-LTE line intensity 2-22

3 Observations with WSRT

3.1 The observations 3-1

3.2 The Spectra 3-4

3.3 Data Analysis and Calibration 3-5
  3.3.1 Averaging the spectra to detect Helium Line 3-11

3.4 Modelling of $Hn_1\alpha$-$Hn_2\alpha$ and $Hn_1\alpha$-$Hn_2\beta$ lines 3-12
  3.4.1 Line features and Parameter extraction 3-15
  3.4.2 Modelling results of $H271\alpha$-$H165\alpha$ lines 3-16
    3.4.2.1 Departure Coefficients for modelling 3-16
  3.4.3 Conclusion 3-17

4 Observations with Ooty Radio Telescope

4.1 The Ooty Radio Telescope(ORT) 4-1

4.2 The ORT receiver system at block diagram level 4-2

4.3 ORT System Temperature 4-4

4.4 ORT with a New Digital Backend 4-5

4.5 RRL Observations with ORT 4-8
  4.5.1 The Observations 4-8
  4.5.2 Test for frequency switching 4-13
  4.5.3 Data Calibration 4-14
  4.5.4 The Spectral line observational band 4-16
  4.5.5 Velocity in the Local Standard of Rest 4-18
  4.5.6 First Line detection Using ORT-New digital backend 4-21
  4.5.7 A survey of RRLs in the inner Galaxy 4-22

4.5.8 Scale height of ELDWIM from ORT data 4-23

5 Discussion of Observed RRLs

5.1 Dependence of Line intensity on physical parameters 5-1

5.2 Line emission from a spherical cloud 5-15

5.3 Helium line towards G18.0 +1.8 5-18

5.4 Basic discussion of photoionization around a star 5-20

5.5 Helium line limits towards other positions at ~1.4 Ghz 5-27

5.6 An attempt to detect He-line with ORT data 5-29

5.7 Discussion and Interpretation of Helium line intensities 5-34
  5.7.1 Line profiles and their implications 5-34
  5.7.2 N_{He+}/N_{H+} ratio and the ELDWIM ionization problem 5-43

6 Interference Detection Techniques

6.1 Introduction 6-1

6.2 Radio Spectral Line Observations 6-1

6.3 Interference 6-2

6.4 RFI Detection 6-3
  6.4.1 Direct Method 6-5
  6.4.2 Difference Method 6-6
  6.4.3 Added-Difference Method 6-7

Appendix- I

A An octave tool to edit interference manually from a spectrum

B A subroutine to resample a spectrum to a different resolution

C Subroutine to shift a spectrum by arbitrary channels

D Practical application of resampling and shifting subroutines

E Code to find RRL frequency

F General code to search for a transition resulting in a specified RRL frequency

Appendix-II

A Derivation of expected maximum for a N-channel gaussian noise

B Derivation of expected maximum difference for a N-channel gaussian noise

C Demonstration Programs

Synopsis

The diffuse ionized component in the solar neighbourhood and outer Galaxy(referred to as the Warm Ionized Medium; WIM) is well studied using observations of Hα radiation(Haffner et.al 2003). However Hα radiation from the inner Galaxy($|l| < 50^{o}$) cannot be observed as there is large extinction due to scattering. Low frequency radio recombination line(RRL) observations (<2 GHz) have revealed the existence of an extended low density ionized component(Lockman 1976, Mezger 1978, Anatharamaiah 1985). The typical density of this component is 5-10 cm^{-3} (Roshi 2001). This is more than an order of magnitude larger than that of WIM. In the literature this low density component has been clubbed with the WIM and is referred to as the Extended Low Density Warm Ionized Medium(ELDWIM)(Mezger 1978, Petuchowski & Bennet 1993, Heiles et al. 1996a). Earlier observations have indicated that, in the inner Galaxy, the ELDWIM is semi-pervasive with a filling factor of about a few percent (Roshi & Anantharamaiah 2001). It has been suggested that more than 50% of the Lyman continuum photons produced in the inner Galaxy go into ionizing the ELDWIM(Mezger 1978). Thus the ELDWIM forms an important component of the interstellar medium in the inner Galaxy. Although many observational studies of the ELDWIM exists, there are several unanswered questions. For example, the relationship between the WIM and the ionized component in the inner Galaxy needs to be investigated further. The physical properties of the low density component is uncertain, although it has been suggested that it forms outer envelopes of HII regions(Anatharamaiah 1985) or it is a collection of evolved HII regions (Shaver 1976). Most importantly, the ionization of the ELDWIM is not well understood(Heiles et al. 1996b).

The present work aimed at doing a study of ELDWIM at multi frequency level. The observations were carried out with different telescopes. These are WSRT(Westerbrok Synthesis Radio Telescope, Netherlands), GMRT(Giant meter wave radio telescope, Narayangaon Pune) and ORT(Ooty Radio Telescope, RAC Ooty). The first two of these telescopes are internationally competative telescopes that operate at multifrequencies. Frequency bands had to be selected by the interference conditions and time availability. This resulted in the selection of only one band(~1.4 GHz) for WSRT. However the observations with GMRT didn't seem to be feasible(ack. analysis of the data was done by D.Anish Roshi) and had to be dropped. ORT operates at a frequency of ~326.5 MHz with a band width of 15 MHz. Observations with ORT were carried out with the new digital backend that was augumented to it for the first time. The new digital backend offered a narrow bandwidth of ~1MHz for spectral line observations. So only one RRL transition could be observed at a time. But due to non-availability of a suitable broad band amplifier(use was made of the ORT's own dedicated amplifier which has a 3dB gain band width of ~2MHz) for the LO(Local Oscillator) observations had to be restricted to only one transition H271α . ORT was used to obtain a line map of the Galactic region with $-30^{\circ} < l < 80^{\circ}$ and $-3^{\circ} < b < 3^{\circ}$ with a beam resolution of $2^{\circ} \times 2^{\circ}$. This map didn't exist so far and constitutes a new study done towards ELDWIM in the inner Galaxy. Numerous new line detections were made towards new positions.

The WSRT offered 8 spectral bands in the incoherent addition mode each with a bandwidth of 5 MHz around ~1.4 GHz. Each of these spectral bands was configured to detect RRL from individual transitions H165-171α(7-bands) and H208β(the last 8th band). The primary objective of this project was to detect the associated He165-171α line to understand the ionization of ELDWIM. Since the first ionization potential of He(24.6 eV) is much larger than that of H (13.6 eV), measuring the amount of ionized helium can provide constraints on the spectrum of the ionizing photons. Earlier RRL Observations have indicated that the ratio of the number of helium to hydrogen ions(N_{He+}/N_{H+}) in the ELDWIM is in the range 0 to 0.054 (Heiles et al. 1996b). This ratio is smaller than the generally accepted cosmic abundance of He(N_{He}/N_{H} ~0.1), indicating that all helium atoms in the ELDWIM are not ionized. Order magnitude calculations indicate that the observed ratio in the ELDWIM requires the surface temperature of the ionizing star to be <35000K, if we consider a standard HII region picture. With the current knowledge of the initial mass function and the total Galactic star formation rate it is difficult to realize such a cool ionization spectrum together with the total Galactic ionization requirement for ELDWIM and the HII regions. This has been refered to as the ***ionization problem***(Heiles et al. 1996b). However such calculations are not completely reliable or exhaustive and alternate ways to explain the spectrum must be found.

Helium RRLs from the ELDWIM are much weaker than the hydrogen RRLs, hence longer integration time is needed to detect them from specific directions. Earlier attempts to detect He RRLs were made by averaging spectra obtained towards different directions in the inner Galaxy(such an attempt has also been done in this work using previous ORT data towards >50 positions). While such spectrum provides information about the average helium ionization, they are not suitable to address the ionization problem. To get a better understanding of this problem it becomes necessary to observe specific individual positions and study them in detail. The positions selected in the present work were observed to exhibit hydrogen line strengths of >50mK in previous attempts. Care was also taken to see that these sources are away from compact continuum sources so as to target ELDWIM alone. Here an attempt has been made to detect the helium RRL by averaging the spectra from all the 7-spectral bands(H165-171α) which resulted in bringing down the rms in the spectra down to < 1mK. However this is an average rms across a relatively wide region in the spectrum excluding the line appearing zones. The rms in specific portions in the band is much smaller than this(~0.7mK).

The observed hydrogen RRLs from ORT(328 MHz) and WSRT(1.4 GHz) were modelled to obtain constraints on the number density n_e in ELDWIM which comes out to be around ~10 cm^{-3} towards majority of positions. The modelling was done for different filling factors as would be practically the case. ORT observations towards higher Galactic latitudes have given the *l-v* diagram and line intensities that didn't exist at ~328MHz so far. The smoothed band averaged spectra corresponding to WSRT data have produced He line detection towards 5 positions. An upper limit has been adopted from the rms in the spectra for the non-detection positions. The detected He line towards G18.0 +1.8 has been modelled using uniform density spherical cloud(the derivation necessary for this was also made) to get an idea of the star temperature necessary to produce the observed line strength and the He-H stromgen radius ratios(Osterbrock 1989). To verify the connection between HII regions and He line detection, the identified HII regions in the vicinity(<500pc) of the line originating regions were counted. A weightage scheme for associating the relevant surrounding HII regions with line detection has been adopted. The results of this analysis indicate a good connection between He line detection and higher weightage for surrounding HII regions. The non-detection of He line towards certain positions like G26.5 0.0 and G28.0 0.0 form another interesting aspect regarding the ionization problem of helium. These regions lie in the plane of the Galaxy . Even though strong hydrogen lines have been detected towards these directions there seems to be no sign of He line whatsoever. Such regions can be used to cross check the theories of He line detection/non-detection. In this study the weightage figure for these regions turns out to be much lower than for other positions, indicating the connection between HII regions and He line detection.

It should be noted that the observations with ORT were done with a new-digital backend, that had to be tested for feasibility of its functioning for spectral line observations. This involved struggle with day to day technical problems with hardware, software and interference. As a result the tenure at RAC lasted for about dense 19 months. During these months the main problems that would be mentioned are as follows. Major interference hunting, both internal and external(visiting specific places like CRL or Melkavati, I would like to acknowledge the help of T.Prabu here) or aborting observations due to interference. Computer malfunctioning(which basically was computer hanging due to errors in the raid disks' functioning which store data at a high speed) was another problem which was to an extent that special watch-dog codes had to be written to monitor the data acquistion streamline and caution the observer. Malfunctioning of the broad band amplifier meant to amplify the LO signal fed to the modules. Apart from these there were problems with ORT itself that also hindered the process of observation.

The software required to analyse ORT as well as WSRT data were developed independently. The WSRT data was reduced using cfitsio library. Automatic interference editing code was developed for the ORT data which helped in efficient processing of data. The theory of operation of these automatic interference detecting techniques has also been developed and given in the thesis material(Chapter 6 and Appendix-II). The derivations given in the theory to my knowledge are original and form a part of work for this thesis. Apart from this other useful codes like, spectrum resampling to change the resolution, spectrum shifting using fourier transformation, RRL frequency calculator function and RRL transition search function in octave have been given in Appendix-I.

Chapter 1

Introduction

1.1 What are Radio Recombination Lines ?

From the Bohr's theory of the hydrogen atom when an electron makes a transition from a higher energy level(higher principal quantum number) to a lower energy level(lower principal quantum number) it emits a quantum of radiation which is equal to the energy difference between the two levels. Even though modern quantum mechanics gives a much better picture of the atom than the simple model of what Bohr had proposed to start with, his model is still applicable to a high precision when the energy levels(principal quantum numbers) involved are high enough even in a multielectron atomic system like helium or carbon. Application of Bohr's theory to the transition in a hydrogen atom from a level n=272 to n=271 gives the frequency of the emitted photon as 328.5958 MHz , which lies in the radio regime and hence can be called a radio line. If this transistion were to occur in a Carbon or Helium atom this frequency would be slightly different, towards higher end to be precise, due to the reduced mass difference in the atoms. The electron would see the nucleus and the remaining electrons forming a central core with a net charge of a single proton, virtually like a hydrogen atom but with a different central mass and hence a different frequency. These radio lines originate in the insterstellar medium where there is copious amounts of hydrogen(also other elements but, in much smaller amounts) which is being ionized by the photons from the stars. The electrons recombining with the ions cascade to the lower energy levels emitting these radio frequency photons and are hence called Radio Recombination Lines(RRL). Even though thought to be undetectable due to stark broadening by early investigators(Van de Hulst, 1945) RRLs were eventually detected as early as 1964 by Sorochenko and Borodzich following the prediction due to independent calculations done by Kardashev in 1959 and other subsequent refinements brought in the theory.

1.2 A Brief History of RRL Observations

Bohr's theory of the atom explained the already known spectral line nature of atomic radiation. The already observed series were easily explained applying Bohr's theory, however the new outcomes of the theory, especially those with minute differences of energy could not be tested with the then available laboratory techniques and capabilities. Astronomical observations promised a better option for detecting the low energy photons resulting from the transitions between the higher principal quantum numbers. One can only see the radiation resulting from transitions at higher levels by having very low densities since these atomic excitations will not be disturbed by the neighbouring atoms. Such a density would occupy a very large volume to produce visible intensities and hence is not observable in a typical laboratory. Van de Hulst has been considered to be the first to have considered the possibility of detecting these radio line transitions occuring between the highly excited states of atoms with regard to the interstellar hydrogen. Unfortunately based on wrong calculations for stark broadening he came to a conclusion that the RRL of hydrogen would be too dispersed and undetectable. However the problem was independently considered by Kardhshev(1959) who arrived at an affirmitive conclusion. His calculations for radio line intensity and linewidth for hydrogen in the interstellar medium suggested affirmatively the detection of RRL in **HII** regions.

The preliminary attempts to detect RRL from hydrogen were made by Egorova and Ryzkov (1960) with the Pulkovo telescope. The RRL considered was from the transition H271α (n=272 to 271, $\Delta n=1$ so alpha , $\lambda=91.2$cm) searched in the Galactic plane around longitude, $l=60^{\circ}$ to 115° , but gave a negative result. After this, the calculations done by Griem(1960) regarding the theory of spectral line broadening in plasmas suggested the most probable detection in cm range at $\lambda=2$-5cm, in bright and spatially extended **HII** regions, which were the Omega and Orion nebulae. Following this in april 1964 using an improved radio meter with the 22cm radio telescope at Lebedev Physical institute in Puschino, Sorochenko and Borodzich detected the hydrogen RRL H90α ($\lambda=3.38$cm) towards the omega nebula. The line could be clearly seen even in single spectrograms, the following observations carried out during the next few months showed the agreement between the expected doppler shift due to earth's rotation and provided proof for its cosmic origin. At about the same time as the above group the Pulkovo group(Dravskikh et.al,, 1965) also detected a convincing RRL H104α. These detections were presented to 12th IAU General Assembly on August 31, 1964- due to the small difference of about a month in these detections the two Russian groups agreed to consider this day to be the official date of discovery of radio lines emitted by highly excited atoms and were subsequently named “Radio Recombination Lines” or RRLs, as the radiation is preceded by the recombination. Following this a number of investigators detected RRLs from hydrogen from different sources. In 1966 Lilley et al. reported the detection of RRLs from helium in omega, which was followed by detection of carbon RRL C109α by Goldberg and Dupree(1967). These investigations well established the field of RRL giving impetus to astronomical research using RRL as a tool to probe into space. Today the RRLs have become an effective tool in understanding the insterstellar medium, probing its different components and understanding the physical properties like density and temperature. The next section discusses briefly upon interstellar medium.

1.3 The Interstellar Medium

RRL form an effective tool in understanding the Interstellar Medium(ISM), which forms only about 3% of the total mass of the Galaxy (1.5×10^{11} $M_{\odot}$) but occupies a greater volume. The study of ISM is essential in understanding the evolutionary processes occuring in the Galaxy, there is a continous exchange of matter between the ISM and the stars. The stars are formed out of the gas in the ISM due to gravitational collapse of clouds. Such collapse eventually starts the thermonuclear reactions at its center where the hydrogen is burned to helium and subsequently other higher elements are formed. Thus the star becomes an element sysnthesising factory. The star returns matter to the ISM in the form of stellar winds,novae and supernovae explosions enriching the ISM matter with new elements and changing its chemical composition. The radiation from the star also effects the chemical and physical properties of the ISM. The star ionizes the surrounding ISM by UV radiation forming **HII** regions which expand and eventually leave the star. Ultimately a part of the mass gone into the stars returns to the ISM only to give birth to a new generation of stars with enriched chemical composition. This symbotic relation between the stars and ISM has been termed as astration in the literature. Hydrogen forms a major component of the ISM accounting for about 70% of the mass, about 28% is accounted by helium the remaining 2% by all other elements. About half of this hydrogen is in the form of molecules inside dense, cold clouds. The remaining half is either in ionized or atom form. These forms of hydrogen are organized in different components of the ISM. The molecular hydrogen is radio silent, though it can emit infrared lines. Its study through direct observation of infrared radiation is however limited due to high opacity at this wavelength. It is more conveniently studied by indirect means, by radio emission from other molecules like CO having exciting collisions with it. The next section briefly discusses upon the different components of the interstellar medium.

1.3.1 Components of the Interstellar Medium

The most abundant element in the ISM is hydrogen as has been already mentioned. This hydrogen is present in the form of a variety of components both neutral as well as ionized, having different densities and temperatures, since the ISM is dynamically active. The regions surrounding the stars ionized by its UV radiation are called as emission nebulae since their spectra show lines in emission. These nebulae emit both continuum as well as line radiation. The continuum radiation is emitted by the interaction of free electrons with ions, where as the line radiation comes from the deexciation of excited atoms and ions. The nebulae are further classified as diffuse nebulae, supernova remnants and planetary nebulae. The diffuse nebulae are connected with the birth of the stars where as the later originate from the death of stars, which either died in a violent explosion(supernova) or have faded due to their old age(planetary nebulae). All of these emit in the radio spectrum. The atoms in these nebulae are ionized by the stars UV radiation. The newly formed ions and electrons either recombine to lose their energy in the form of photons or by collision with the neighbouring atoms, thus transfering the stars radiation energy to its surrounding gas, heating it up. The diffuse nebulae are of irregular shapes and sizes and lie close to the cold clouds from which they originate. The ionizing photons from the central star penetrate into the surrounding gas untill they become dilute enough, hence the gas has an ionization boundary. The part of the region where the central star is capable of maintaining a balance between ionization and recombination is termed as stromgren sphere. On the other hand some times the photons escape into the ISM due to insufficient amount of gas to stop them. Depending upon the distribution of the adjacent cold gas and the amount of radiated energy from the star the diffuse nebulae take different shape and sizes. The more the radiant energy the more can it ionize and hence a larger ionized region, where as the distribution of the cold gas determines the way the photons transfer their energy to the gas causing it to expand and giving it a shape. In most of the diffuse nebulae the hydrogen is almost all ionized and these are called **HII** regions (**HI** being the neutral atomic hydrogen), which are hot regions with typical temperatures of the order of 10^4 K and densities in the range 1-10^4 cm^{-3} . The regions with $n_e>10^4$ cm^{-3} and sizes << 1pc are called ultra compact **HII** regions . Most of these regions have been observed using RRLs which have yielded valuable information about their physical properties like density and temperature.

Apart from the star surrounding **HII** regions, other distinguished diffuse components have also been recognised which have been termed as **Cold Neutral Medium**(**CNM**, T~80K) which are dense **HI; Warm Neutral Medium**(**WNM,** T<8000K, warm low density **HI,** Kulkarni & Heiles 1987), **Warm Ionized Medium**(**WIM,** T~10^4K, n_e~0.03cm^{-3} , McKee & Ostriker 1977), **Hot Ionized Medium**(**HIM,** T~10^6K, n_e~0.003cm^{-3}) and the **Extended Low Density Warm Ionized Medium**(**ELDWIM,** T~10^3 to 10^4 K, n~1-10cm^{-3}). However the theory of RRL(Shaver 1975) suggests that below 1GHz RRL are unobservable from high density **HII** regions due to continuum opacity and pressure broadening. The ELDWIM seems to be a more favourable candidate for the low frequency RRLs. The study presented here is in fact the observation of ELDWIM at 1.4 GHz and 327MHz, using the Westerbrok Synthesis Radio Telescope(**WSRT**) and the Ooty Radio Telescope(**ORT**). The following section discusses briefly the significance and the current understanding of ELDWIM.

1.3.2 Extended Low Density Warm Ionized Medium(ELDWIM) & Present work

The ELDWIM was first considered by Mezger(1978) who called it as the Extended Low Density fully ionized gas, which extends from the galactic center to ~13kpc and ~100pc above and below the plane. However continuum radiation from this particular medium was first discovered by Westerhout(1958) in his Dwingeloo survey, who also calculated the upper limits on density and total mass of ionized hydrogen in the Galaxy. Later investigators have switched to call this component as Extended Low Density Warm Ionized Medium(Petuchowski & Bennett 1993, Heiles 1994). The recent estimated densities of **ELDWIM** are 1~10cm^{-3} (Murray & Rahaman 2010), which is an order of magnitude higher than the **WIM,** with temperatures of the order of 3000-8000K. It has been proposed that more than 50% of Lyman continuum photons originating in the inner galaxy are responsible for ionizing the ELDWIM. The origin, morphology and ionization mechanism of this medium are uncertain. It has been thought to be as a collection of evolved HII regions(Shaver 1976) or perhaps it forms the outer envelopes of HII regions(Anantharamaiah 1985). Where it has been suggested that by the sizes of HII region envelopes inferred from observations and due to their large number, almost every line of sight intersects these envelopes in the inner Galaxy($l<40^{o}$)giving the observed Galactic ridge recombination lines.

The present work was encouraged by these facts and an attempt has been made to investigate the physical properties by modelling of ORT and WSRT data. The WSRT data was used to detect the helium line to understand the ionization spectrum. The helium ionization potential(24.6eV) is higher than that of hydrogen(13.6eV). The detection and the amplitude of helium would indicate the ionization condition of ELDWIM. Earlier RRL observations have indicated that the ratio of the number of helium to hydrogen ions(N_{He+}/N_{H+}) in the ELDWIM is in the range 0 to 0.054(Heiles et.al.1996b). This ratio is smaller than the generally accepted cosmic abundance of He(N_{He}/N_{H} ~ 0.1), indicating all helium in ELDWIM to be essentially unionized. According to order of magnitude calculations this observed ratio in ELDWIM requires the surface temperature of the ionizing star to be <35000K, if a standard HII region condition were to be considered. The current knowledge of initial mass function and the total Galactic star formation rate make it difficult to realize such a cool spectrum together with the total Galactic ionization requirement for the ELDWIM and the HII regions. This has been called as the ***ionization problem***. However such calculations are not completely reliable or exhaustive and alternate ways to explain the spectrum must be found.

Helium RRL from ELDWIM are much weaker than the hydrogen RRL, hence longer integration time is needed to detect them from specific directions. Earlier attempts to detect He RRL were made by averaging spectra obtained towards different directions in the inner Galaxy. Such an attempt was also under taken in the present work using previous ORT data. While such spectrum provide information about the average helium ionization, they are not suitable to address the *ionization problem*. Here an attempt(WSRT observations) has been made to observe specific directions with intense hydrogen lines with an intention to detect helium RRL as well. The regions exhibiting double components were avoided in order to exclude compact HII regions. A sensitive non-detection of He RRL can also be used to deduce an upper limit for its ionization condition. These regions were choosen by refering the literature in order to make sure that the regions are true representatives of ELDWIM. The WSRT data has produced a few He line detections. Higher values of the ratio N_{He+}/N_{H+} than earlier values have been obtained towards many of these detected positions. A high value of 0.082 has been seen towards G17.4 +1.5 which is ~ 0.1 within errors. An attempt has been made to correlate these ELDWIM clouds with the surrounding HII regions within a distance of 500pc. The weighting scheme produces consistent results of He detection w.r.t the number of HII regions surrounding the line originating region.

The ORT data has been used to obtain a map in RRL at a frequency of 327MHz which yet didn't exist. The area covered is in the range ,$-30 \leq l \leq 78$ with $b=\pm3^{o}$. RRL observations in the higher latitude which didn't exist so far form a new study of ELDWIM in these regions. The scale height of these ELDWIM clouds has also been obtained in order to have an idea of distribution of ELDWIM along the Galactic latitude. Along with this the software required to analyse the ORT as well as WSRT data were discretly developed independently.

Chapter 2

Understanding Recombination Lines

2.1 Physics of RRL

The physics of RRL is a well understood subject. The various physical processes occuring in gaseous nebulae have been mathematically formulated and cross checked with observations. The various interactions occuring between different species of components of a gaseous nebulae give rise to the observed radiation. The acceleration of electrons encountering ions give the thermal Bremsstrahlung. Atomic and molecular transitions give line radiation. As discussed in chapter-1, one of the components of the interstellar medium is HII regions surrounding young massive stars. Inside the HII regions the hydrogen is ionized to proton and electron by the photons of the star. The electrons recombine to proton at an excited state and then cascade down to produce recombination lines. The HII regions are a primary source of RRL at higher frequencies. An ionization equilibrium exists in the HII regions which implies continous ionization and recombination of hydrogen. A given star can ionize hydrogen to a certain extent, which can be understood as follows. As the photon flux propagates into the gas it is deprived of photons that can ionize the gas. An equilibrium state is established within a certain region within which the number of ionizations equals the number of recombinations. For a spherically symmetric ionized region the radius of the sphere is called the stromgren radius. This radius is a function of the type of star and the density of the gas surrounding the star(Stromgren 1939). If the size of the nebulae is small compared to the ionizing capacity of the star then photons at the boundary escape into the interstellar medium(density bound). However if this size is larger then the gas will be ionized to certain finite distance and those HII regions are said to be *ionization bounded*.

The recombinations occur at the rate of 10^4 to 10^8 per sec, where as the lifetimes of photo-ionization are of the order of ~10^8 sec which is extremely large compared to life times of the excited levels. Hence a continuos ionization of hydrogen always occurs.

The photoelectrons acquire kinetic energy from the photons of the star. The ionization potential of hydrogen is 13.6eV, the energy of the photon in excess to this is acquired by the electron which goes into heating the gas. The electron-electron collisions in the nebula are perfectly elastic. The electrons soon acheive a common temperature due to collisions amongst themselves. Also the electrons move much faster than the ions and hence undergo a larger number of collisions amongst themselves which thermalizes them. However the collision of electrons with the heavy ions gives rise to bremstrahlung radiation. The acceleration of the electron leads to the production of a number of continuum photons which loosely speaking forms a flat spectrum, since the encounter of electron with the ion(mostly proton) is very short when compared to the radio wavelength.

The mathematical formulation of the essential processes in the interstellar gaseous nebulae is given in the following sections.

2.1.1 RadiationTransfer

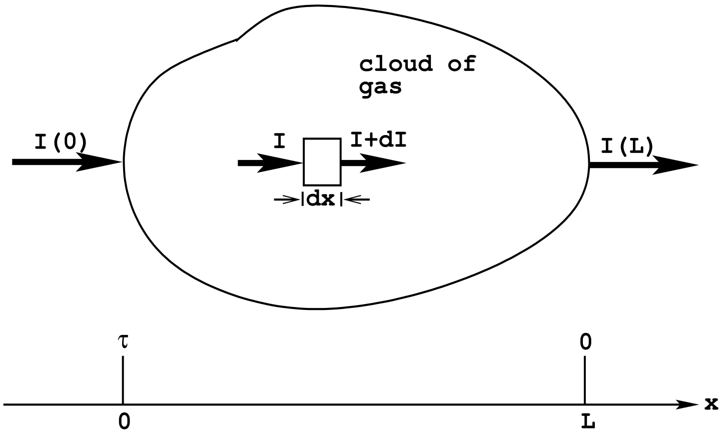

Fig 2-1: Radiation transfer through a medium

Before proceeding on to the mathematical understanding of the relevant astrophysical processes it would be more beneficial to first consider the radiation transfer through a medium. Radiation transfer involves loss and gain of radiation as it propagates through the gas. These gains and losses are incorporated in the absorption and emission coefficients of various processes. The incident radiation(I(0) in fig-1) loses intensity due to absorption and scattering in other directions than that of propagation and its intensity reduces. On the other hand photons are also added to the direction of propagation by emission from the medium in the direction of propagation. This change in intensity of radiation can be written as

$$dI = -I\kappa\, dx + j\, dx \tag{2.1}$$

where x is along the line of sight of the observer, κ is the absorption coefficient which accounts for the losses in the radiation. Where as j stands for all the additions to the radiation in propagation. The first term gives the differential extinction of intensity and the second term gives differential reinforcement of intensity. The intensity of radiation reaching the observer is obtained by integrating the above equation all along the length from farthest side of the cloud to the point of observation. This can be written as

$$I(L) = \int_0^L dI = I(\tau)e^{-\tau} + \int_0^{\tau} \frac{j}{\kappa} e^t\, dt \tag{2.2}$$

The first term on the extreme right hand side of above equation is just the incident background radiation that is attenuated by the cloud where as the second term takes care of the contribution from the cloud, both emission and absorption. The new quantity τ introduced here is called the *optical depth* of the cloud defined as

$$\tau = -\int_{x_1}^{x_2} \kappa(x)\, dx \tag{2.3}$$

integrated along the length of the medium. Its a convenient quantity to account for the loss of radiation. In most cases κ is not known and also it varies along the line of sight. τ takes care of the variation of absorption coefficient in the integral form. The factor $e^{-\tau}$ is directly proportional to the attenuation or the loss of radiation and $(1 - e^{-\tau})$ is proportional to the fraction of original surviving radiation at the end of propagation. The ratio j/κ appearing in the equation (2.2) is called the source function of the medium usually denoted as S. In a medium where radiation has acheived an equilibrium with matter(thermal equilibrium), source function is quite easy to specify. From Kirchoff's law of thermodynamics

$$j/\kappa = B_\nu(T) \qquad (2.4)$$

$B_\nu(T)$ is the Planck function characterising the radiation from a black body given by

$$B_\nu = \frac{2h\nu^3}{c^2}\frac{1}{e^{h\nu/kT}-1} \qquad (2.5)$$

In the radio regime where the photon energy hν is much smaller compared to kT ($h\nu << kT$) the above function reduces to

$$B_\nu = \frac{2\nu^2 kT}{c^2} \qquad (2.6)$$

which is known as the Rayleigh-Jeans approximation of the Planck Function.
Using this, the radiative transfer equation(2.2) can be written as

$$I_\nu = I_{0\nu}e^{-\tau_\nu} + B_\nu\left(1-e^{-\tau_\nu}\right) \qquad (2.7)$$

Where the subscript ν indicates that the radiation is considered at frequency ν alone. $I_{0\nu}$ is the initial incident radiation that gets attenuated by the medium. The radiation intensity can also be expressed in terms of brightness temperature $T_{b\nu}$ which is the temperature at which $B_\nu(T_{b\nu})$ would produce the observed intensity. The above expression in terms of brightness temperature can be written as

$$T_{b\nu} = T_{0b\nu} + T\left(1 - e^{-\tau_\nu}\right) \qquad (2.8)$$

It is quiet common in radio astronomy to use the brightness temperature instead of intensity to describe the radiation from heavenly bodies. This also makes it compatible with the telescope jargon, where the receiver and the antenna are thought in terms of temperature.

The next step would be to acquire an understanding of optical depth due to different processes and apply this knowledge in the interpretation of the observed radiation.

2.1.2 The Thermal Continuum Radiation and its Optical Depth

In a typical HII region the continuum radiation comes from two components, the heated dust and the deccelerative collisions of charged particles, the Bremsstrahlung radiation(a german word for braking radiation). Bremsstrahlung radiation is also called the free-free emission, since the particles are unbounded in the initial and final states of this process. The important quantity that should be calculated regarding Bremsstrahlung is its absorption coefficient. The encounter of the electron with the ion involves a variety of impact parameters. When the interaction takes place at close distances the fields are intense and hence larger accelerations are produced. This leads to continuum radiation in the X-ray regime. For the radio regime these interactions occur at larger distances and hence smaller accelerations are involved. The difference between the initial and final kinetic energy of the electrons during collisions goes out as photons. The emitted photon energies are negligible compared to the kinetic energy of the electrons. Another assumption that is made during the calculation of Bremsstrahlung absorption coefficient is, the time taken by the electron to undergo a 90° turn is considered to be much larger than the reciprocal of the emitted frequency. Implying that the period of the emitted wave train is much shorter than the period of interaction. Integration is performed over a limited range of impact parameters with the electrons having a Maxwellian distribution. Following Oster(1961) the free-free absorption coefficient valid for the radio regime is given by

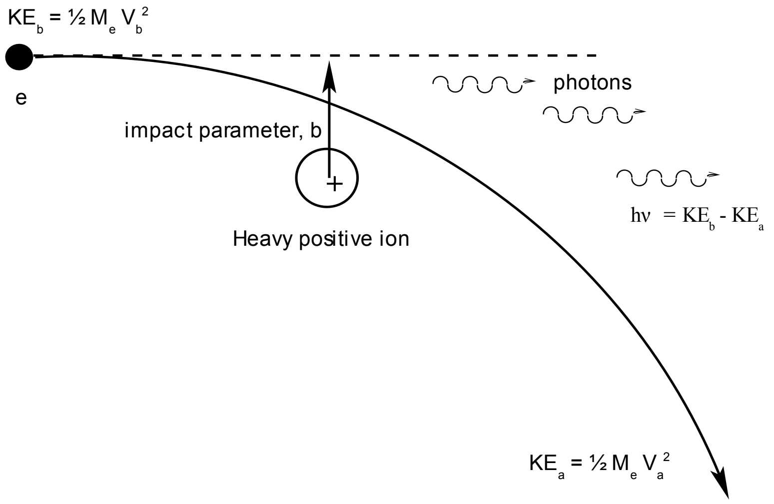

Fig2-2: Electron-Ion collision releasing bremsstrahlung radiation.

$$K_c = \frac{N_e N_i}{\nu^2 T_e^{3/2}} \left[\frac{8Z^2 e^6}{3c(2\pi)^{1/2} (M_e k)^{3/2}} \right] ln \left[\frac{(2kT_e)^{3/2}}{\pi \nu Z \gamma^5 M_e^{1/2} e^2} \right] \tag{2.9}$$

where γ = 7.87 x 10^9 sec^{-1} , N_e,N_i are the electron and ion densities. T_e is the electron temperature. Z is the atomic number of the ion, M_e is the electron mass, ν is the frequency and e is the electronic charge. Substituting numerical values for the parameters in the eqn-2.9, the continuum optical depth can be written(Shaver 1975) as

$$\tau_c = 0.0314 \frac{EM}{\nu^2 T_e^{3/2}} \left[1.5 ln T_e - ln(20.18 \nu) \right] \tag{2.10}$$

which has been approximated by Altenhoff et.al(1960) as

$$\tau_c = 8.235 x 10^{-2} \ \nu^{-2.1} T_e^{-1.35} \ EM \tag{2.11}$$

EM is the emission measure, quantified as

$$EM = \int_0^s N_e^2 ds$$

N_i is the total ionic density. The units are N_i,N_e (cm^{-3}), EM(pc cm^{-6}), T_e(K) and ν(GHz). The continuum optical depth is a function of frequency. In a typical HII region the gas is optically thin at higher frequencies(ν > GHz) and thick at lower frequencies. Equation (2.8) due to the contribution from the gas alone and neglecting the background can be written as

$$T_{b\nu} = T_e \left(1 - e^{-\tau_{c\nu}} \right) \tag{2.12}$$

where T_e is the electron temperature and $\tau_{c\nu}$ is the continuum optical depth at frequency ν. In the optically thin case $\tau_{c\nu}$ << 1, the above equation reduces to

$$T_{b\nu} = T_e \ \tau_{c\nu} \tag{2.13}$$

where as for a optically thick case $\tau_{c\nu} >> 1$, so that the observed brightness temperature becomes

$$T_{b\nu} = T_e \tag{2.14}$$

In practice the telescope measures the source flux density rather than the source intensity as given by equation (2.7). The flux density is the integral of intensity over the solid angle of the source Ω_S

$$S_\nu = \int_{\Omega_S} I_\nu d\Omega \tag{2.15}$$

The two limiting cases for the flux density take the form

$$\begin{aligned} S_\nu \;\alpha\; \nu^{-0.1} \;,\; \tau_{c\nu} \ll 1 \\ S_\nu \;\alpha\; \nu^2 \;,\; \tau_{c\nu} \gg 1 \end{aligned} \tag{2.16}$$

When the medium is optically thick the radiation from it is like that from a blackbody at temperature T_e . Where as the spectrum is nearly flat for the optically thin case having a weak dependence on frequency as shown in fig-3. The observations of Orion Nebula(Terzian & Parrish, 1970) are very well described by these limiting cases. ν_t is the turn over frequency which demarkates the two regimes of optical depth.

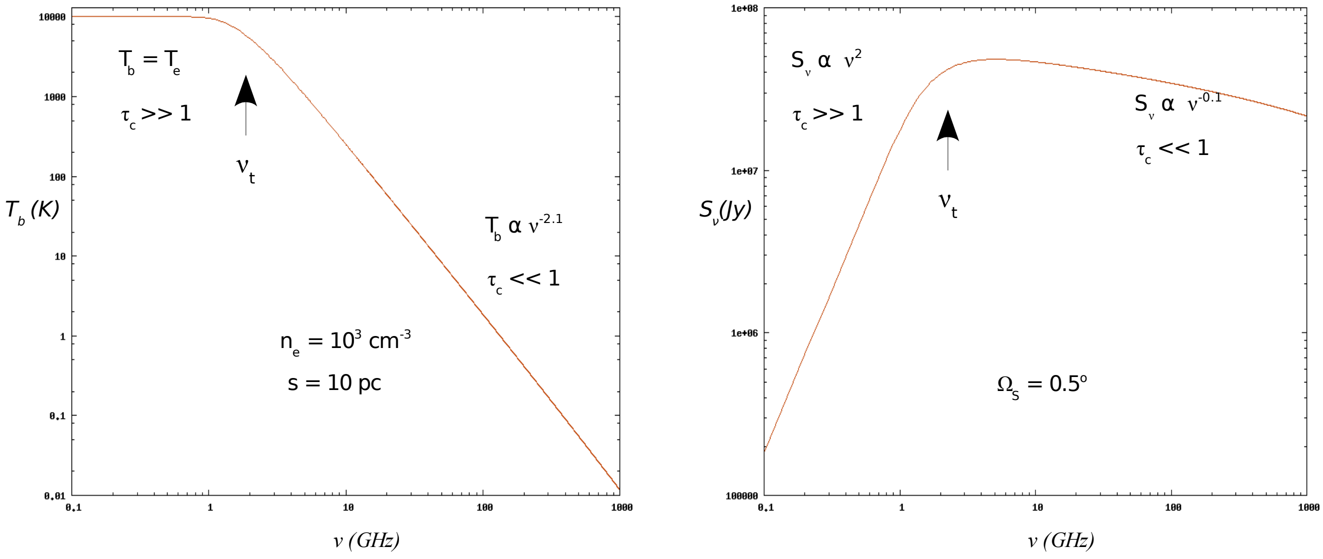

Fig 2-3: Plots of continuum Brightness Temperature / Flux Vs Frequency for hydrogen.

2.1.3 RRL Frequencies

For the radio regime the Bohr's formula is very well applicable. In HII regions where the hydrogen continuously ionizes and recombines, atoms end up in highly excited states. The excited atoms cascade down to lower energies . The jump from a higher level to lower level can involve a single step(i.e principal quantum number Δn = 1) or multiple steps(Δn = 2,3 etc). The probability of dexcitation in a single step has the maximum probability and hence the line is more intense. A transistion from a energy level n+1 to n in hydrogen is denoted by a standard notation as H$n\alpha$. In general for an arbitrary element, H can be replaced by X or by the symbol of the particular element. Similarly transistions involving Δn=2 are represented as H$n\beta$ and likewise. The frequency of the photon when the hydrogenic atom(Z=1) makes a transistion from a energy level n_2 to energy level n_1 is given by

$$\nu = \frac{Z^2 e^4}{8\varepsilon_0^2 h^3}\left[\frac{m_e M_x}{m_e + M_x}\right]\left(\frac{1}{n_1^2} - \frac{1}{n_2^2}\right) \tag{2.17}$$

M_x is mass of the core of the hydrogenic atom X and m_e is the mass of the electron. This formula can be further simplified by writing in terms of Rydberg constant R_∞ ,

$$\nu = R_x c Z^2\left(\frac{1}{n_1^2} - \frac{1}{n_2^2}\right)$$

where

$$R_x = \frac{R_\infty}{\left(1 + \frac{m_e}{M_x}\right)} \quad ; \; R_\infty = 109737.31 cm^{-1}$$

Two useful programs for RRL calculation and search have been given in appendix-I.

2.1.4 The Line Radiation: Coefficients and Optical depth

The line radiation coming out of a medium depends on the level populations of atoms. In thermodynamic equilibrium the number of atoms occupying an energy level n is given by the Saha-Boltzmann equation

$$N_n = N_e N_{x^+} \left(\frac{h^2}{2\pi m_e k T_e} \right)^{3/2} \frac{\omega_n}{2} e^{\chi_n} \tag{2.18}$$

Units are N_{x+}, N_e (cm^{-3}) of ion and electron densities, T_e(K) of electron temperature. $\omega_n = 2n^2$ is the statistical weight of the level n. The remaining terms have the usual meaning.

$$\chi_n = \frac{E_n}{kT_e} = \frac{hcR_x Z^2}{n^2 kT_e} \approx \frac{1.58 x 10^5 Z^2}{n^2 T_e} \tag{2.19}$$

E_n is the ionization potential of the level n. The number of spontaneous transitions(cm^{-3} sec^{-1}) from upper level n to lower level m are given by

$$S_{n,m} = N_n A_{n,m} \tag{2.20}$$

where N_n are the number of atoms occupying the level n. $A_{n,m}$ is the Einstein-A coefficient for spontaneous emission. The net number of induced transitions(cm^{-3} sec^{-1}) from the level n to the level m is given by ,

$$I_{n,m} = \left[N_n B_{n,m} - N_m B_{m,n} \right] I_\nu \tag{2.21}$$

Here $B_{n,m}$ and $B_{m,n}$ are Einstein-B coefficients of induced emission and absorption respectively for levels n and m respectively, which are related as

$$B_{n,m} = \frac{c^2}{2h\nu^3} A_{n,m} \; ; \; B_{n,m} = \frac{\omega_m}{\omega_n} B_{m,n} \tag{2.22}$$

It is interesting to compare radiation contribution from spontaneous and induced transitions in the radio regime. The ratio of stimulated to spontaneous transitions can be written using the above equations as,

$$\frac{B_{n,m} I_\nu N_n}{A_{n,m} N_n} = \frac{1}{e^{h\nu/kT_e} - 1} \approx \frac{kT_e}{h\nu} \tag{2.23}$$

corresponds to the frequency of photon resulting from transition from level n to m. For radio regime, hν << kT$_e$, so this ratio is enormously large. i.e the contribution from stimulated emission is very large compared to spontaneous emission. In general it is inversly proportional to frequency for a given temperature T$_e$. Normally the stimulated emission is included into absorption by making it negative and it is called negative absorption.

The line emission coefficient is given by,

$$j_\nu^* = S_{n,m}\frac{h\nu}{4\pi}\varphi_\nu$$

$$= N_n A_{n,m}\frac{h\nu}{4\pi}\varphi_\nu \qquad (2.24)$$

* indicates Local Thermodynamic Equilibrium(LTE) and φ_ν is the profile function of the line which is normalised as

$$\int_{-\infty}^{+\infty}\varphi_\nu d\nu = 1 \qquad (2.25)$$

Next, the line absorption coefficient can be written as,

$$\kappa_\nu{}^* = I_{n,m}\frac{h\nu}{4\pi I_\nu}\varphi_\nu$$

$$= \frac{h\nu}{4\pi}\varphi_\nu\left(N_m B_{m,n} - N_n B_{n,m}\right) \qquad (2.26)$$

Using Boltzmann's equation for the population of two quantum levels

$$\frac{N_n}{N_m} = \frac{\omega_n}{\omega_m}e^{-h\nu/kT_e} \qquad (2.27)$$

and the above equations, the LTE absorption coefficient can be written as

$$\kappa_\nu^* = \frac{h\nu}{4\pi}\varphi_\nu N_m B_{m,n}\left(1 - e^{-h\nu/kT_e}\right) \qquad (2.28)$$

which for the radio regime approximates to

$$\kappa_\nu^* \approx \frac{h^2\nu^2}{4\pi k T_e}\varphi_\nu N_m B_{m,n} \tag{2.29}$$

For the sake of convenience we express B coefficient in terms of oscillator strength $f_{m,n}$

$$f_{m,n} \approx \frac{mch\nu}{4\pi^2 e^2}B_{m,n}$$

$$\frac{f_{m,n}}{m} = K(\Delta m)\left[1 + \frac{3}{2}\frac{\Delta m}{m} + \ldots\right]$$

$$with\ K(1) = 0.1908\ ,\ K(2) = 0.02633\ ,\ K(3) = 0.00810\ \ldots$$

and use Saha-Boltzmann equation to obtain N_m. After replacing the numerical values of various constants and simplification the LTE absorption coefficient can be written as,

$$\kappa_\nu^* = 1.628\times10^{-3}\ \frac{N_e N_{x^+}}{T_e^{5/2}}\nu\, n^3 \varphi_\nu e^{\chi_n}\frac{f_{m,n}}{m}\ psc^{-1} \tag{2.30}$$

where N_e, N_{x+} (cm^{-3}) and T_e(K). The LTE optical depth can be written as

$$\tau_\nu^* = \int_0^S \kappa_\nu^* ds$$

S is the path length through the medium.

2.2 Line Broadening Mechanisms

2.2.1 Lorentz Broadening

RRL radiation undergoes several kinds of broadenings. The foremost amongst these is the natural broadening which is due to the intrinsic property of the atom that the emitted wave train is finite and its amplitude exponentially decreases with time.

The profile due to this broadening mechanism is given by

$$\varphi(\nu) = \frac{\gamma}{\pi^2\left[4(\nu - \nu_0)^2 + (\gamma/2\pi)^2\right]} \tag{2.31}$$

where γ is the called the damping constant given by

$$\gamma = \frac{8\,\pi^2 e^2}{3\,m\,c^3}\nu_0^2$$

which has been derived from classical considerations of a damped harmonic oscillator. The damping constant can also be derived quantum mechanically as

$$\gamma = \sum_{n'} A_{nn'} \tag{2.32}$$

where the sum of the spontaneous transition rate coefficient is carried out over all lower states n'. This gives the broadening of one level. When two levels are involved it turns out that the damping constant is equal to the sum of the individual damping constants,

$$\gamma = \gamma_{n_2} + \gamma_{n_1} \tag{2.33}$$

The total spontaneous transition rate from level n_2 is,

$$\gamma_{n_2} = \sum_{n_1=1}^{n_2-1} A_{n_2,n_1} \tag{2.34}$$

with a similar consideration for the other level the full width at half maximum (FWHM)for the line can be written as,

$$\frac{\Delta\nu}{\nu_0} = \frac{1}{2\pi\nu_0}\left(\gamma_{n_2} + \gamma_{n_1}\right) \approx \frac{1}{\pi\nu_0}\sum_{n_1=1}^{n_2-1} A_{n_2,n_1}$$

the last approximation takes into account the fact that the rates are about the same for the upper and the lower levels when n >> Δn. In the radio regime the sum, A_n(of spontaneous probabilites from level n), in the above expression can be approximated(Sobelmann et.al 1995) as

$$A_n \approx 2.4\times10^{10}\frac{\ln n}{n^5} \;,\; n > 20$$

Using this approximation the FWHM for n>20 can be written as

$$\frac{\Delta\nu}{\nu_0} \approx \frac{1.2\times10^{-6}\;\ln n}{n^2} \qquad (2.35)$$

For example at n = 271, this fractional width would be 9.15 x 10^{-11} or 27 x 10^{-3} kms^{-1} which is extremely small when compared to those due to other broadening mechanisms, which are about to follow. Hence the intrinsic broadening is mostly neglected.

2.2.2 Doppler Broadening

Doppler broadening occurs from radiation emitted by moving atoms. If a Maxwellian distribution of gas were to be considered then at a temperature T the atoms would have a velocity distribution given by

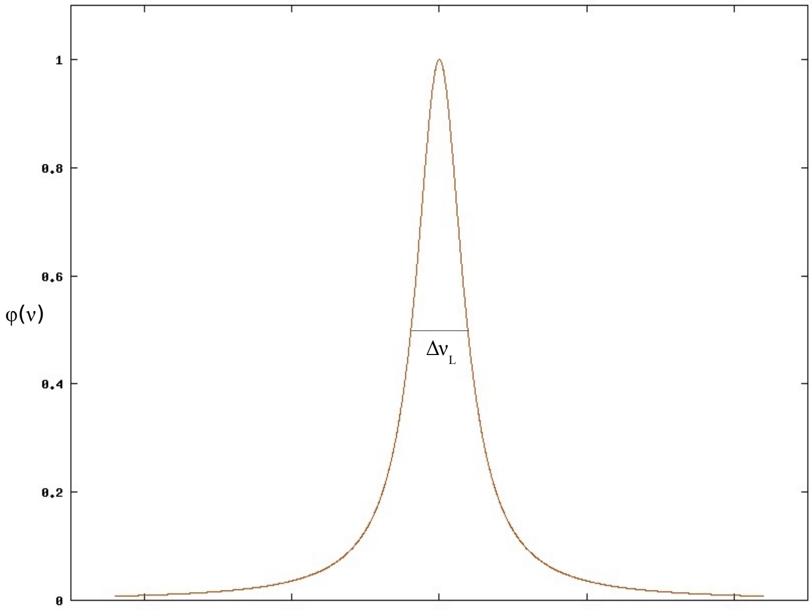

Fig 2-4: The Lorentz line profile as per (2.31), the broad wings are characteristic of this profile, here $\nu_0 = 1.4\ 10^{15}$ *Hz .*

$$\frac{dn_v}{n} = 4\pi\left(\frac{M}{2\pi kT}\right)^{3/2} e^{-Mv^2/kT} v^2 dv \tag{2.36}$$

where dn_v is the number of atoms with speed between v and v+dv. n is the total number of atoms and other terms have the usual meaning. The probability that an atom has a x-component of velocity between v_x and $v_x + dv_x$ is given by

$$n_x dv_x = n\left(\frac{M}{2\pi kT}\right)^{1/2} e^{-Mv_x^2/kT} dv_x \tag{2.37}$$

Due to symmetry the x-axis could be chosen along any direction. So it can be aligned along the line of sight of the observer, to consider the relative motion of atoms.

Applying classical formula for Doppler shift we can write for the frequency shift in the observed line radiation as

$$\Delta\nu = -\frac{\Delta v_x}{c}\nu_0 \tag{2.38}$$

where ν_0 is the rest emission frequency from the atom. Considering a standard HII region of temperature 10^4 K the most probable velocity of the hydrogen atom would be $v_p = (2kT/M)^{1/2} \sim 13\ \mathrm{kms}^{-1}$. This can be compared with the intrinsic broadening in the previous section. This justifies the fact that intrinsic broadening is negligible when compared to Doppler broadening. The intensity interval of the line dI(v) between frequency ν and $\nu+d\nu$ is proportional to the number of the emitters dn_x in the velocity interval v_x and v_x+dv_x in the beam of the antenna. In the case of pure Doppler broadening this leads to a gaussian profile of the line so that the total intensity I is proportional to the total number of emitters n. This pure Doppler broadened line intensity distribution can be written as,

$$I(\nu) = I\,\varphi_G(\nu) \tag{2.39}$$

where the gaussian profile function $\varphi_G(\nu)$ is given by

$$\varphi_G(\nu) = \frac{2}{\Delta\nu_G}\sqrt{\frac{\ln 2}{\pi}}\; e^{-4\ln 2\left(\frac{\nu_0-\nu}{\Delta\nu_G}\right)^2} \tag{2.40}$$

$\Delta\nu_G$ is the FWHM of the profile given by

$$\Delta\nu_G = \frac{2\nu_0}{c}\sqrt{\ln 2\,\frac{2\,kT}{M}} \tag{2.41}$$

Along with doppler effect the line is also broadened due to microturbulence which is the motion of cells within the beam of the telescope. Usually the beam is much larger and the cells are unresolved. Hence this relative motion of cells is termed as microturbulence. The velocity distribution of these cells is gaussian. The observed line profile is a result of convolution of the thermal and turbulence gaussians, which is another guassian with width equal to the quadratic sum of the two individual gaussians.

$$\Delta V_D^2 = \Delta V_G^2 + \Delta V_T^2 \tag{2.42}$$

Where ΔV_D is the resulting width, ΔV_G and ΔV_T are the thermal and microturbulence widths. The total Doppler width can also be written in terms of the gas temperature and

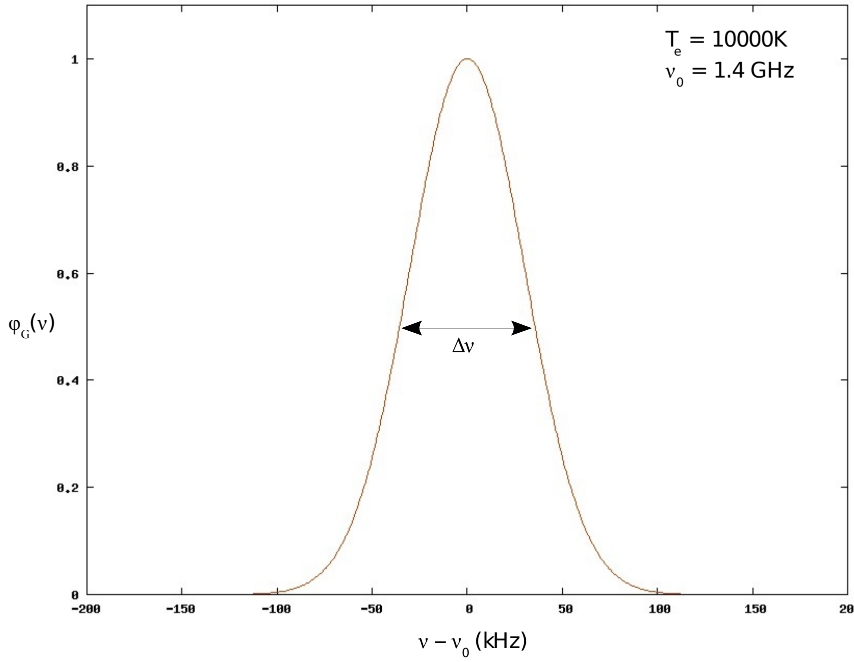

Fig 2-5: Normalized Gaussian Line Profile as per (2.40) for hydrogen, notice the short wings compared to Lorentzprofile.

turbulence velocity V_T as

$$\Delta V_D = 2\sqrt{\ln 2}\sqrt{\frac{2kT}{M} + \Delta V_T^2}. \tag{2.43}$$

2.2.3 Pressure Broadening

Pressure broadening occurs due to collision of the emitting atom with other species like protons, ions and electrons present in the astronomical plasma. Collisional broadening specifically for RRL have been calculated. Griem(1967) using modified classical theory obtained the ion(elastic) and electron(inelastic) impact broadenings as

$$\Delta\nu_{ci} \approx \frac{3}{2\sqrt{\pi}}\left(\frac{h}{2\pi m_e}\right)^2\left(\frac{M}{kT_e}\right)^{1/2} N_i n^2\left[\frac{3}{2}+\frac{2}{e^2}\ln\left(\frac{2n}{3}\right)\right]\left(0.5+\ln\left[\frac{m_e\lambda}{hn}\left(\frac{kT_e}{M}\right)^{1/2}\right]\right)$$

where $\Delta\nu_{ci}$ is the FWHM, the index i indicates ion impact, λ is the wavelength of the line, n is the principal quantum number and e is the base of natural logarithm. The other terms have their usual meaning. After simplification this can be approximated as

$$\Delta\nu_{ci} \approx \frac{6.7\times10^{-5}}{\sqrt{T_e}}N_i n^2\ln(172n)\left[\ln\left(9.4\times10^{-3}n^2\sqrt{T_e}\right)\right] \tag{2.44}$$

where N_i is in cm^{-3} and T_e is in K. The inelastic electron impact broadening is given by

$$\Delta\nu_{ce} \approx \frac{5}{3\sqrt{2\pi}}\left(\frac{h}{2\pi m_e}\right)^2\left(\frac{m_e}{kT_e}\right)^{1/2} N_e n^4\left[0.5 + \ln\left(\frac{2\pi kT_e\lambda}{hcn^2}\right)\right]$$

which has been evaluated(Griem 1974) as,

$$\Delta\nu_{ce} = \frac{5.16\times10^{-6}}{\sqrt{T_e}}\ln\left(8.25\times10^{-6}T_e\ n\right) \tag{2.45}$$

A more accurate quantum theory (Gee et.al 1976, Beigmann 1977, Smirnov 1985) gives the following results for the electron and ion impact broadenings

$$\Delta\nu_{ce} = 8.2\ N_e \left(\frac{n}{100}\right)^{\gamma} \left(1 + \frac{\gamma}{2}\frac{\Delta n}{n}\right) \tag{2.46}$$

N_e is in cm^{-3}, γ is a function of n which varies slowly in the radio regime. γ changes inversely with temperature, however this variation is small. The average value of γ is 4.5 .

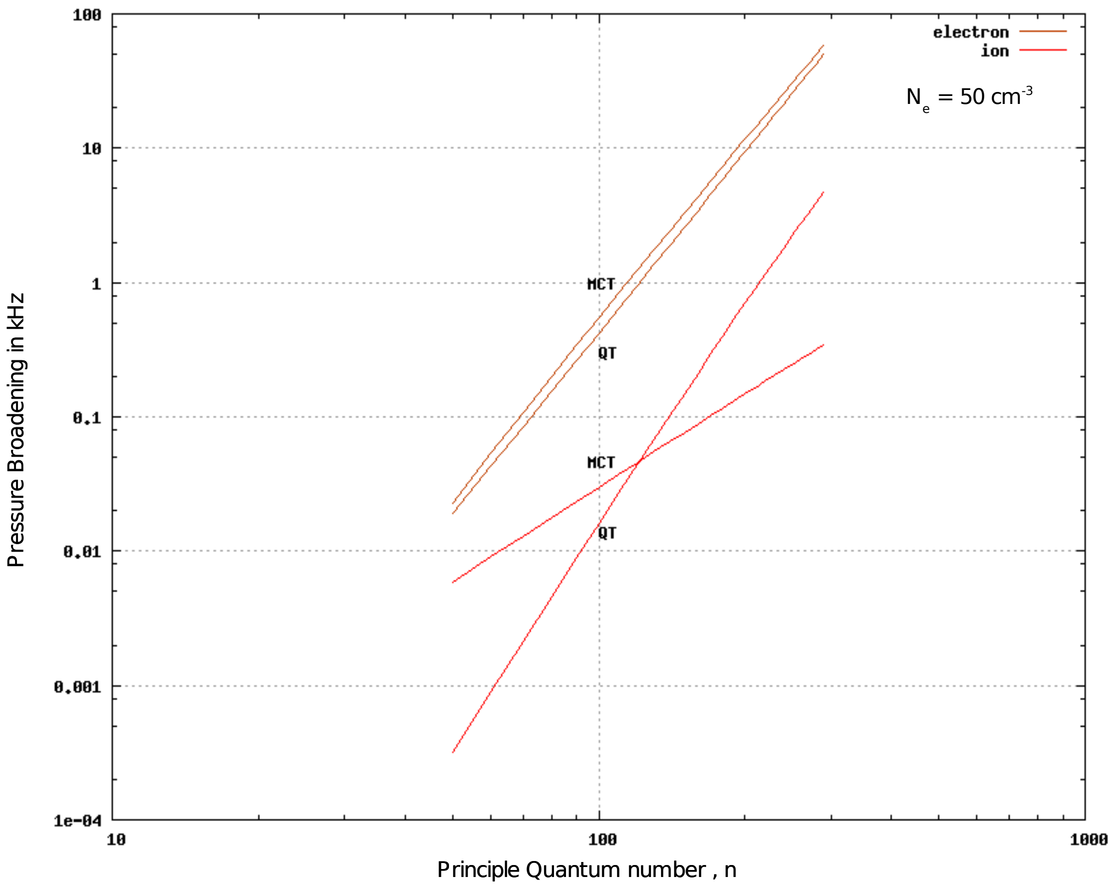

Fig 2-6: Pressure broadening of hydrogen RRLs from n=50 to 300. The upper lines correspond to electron impact brodening and the lower two correspond to ion impact broadening. MCT indicates the curves are from modified classical theory where as QT are from quantum theory. One can see that the electron impact broadening far exceeds that due to ions.

$$\Delta\nu_{ci} = \left(0.06 + 2.5\times10^{-5} T_e\right) \left(\frac{n}{100}\right)^{\gamma_i} \left(1 + \frac{2.8\,\Delta n}{n}\right) N_i \tag{2.47}$$

where $\gamma_i = 6 - 2.7 \times 10^{-5}\, T_e - 0.13(n/100)$. The figure above shows the theoretical plots obtained from the modified classical and the more recent quantum approaches. The plots clearly show that the electron impact broadening is more important than the ion impact broadening.

2.2.4 The Voigt Profile

The observed profile is a combination of profiles due to doppler(gaussian) and pressure(Lorentzian) which get convolved to produce a composite profile called the Voigt profile. The Doppler broadening involves the velocities of the atoms while the pressure broadening mostly concerns with the velocities of the electrons. The two velocity distributions are essentially independent and the two line profiles, a Gaussian(Doppler, $_{LD}$) and a Lorentzian(Pressure, $_{LP}$), get convolved to produce a composite line profile as

$$\varphi_L(\nu) = \int_{-\infty}^{\infty} \varphi_{LD}(\nu')\,\varphi_{LP}(\nu-\nu')\,d\nu' \tag{2.48}$$

which is normalized as

$$\int_{-\infty}^{\infty} \varphi_L(\nu)\,d\nu = 1 \tag{2.49}$$

so that the intensity function for the line can be written as

$$I_L(\nu) = I_0\varphi_L(\nu) \tag{2.50}$$

After substituting and convolving the respective Gaussian and Lorentzian profiles the Voigt profile can be expressed as

$$\varphi_L(\nu) = 2\sqrt{\frac{2}{\pi}}\frac{1}{\Delta\nu_D}H(a,v) \tag{2.51}$$

where the Voigt function H(a,v) is given by,

$$H(a,v) = \frac{a}{\pi} \int_{-\infty}^{\infty} \frac{e^{-t^2}}{a^2+(v-t)^2}\, dt \qquad (2.52)$$

The width of the Voigt profile has been approximated as(Smirnov 1985)

$$\Delta\nu_L = 0.5343\,\Delta\nu_{LP} + \sqrt{\Delta\nu_{LD}^2 + (0.4657\,\Delta\nu_{LP})^2} \qquad (2.53)$$

where $\Delta\nu_L$, $\Delta\nu_{LD}$ and $\Delta\nu_{LP}$ are the full widths at half intensity of the Voigt, Gaussian and the Lorentzian profiles. Plots of comparison of Doppler and Voigt broadenings have been given in the figure above for different densities as a function of principal quantum number(or frequency). The theoretical results obtained above have been tested in detail by observations on Orion nebula(Smirnov et al., 1984). A good agreement between theory and observations has been seen.

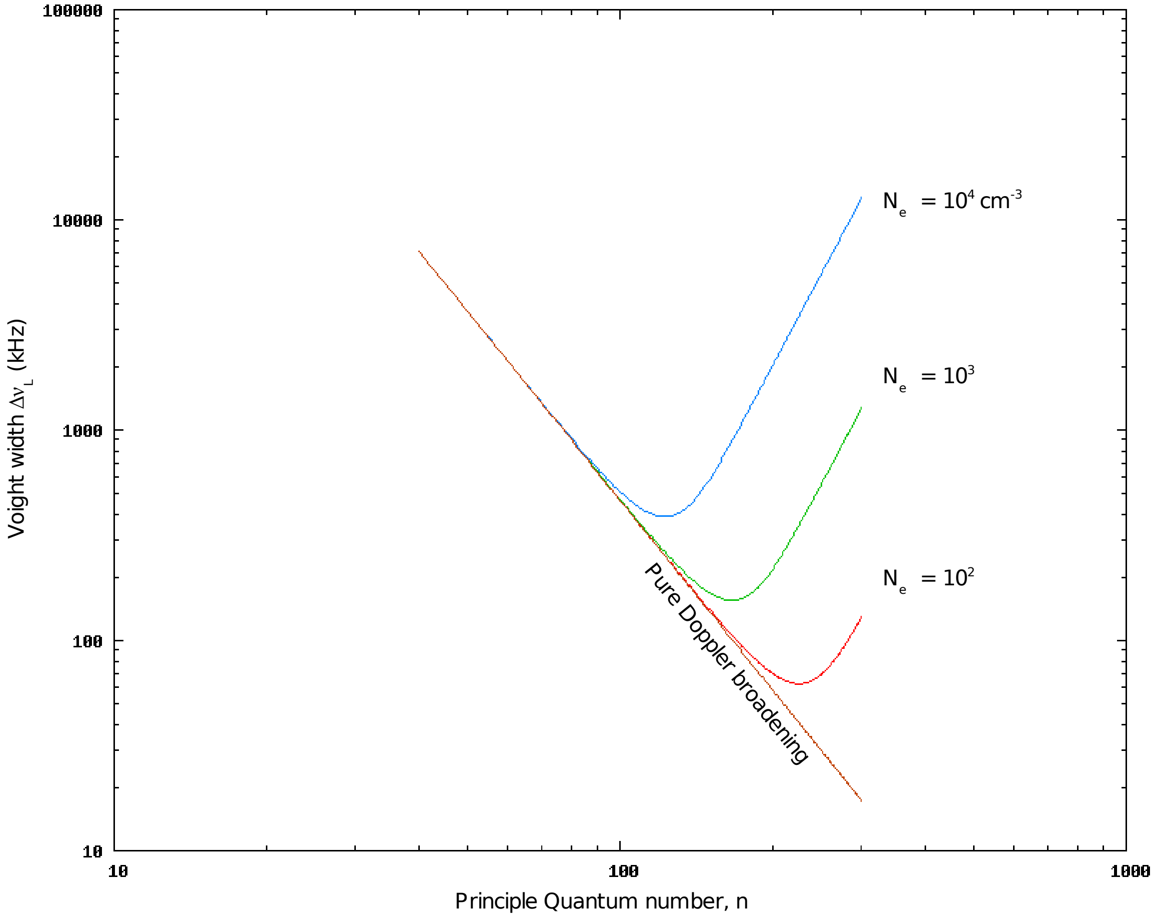

Fig 2-7: Plot of Voigt width Vs Quantum number, the straight line is pure Doppler broadening for a temperature of 10^4*K , the curved lines represent the sum of Pressure and Doppler broadenings for different densities according to smirnov approximation (2.53).*

2.3 Non-Local Thermodynamic equilibrium

2.3.1 Departures from LTE and the departure coefficients

The intensities of lines from astrophysical plasma do not fit with their LTE description. A thermodynamic equilibrium is a situation where the energy exchange between radiation and gas is efficient enough that a single parameter, temperature, can be used to describe both of them. The term local thermodynamic equilibrium is used when thermal equilibrium exists or is near to it in certain localized situations. Spectroscopically , LTE means the rates of in and out from a level are in detailed balanced. This applies to collisions as well. The rate into a level through one process is in balance by its reverse process. However in astrophysical plasma which is an open system this condition almost never holds. The astrophysical plasma is described by non-local thermodynamic equilibrium(non-LTE). In a non-LTE situation the level populations are written as

$$N_n = b_n N_n^{*} \tag{2.54}$$

where N_n^* is the LTE population given by Saha-Boltzmann equation and b_n is N_n departure coefficient which is a factor first introduced by Menzel(1937) to account the departures from LTE populations. The b_n factors are obtained by equating the various processes that take the atom out of the level n with those that take it into the level n. A general expression for this statistical equilibrium of level n can be written as

$$N_n \sum_{n \neq m} P_{nm} = \sum_{n \neq m} N_m P_{mn} \tag{2.55}$$

the P's are the rates of different processes in statistical equilibrium. This can be expanded to show the different processes as

$$\begin{aligned} N_n \left(\sum_{m=n_0, m \neq n}^{\infty} \left(C_{nm} + B_{nm} I_\nu \right) + \sum_{m=n_0}^{n-1} \left(A_{nm} + C_{ni} + B_{ni} I_\nu \right) \right) &= \\ \sum_{m=n_0, m \neq n}^{\infty} N_m \left(C_{mn} + B_{mn} I_\nu \right) + \sum_{m \neq n+1}^{\infty} \left(N_m A_{mn} + N_e N_+ \left(\alpha_n^r + \alpha_n^3 \right) \right). & \end{aligned} \tag{2.56}$$

In the above equation on the left which stands for the total depopulation of level n, the first sum accounts for collisional transitions and stimulated emission from the level n with n_0 being the lowest energy level. The second sum includes spontaneous emission, collisional and photo ionization. On the right we have, the total population rate the first sum of which accounts for collisional and stimulated transitions into the level n. The second sum includes spontaneous transitions and recombinations. The two alphas with respective superscripts stand for radiative and 3-body recombinations. The above set of equations is solved along with the equation connecting non-LTE population N_n with LTE population N_n^*. The dimensionless variable $b_n = N_n/N_n^*$ is called the departure coefficient. b_n is a function of electron temperature, volume density and background radiation field intensity.

2.3.2 The non-LTE optical depth

The non-LTE line optical depth is obtained by introducing the departure coefficient b_n into the equation (2.24) and (2.26) for line emission and absorption respectively. The non-LTE emission coefficient is given by

$$j_L = b_m j_L^* = b_n N_n A_{n,m} \frac{h\nu}{4\pi} \varphi_\nu \tag{2.57}$$

as mentioned earlier the star indicates LTE value. The non-LTE absorption coefficient can be related to LTE coefficient as

$$\begin{aligned} K_L &= b_m \left[\frac{1 - \frac{b_n}{b_m} e^{-h\nu/kT_e}}{1 - e^{-h\nu/kT_e}} \right] K_L^* \ , \ n>m \\ &\approx b_n \left[1 - \frac{kT_e}{h\nu} \frac{\Delta b}{b_n} \right] K_L^*, \ \ h\nu/kT_e \ll 1 \ , \Delta b = b_n - b_m \\ &\approx b_m \left[1 - \frac{kT_e}{h\nu} \frac{d \ln b_m}{dm} \Delta m \right] K_L^* \ , \ b_m \gg \Delta b, \ m \gg \Delta m \end{aligned} \tag{2.58}$$

where the quantity in the brackets is called the amplification factor and is written as

$$\beta_m = 1 - \frac{kT_e}{h\nu}\frac{d\ln b_m}{dm}\Delta m$$

The non-LTE optical depth can thus be written as

$$\tau_L = \int_0^S K_L ds = b_m \beta_m \int_0^S K_L^* ds = b_m \beta_m \tau_L^* \qquad (2.59)$$

As defined above β is given by the derivative of b_n coefficients with n. In the radio regime the factor along with the derivative in the expression for β assumes a large value. A slight difference in the level populations can thus result in significant magnitudes of β giving large optical depths compared to LTE situation. The sign of β also determines the line strength. Its negative value implies population inversion which is favourable for stimulated emission. The stimulated emission can be brought about by continuum radiation of the cloud or the background non-thermal radiation incident on the cloud. Low frequency RRLs from low density regions would be expected to be dominated by stimulated radiation.

2.3.3 Non-LTE line intensity

The general radiative transfer equation for a gaseous nebula can be written as

$$\frac{dI_\nu}{ds'} = j_\nu + \frac{I_{nc}}{S} - KI_\nu \qquad (2.60)$$

which has the solution

$$I_\nu = I_0 e^{-\tau} + \left(S + \frac{I_{nc}}{\tau}\right)\left(1 - e^{-\tau}\right) + I_f \qquad (2.61)$$

I_0 and I_f are the incident and emerging intensities from the back and front of the cloud respectively. I_{nc} is the nonthermal radiation distributed within the cloud. The source function S can be written as

$$S = \frac{j_L + j_C}{k_L + k_C};\ \frac{j_L}{K_L} = \frac{j_C}{K_C} = B\left(T_e\right)$$

so that

$$S = B\left(T_e\right)\left[\frac{b_n \tau_L^* + \tau_C}{\tau_L + \tau_C}\right] \tag{2.62}$$

In terms of brightness temperature equation (2.61) can be written as

$$T = T_0 e^{\left(-\tau_L + \tau_C\right)} + \left[\frac{T_e\left(b_n \tau_L^* + \tau_C\right) + T_{nc}}{\tau_L + \tau_C}\right]\left(1 - e^{-\left(\tau_L + \tau_C\right)}\right) + T_f \tag{2.63}$$

The line temperature is extracted by substracting the continuum. The excess line temperature is given by

$$\begin{aligned} \Delta T_L = {} & T_0\left[e^{-\tau_C}\left(e^{-\tau_L} - 1\right)\right] + T_e\left[\left(\frac{b_n \tau_L^* + \tau_C}{\tau_L + \tau_C}\right)\left(1 - e^{-\left(\tau_L + \tau_C\right)}\right) - \left(1 - e^{-\tau_C}\right)\right] \\ & + T_{nc}\left[\frac{1 - e^{-\left(\tau_L + \tau_C\right)}}{\left(\tau_L + \tau_C\right)} - \frac{1 - e^{-\tau_C}}{\tau_C}\right] \end{aligned} \tag{2.64}$$

In the optically thin case($1 \gg \tau_c \gg |\tau_L| \gg \tau_L{}^*$) the line temperature can be written as

$$\Delta T_L \approx \tau_L^*\left[b_n T_e - b_m \beta\left(\tau_C T_e/2 + T_{nc}/2 + T_0\right)\right] \tag{2.65}$$

in case $T_0 = T_{nc} = 0$, the ratio of LTE line strength to non-LTE line strength can be written as

$$\frac{\Delta T_L}{\Delta T_L{}^*} = \frac{\Delta T_L}{\tau_L^* T_e} = b_m\left(1 - \frac{\beta_n \tau_C}{2}\right) \tag{2.66}$$

where β_n(usually negative) has been defined above.

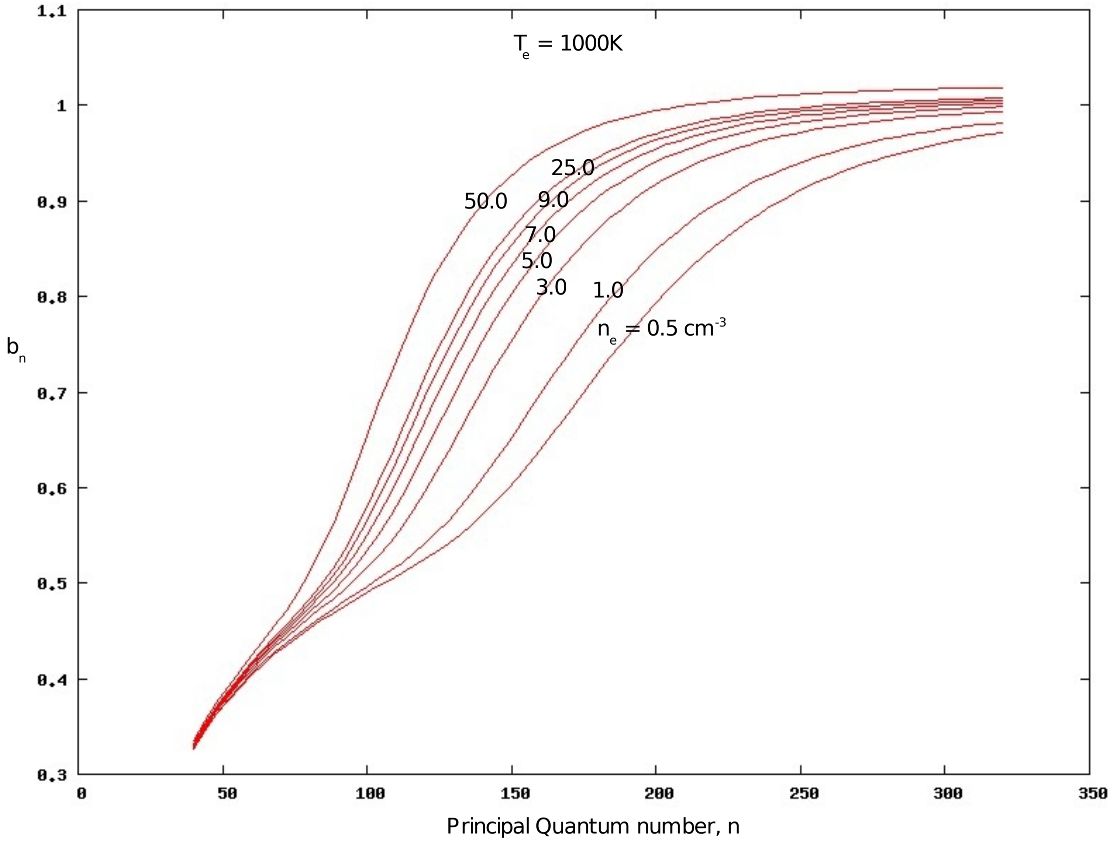
T_e = 1000K
b_n
25.0
50.0
9.0
7.0
5.0
3.0
1.0
$n_e = 0.5$ cm^{-3}
1.1
1
0.9
0.8
0.7
0.6
0.5
0.4
0.3
0
50
100
150
200
250
300
350
Principal Quantum number, n

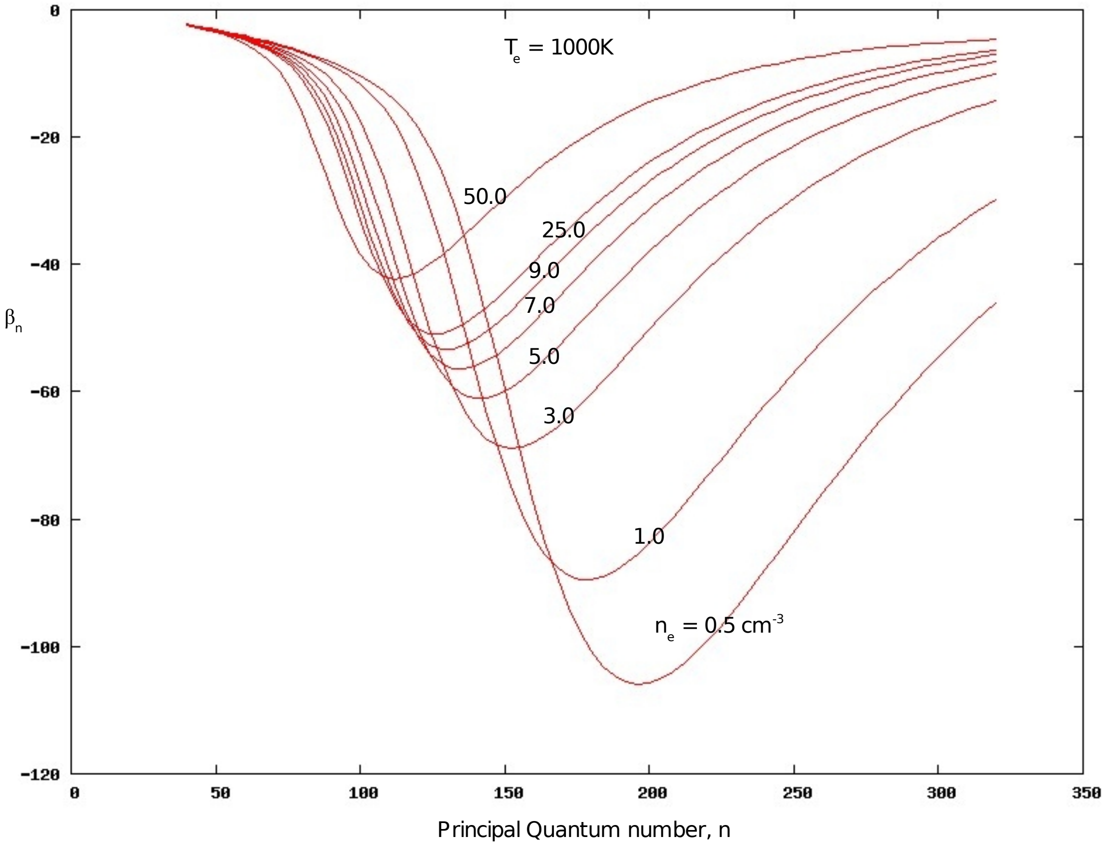
T_e = 1000K
β_n
50.0
25.0
9.0
7.0
5.0
3.0
1.0
$n_e = 0.5$ cm^{-3}
0
-20
-40
-60
-80
-100
-120
0
50
100
150
200
250
300
350
Principal Quantum number, n

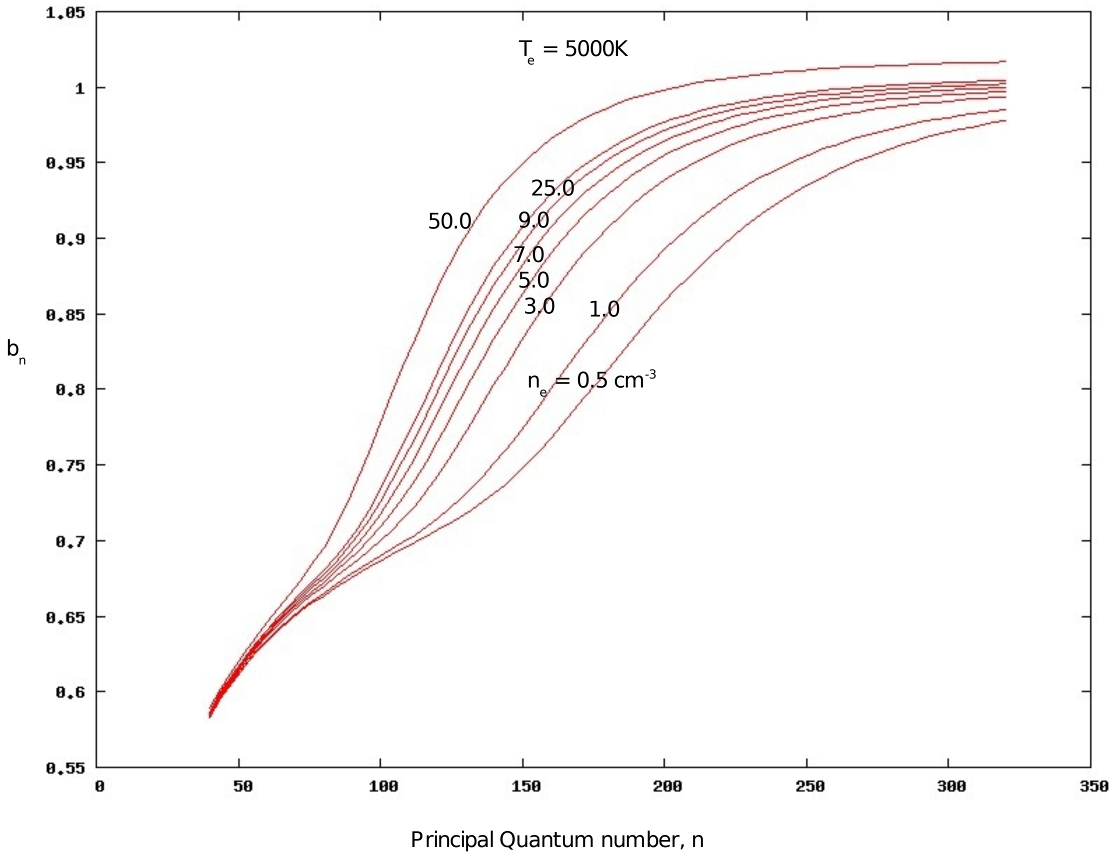
T_e = 5000K
b_n
1.05
1
0.95
0.9
0.85
0.8
0.75
0.7
0.65
0.6
0.55
0
50
100
150
200
250
300
350
Principal Quantum number, n
50.0
25.0
9.0
7.0
5.0
3.0
1.0
n_e = 0.5 cm^-3

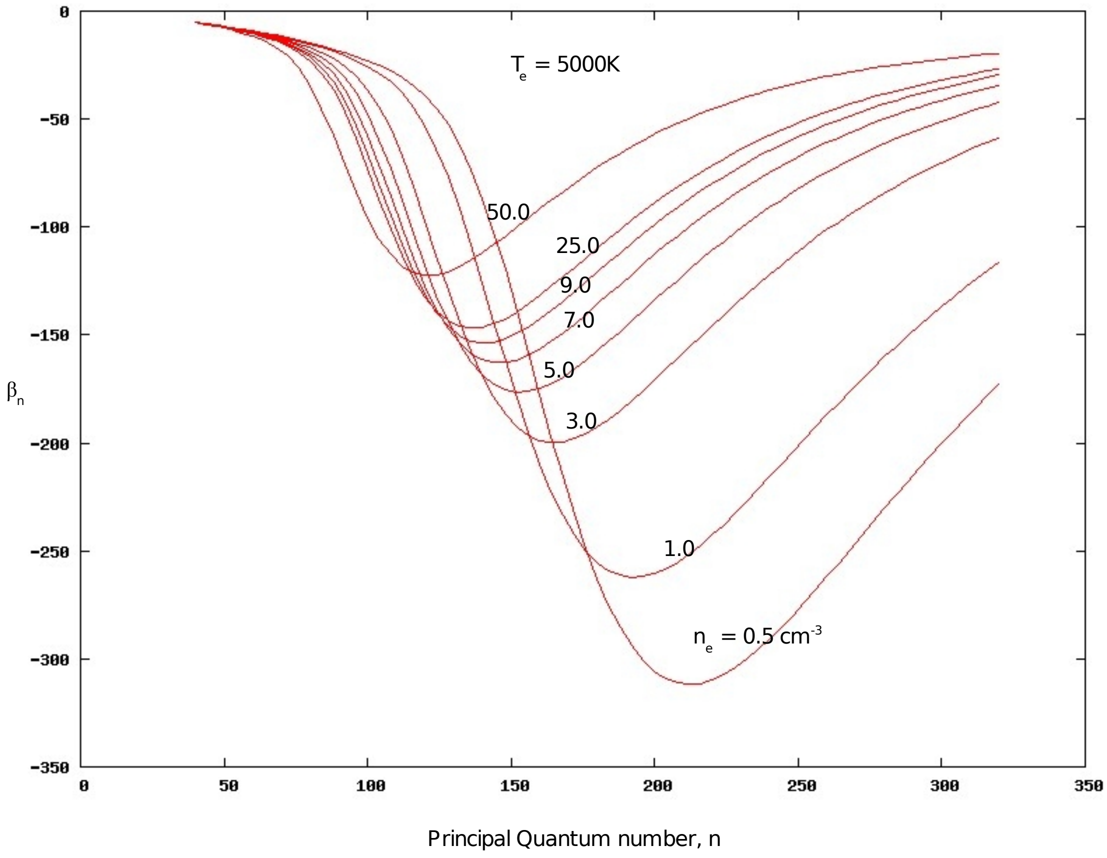
T_e = 5000K
β_n
0
-50
-100
-150
-200
-250
-300
-350
0
50
100
150
200
250
300
350
Principal Quantum number, n
50.0
25.0
9.0
7.0
5.0
3.0
1.0
n_e = 0.5 cm^-3

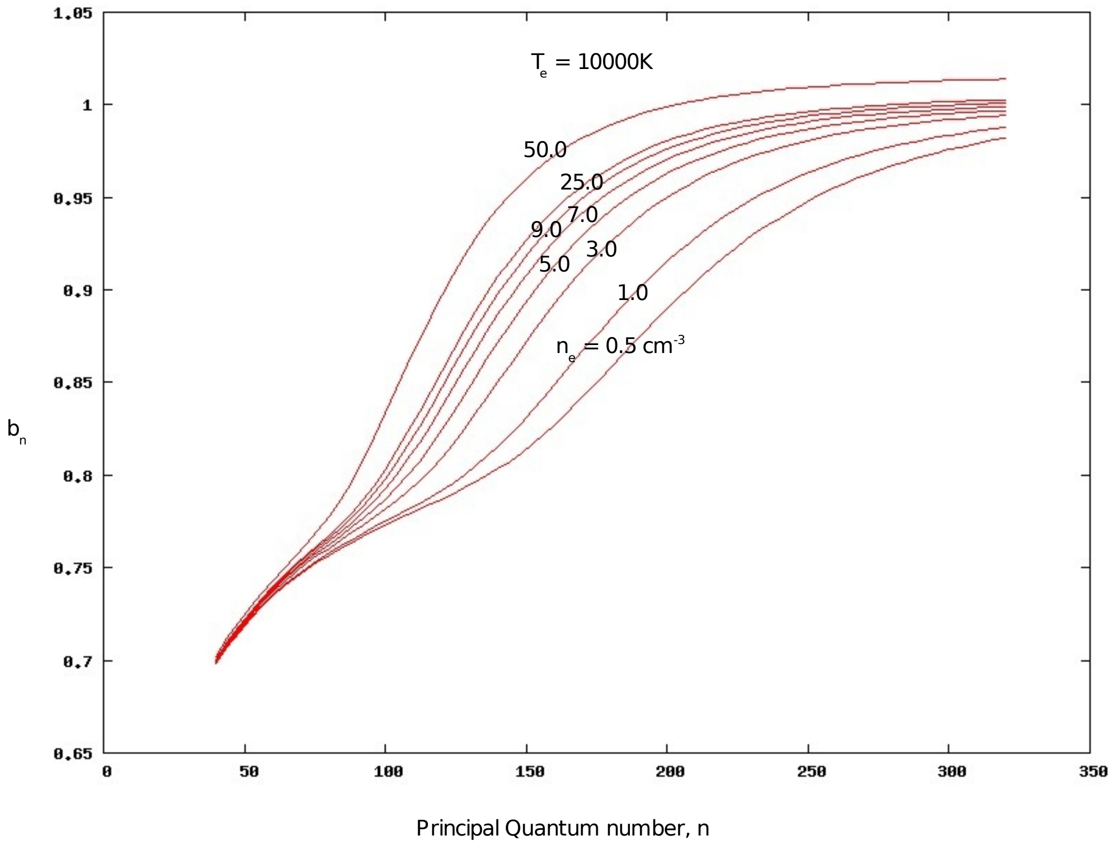

T_e = 10000K
50.0
25.0
7.0
9.0
3.0
5.0
1.0
n_e = 0.5 cm^{-3}
b_n
1.05
1
0.95
0.9
0.85
0.8
0.75
0.7
0.65
0
50
100
150
200
250
300
350
Principal Quantum number, n

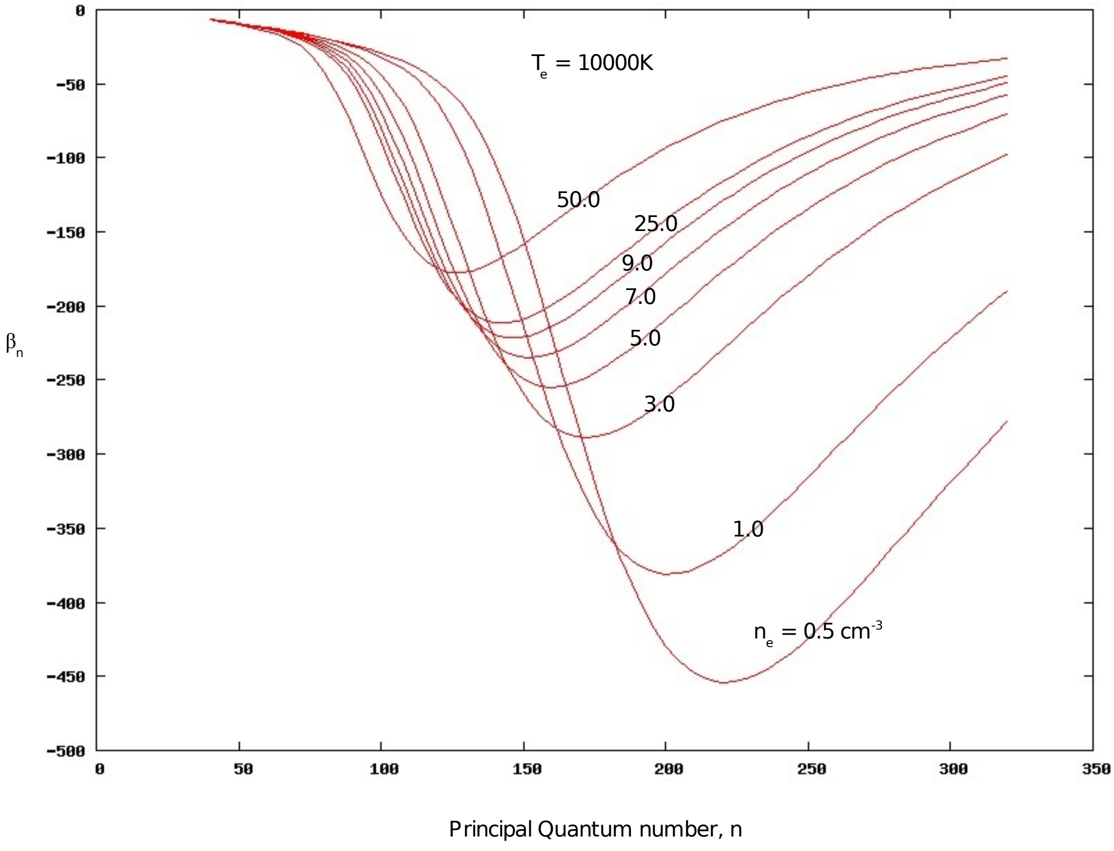

T_e = 10000K
50.0
25.0
9.0
7.0
5.0
3.0
1.0
n_e = 0.5 cm^{-3}
β_n
0
-50
-100
-150
-200
-250
-300
-350
-400
-450
-500
0
50
100
150
200
250
300
350
Principal Quantum number, n

Chapter 3

Observations With WSRT

3.1 The Observations

The Westerbork Synthesis Radio Telescope(WSRT) is an aperature synthesis interferometer that consists of a linear array of 14 circular antennas each with a diameter of 25m. These are arranged on a 2.7 km East-West line. Ten of the telescopes are on fixed mountings while the remaining four dishes are movable along two railtracks. In the incoherent addition mode WSRT offers 8 IF bands each with a bandwidth of 5MHz which were used to detect 7 Hnα lines(n=165 to 171) and one Hnβ(n=208) line around 1.4GHz. These bands also covered 3 more Hnβ lines(n=210,214 and 215) which appear within the total bandwidth. The primary objective of the observation was to detect helium line by averaging the spectra from the 7 bands. The Hnα & Hnβ lines were used to model the ELDWIM along with the Hnα lines from ORT data(H271α).

Observations were carried out using dual frequency switching which is the shifting of the spectral line between two specific positions in the band. The figure below shows the idea behind using this type of frequency switching. The frequency switching is acheived by changing the local oscillator(LO) of the instrument between two values LO1 and LO2 so that the spectral line to be observed appears more or less at specific convenient positions in the band. One of the spectrum is called Ton spectrum while the other is called Toff spectrum. The idea of dual frequency switching is to extract the line sitting on the continuum power. The continuum power is more or less uniform throughtout the band. The bandshape is characteristic of the instrument and represents the gain variation across the band. Since LO1 and LO2 differ by small amounts it is assumed that the band shape of the instrument does not change grossly between these two LO settings. A substraction of Toff from Ton results in the elimination of the background continuum power, only the spectral lines and the residual baseline will remain.

Typical (Ton – Toff)/Toff ratio has also been shown in the figure with sufficient exaggeration for clarity. Within the bandwidth of 5MHz the line was shifted by 2MHz keeping the average of the hydrogen and helium rest frequencies at the center of the band. Due to motion of the line emitting medium these rest line frequencies suffer Doppler shifting across the band. This shift in the frequency is normally expressed in terms of velocity using the Doppler relation,

$$\Delta v = \frac{\Delta \nu}{\nu_0} c . \tag{3.1}$$

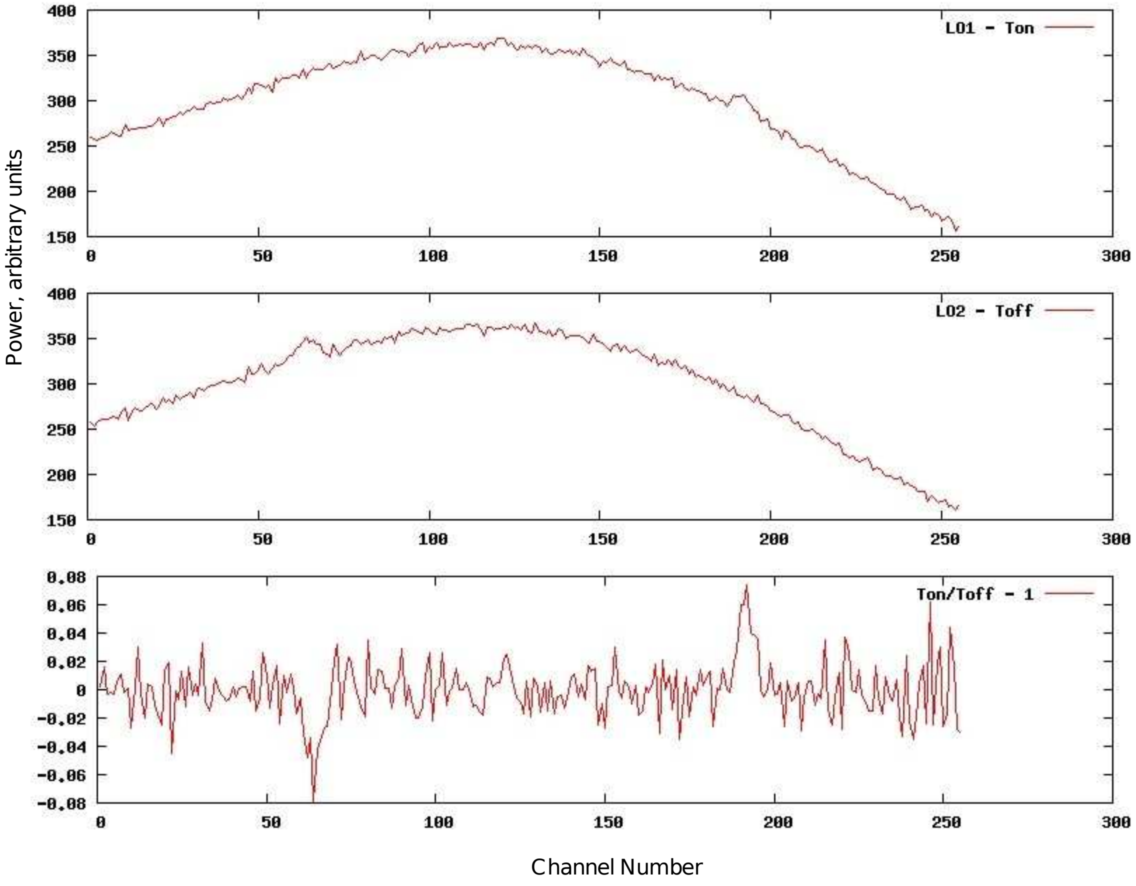

Fig 3-1: Typical power spectra towards a source. A change of LO shifts the position of occurence of the spectral line. The bottom figure shows (Ton-Toff)/Toff with gross exaggeration to make the idea clear. In actual spectra corresponding to a second or a minute the lines are hardly recognizable. Only after averaging sufficient number of spectra collected over time do the spectral lines appear to be distinguishable from the noise.

Again this velocity shift is considered in the Local standard of Rest(which is to follow the mean motion of the material in the solar neighborhood) and is designated as V_{LSR}(Velocity in the Local Standard of Rest). More on V_{LSR} can be found in chapter-4.

Table-2 gives the fitted parameters towards different sources. These positions were selected from previous observations(Lockman et al. 1976 , Heiles et al. 1996) with hydrogen line temperature greater than 50mK. Assuming that this would also give a fair chance to detect the helium line as well. Each source has been observed for 48 minutes. Unfortunately the He line feature has been seen towards only one position i.e G18.0 +1.8.

The table of sought after transitions is given here in table-1,

Transition	ν_{rest}*(Hydrogen) GHz*	ν_{rest}*(Helium) GHz*
165α	*1.450716*	*1.451307*
166α	*1.424734*	*1.425314*
167α	*1.399368*	*1.399938*
168α	*1.374601*	*1.375161*
169α	*1.350414*	*1.350965*
170α	*1.326792*	*1.327333*
171α	*1.303718*	*1.304249*
208β	*1.44072*	
Other β-transitions		
210β	*1.400138*	
214β	*1.323433*	
215β	*1.305136*	

Table 3-1: The sought after transitions for the WSRT bands

The corresponding ORT parameters for different positions are given in table 3-3. The plots of line detections towards these positions at 328.5958 MHz have been displayed following table-2.

Source (G.C)		T_L (mK)		V_{LSR} (km/s)		ΔV_{LSR} (km/s)	
l	*b*	H165α	H208β	H165α	H208β	H165α	H208β
7.2	-0.7	41.3(1.2)	15.9(5.6)	17.9(0.47)	20.4(2.4)	32.3(1.1)	13.8(5.6)
15.8	-0.5	32.8(1.1)	---	30.3(1.6)	---	36.2(3.0)	---
		14.2(2.6)		60.7(2.3)		23.6(4.1)	
17.4	1.5	28.7(4.0)	15.3(2.7)	20.7(0.6)	28.8(2.8)	16.9(2.0)	32.3(6.6)
		21.7(3.7)		30.2(2.1)		37.7(2.6)	
18.6	-0.8	17.4(7.1)	---	46.9(12.5)	---	44.7(11.6)	---
		22.4(13.2)		66.7(1.3)		26.3(6.4)	
19.2	1.7	53.6(1.2)	13.8(3.7)	25.8(0.3)	25.7(2.8)	30.3(0.8)	21.2(6.5)
23.4	-0.6	46.4(2.7)	14.5(2.0)	66.0(1.9)	75.8(4.0)	32.2(2.9)	56.7(9.3)
		29.7(3.6)		95.5(2.6)		29.1(3.7)	
26.5	0	31.7(2.1)	13.4(2.1)	71.0(1.5)	96.0(3.4)	25.7(2.7)	42.7(7.9)
		75.8(1.6)		102.6(0.7)		30.7(1.4)	
28.0	0	11.3(1.2)	11.5(3.3)	53.6(6.9)	93.0(4.8)	53.0(13.6)	33.9(11.3)
		47.5(2.8)		96.7(1.0)		31.8(1.8)	
16.3	1.3	31.3(1.3)	9.7(2.7)	26.4(0.6)	19.9(4.6)	29.2(1.4)	33.8(10.9)
18.0	1.8	127.1(1.8)	34.2(3.7)	27.3(0.2)	27.5(1.3)	26.9(0.4)	24.3(3.1)
12.6	-0.6	66.0(1.5)	16.7(2.2)	32.9(0.7)	35.8(3.0)	33.1(1.6)	45.4(7.0)
		19.6(2.7)		62.3(1.6)		19.9(3.3)	

Table 3-2: The fitted parameters to observations towards different positions with WSRT. Multiple entries correspond to multiple components. The values in the paranthesis are errors on the parameters.

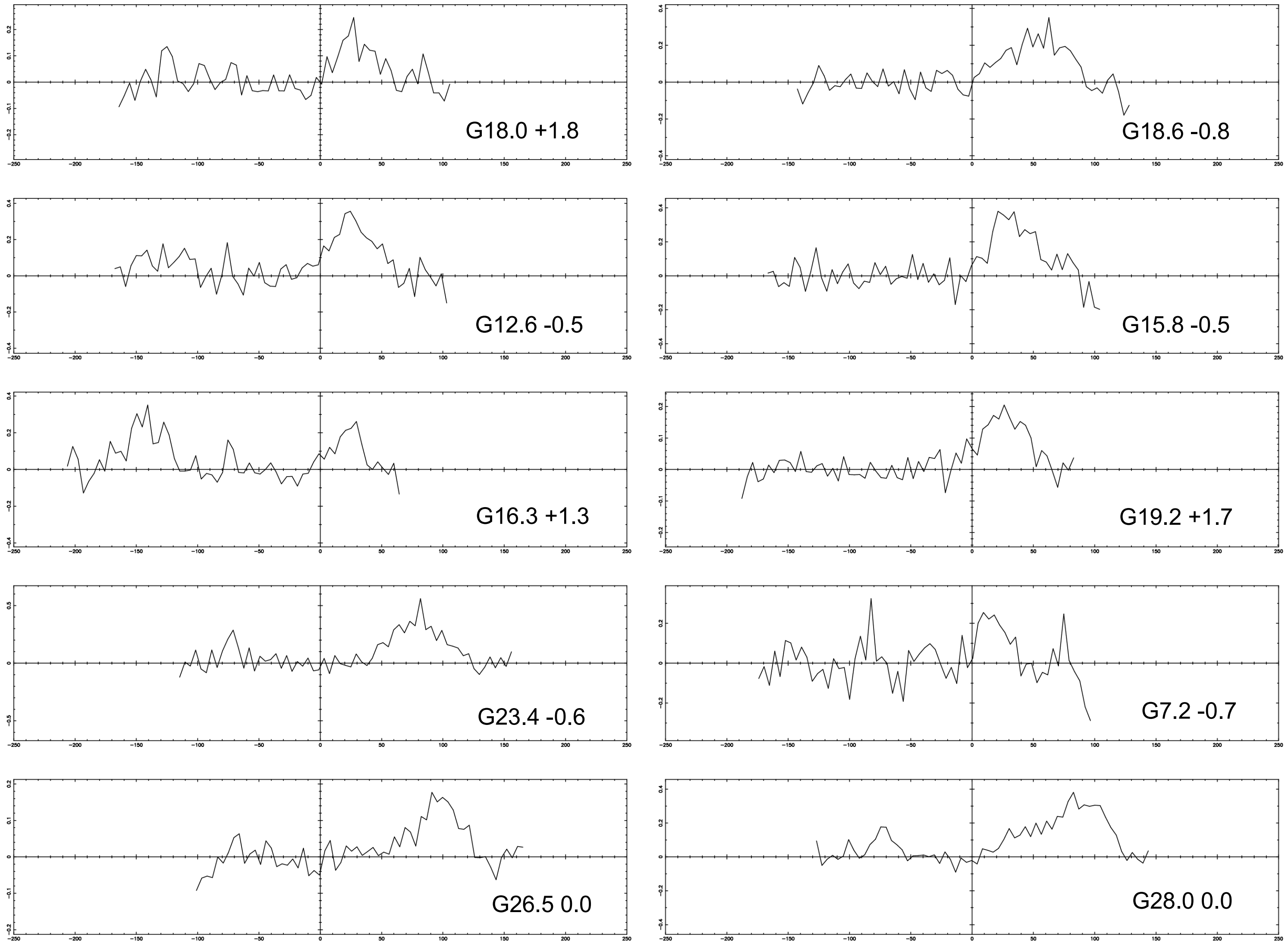

ORT observations towards the positions in table-3. The abscissa is V_{LSR} and the ordinate is temperature in K.

Source		*T_L (mK)*	*V_{LSR} (km/s)*	*ΔV_{LSR} (km/s)*
l	*b*	*H271α*	*H271α*	*H271α*
7.2	*-0.7*	*255.7*	*15.9*	*24.6*
15.8	*-0.5*	*324.0, 126.0*	*28.8, 65.1*	*27.5, 28.8*
18.6	*-0.8*	*85.0, 212.0*	*24.4, 59.8*	*23.1, 39.8*
19.2	*1.7*	*180.7*	*25.5*	*42.5*
23.4	*-0.6*	*273.0, 196.0*	*67.9, 96.7*	*32.5, 28.0*
26.5	*0*	*80.6, 186.5*	*70.3, 101.1*	*35.9, 29.5*
28.0	*0*	*146.3, 345.0*	*42.4, 90.1*	*38.7, 42.8*
16.3	*1.3*	*267.0*	*23.0*	*24.5*
18.0	*1.8*	*177.4*	*28.2*	*32.4*
12.6	*-0.6*	*281.4, 110.4*	*22.1, 47.6*	*27.6, 18.5*

Table 3-3: The ORT parameters for the positions observed using WSRT.

3.2 The Spectra

The plots of spectra obtained towards different positions corresponding to all the 8-bands have been displayed on the following pages. Each spectrum in these plots is an average of 14 x 23 $(T_{on}-T_{off})/T_{off}$ auto-correlations obtained for each band from 14 antennas. The signal to noise ratio is quiet high except for the 8th band(H208β) which suffered major interference problems and hence major portion of the data was useless. Only a few antennas were used to obtain the 8th band spectra. The H208β line inspite of poor signal to noise ratio is clearly discernable in the average spectrum towards many sources. Some sources have exhibited multiple hydrogen line components, which probably originated in different nearby regions. The 3rd band also contains the H210β line which occurs at a V_{LSR} of -165.3 km/s from the associated H167α line. Further the associated carbon line which would occur at a V_{LSR} of -149.7 km/s relative to the Hnα line appears in the averaged smoothed spectra. This line occurs only towards a few band averaged spectra adjacent to the helium feature. However helium line feature has been seen towards 5 positions. Fig-2 displays one such detection towards G18.0 +1.8. The parameters fitted to this feature are in close agreement with the expected V_{LSR} for the

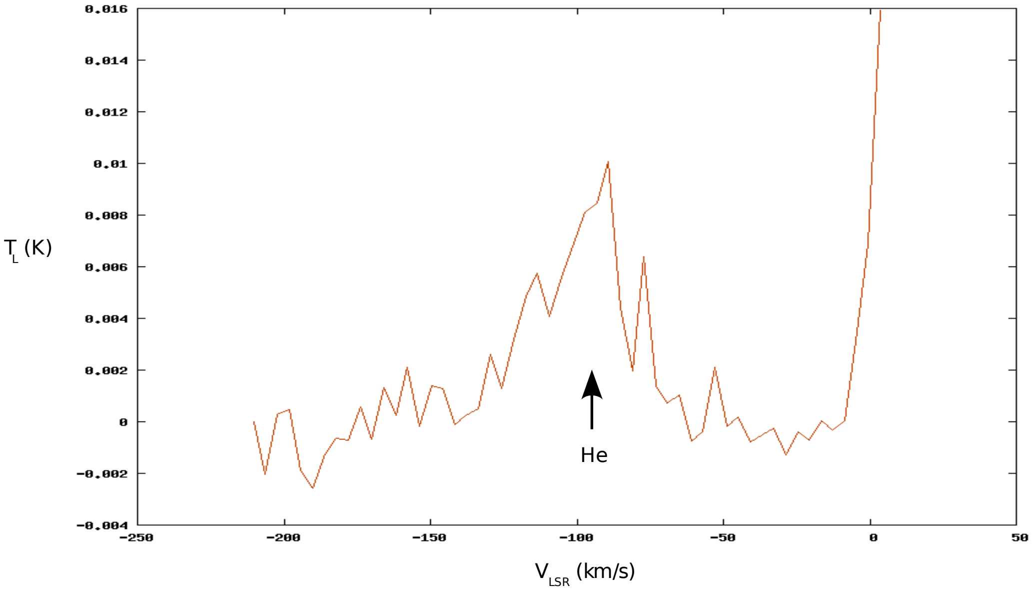

Fig 3-2: Helium line feature which is expected near -100km/s in this band averaged spectrum towards G18.0 +1.8. The abscissa is V_{LSR} in km/s and ordinate is T_L in K.

Henα line. The line amplitude is around 70% of what is expected from the helium to hydrogen abundance ratio. The higher line width can be explained as a result of pressure broadening if the line is orginating in a different region with higher density.

3.3 Data Analysis and Calibration

The data was acquired in fits format. The auto-correlations were extracted from the fits file using cfitsio library. These auto-correlations were power spectra obtained for a minute data per LO setting i.e LO1(T_{on}) & LO2(T_{off}). The 48 minute observation gave 48 spectra. The frequency switching was done per minute, so each LO setting had 24 spectra. Further the 24 spectra were obtained for each antenna. A $(T_{on}-T_{off})/T_{off}$ of these spectra was done as explained in section 3.1. An average of all such spectra and a folding of this to further average the lines in the two portions of the averaged spectrum(refer fig-1) resulted in the following plots(pg 6-11). These correspond to each band of observation as given in table-1. To obtain the ordinate in Kelvin the $(T_{on}-T_{off})/T_{off}$ was multiplied by an average system temperature. This was an average of the measured system temperature per minute. T_{on} or T_{off} is a measure of system temperature. Need less to say the final spectra shown have been corrected for poor baselines by polynomial fitting to portions of the spectrum not containing any astronomical lines. Also before polynomial fitting the interference existing channels were edited, so that they do not

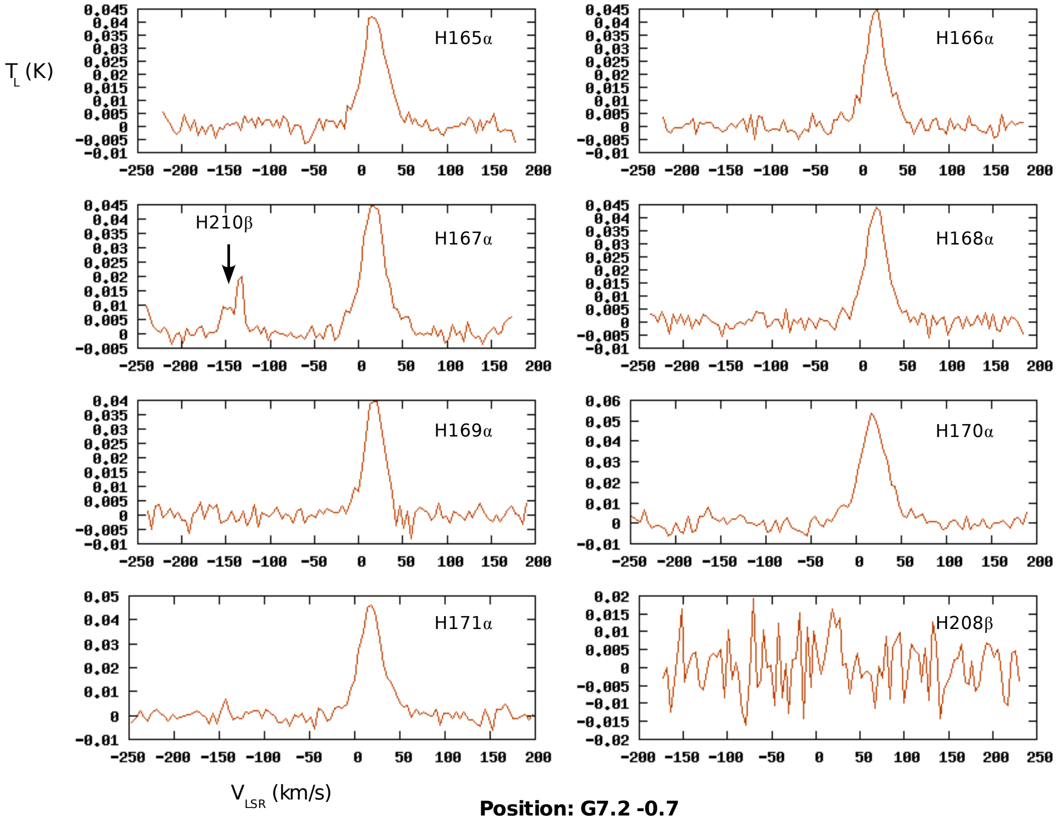

Position: G7.2 -0.7

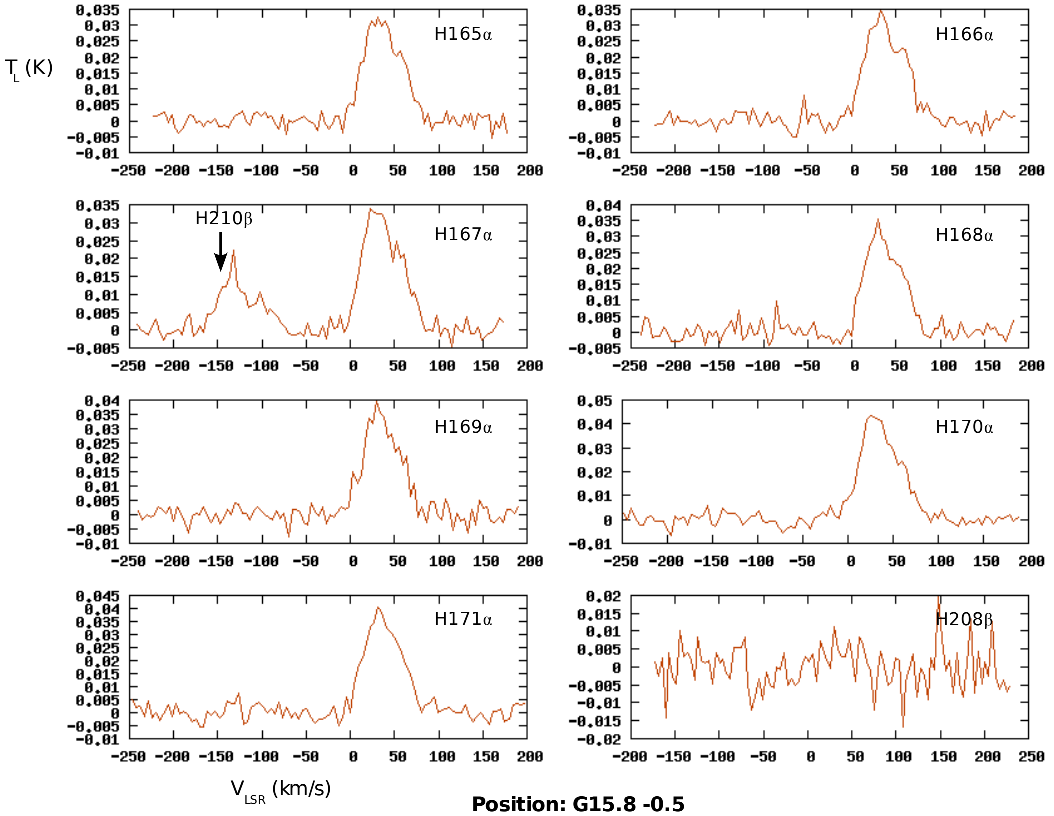

Position: G15.8 -0.5

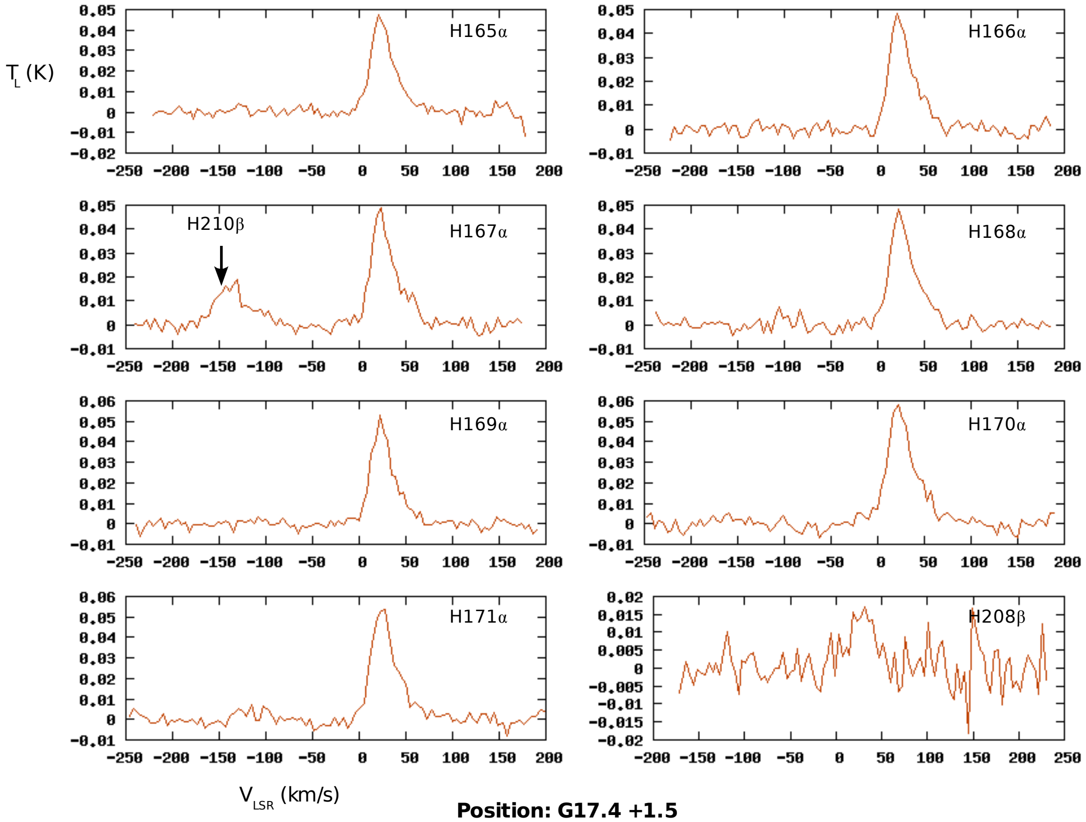

Position: G17.4 +1.5

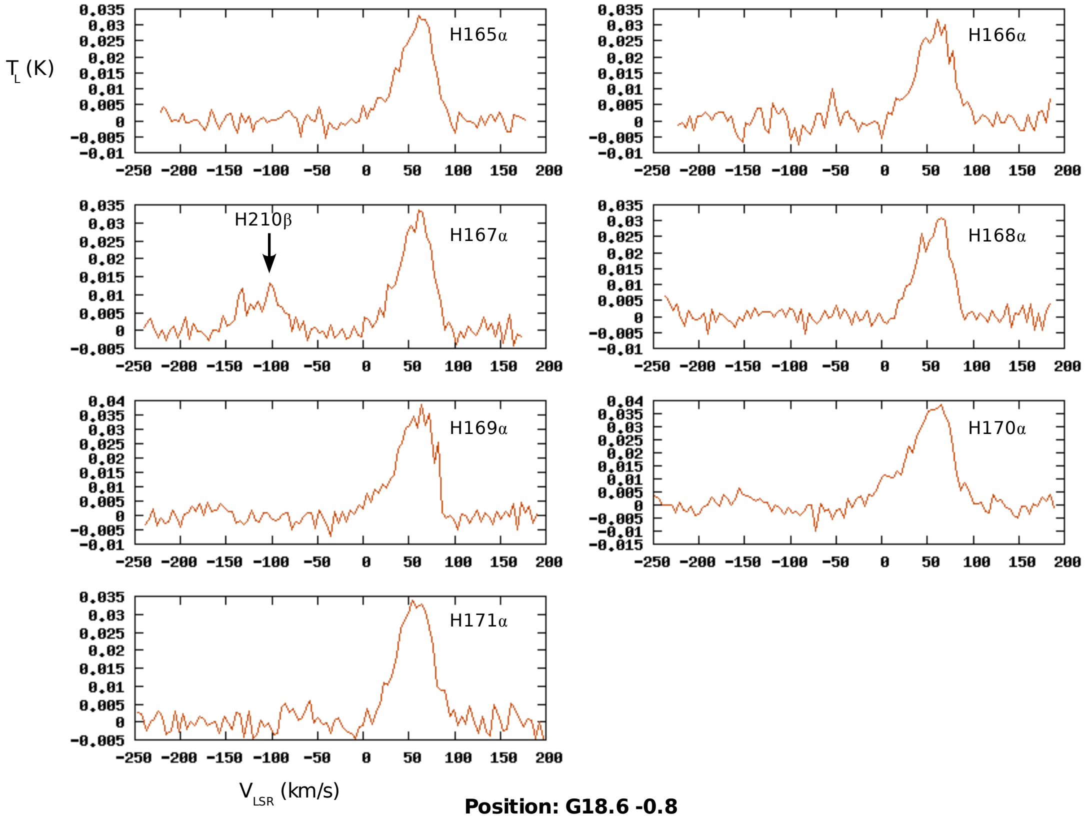

Position: G18.6 -0.8

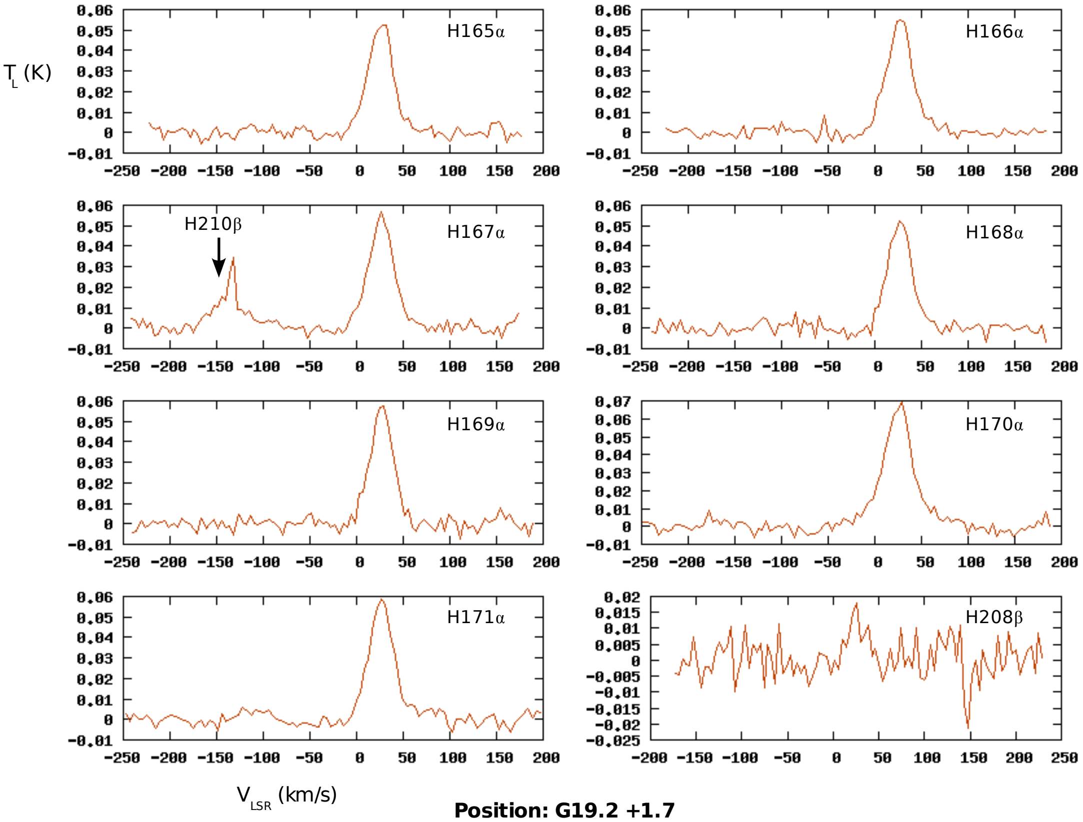

Position: G19.2 +1.7

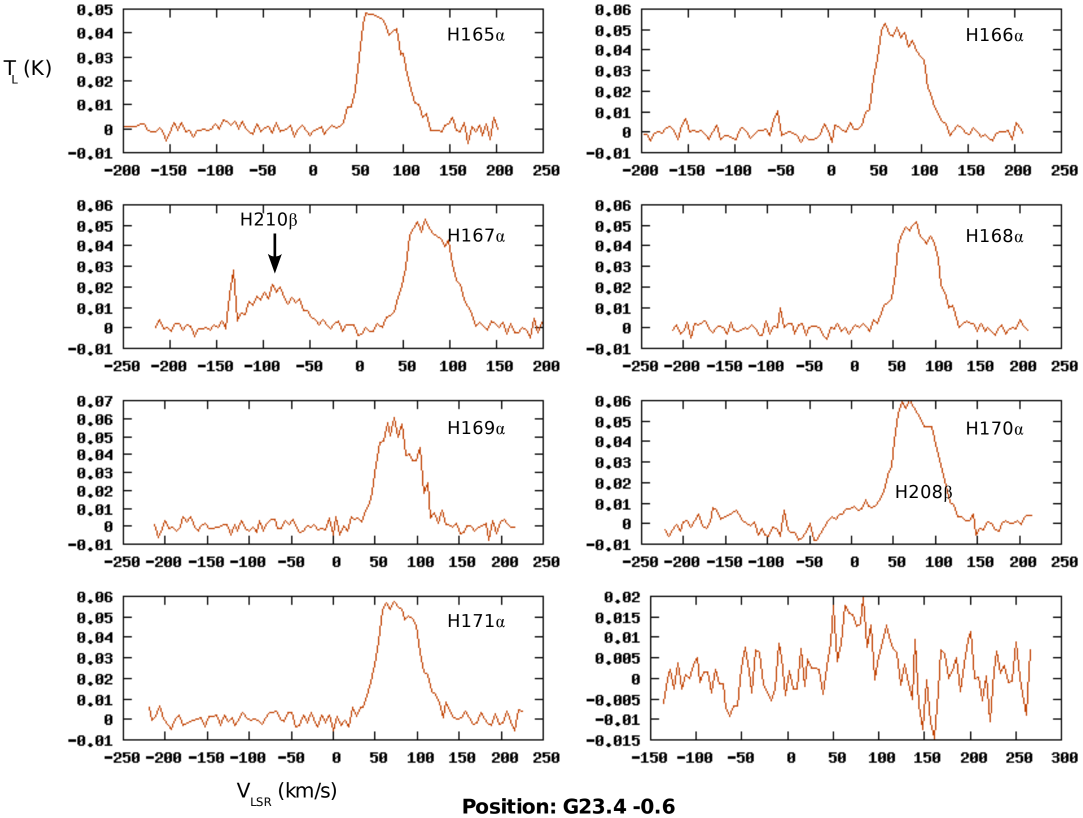

Position: G23.4 -0.6

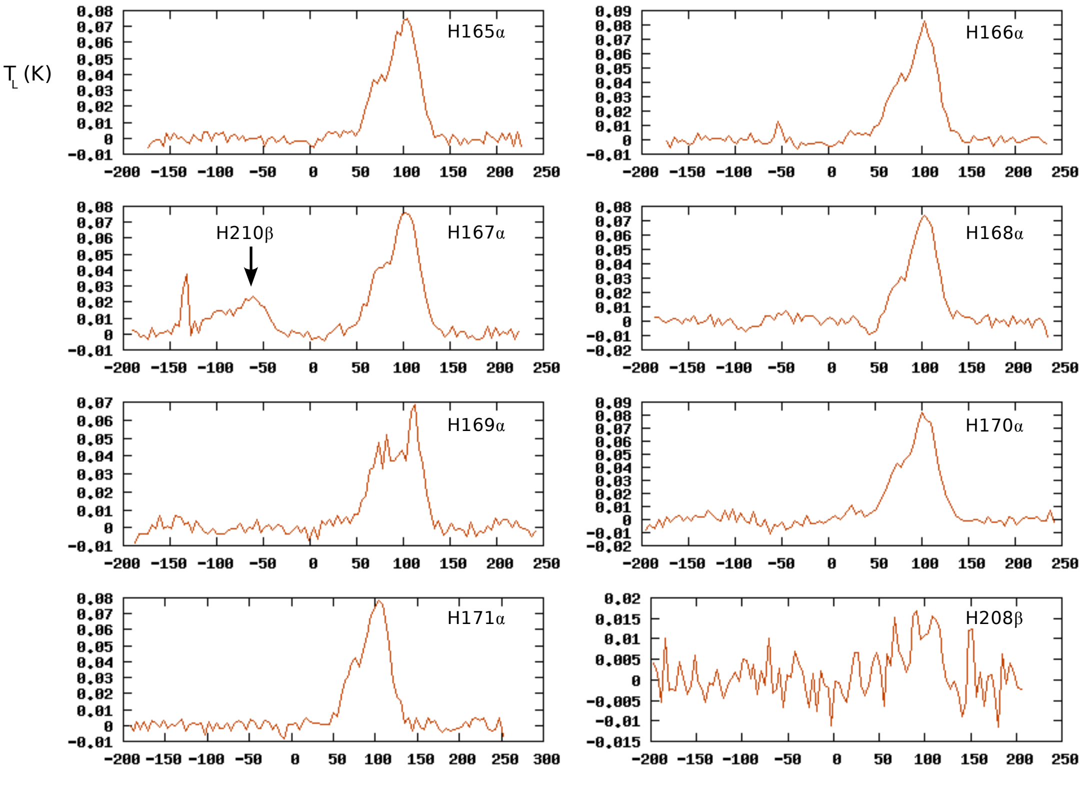

Position: G26.5 +0.0

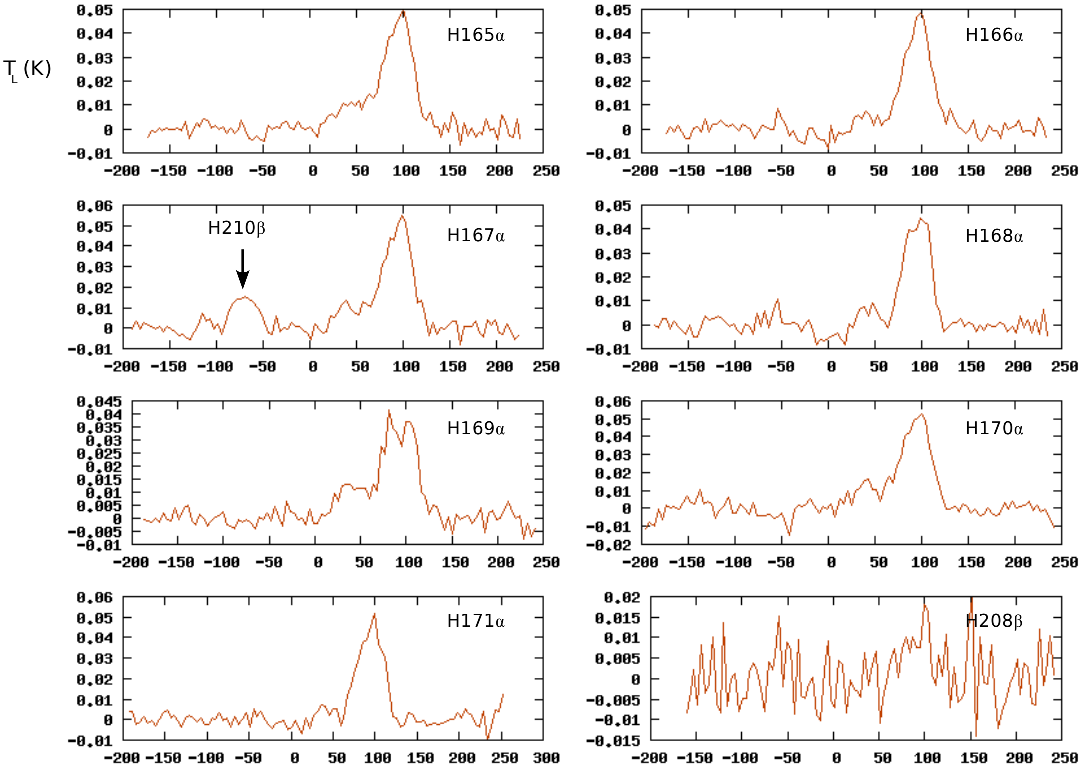

Position: G28.0 +0.0

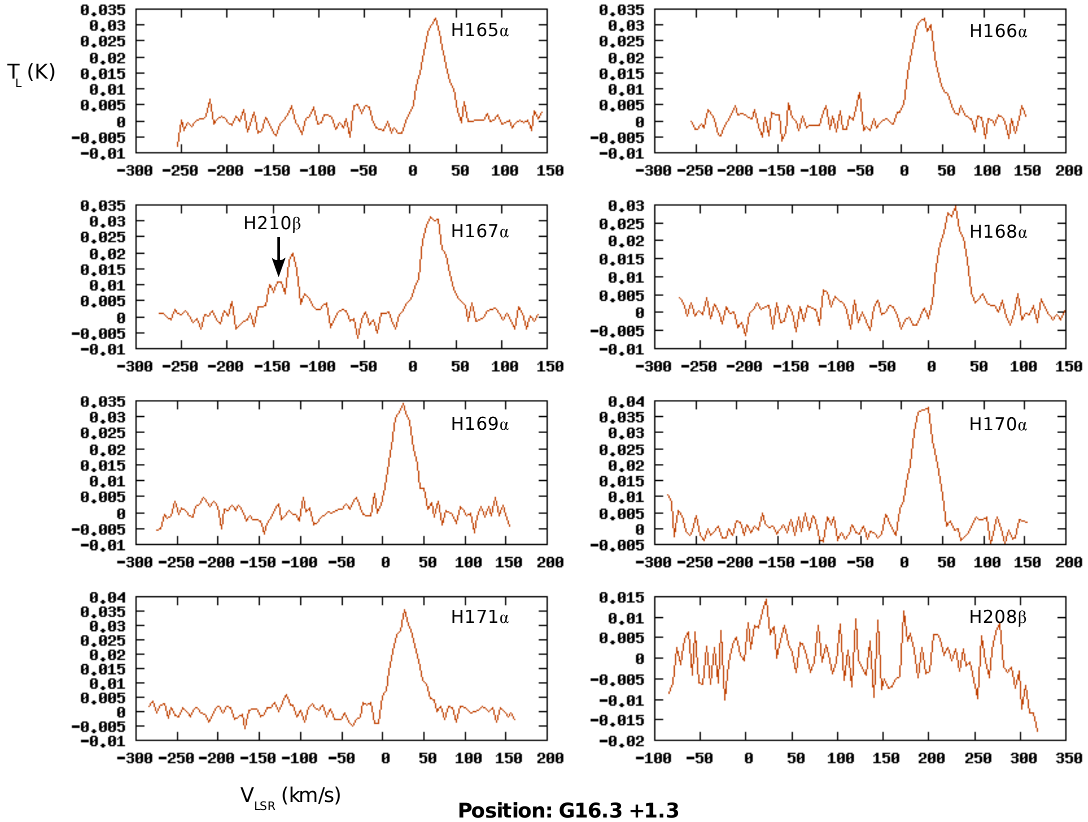

Position: G16.3 +1.3

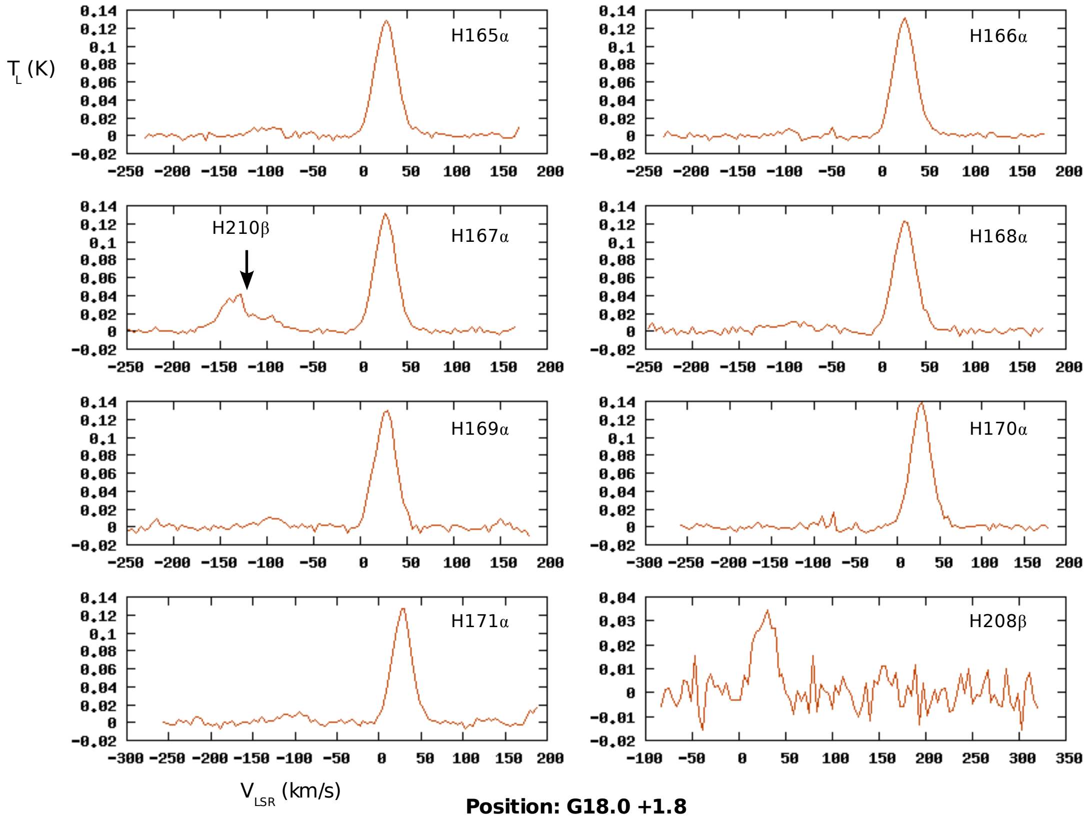

Position: G18.0 +1.8

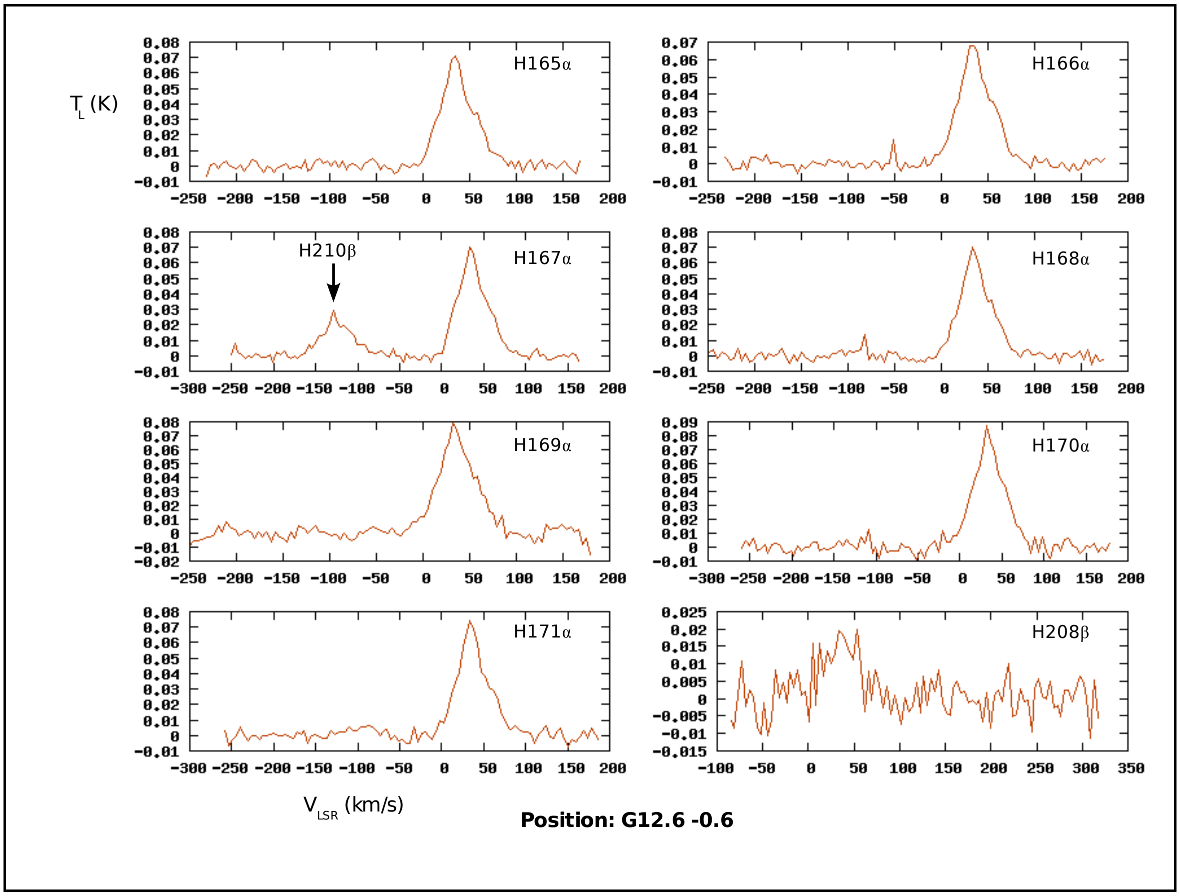

contribute to the polynomial. In case there was an ambiguity whether the seen feature was interference or an astronomical line, the portion of the spectrum was not included in polynomial fitting.

3.3.1 Averaging the spectra to detect Helium Line

Since each spectra had a different resolution, to obtain the band average for improved signal to noise ratio the individual spectra had to be brought to a common resolution by resampling each spectrum using fourier transformation. Further the lines were aligned by fourier shifting for averaging(the Appendix contains these two useful subroutines for resampling and shifting a spectrum for general radio spectral line work) with respect to a individual reference spectrum. The equation for the average spectrum can be written as

$$S_{avg} = \frac{\dfrac{S_1}{\sigma_1^{\ 2}}+\dfrac{S_2}{\sigma_2^{\ 2}}+\ldots+\dfrac{S_n}{\sigma_n^{\ 2}}}{\dfrac{1}{\sigma_1^{\ 2}}+\dfrac{1}{\sigma_2^{\ 2}}+\ldots.+\dfrac{1}{\sigma_n^{\ 2}}} \tag{3.2}$$

where S1, S2 etc are the fourier shifted individual spectra and σ1, σ2 etc are the standard deviations in the individual spectra. These can be obtained by sampling the noise in the spectrum in a clean region away from the lines.

3.4 Modelling of $Hn_1\alpha$ - $Hn_2\alpha$ & $Hn_1\alpha$ - $Hn_2\beta$ lines

To understand the physical properties of the line orginating regions model clouds with various number densities and temperatures were considered. The calculation of expected line strength from these clouds was made using the theory described in chapter 2. The basic idea behind modelling of a gas cloud is simple. Consider a cloud of gas with almost all the hydrogen in it ionized. This cloud is characterised by its number density of electrons, n_e(hydrogen ions and electrons being in equal numbers) and their temperature T_e. The variable parameters that give rise to different observable line strengths from this model cloud are the path length of the gas along the line of sigtht and the beam filling factor of the cloud. Varying path lengths give different emission measures and beam filling factor has an effect on the observed temperature of the line which is given as below,

$$T_{obs} = T_l \; f_{beam} \tag{3.3}$$

$$f_{beam} = \frac{\Omega_{source}}{\Omega_{beam}} \tag{3.4}$$

T_l is the line strength if the source had completely filled the beam i.e the true line strength from the source without beam dilution. With these considerations the model clouds here are essentially of cylindrical geometry. The face of the cylinder being perpendicular to the beam determines the filling factor and the its length determines the emission measure $n_e^2 s$. The cloud with a fixed n_e and T_e is considered at different beam filling factors and the required emission measure is calculated to produce the observed line temperature. Clouds for different values of n_e and T_e are treated in this manner and a set of curves plotting the required emission measure, EM Vs number density n_e for different temperatures is obtained. So a set of curves(EM Vs n_e) can be obtained for a particular line frequency with particular beam filling factor. When such a set of curves is overplotted for different line frequencies with corresponding filling factors(say, f_{beam}=1.0 for smaller beam observation and f_{beam}=0.5 for larger beam observation) a crossing of curves occurs marking the common EM and n_e . This technique can be used to constrain n_e in the observed cloud. It is seen that where as for $Hn_1\alpha$ – $Hn_2\alpha$ modelling the intersection of curves are quiet less scattered with respect to temperature from some mean value than the curves obtained from $Hn_1\alpha$ – $Hn_2\beta$ modelling. This fact can be used to eliminate some of the temperatures in the $Hn_1\alpha$ – $Hn_2\alpha$ modelling, thus constraining the temperature.

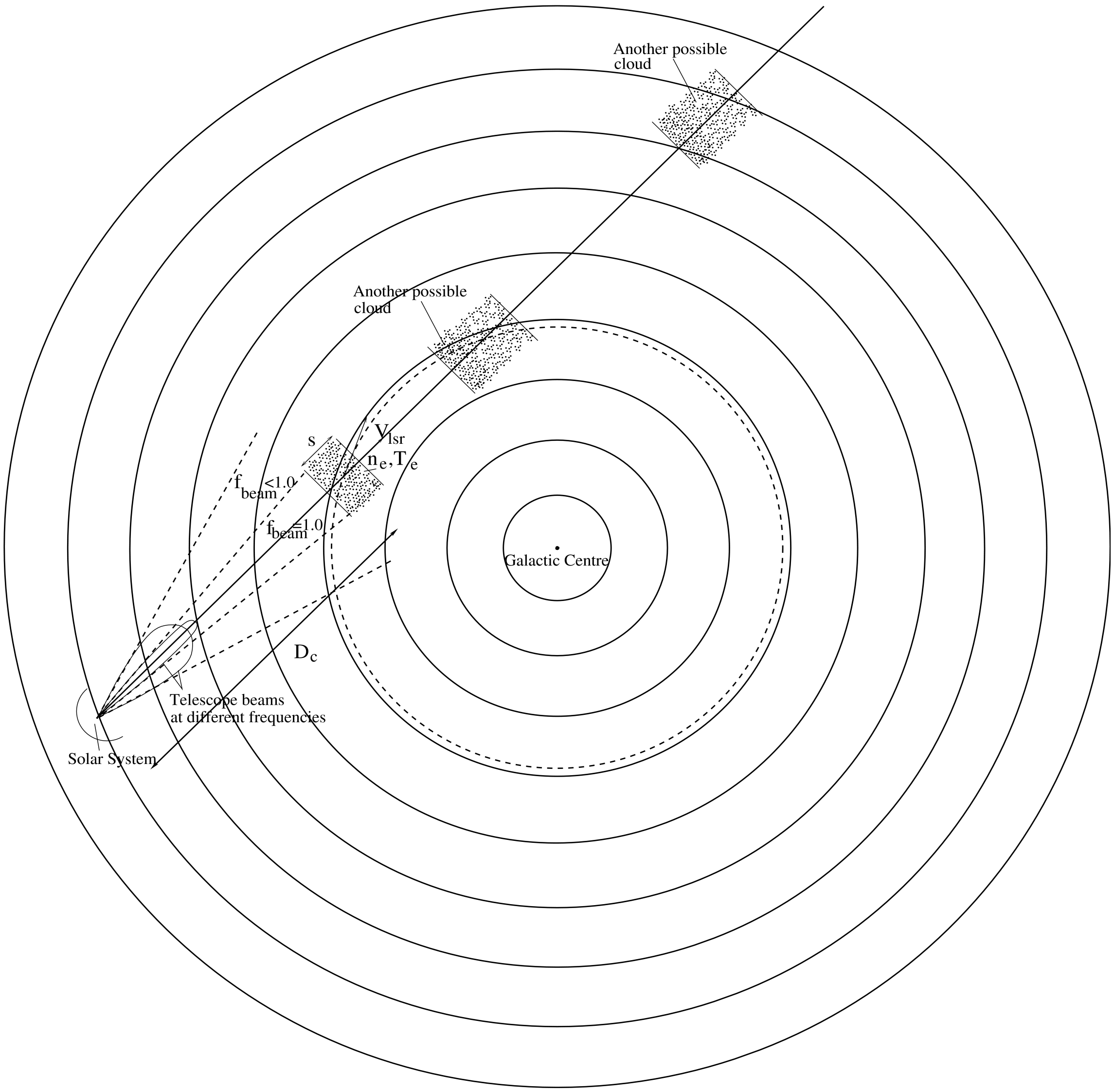

Fig 3-3: Illustration showing the model cloud in the line of sight of the telescope.

The actual model cloud just doesn't produce its own radiation but also has a background field impinging on it. To get an estimate of this background field it is necessary to know the location of the cloud in the Galaxy(refer the illustration in fig-3). The observed V_{LSR} of the radio line can help in placing the cloud if a suitable Galactic rotation curve is chosen from the literature. In the modelling presented here the Galactic rotation curve proposed by Burton and Gordon(1978) was chosen. For a given V_{LSR} it is seen that more than one location are possible along the line of sight. One of these is close by while the other is likely to be distant. The distant cloud suffers from large beam dilutions and also demands larger emission measures to compensate for this, so is less likely to be a possible candidate. The near by cloud is a better candidate in this sense. However it is possible that other clouds in the line of sight also contribute to the observed line temperature, which results in the appearance of multiple components. The Galactic rotation curve along with the observed V_{LSR} of the line locates the cloud at a particular position in the Galaxy. From this it is possible to estimate the distance to

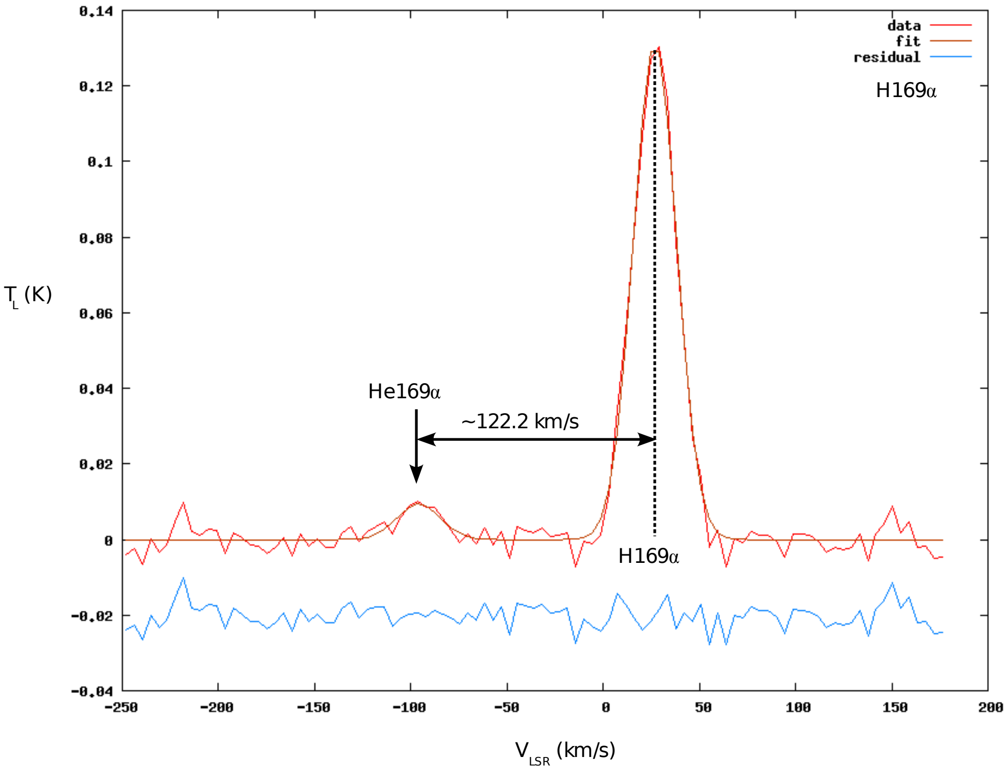

Fig 3-4: An example of gaussian fitting for spectrum towards G18.0+1.8. The residual has been plotted at an offset of -0.02 for clear visibility. The residual as can be seen is purely noise with nearly zero mean. The line features from left are He169α at -96.0 km/s and H169α at 27.0 km/s. The sum of these is within the net error(~3km/s) on the position parameters.

the cloud from the solar system. The observed continuum temperature T_c towards the source is assumed to be distributed all along the line of sight till the other end of the Galaxy(this can be understood in terms of the continuum optical depth τ_c). The background radiation field is a result of the distribution behind the cloud and can be written as

$$T_{bg} = T_c \ (1 - \frac{D_C}{D_G}) \tag{3.5}$$

D_G being the assumed average extent of the Galaxy along the line of sight from the solar system. T_{bg} is the background temperature behind the cloud and D_C is the distance to the cloud. Apart from the background radiation field there is also radiation that originates in the forefront of the cloud and nonthermal radiation that is distributed within the cloud. Radiation originating in the forefront however will not contribute to the line, but the nonthermal radiation is processed through the cloud along the line of sight and hence contributes to the line temperature. The nonthermal part within the cloud is considered quantitively similar to (3.5),

$$T_{nc} = \frac{T_C}{D_G} s \tag{3.6}$$

where s is the optical path length of the cloud along the line of sight.

3.4.1 Line features and Parameter extraction.

Almost all the line features could be very well fitted with gaussian waveforms. The quality of fit is justified by the residual from the data after substraction of the fitted gaussian. The gaussian fitting was done using “leasqrdemo.m” program in octave with required modifications. The program essentially fits a gaussian to the line feature such that the square of the deviations are minimised. A fit to one of the spectrum is shown in the fig-4. The residual obtained by the substraction of the fitted gaussian indicates a good fit being purely noise and distributed about zero mean. The broad helium line feature occurs in almost all the 7 bands towards G18.0+1.8(pg-10).

3.4.2 Modelling results of H271α – H165α lines

The H271α line was observed towards the positions given in table-1 using Ooty Radio Telescope(ORT). ORT is located at a longitude of 283° 19' 58", latitude of 11° 22' 56" and has an altitude of 2150m above sea level. The telescope is parabolic cylinder which is 530m in length and 30m in width. This cylinder is divided into 22 modules which have been designated as 11 north modules and 11 south modules. Each module has a group of 48 dipoles along its focal length. Each of these modules has a half power beam width of 2°.3(RA) x 2°.2 sec(δ)(DEC). The telescope operates at a center frequency of about 327MHz. The beam of ORT is about 16 times larger in solid angle than the WSRT beam at ~1.4GHz. The H271α and H165α transitions produce radio lines at frequencies 328.5958MHz and 1.450716GHz respectively. The lines are well separated in frequency so are suitable for understanding the physical properties of ELDWIM. Which means to say significantly different values of the various parameters (b_n, β_n, τ_l, τ_c ... etc) at the two frequencies. Thus when one considers the line temperature as a function of a single independent variable(here the electron number density n_e) the profile of the curves of the other dependent quantities, here the emission measure ($n_e^2 s$), follow significantly different trends for the two frequencies. Since the beams are drastically different at the two observing frequencies this allows for different beam filling factors for the respective beams to be used in modelling.

3.4.2.1 Departure Coefficients for Modelling

A modified version of Walmsley's bnprog.f program was used to calculate the b_n-β_n values for different densities and temperatures of model clouds for ELDWIM. The β_n values for Hnβ transitions were calculated from the b_n values obtained from the above program using the equation below.

$$\beta_{n,\beta} = 1 - \frac{kT_e}{h\nu}\frac{b_{n+2}-b_n}{b_{n+2}} \tag{3.7}$$

The departure coefficients b_n apply to all the Rydberg atoms whose core can be

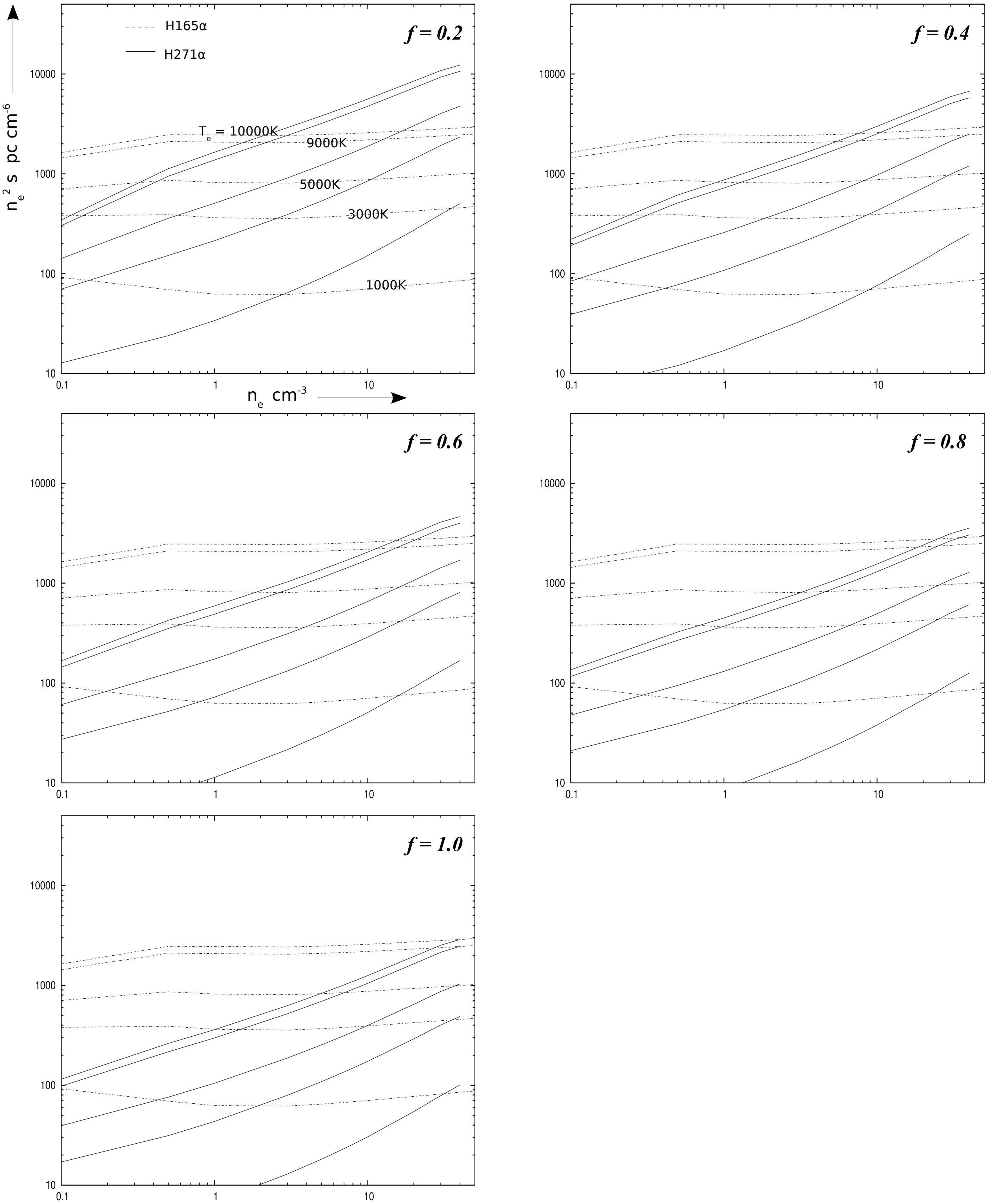

Fig 3-5 : EM (cm^{-6} pc) Vs n_e (cm^{-3}, abscissa) plots towards the position G7.2 -0.7 for the second component. " f " corresponds to filling factor for ORT beam. The number density is well constrained between 2.0 – 40.0 cm^{-3} for these filling factors. The labels in the first plot (top left corner) apply to the remaining plots as well.

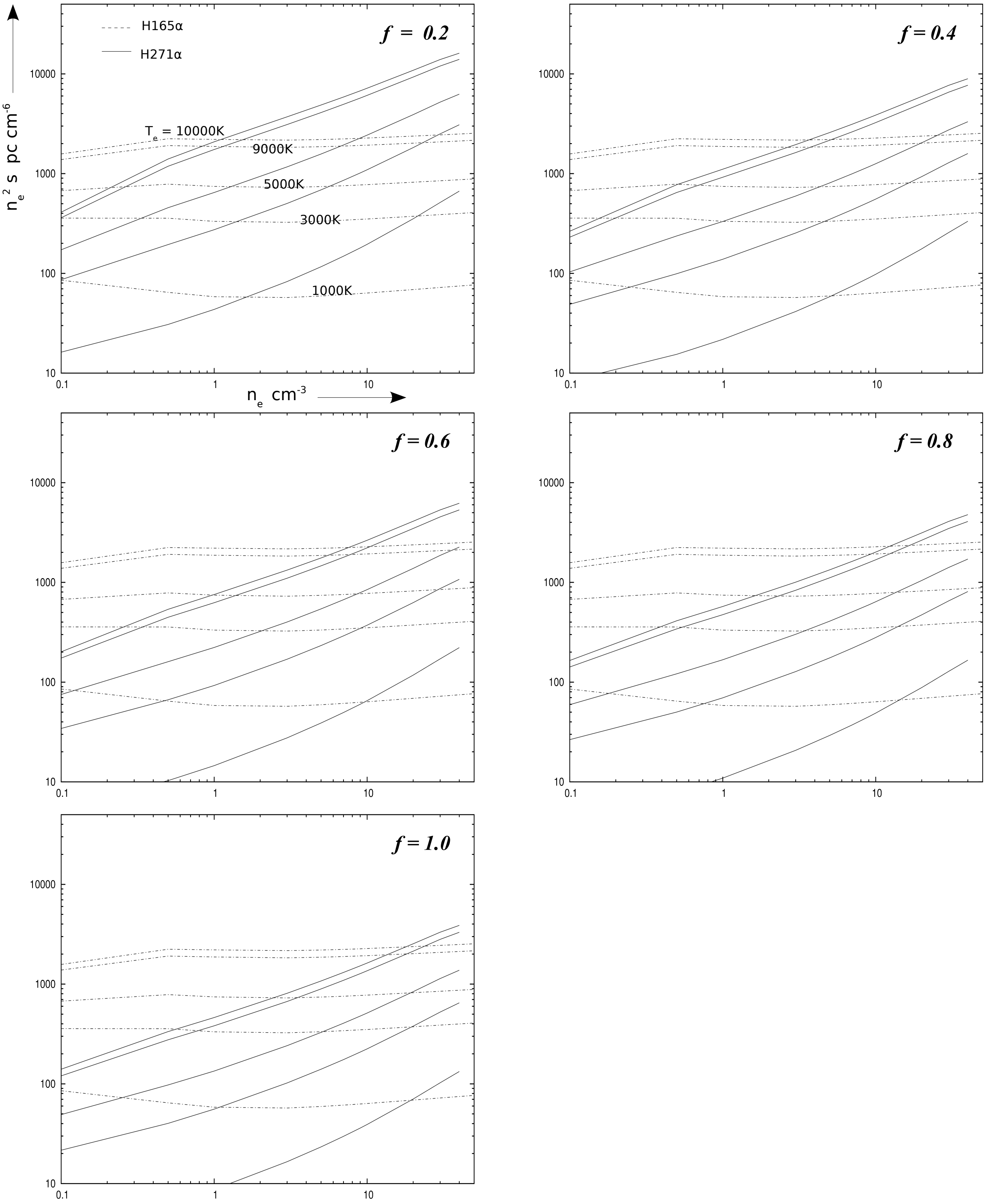

Fig 3-6 : EM (cm^{-6} pc) Vs n_e (cm^{-3}, abscissa) plots towards the position G15.8 -0.5 for the first component. “ f ” corresponds to filling factor for ORT beam. The number density is well constrained between 1.0 – 20.0 cm^{-3} for these filling factors. The labels in the first plot (top left corner) apply to the remaining plots as well.

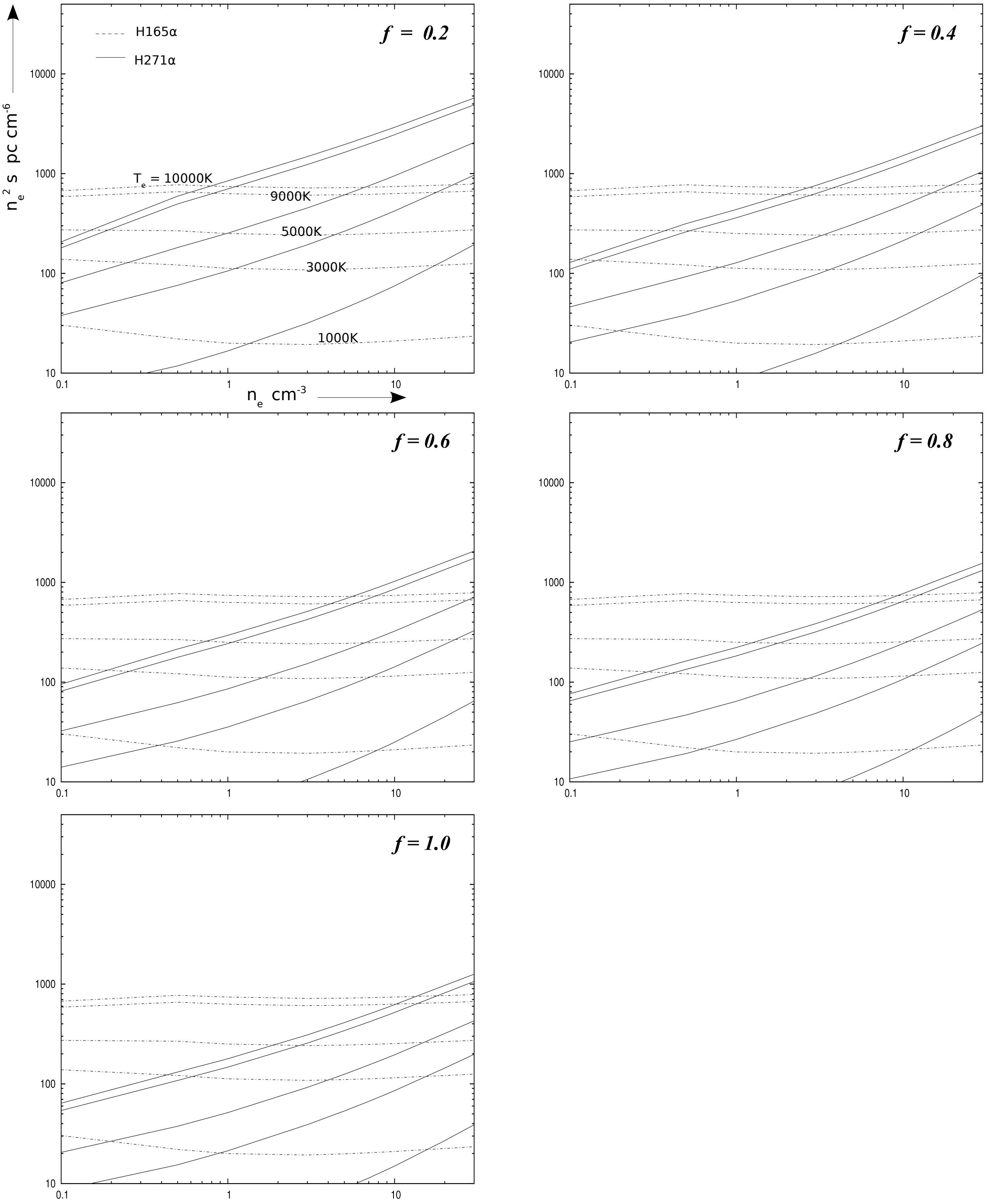

Fig 3-7 : EM (cm^{-6} pc) Vs n_e (cm^{-3}, abscissa) plots towards the position G15.8 -0.5 for the second component. " f " corresponds to filling factor for ORT beam. The number density is well constrained between 1.0 – 15.0 cm^{-3} for these filling factors. The labels in the first plot (top left corner) apply to the remaining plots as well.

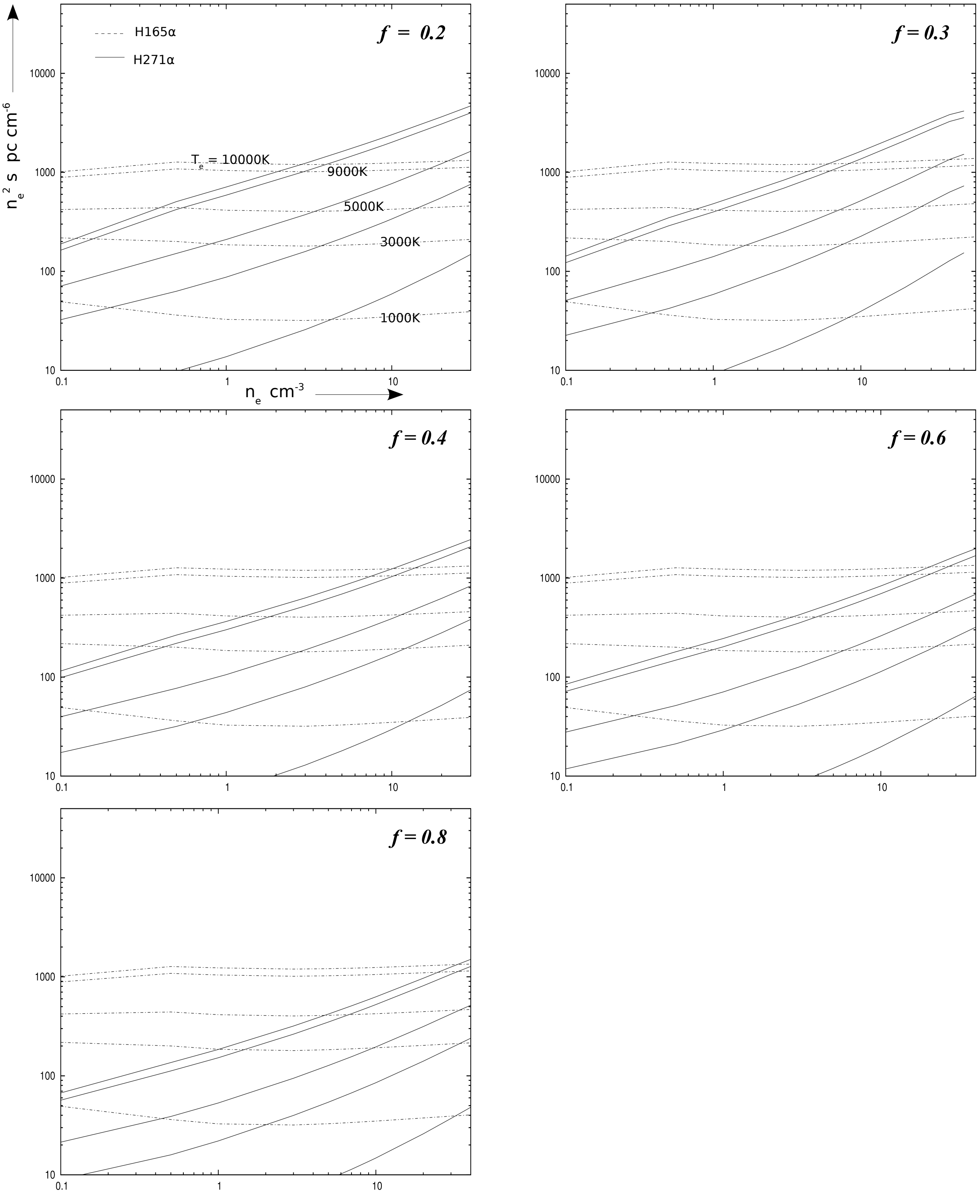

Fig 3-8 : EM (cm^{-6} pc) Vs n_e (cm^{-3}, abscissa) plots towards the position G18.6 -0.8 for the first component. " f " corresponds to filling factor for ORT beam. The number density is well constrained between 3.0 – 30.0 cm^{-3} for these filling factors. The labels in the first plot (top left corner) apply to the remaining plots as well.

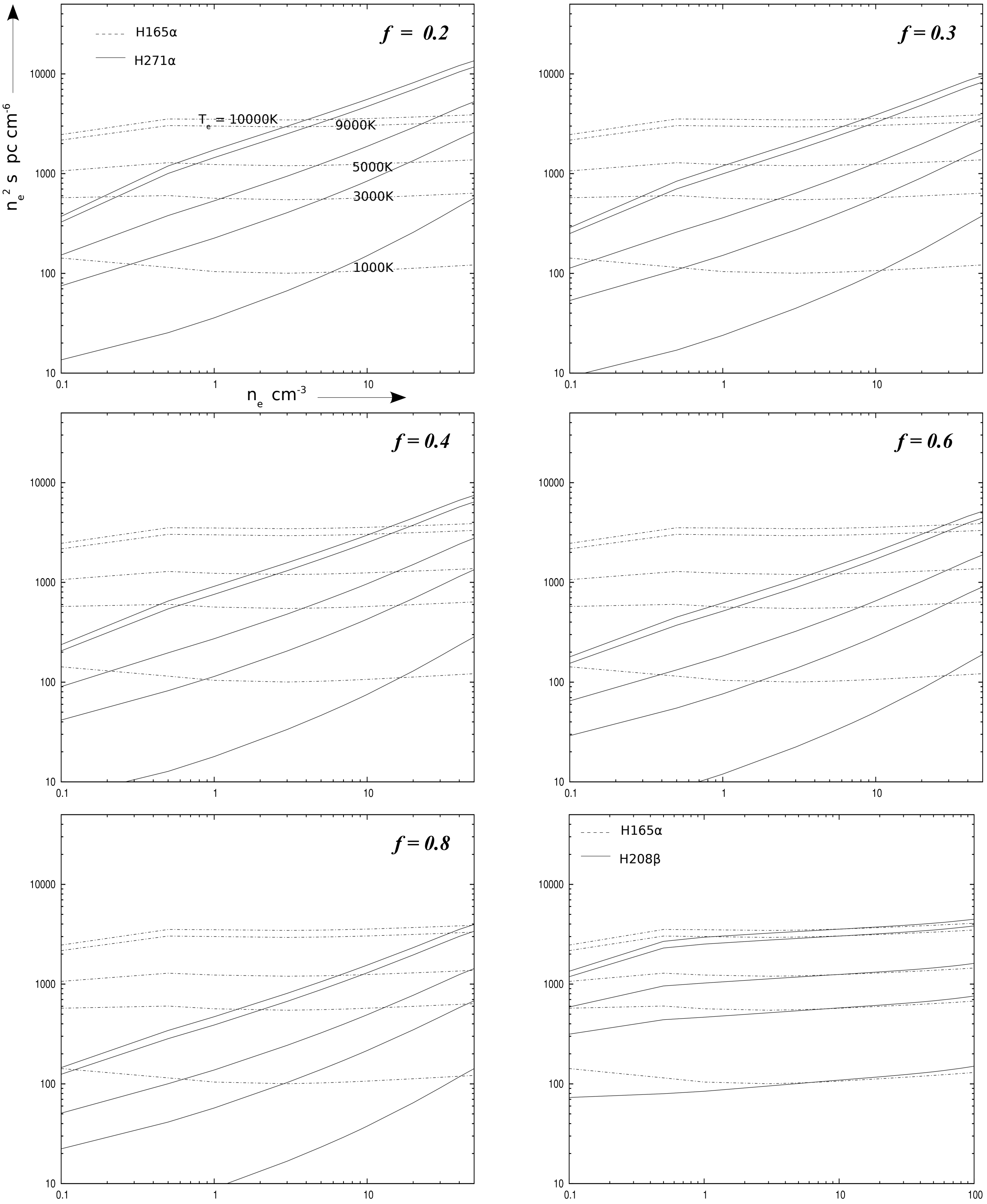

Fig 3-9 : EM (cm^{-6} pc) Vs n_e (cm^{-3}, abscissa) plots towards the position G19.2 +1.7. " f " corresponds to filling factor for ORT beam. The number density is well constrained between 4.0 – 50.0 cm^{-3} for these filling factors. The labels in the first plot (top left corner) apply to the remaining plots as well. The β line modelling which uses a single component fitted to its spectrum is constrained at 10 cm^{-3}. The errors on the β line parameters are large enough that they can produce any value from the α modelling.

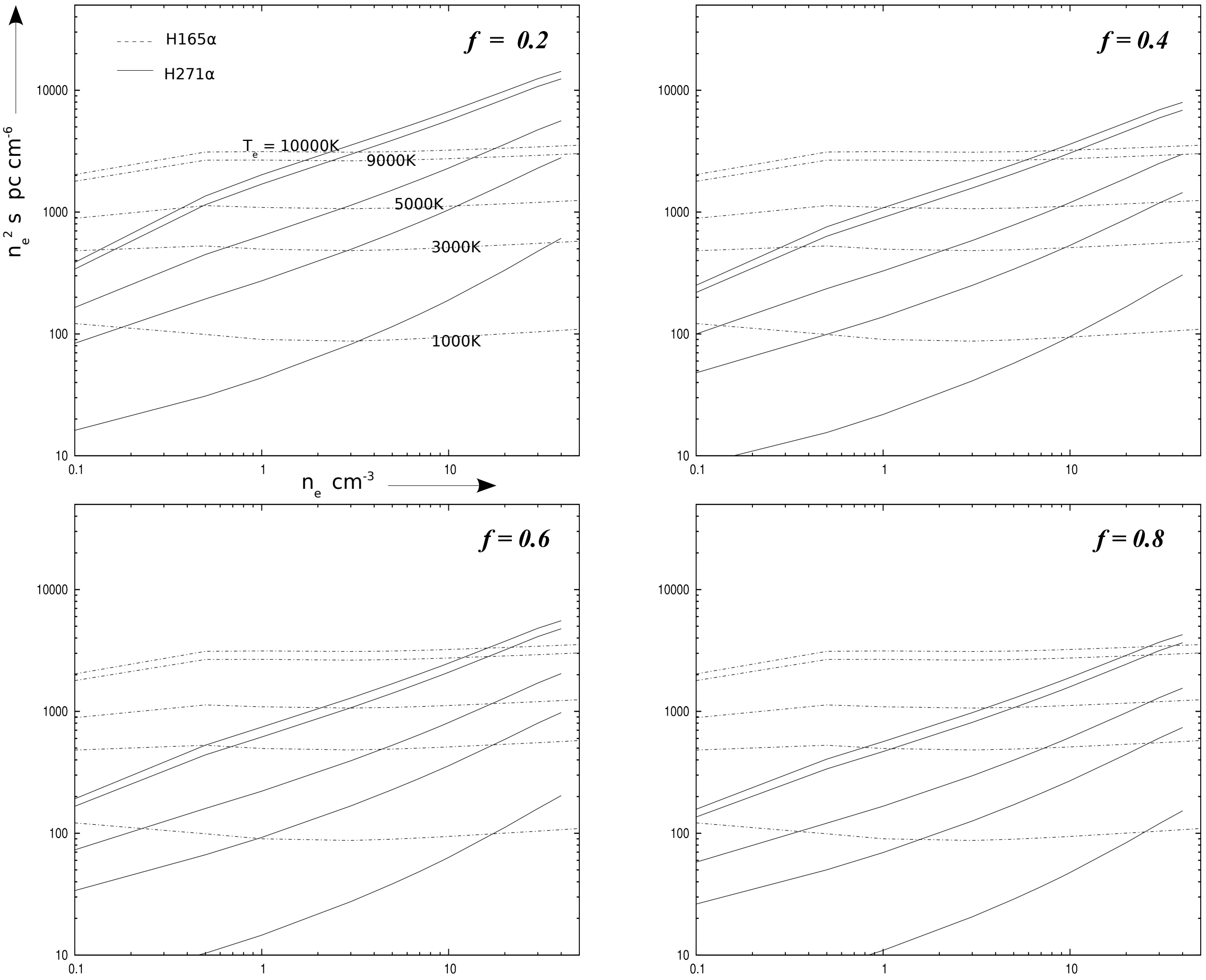

Fig 3-10 : EM (cm^{-6} pc) Vs n_e (cm^{-3}, abscissa) plots towards the position G24.3 -0.6 for the first component. " f " corresponds to filling factor for ORT beam. The number density is well constrained between 2.0 – 25.0 cm^{-3} for these filling factors. The labels in the first plot (top left corner) apply to the remaining plots as well.

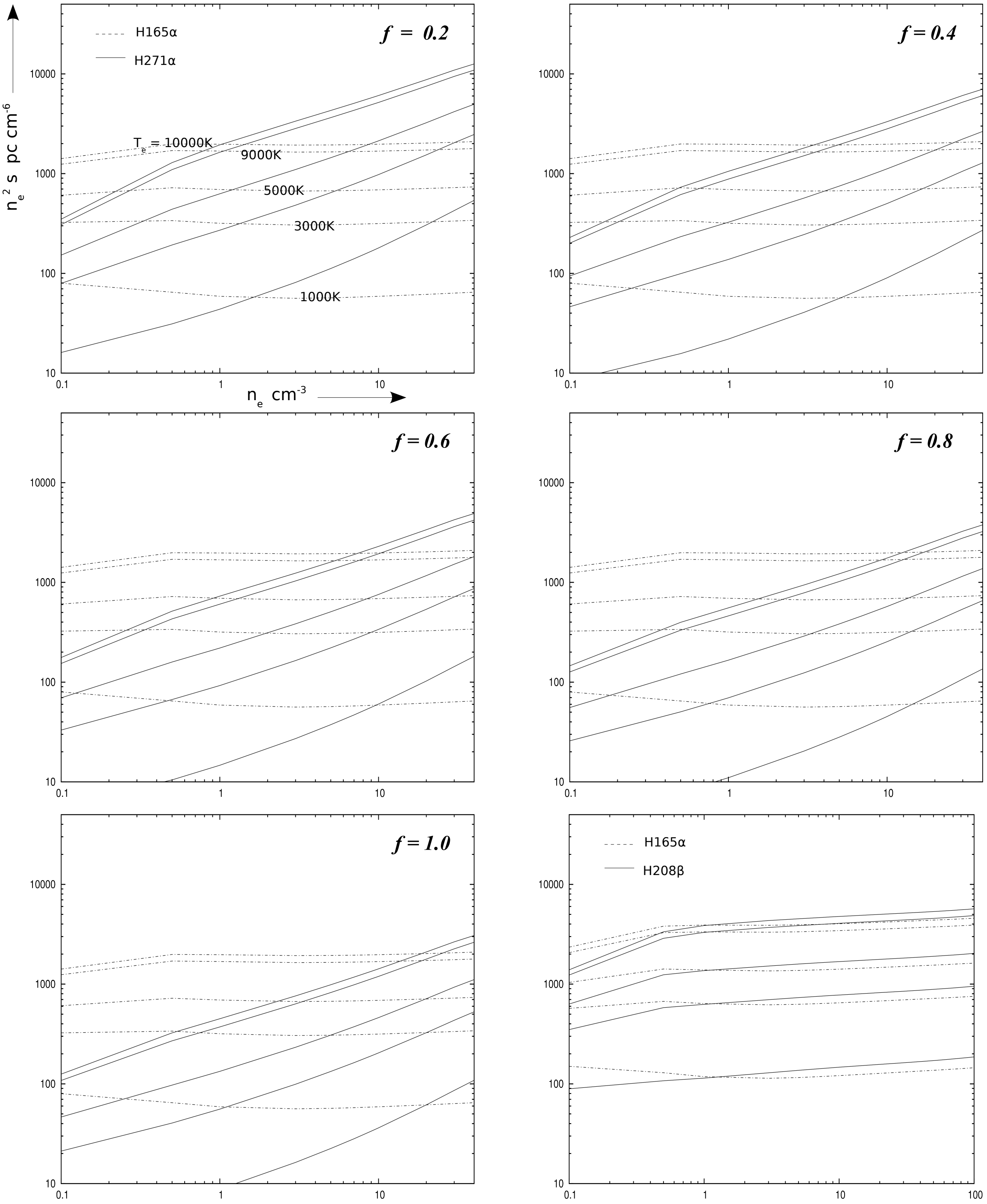

Fig 3-11 : EM (cm^{-6} pc) Vs n_e (cm^{-3}, abscissa) plots towards the position G24.3 -0.6 for the second component. " f " corresponds to filling factor for ORT beam. The number density is well constrained between 1.0 – 20.0 cm^{-3} for these filling factors. The labels in the first plot (top left corner) apply to the remaining plots as well. The β line modeling which uses a single component fitted to its spectrum is constrained at 1 cm^{-3}. The errors on the β line parameters are large enough that they can produce any value from the α modeling.

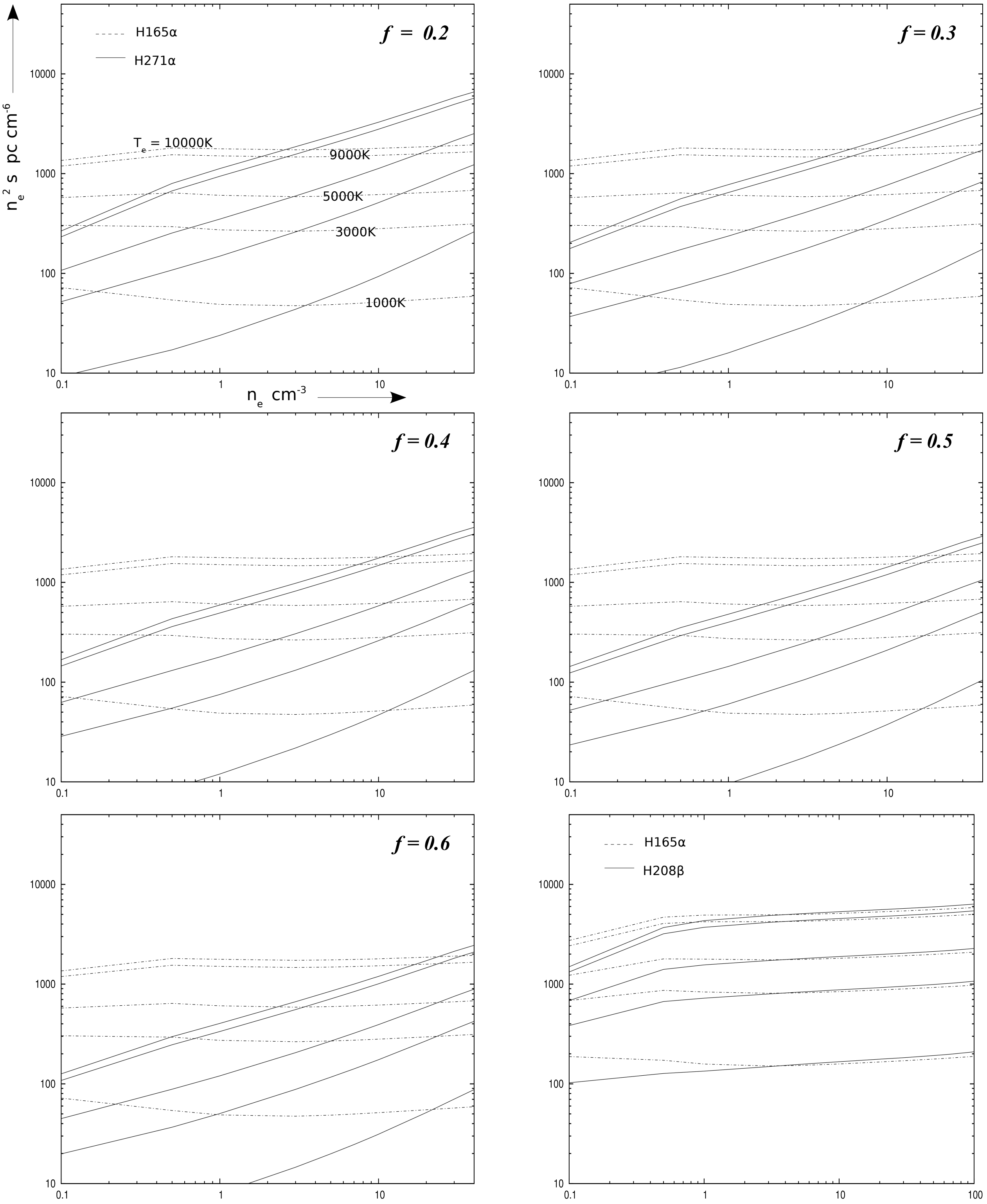

Fig 3-12 : EM (cm^{-6} pc) Vs n_e (cm^{-3}, abscissa) plots towards the position G26.5 +0.0 for the first component. " f " corresponds to filling factor for ORT beam. The number density is well constrained between 2.0 – 20.0 cm^{-3} for these filling factors. The labels in the first plot (top left corner) apply to the remaining plots as well. The β line modeling which uses a single component fitted to its spectrum is constrained at 4.0 cm^{-3}. The errors on the β line parameters are large enough that they can produce any value from the α modeling.

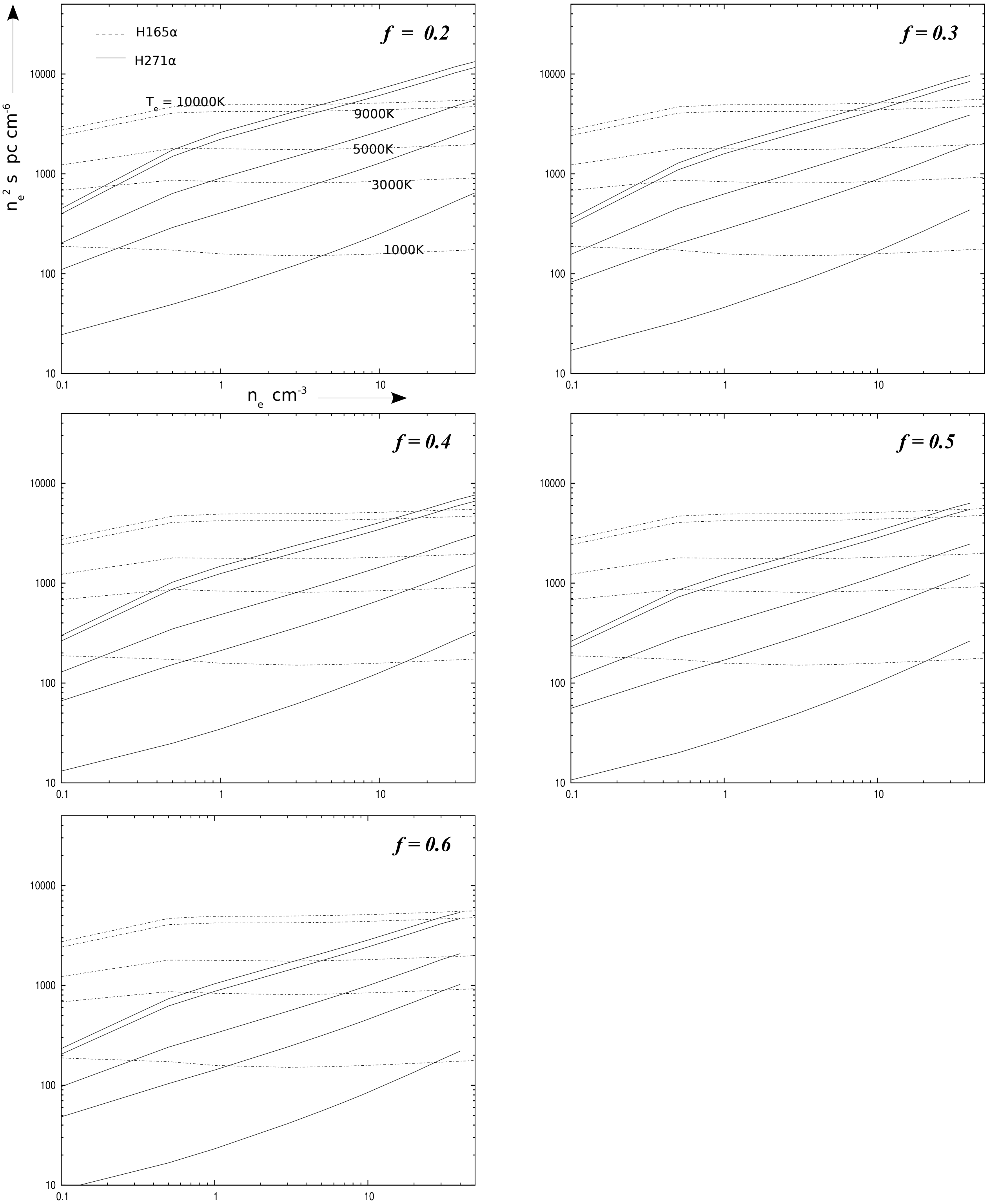

Fig 3-13 : EM (cm^{-6} pc) Vs n_e (cm^{-3}, abscissa) plots towards the position G26.5 +0.0 for the second component. " f " corresponds to filling factor for ORT beam. The number density is well constrained between 4.0 – 40.0 cm^{-3} for these filling factors. The labels in the first plot (top left corner) apply to the remaining plots as well.

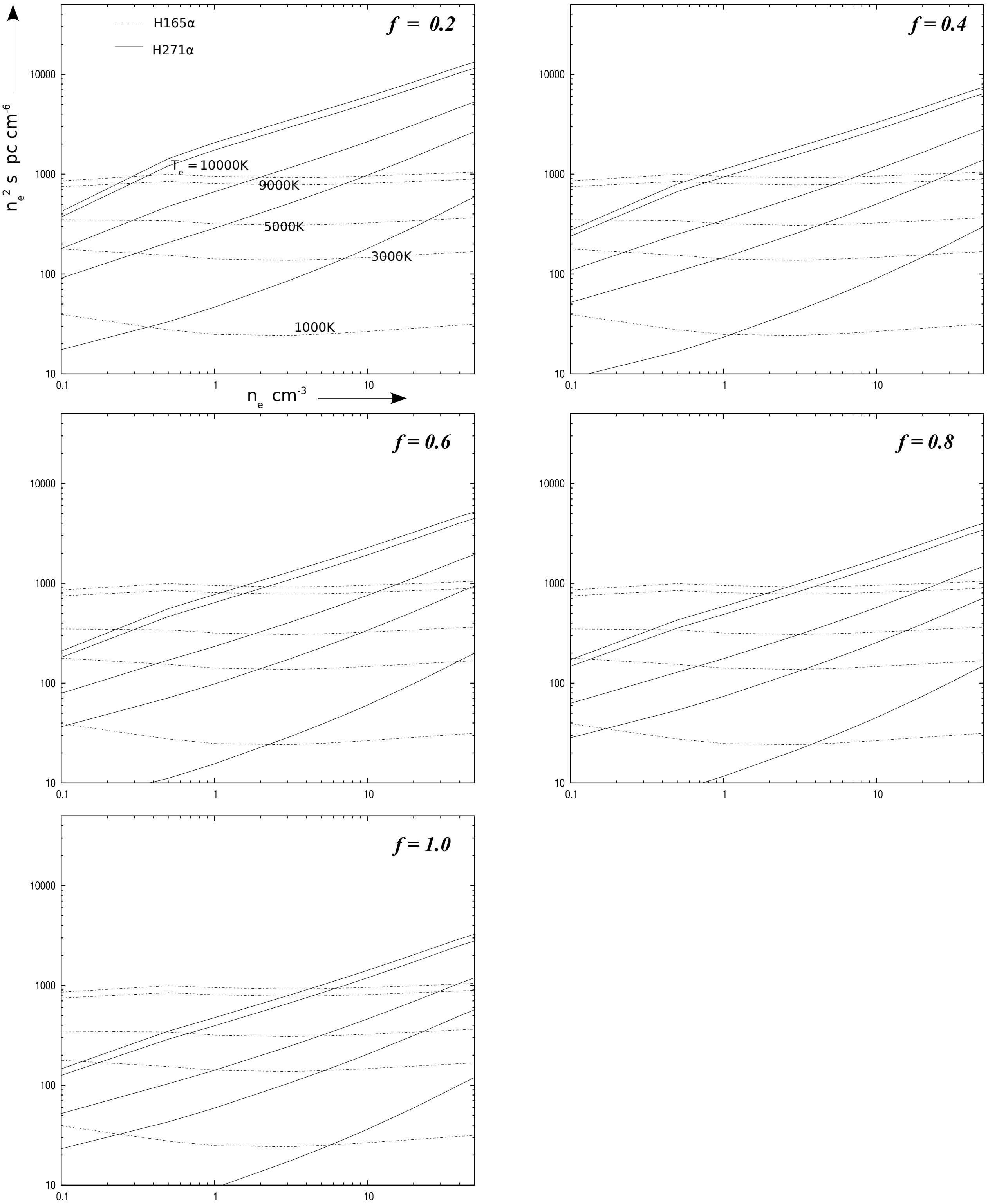

Fig 3-14 : EM (cm^{-6} pc) Vs n_e (cm^{-3}, abscissa) plots towards the position G28.0 +0.0 for the first component. " f " corresponds to filling factor for ORT beam. The number density is well constrained between 0.3 – 5.0 cm^{-3} for these filling factors. The labels in the first plot (top left corner) apply to the remaining plots as well.

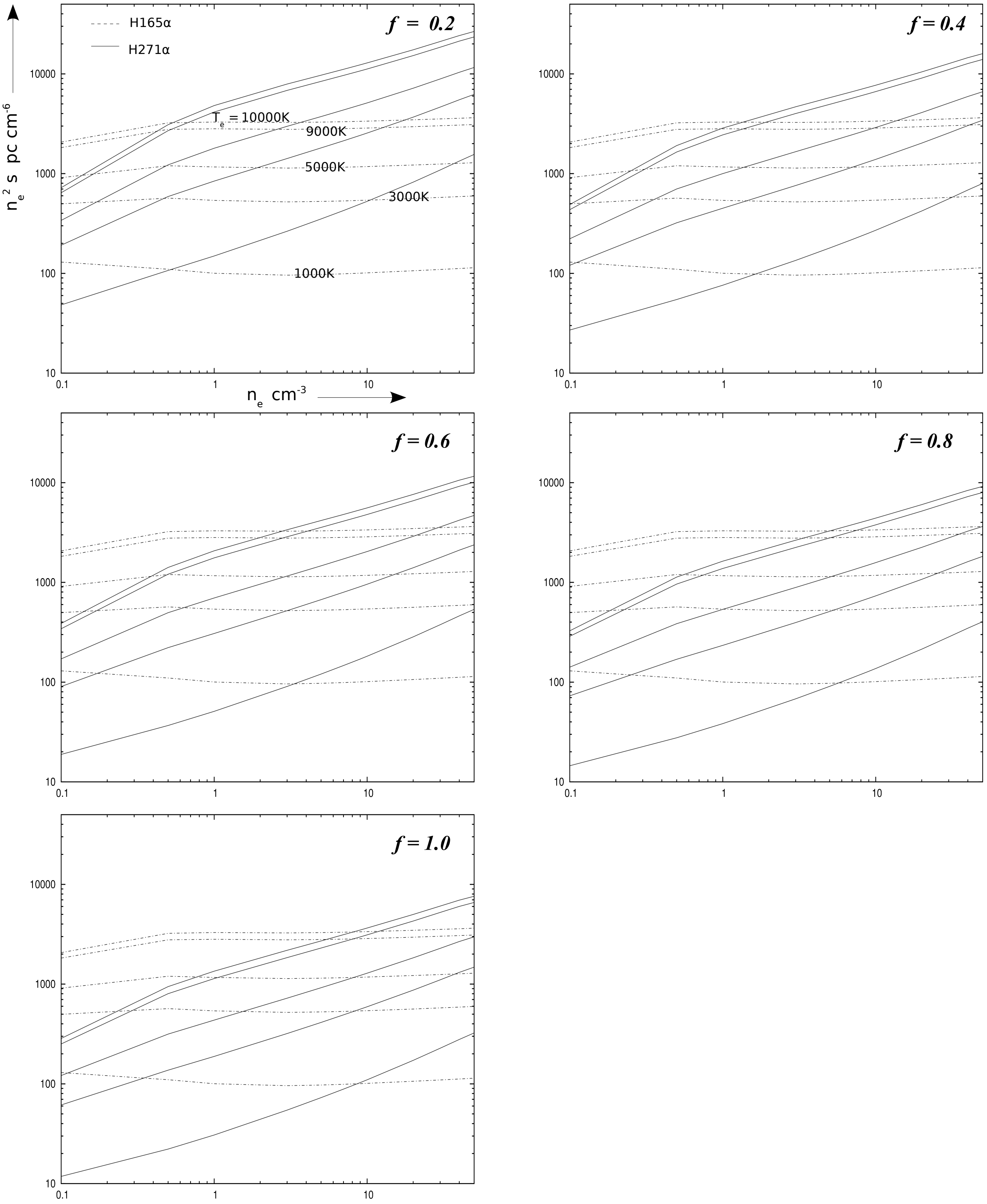

Fig 3-15 : EM (cm^{-6} pc) Vs n_e (cm^{-3}, abscissa) plots towards the position G28.0 +0.0 for the second component. " f " corresponds to filling factor for ORT beam. The number density is well constrained between 0.5 – 8.0 cm^{-3} for these filling factors. The labels in the first plot (top left corner) apply to the remaining plots as well.

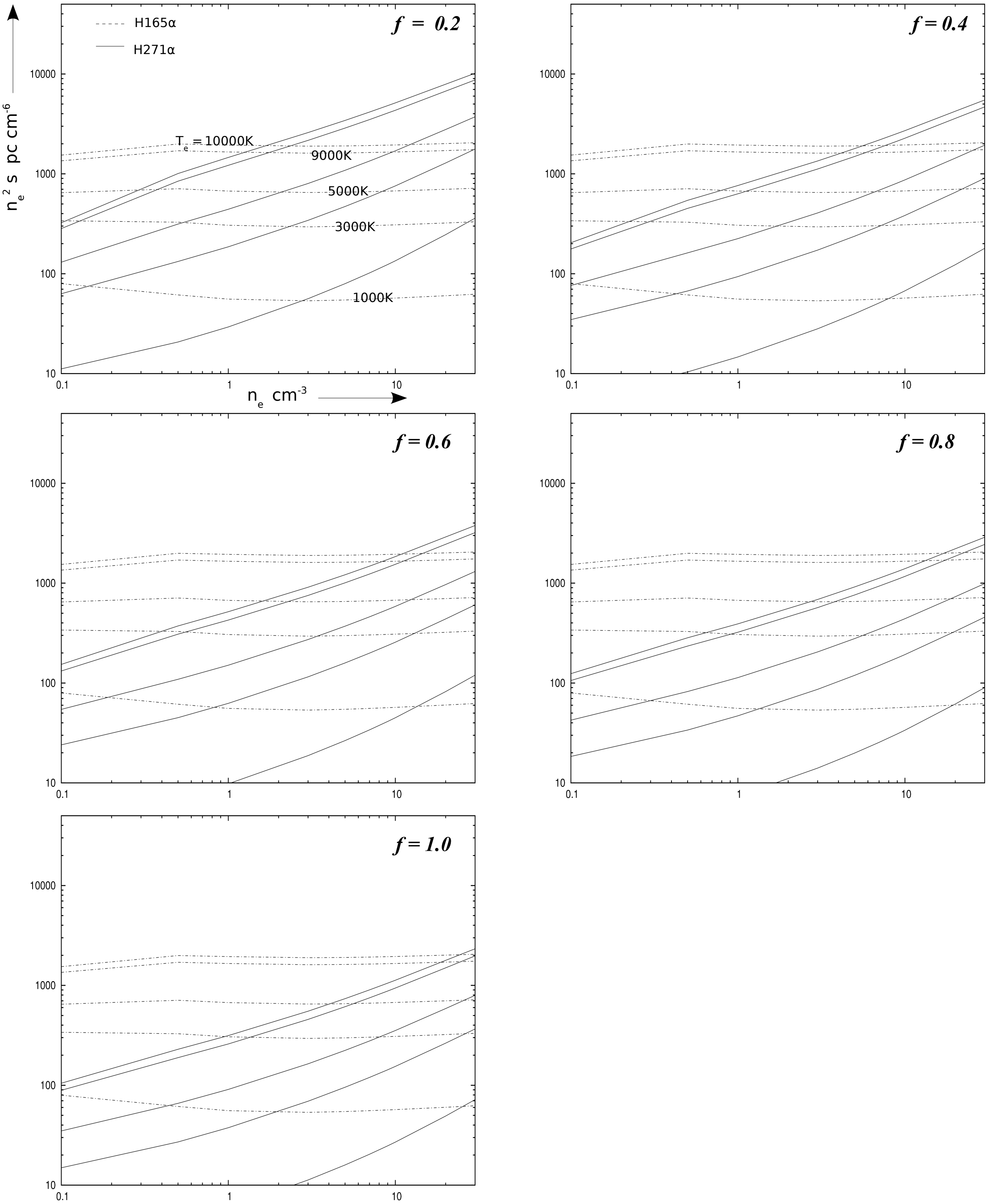

Fig 3-16 : EM (cm^{-6} pc) Vs n_e (cm^{-3}, abscissa) plots towards the position G16.3 +1.3 . " f " corresponds to filling factor for ORT beam. The number density is well constrained between 2.0 – 25.0 cm^{-3} for these filling factors. The labels in the first plot (top left corner) apply to the remaining plots as well.

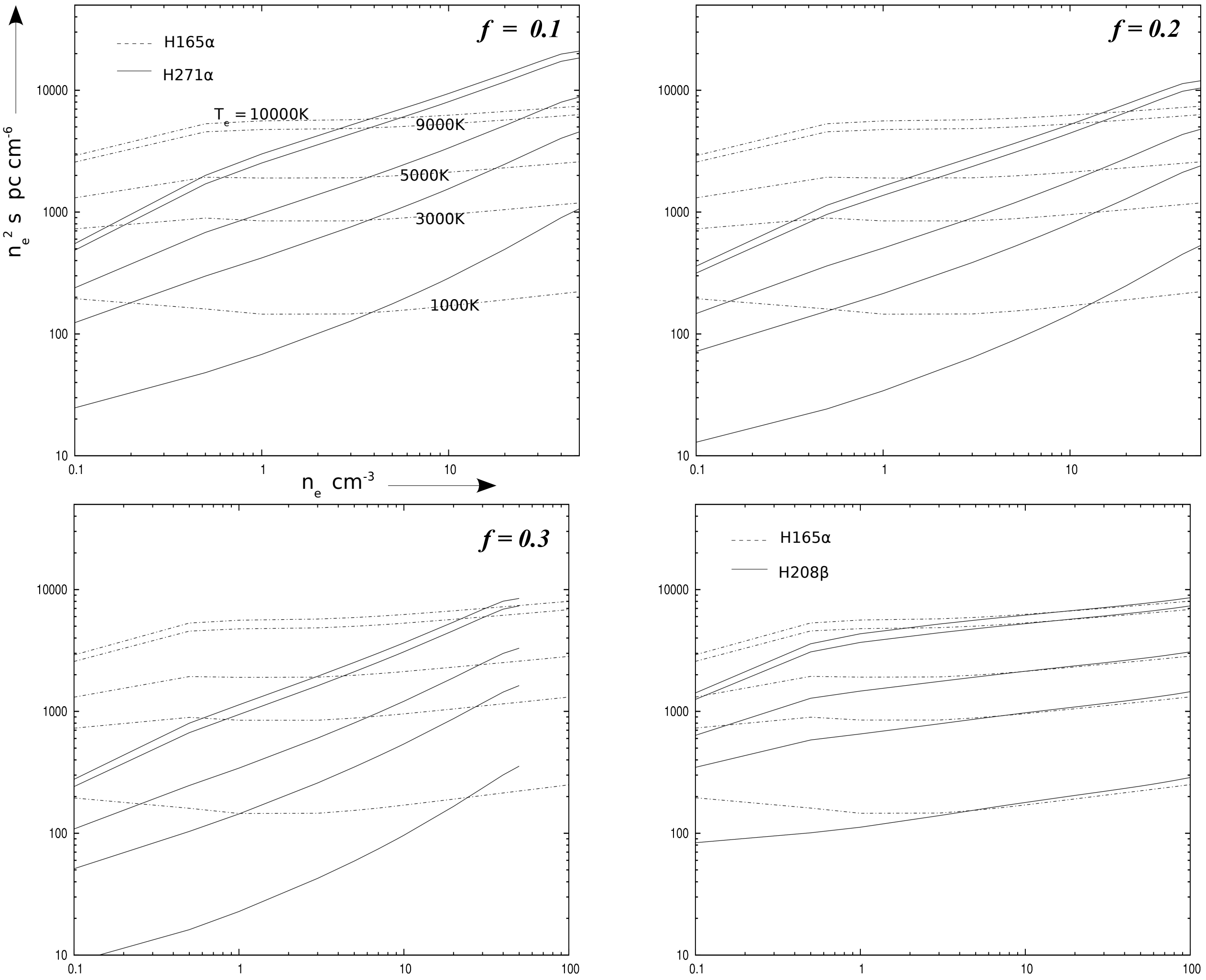

Fig 3-17 : EM (cm^{-6} pc) Vs n_e (cm^{-3}, abscissa) plots towards the position G18.0 +1.8 . "f " corresponds to filling factor for ORT beam. The number density is well constrained between 4.0 – 30.0 cm^{-3} for these filling factors. The labels in the first plot (top left corner) apply to the remaining plots as well. The β line modeling which uses a single component fitted to its spectrum is constrained at 15.0 cm^{-3}. The errors on the β line parameters are large enough that they can produce any value from the α modeling.

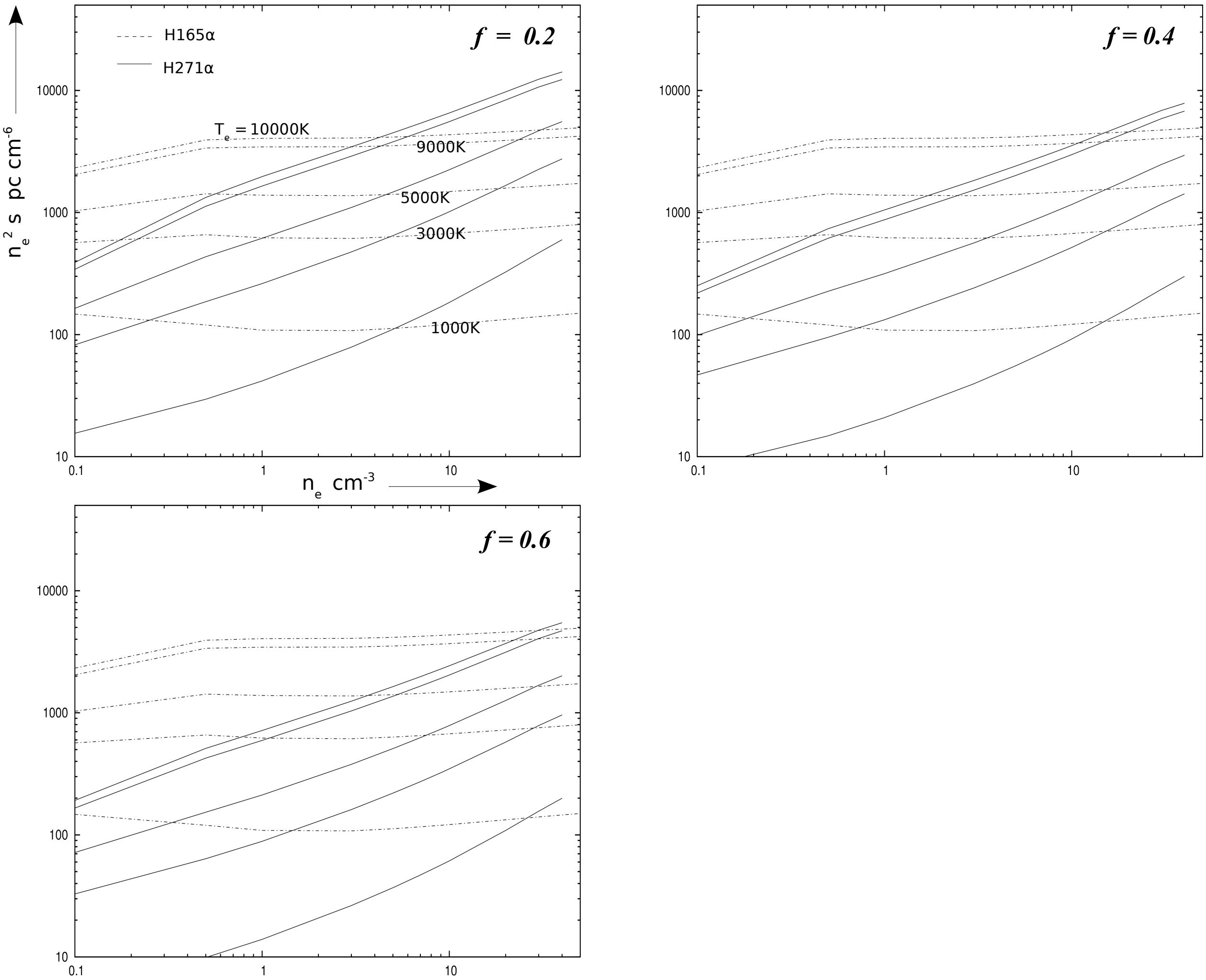

Fig 3-18 : EM (cm^{-6} pc) Vs n_e (cm^{-3}, abscissa) plots towards the position G12.6 -0.6 for the first component. " f " corresponds to filling factor for ORT beam. The number density is well constrained between 4.0 – 30.0 cm^{-3} for these filling factors. The labels in the first plot (top left corner) apply to the remaining plots as well.

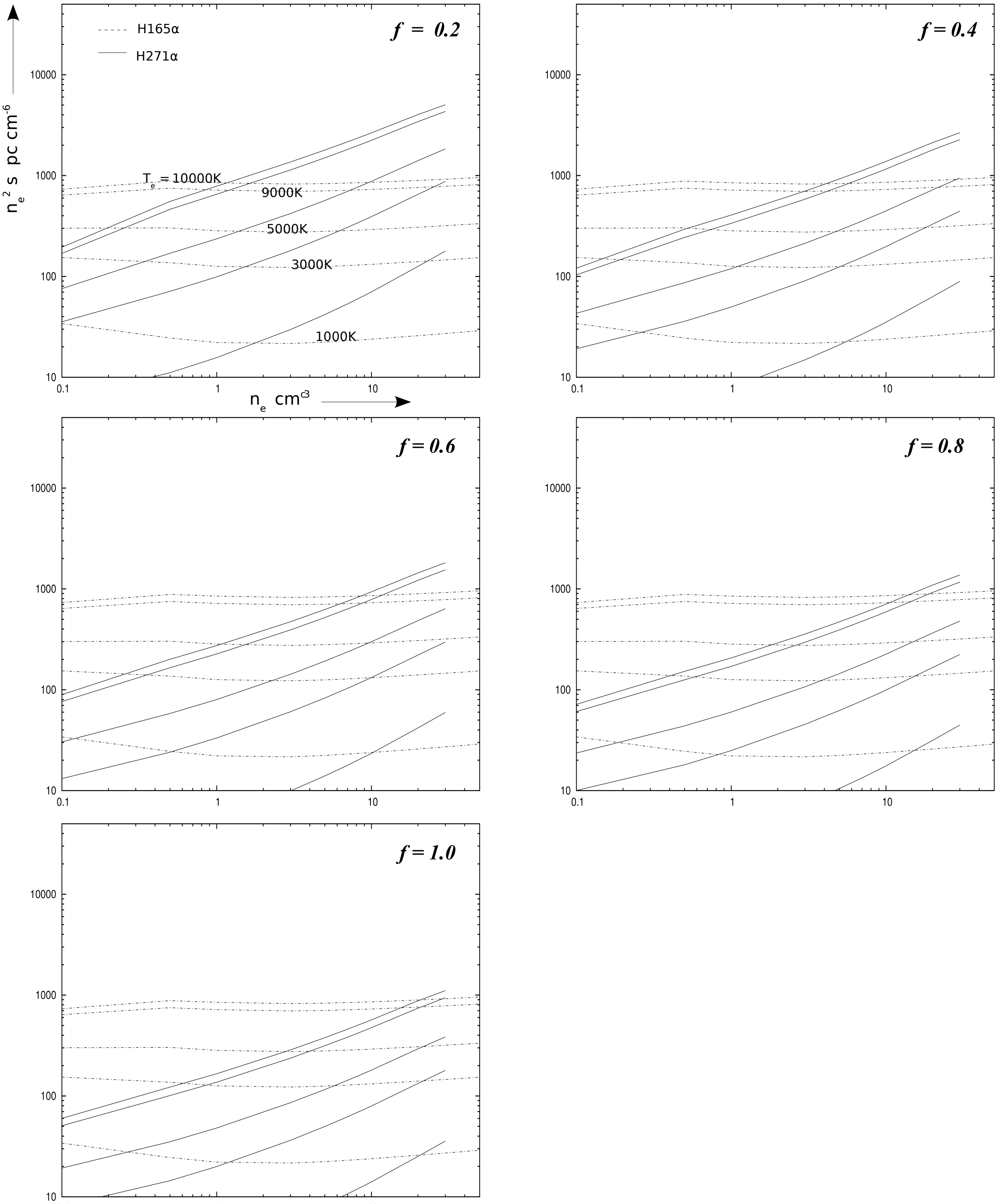

Fig 3-19 : EM (cm^{-6} pc) Vs n_e (cm^{-3}, abscissa) plots towards the position G12.6 -0.6 for the second component. " f " corresponds to filling factor for ORT beam. The number density is well constrained between 1.0 – 20.0 cm^{-3} for these filling factors. The labels in the first plot (top left corner) apply to the remaining plots as well.

very b_n-β_n coefficients were used to model the Henα line as well.

Modelling results for different sources have been plotted from fig-5. The modelling was done for various filling factors. However some of the models can be ruled out by considering the observed line widths. The pressure broadening can be calculated independently at different frequencies and the residual broadening is attributed to doppler broadening. The doppler broadening is a combination of microturbulence and thermal motion in the gas, as discussed in chapter-2. The obtained doppler width is attributed due to a net temperature called dispersion temperature T_D.

$$\Delta\nu_D = \frac{\nu}{c}\left[\frac{2kT_e}{M_x} + \frac{2}{3}V_T^{\,2}\right]^{1/2} = \frac{\nu}{c}\left[\frac{2kT_D}{M_x}\right]^{1/2} \qquad (3.8)$$

where $\Delta\nu_D$ is the observed doppler width.

3.4.3 Conclusion

The modelling towards different sources suggests that the average number density of ELDWIM is ~10 cm^{-3} with volume filling factors of 0.2-0.6. This range of number density produces the observed line strength at all the temperatures considered in the modelling. The number density at the common emission measure at the two frequencies(328MHz, 1.4GHz) is almost constant with temperature as can be seen in the EM Vs n_e plots. With a common emission measure and the same number density at the two frequencies the cylindrical cloud has the same line of sight extent s. With this fact the beam filling factor now becomes the volume filling factor as said above. The lower filling factors seem to be more realistic with the observed data. These are more consistent with the observed line widths which in many cases has been observed to be gaussian and hence mainly dopplerian. The residual spectrum after removing the fitted gaussian is almost noise with zero mean, suggesting a good fit. Significant pressure broadening would have made this difficult, since pressure broadening being Lorentzian is much broader towards the wings of the profile. A table of obtained number densities towards different positions is given in table-4. However the band-averaged spectra with better signal to noise ratio show good signs of pressure broadening in both hydrogen & helium lines towards a few positions(chapter-5).

Source		***filling factor range***	***n_e range***
l	***b***	$\left(\Omega_{Src}/\Omega_{Beam}\right)_{ORT}$	***(cm^{-3})***
7.2	*-0.7*	*0.2 - 0.6*	*2.0 – 15.0*
15.8	*-0.5*	*0.2 – 0.6(1)*	*1.0 – 8.0(1)*
		0.2 – 0.6(2)	*0.8 – 6.0(2)*
18.6	*-0.8*	*0.2 – 0.6(1)*	*2.0 – 20.0(1)*
		-”- (2)	*0.6 – 3.0(2)*
19.7	*1.7*	*0.2 – 0.6*	*4.0 – 25.0*
23.4	*-0.6*	*0.2 – 0.6(1)*	*2.0 – 15.0(1)*
		-”-(2)	*1 – 7.0(2)*
26.5	*0.0*	*0.2 – 0.6(1)*	*2.0 – 20.0(1)*
		0.2 – 0.4(2)	*5.0 – 15.0(2)*
28.0	*0.0*	*0.2 – 0.8(1)*	*0.3 – 3.0(1)*
		0.2 – 0.8(2)	*0.6 – 5.0(2)*
16.3	*+1.3*	*0.2 – 0.6*	*1.0 – 10.0*
18.0	*+1.8*	*0.1 – 0.3*	*4.0 – 25.0*
12.6	*-0.6*	*0.2 – 0.6(1)*	*5.0 – 25.0(1)*
		0.2 – 0.6(2)	*1.0 – 8.0(2)*

Table 3-4: Number densities corresponding to different sources. The number in the paranthesis indicates the hydrogen line component from left. For more details refer the individual modelling plots.

Chapter 4

Observations with Ooty Radio Telescope.

4.1 The Ooty Radio Telescope(ORT)

The ORT is situated near the town Ooty, south India at a longitude of 283.3° and latitude of 11° 23'. ORT(Swarup et.al 1971) is an off-axis parabolic cylinder with a length of 530m and width of 30m. The telescope is located on a hill which has a natural slope of 11.4° equal to the geographical latitude of the place this gives it the feature of equatorial mount, as the axis of the telescope is now parallel to the rotation axis of earth. The operating frequency of the telescope is centered at 326.5 MHz with a maximum bandwidth of 15MHz at the front-end. The reflecting surface of the clylinder is made of 1100 stainless steel wires running parallel to each other along the entire length of the telescope. These are supported by 24 steerable frames at regular intervals. An array of 1056 half-wave dipoles in front of a 90 degrees corner reflector forms the primary feed of the telescope. With equatorial mount the telescope can track a celestial source in the sky for about 9.5 hours at a stretch by mechanical rotation of the cylinder in the east-west direction from -4^h07^m to 5^h26^m. The telescope is steerable electronically in declination by introducing suitable phase and delay gradients along the dipole array. This range is -60° to +60°.

The 1056 dipoles are in groups of 48. The signals recieved by these groups are added in phase to form 22 group outputs, each known as a module. The telescope is divided into northern part and southern part. The northern modules are designated as N1 to N11 and the southern modules as S1 to S11. The signal from each module is down converted to an IF of ~30MHz with a bandwidth of 15MHz at the front end. The down conversion is achieved by mixer action by sending an LO signal to all the modules over equal length cables from a common source in the receiver room. The beam width due to eachmodule is 2.3° in east-west and 2.2° sec(δ) in the north-south, where δ is the declination. This forms the observing mode and beam for the current project of RRL observations. The outputs from the 22 modules of the ORT are brought to the receiver room for further processing. These signals are separately combined with proper delay compensations for geometric path lengths in a beam forming network to form 12 beams for each half of the ORT.

4.2 The ORT Receiver system at block diagram level

The basic block diagram of the ORT system is as shown in fig-1,

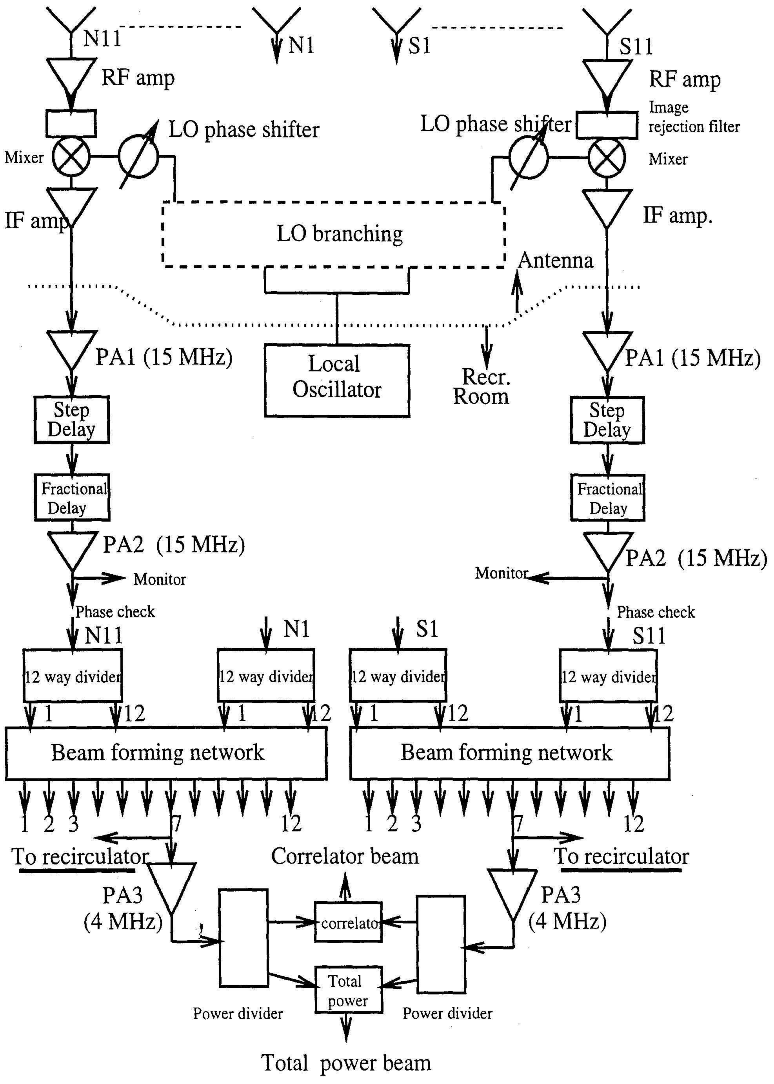

Fig 4-1: The basic block diagram of ORT(Anish Roshi.D. 1995). The output to the new digital backend system goes after PA1.

As described in sec-1 each module consists of an array of 48 dipoles. The outputs from these dipoles are amplified using Low Noise Amplifiers(LNA) and combined after proper phase shifting through phase shifters as shown in the fig-2. These phase shifters compensate for the phases between the 48 dipoles calculated for the center frequency for a specified declination. This combined signal after amplification and passing through a image rejection filter is downconverted to an IF of 30MHz by mixing with a local oscillator nominally set to 296.5 MHz(refer fig-2). The local oscillator is located in the receiver room. It should be mentioned here that for the sake of present observations this LO at 296.5 MHz was replaced by a Rhode & Schwarz oscillator which could set a slightly different & desired frequency than 296.5 MHz. This facilitated the dual dicke swithching used for spectral line observations as described in chapter 3. The beam width for this observation was that formed by individual modules which is ~ 2° x 2° . The single module system at a block diagram level is given in fig-2.

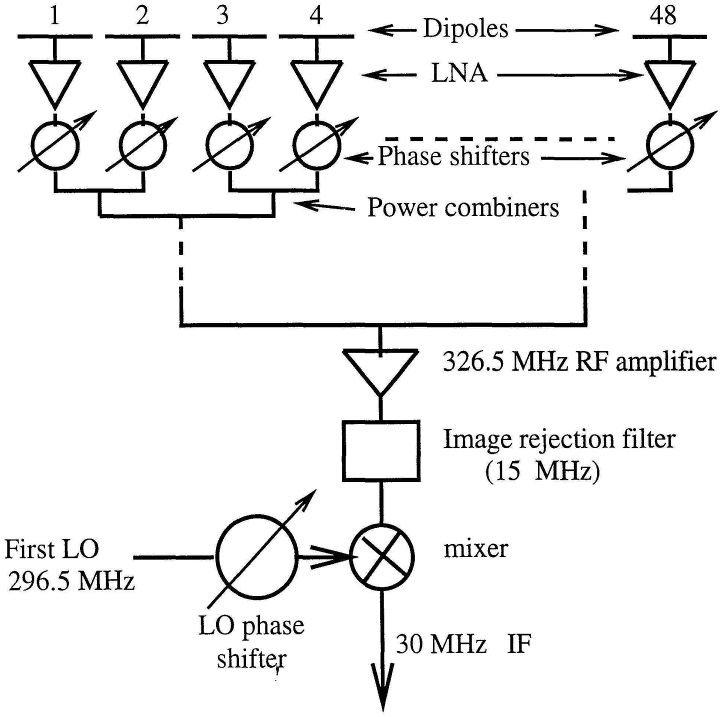

Fig 4-2: The single module system for ORT showing the dipoles, LNA and down conversion to IF(Anish Roshi.D. 1995).

The 30MHz IF is brought to the receiver room from all the 22 modules using equal length cables. The geometric delay difference between different modules when observing a source at declination δ is compensated by adding or removing cables from the signal path as shown in fig-1. This delay compensation occurs at 30MHz so a net phase difference remains, this is taken care of using phase shifted LO. The delay compensated signal from each module is split into twelve parts and fed to a beam forming network to generate 12 beams centered around the specified declination. The 12 signals from each module of north(N1-N11) and south(S1-S11) are combined module wise to obtain 12 combined north and south signals. These are either added or correlated to get a total power beam or a correlated beam. The correlated beam has a width of 3.3secδ arcmin in the NS direction and 2° in the EW direction. The 12 beams span about ±18' around a specified declination with a separation of 3secδ arcmin . The total power beam has a width of 5.5secδ in NS direction with the same width in the EW direction and same separation between the beams. It should be mentioned here however that for the present observations none of these beams apply. Only the beams formed by individual modules apply, which is 2°.3 in RA and 2°.2secδ in declination. Since data from individual modules were combined to get a total power for each module. The spectra obtained from each module were then averaged to get a single averaged spectrum, one each for north and south.

4.3 ORT System Temperature

ORT is a system which has multiple stages of amplification and attenuation. These stages have their own gains and losses. The system temperature of such a cascade is given by the Friis formula,

$$T_{rec}=T_{s1}+\frac{1}{G_1}T_{s2}+\frac{1}{G_1G_2}T_{s3}+\ldots+\frac{1}{G_1G_2G_3..G_{n-1}}T_{sn} \tag{4.1}$$

where G's and T's are the gains and equivalent noise temperatures of respective stages. In a practical system the gain stages are connected by attenuators(some attenuation is always inevitable). The system temperature in such a case is given by

$$T_{rec}=T_{amb}\frac{(1-\alpha_1)}{\alpha_1}+\frac{T_{r1}}{\alpha_1}+T_{amb}\frac{(1-\alpha_2)}{\alpha_1\alpha_2G_1}+\frac{T_{r2}}{\alpha_1\alpha_2G_1}+\ldots \tag{4.2}$$

where T_{amb} is the common ambient temperature of the attenuators which have the loss factors α_n . T_{rn} are the temperatures of the gain stages(amplifiers) with gains G_n. For ORT equation 4.2 has the necessary number of terms. The higher terms are unnecessary due to their negligible contribution. The various factors are T_{amb},Tr_1,Tr_2,α_1,α_2,G_1 and G_2(295K,50K,110K,0.983,0.398,15dB(=$10^{1.5}$) and 15dB respectively). By plugging these numbers in the above equation T_{rec} comes out to be ~79K. Along with the receiver noise temperature the dipoles also receive emission from sky and ground noise from regions outside the parabolic reflector. The latter is called the spill over noise. These as computed for ORT are 45K and 30K respectively. The total cold sky system temperature is normally taken to be ~150K.

4.4 ORT with a New Digital Backend.

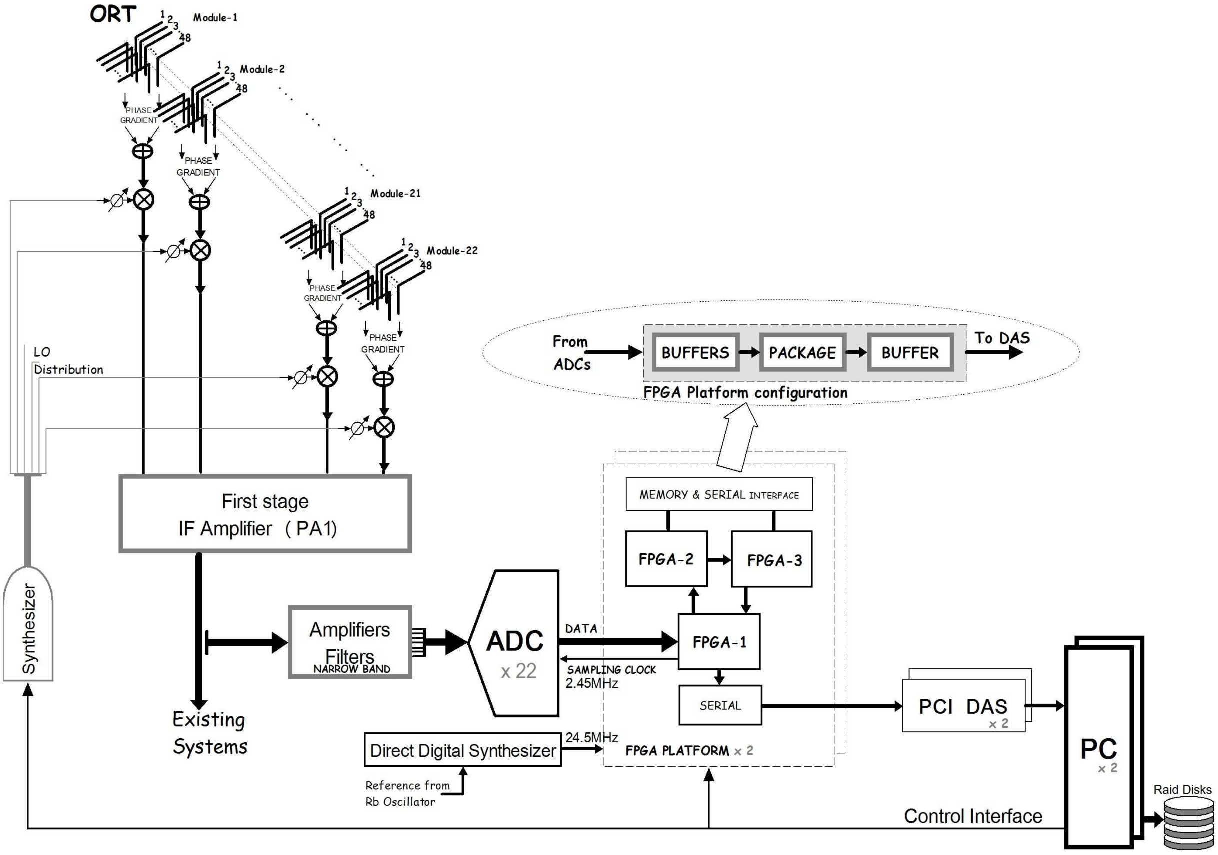

Fig 4-3: ORT system with the new digital backend. The output from PA1 is further amplified and filtered. The filtered output is fed to the ADCs for digitization. The sampling clock for the ADC is 2,449,998.85Hz which is derived from a stable 10 MHz Rb oscillator using direct digital synthesizing technique. The ADCs used are 2 bit quantizer. The output from the ADCs is buffered into the FPGA where they are further processed and streamed into the PC for storage through the PCI-DAS card (see Prabu, 2010, Ph.D thesis for further details).

The observations presented here were made with a new digital backend system(NDBS) built for ORT (Prabu et.al 2010, thesis in preparation). This new digital backend system derives its input after the pre-amplifier PA1 (fig-1:3). The input path and the various stages in this path are shown in fig-4. The signal after amplification from

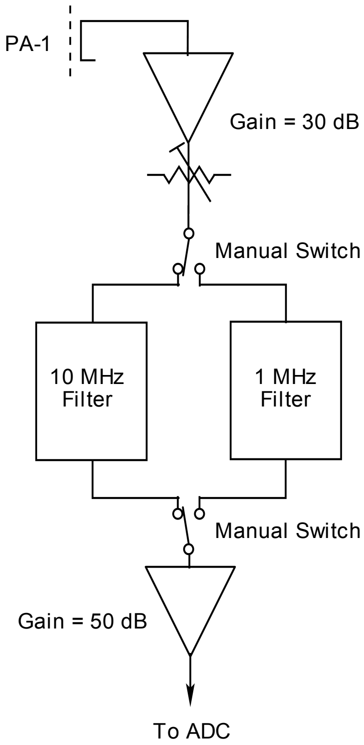

Fig 4-4: Input to the New Digital Backend after PA1.

PA1 passes through two filters before being fed to the ADC for sampling(fig-4). Each filter is designed for specific purpose. The broadband filter(10MHz) is mainly for

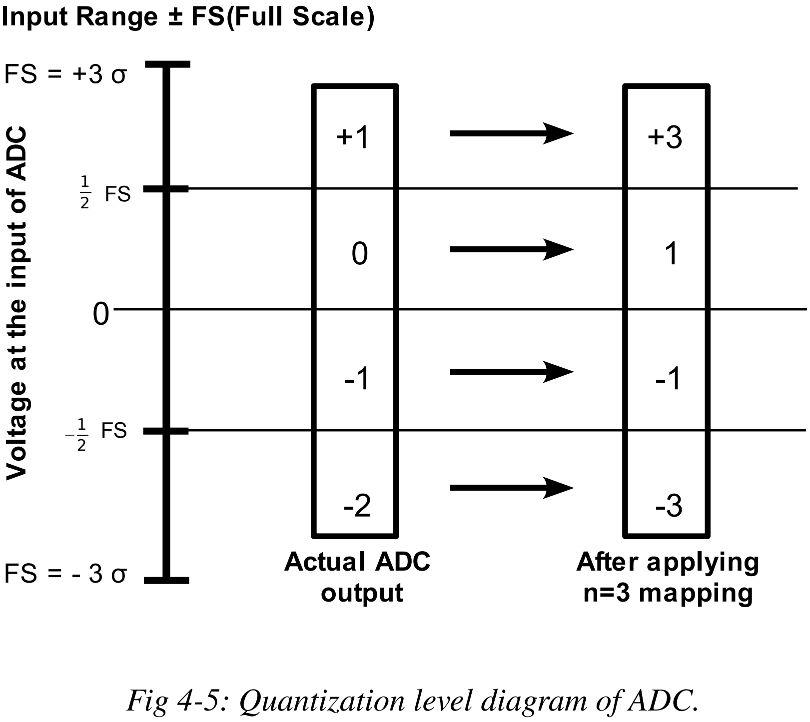

Fig 4-5: Quantization level diagram of ADC.

continuum observations. Where as the narrow band filter(~1 MHz) is meant for the spectral line observations.

The broad band filter is centered around 30 MHz where as the narrow band filter is centered around 31.25 MHz. A manual switch provides the connection to either of the filters and decides the type of observation. For spectral line observations the narrow band filter is used which provides a 3 dB gain band width of 0.8MHz. The filtered signal from each module is further amplified and fed to the ADCs for quantization. The ADCs use a 2-bit quantization scheme as shown in fig-5.

For an IF extending from f_0 Hz to f_m Hz the required sampling rate for the proper digitization is given by the Nyquist sampling rate $2f_m$. The 3dB bandwidth of the broad band filters spans from 25MHz to 35MHz where as that of the narrow band spans from 30.85MHz to 31.65MHz. The frequency that was used to sample the 10MHz IF band is 24.5 MHz and that for the narrow band was 2.45 MHz. These sampling rates provide well above Nyquist sampling rates by factors 1.225 and 1.53 times higher than required for broad and narrow bands respectively. The sampling frequency is derived using a direct digital synthesizer(this essentially uses phase locked loop to increase the frequency) which is fed with a reference frequency of 10 MHz derived from a Rb oscillator.

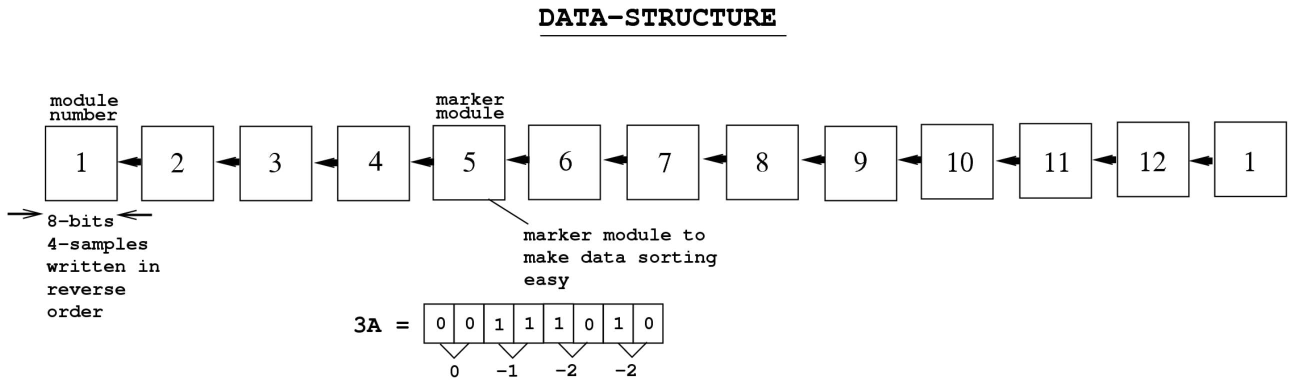

Fig 4-6: Data structure from the new digital backend that is streamed into the PCs. A byte consists of four samples corresponding to a single module. The ADCs come in packets of four. 11 are used for the modules, one remaining ADC is used as a marker which writes a constant signature. This enables the detection of data stream and read it properly.

The power level at the input of the ADC is maintained such that the input signal which is assumed to be gaussian noise satisfies V_{peak}/σ_{signal} equal to 2. Where V_{peak} is the maximum input range of the ADC. The signal is quantized to the outputs +1,0,-1 and -2 as shown in the fig-5 as the signal crosses different threshold points. These are further mapped to the numbers +3,1,-1 and -3 by software during processing of the data. These numbers can be written as x*2 +1 where x is the output from the ADC in 2-bit two's complement format. This mapping is called n=3 mapping and aides to preserve 88% of the original signal to noise after quantization. The outputs from the ADC are buffered into the FPGAs after which they are streamed into the PC for storage through the PCI-DAS cards. The data comes in packets of conventional byte which is essentially 8-bit. 1 byte holds 4 samples of 2-bit data for each module as shown in fig-6. At a sampling rate of 2.45MHz this means 2 x 12 x $2.45x10^6$ bits of data per second from each half of ORT, which means ~7.35MB of data per second. The data from north and south modules are separately stored on two individual computers on raid disks. These PCs also control the LO being fed to ORT through a GPIB card connected to the Rohde and Schwarz oscillator, enabling frequency setting and switching, which is needed for spectral line observations. It should be noted that 1-sec data actually refers to 8MB chunk.

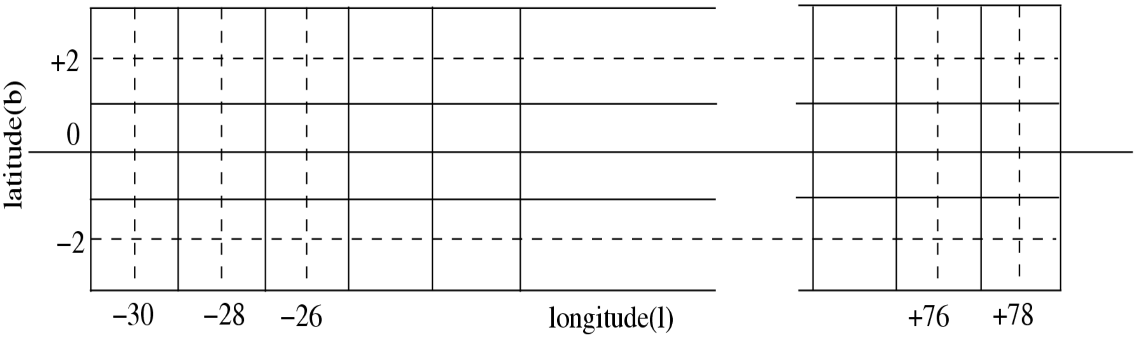

Fig 4-7: Positions observed in the Galactic plane.

4.5 RRL Observations with ORT

4.5.1 The observations

The observations presented in this thesis used the ORT as an incoherent array of 22 antennas. The spectra from the 22 modules are obtained from the recorded voltages and averaged incoherently. This mode of observation provides a beam of 2° x 2° (same as the single module beam). The incoherent mode is ideal of large scale survey of extended spectral line emission(>2°) from astrophysical sense. The new digital backend was used

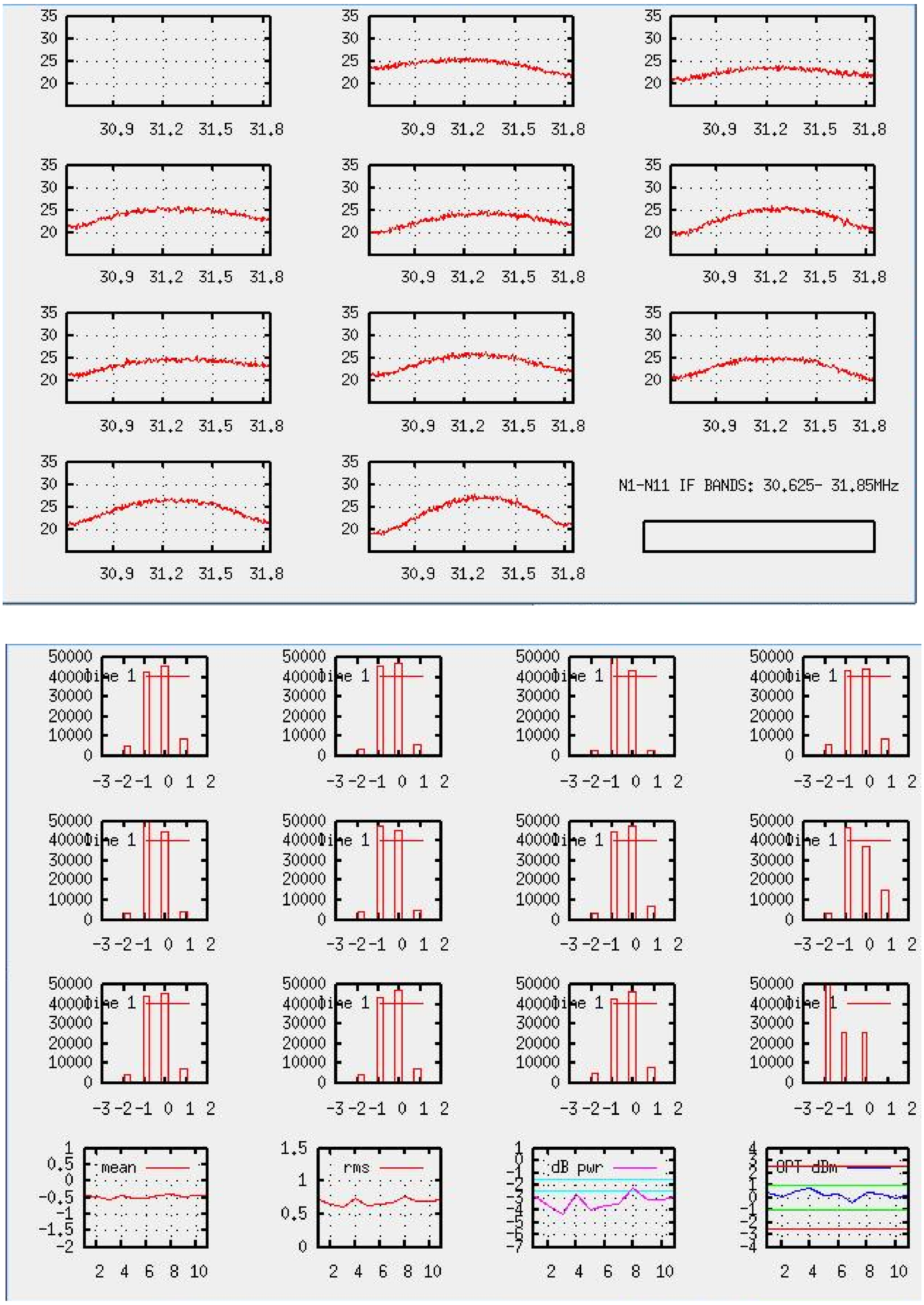

Fig 4-8: ORT band shapes and data characteristics of each module. The gaussian nature of noise(lower plots) at the input of ADC is ploted in the histograms for each module. These short-time data plots also tell about the health of the modules. In the upper plot module N1 is bad. The power levels are ajusted by monitoring the blue line in the extreme lower plot. It is always brought between the green lines for operation in the linear regime of the ADCs.

for the first time to do spectral line observations and as such had to be tested for its functioning. These basic tests were conducted to assure the software and hardware at

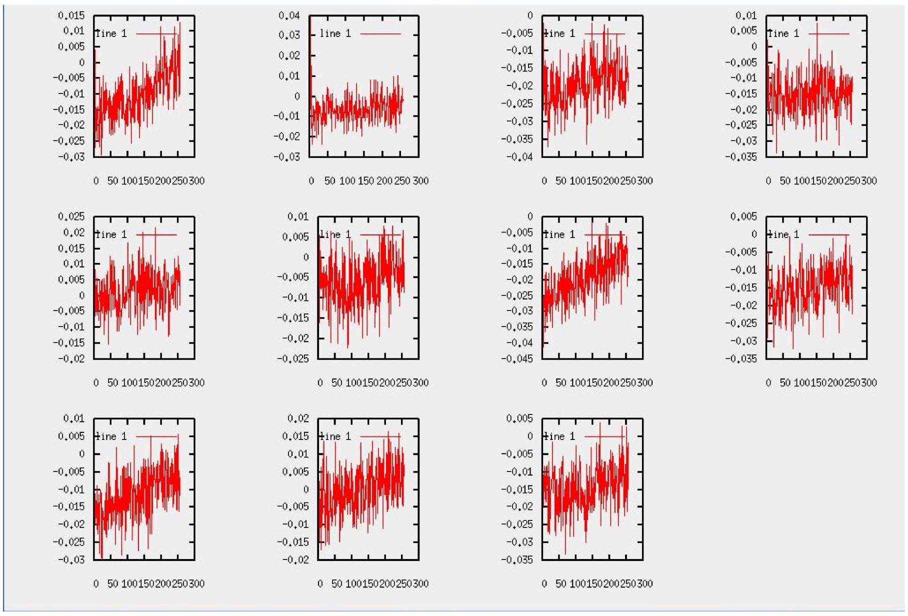

Fig 4-9: $(T_{on} - T_{off})/T_{off}$ plots for short time data collected for 10 seconds. These are the signatures of healthy bands with no interference.

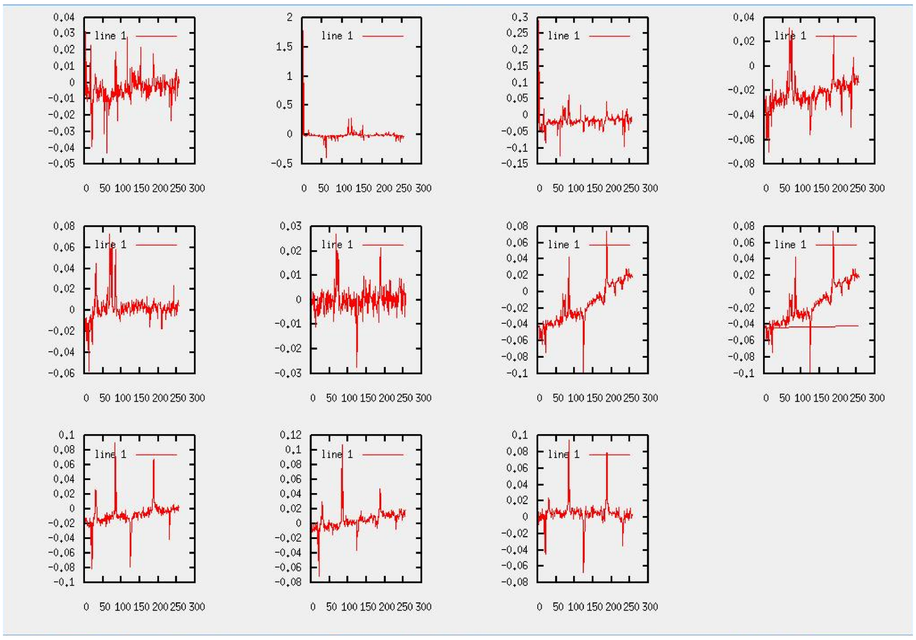

Fig 4-10: $(T_{on} - T_{off})/T_{off}$ plots for short time data collected for 10 seconds. The presence of intense interference can be seen in all the modules. The abscissa is channel number.

different levels. The observation procedure begins with adjusting the power levels at the inputs of the ADC to within the limits of V_{peak}/σ_{signal} ~ 2 and the ADC operates in its linear regime(which corresponds to a input power of -3.0dBm to 1dBm). For this attenuators are provided in the path of the signal from the new amplifiers that were specifically built to amplify the output after PA1, as has been mentioned in the previous sections. The selected transition for observation was H271α which occurs well within the bandwidth of ORT. Due to non-availability of proper broad band power amplifier for the LO, use was made of the dedicated amplifier of ORT at 296.5 MHz. This amplifier has a narrow 3 dB bandwidth of 2MHz and as such the LO frequencies had to be limited. This restricted the observations to only one transition. The observations using other transitions adjacent to n=271 did not produce satisfactory results and hence were abandoned. The typical bandshapes of ORT modules by sampling the data for a short time is as shown in the fig-8. These plots also served to check the quality of data and the health of modules. The presence of any strong interference could be easily checked by giving such a test run.

Programs were also developed to check $(T_{on}-T_{off})/T_{off}$ of the short time data. This helped in checking for interference at low level.

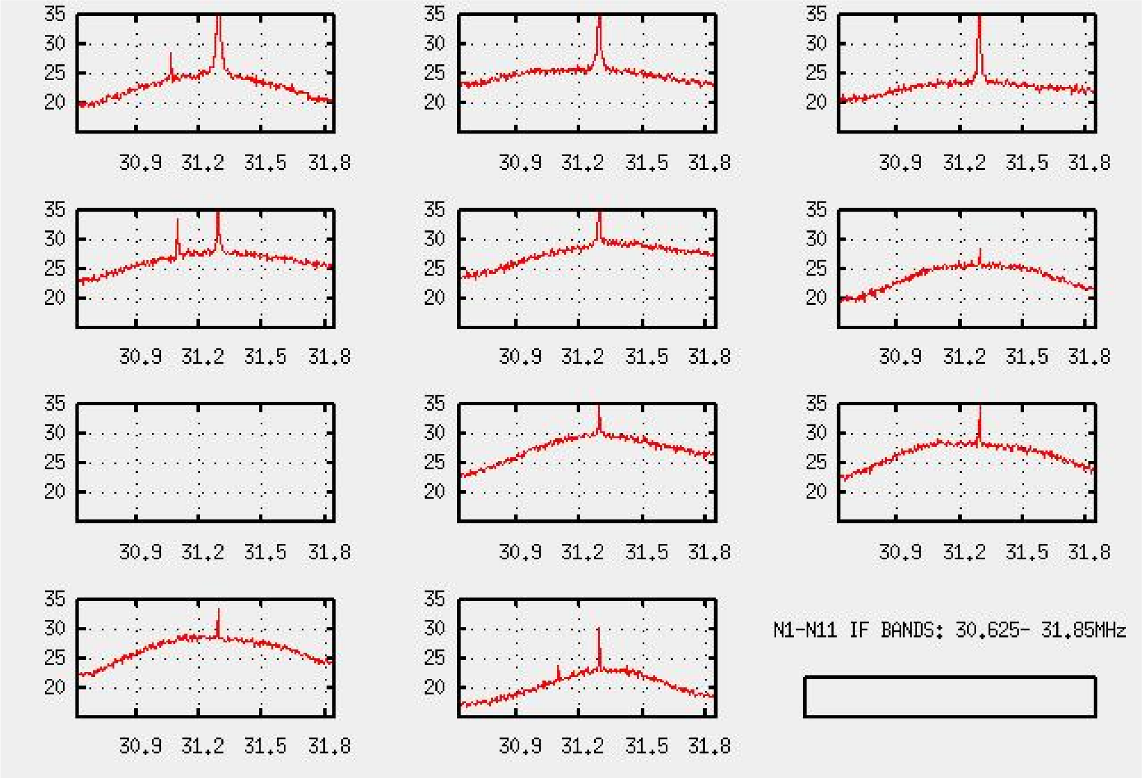

Fig 4-11: Radiated line at 328.5958MHz(H271α). The abscissa is the IF frequency & the ordinate is power in arbitrary units. There is also an accompanying interference line in between 30.9 and 31.2 MHz.

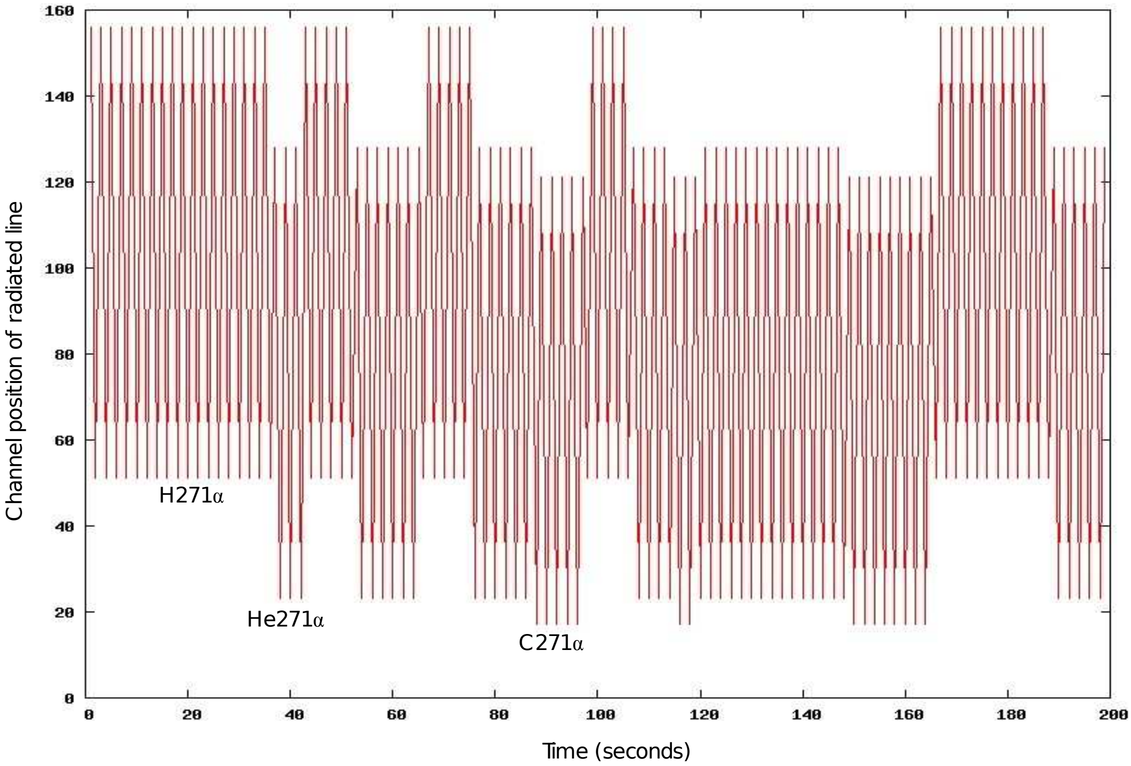

Fig 4-12: Frequency switching test performed on new digital backend. The abscissa is time in seconds and ordinate is the number in which the peak(radiated line) occurs. The radiated line frequencies were the rest frequencies of H, He and C RRLs for specific random time periods. This sequence matched exactly with the record.

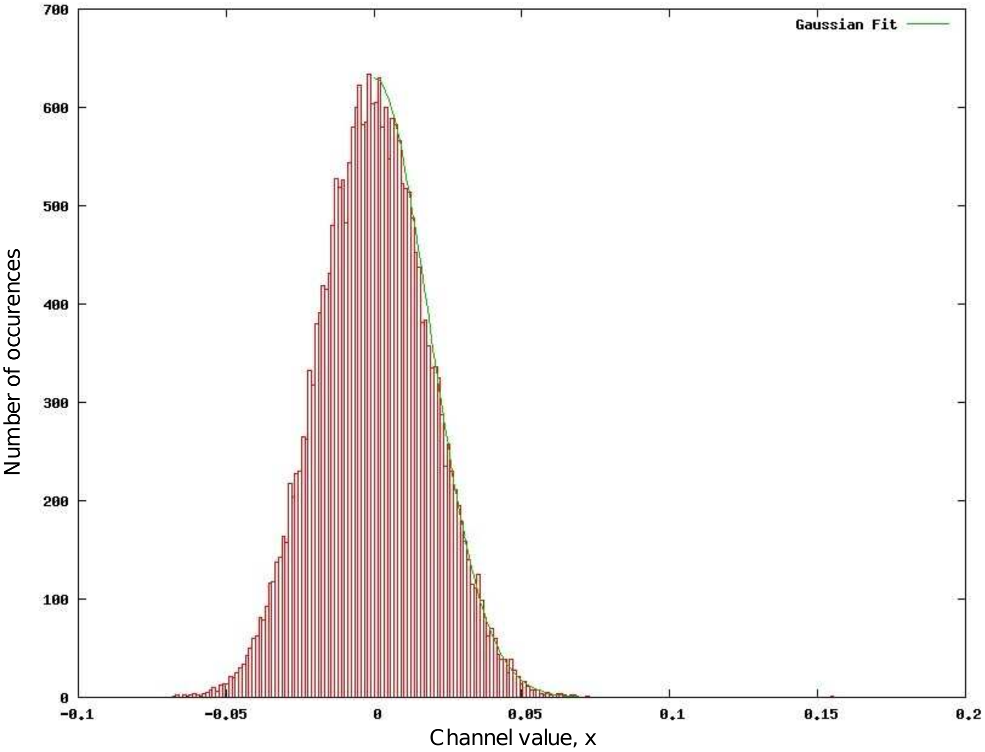

Fig 4-13: The gaussian distribution of noise in $(T_{on}-T_{off})/T_{off}$ *of ORT data after baseline removal. The samples were taken from large set of 1-sec data.*

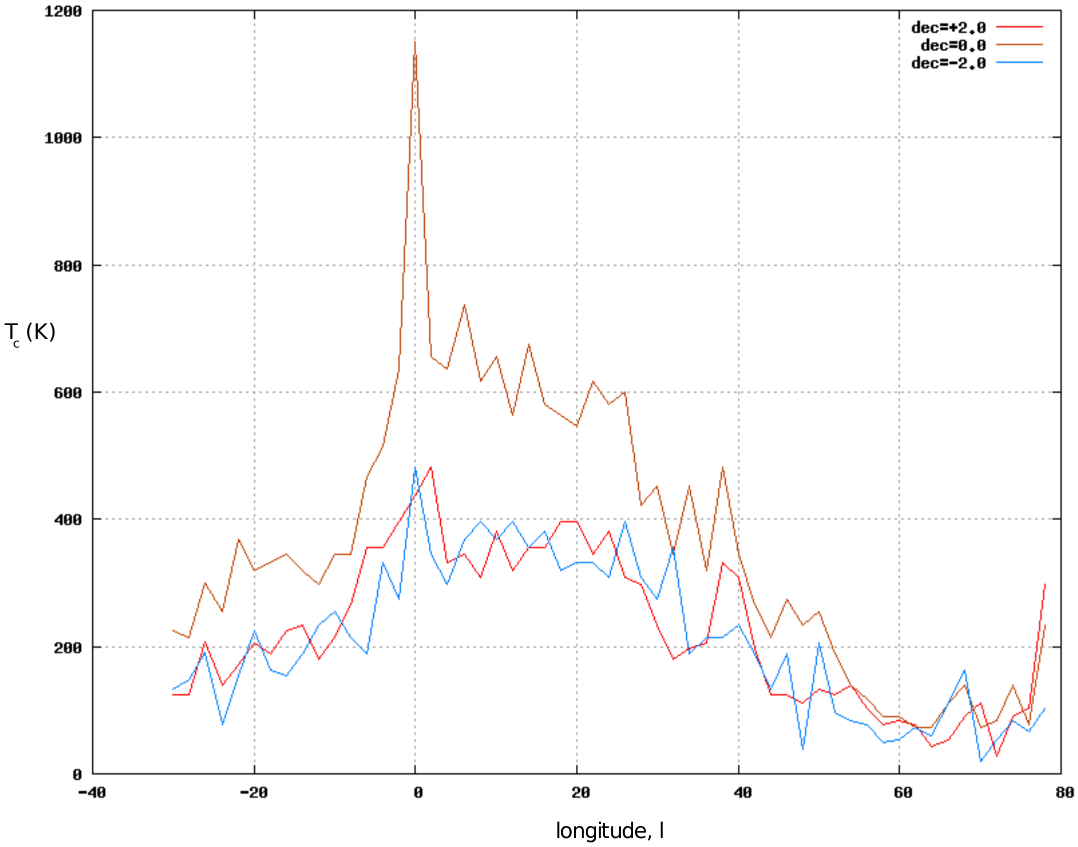

Fig 4-14: Tc measurements towards the map positions. These measurements were done as described in the text. The b=0 positions are consistent with previous observations.

4.5.2 Test for frequency switching.

To start with system was tested for proper frequency switching of LO. This involved radiating a strong line within the observational band. The frequency switching between two LO's would be done every 1-sec. The radiated line appeared in one part of the band in the first second and in the other part for the following second. The difference between the LO's(300kHz) was selected such that the line appeared within the observational band width. The strength of the line was high enough to dominate all the channel values in the 1-sec power spectrum. A mere detection of the highest value in the power spectrum and noting its channel number would tell about the frequency settings of the LO. This was done on every 1-sec spectrum. A plot (fig-12)of channel numbers Vs time showed the expected zigzag every second indicating proper frequency switching of LO per second. The radiated frequency chosen was that corresponding to rest frequencies of hydrogen, helium and carbon. A random frequency sequence of these was radiated and compared with the plots. This test helped in debugging the software codes.

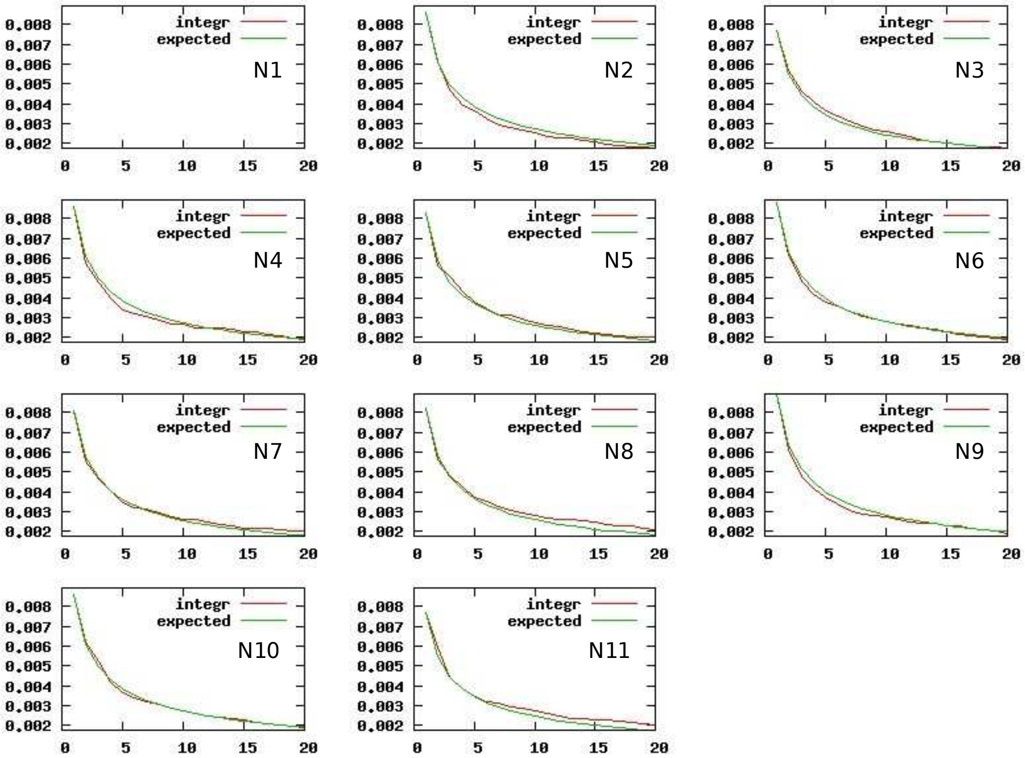

Fig 4-15: Standard deviation of ORT data with integration time. The abscissa is time x 5secs and the ordinate is standard deviation. Except the bad modules(N1 top left corner) almost all of them follow nearly the expected curve.

The standard deviation of ORT data when averaged over time produces $1/\sqrt{n}$ reduction(as shown in fig-15). A histogram of noise in $(T_{on}-T_{off})/T_{off}$ after baseline removal produces a gaussian profile as shown in fig-13.

4.5.3 Data Calibration

$(T_{on}/T_{off} - 1)$ forms a spectrum in units of T_l/T_c . Since T_{on} or T_{off} is a measure of continuum power. $(T_{on} - T_{off})$ does not contain the background power. Dividing this quantity by T_{off} normalizes the gain across the band as shown in the fig-17. The gain variation profile is contained in T_{on} or T_{off} which differ from each other by very small amounts. To express the line amplitude in ^oK it is necessary to measure T_c . With a knowledge of ORT's system temperature(refer section 4.3) and cold-sky temperature it is possible to estimate the continuum temperature of a source. First the telescope was pointed towards the source where the continuum temperature is to be measured. The power level is measured at the output of amplifiers just before being fed to the ADC. The power was measured using a spectrum analyser within a resolution bandwidth of 100kHz by averaging over a period of ~minutes. This power in dBm is a measure of the temperature of the source. This power also includes the electronic system temperature T_{elec}. To estimate T_c alone, T_{elec} has to be eliminated. The power when the telescope is pointed towards the source is

$$T_{on} = T_S' + T_{elec} = 0.65T_S + T_{elec} \tag{4.3}$$

where 0.65 is the beam efficiency of ORT and T_S is the true temperature of the source. Similarly when the telescope is pointed towards a cold region in the sky by keeping the declination constant. This is to avoid the gain variations of ORT with declination. Also the attenuations in the signal path are kept unvaried.

$$T_{off} = 0.65T_{cold\,sky} + T_{elec} \tag{4.4}$$

Using these measurements T_c can be written as,

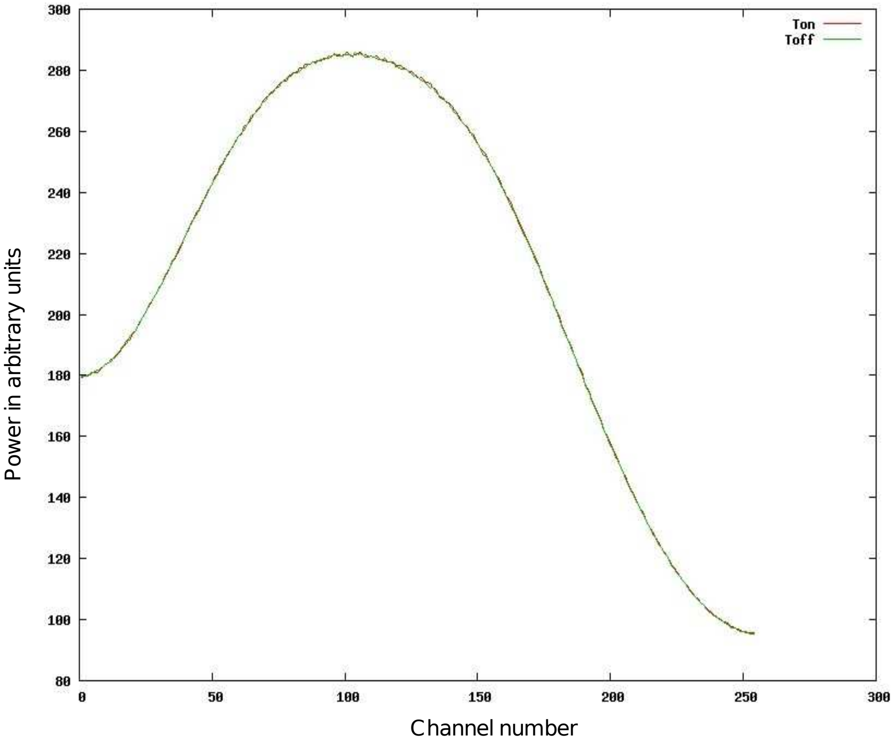

Fig 4-16: The band of module 5 corresponding to 1-sec data.

$$T_c = \frac{123}{0.65}\left[\frac{T_{on}}{T_{off}} - 1\right] + T_{cold\,sky} \tag{4.5}$$

where 123K = $T_{cold\ sky}$ + T_{elec} is the temperature of ORT and $T_{cold\ sky}$ = 36K . A useful expression for T_c in terms of measured power in dBm is,

$$T_c = \frac{123}{0.65}\left[10^{\frac{P_{on\,dBm} - P_{off\,dBm}}{10}} - 1\right] + T_{cold\,sky} \tag{4.6}$$

Now T_l/T_c can be written as ,

$$\frac{T_l}{T_c} = \frac{T_{on} - T_{off}}{T_{off}}\left[\frac{T_c + T_{elec}}{T_c}\right] \tag{4.7}$$

$$T_l = \frac{T_l}{T_c} T_c \tag{4.8}$$

Here T_{elec} which also includes the spill over noise has been taken to be 100K. A plot of measured T_C towards the Galactic plane for different latitudes is given in fig-14.

4.5.4 The Spectral line observational band

The IF for the spectral line observations which is provided with a 3dB gain band width of 0.8MHz is centered at 31.25 MHz. However the entire bandwidth of this mode is given by,

$$Band\,Width = \frac{Sampling\ Frequency}{2} = \frac{2.45}{2} = 1.225\text{MHz}$$

The resolution of the observed band would then depend upon the number of FFT points performed on the data.

$$Band\ Resolution = \frac{Band\ Width}{no.of\ FFT\ points} = \frac{1.225}{256} = 4.785\text{kHz}$$

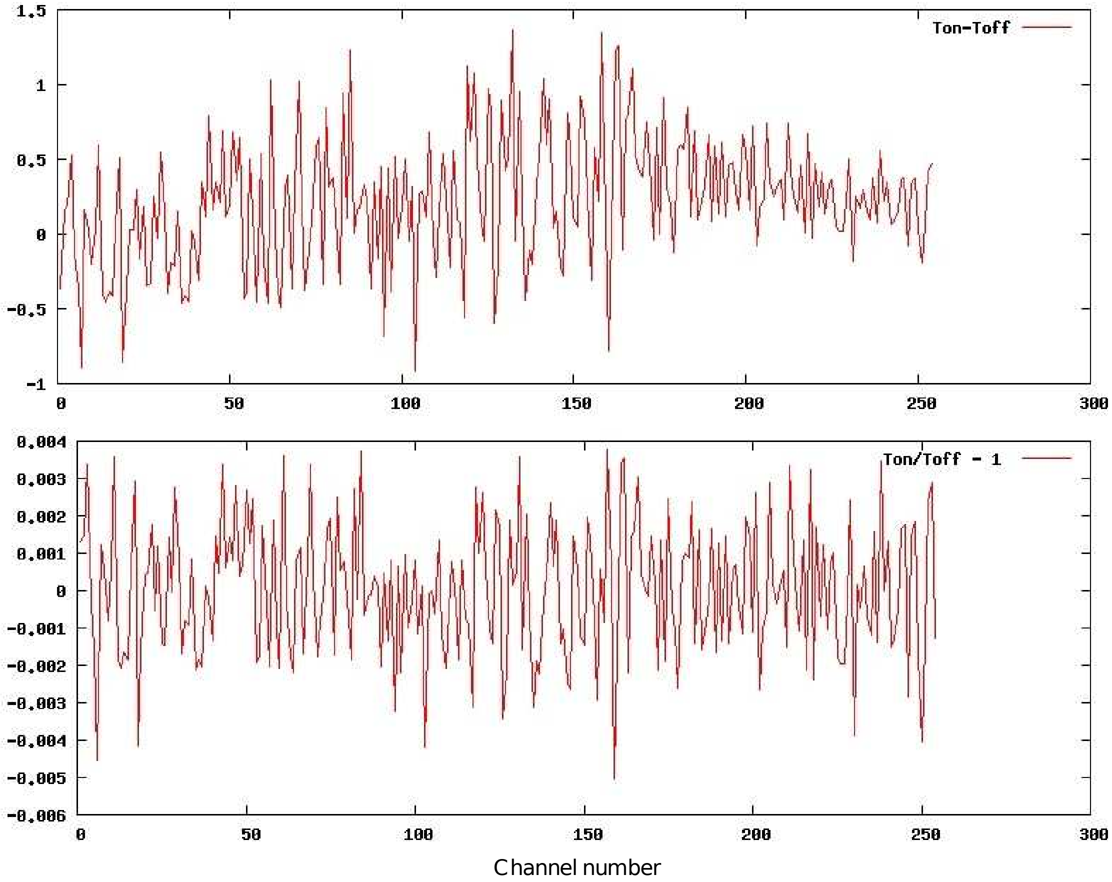

Fig 4-17: (Ton-Toff) upper and (Ton-Toff)/Toff lower , the normalization of gain across the band can be seen in the lower plot. It can be noted that the features in the lower plot are intact. Ton and Toff correspond to 2 settings of LO for 1 second each.

To observe a astronomical spectral line of frequency ν the LO frequencies are calculated such that the spectral line is expected to appear within the 3.0dB gain band width of the IF amplifiers. Since the IF band is fixed this is quiet straight forward to do. The two LO's should be such that the difference between the expected spectral line frequency and the LO frequency should be favourably located symmetrically away from the center of the IF band. This can be written as,

$$\nu_H - \nu_{LO} \sim 31.25 \mp \Delta\nu$$

$$LO_1 - LO_2 = 2\Delta\nu$$

where $\Delta\nu$ is best within the 3dB gain band width of the IF amplifiers. In the present observations $\Delta\nu$ has been chosen to be 150kHz(in some cases 200kHz) due to the low band width of the dedicated LO amplifier of ORT. The T_{on}-T_{off} of 1 sec data has been shown below, note the gain variation across the band. The gain is maximum in the middle while it diminishes towards the extremes. The same spectrum when divided by T_{off} has the gain normalized all across the band, as shown in the following figures. T_{on} and T_{off} have a spectral line each differing by $2\Delta\nu$ on the frequency axis . To improve the signal to noise ratio these lines can be averaged by folding the spectrum in the middle of the two spectral lines. The folding is done finally after the grand colapse of all the data from all the modules(i.e N1-N11). The data from southern half(modules S1-S11) was discarded as it did'nt produce satisfactory results. The data is acquired and processed in chunks of 8MB ->1024x1024x8. The total number of samples in this packet are 2796202 for each module. A 512 point FFT which would actually give 256 channel power spectrum would result in 5460 spectra. Eventually all these 5460 spectra are averaged and are written as 1 spectrum corresponding to 8MB data. A small portion of the data from every 8MB chunk is discarded at the end during processing. The data was acquired in sets of 100secs of T_{on} and T_{off} each. A single run of data acquisition consisted of 10 such sets. The time taken by this run was ~48 minutes. The extra time was due to the time spent in synchronization between north and south PCs. The north PC was the master PC which also controlled through serial port the data acquisition in south PC. So that the acquistion in both PCs started at the same time and was simultaneous. During frequency switching the RS LO was given a settling time of 10ms after immediately switching to the other frequency. This was to ensure a stable LO. RS produced the oscillations at a fixed power level of -3.0 dBm.

4.5.5 Velocity in the Local Standard of Rest

The observed astronomical line does not appear at the expected rest frequency of the transition. Due to the motion of the source and due to the collective motion of the the sun and earth the line is observed at a different frequency depending on the time of observation. To express the motion of the Galactic objects a standard of rest is required. This is the Local Standard of Rest(LSR). Which is the mean collective motion of the objects near the solar system. It is defined as a fictional point that moves around the plane of the Galaxy on a closed orbit in the plane passing through the point containing the sun. The line is to be refered to this system of rest or it is in this frame of rest that the observed frequency of the RRL is expressed. If one were to consider the frequency of line in the frame of earth this would have different relative values at different times.

As the telescope moves due to rotation and revolution of earth and due to the sun's motion with respect to the LSR. The Local Standard of Rest eliminates this problem by having a constant value. So it is constumary to express the RRL frequencies from sources in LSR. Difference frequency can be converted to velocity using Doppler relation. This velocity of shift from the rest frequency(V_{LSR} = 0) in the LSR frame is called Velocity in the Local Standard of Rest(V_{LSR}). It is the radial motion between the projection of V_{LSR} of the telescope(as the frequency measurement is done with the telescope) and the projection of V_{LSR} of the source on the line of sight(line connecting the solar system with

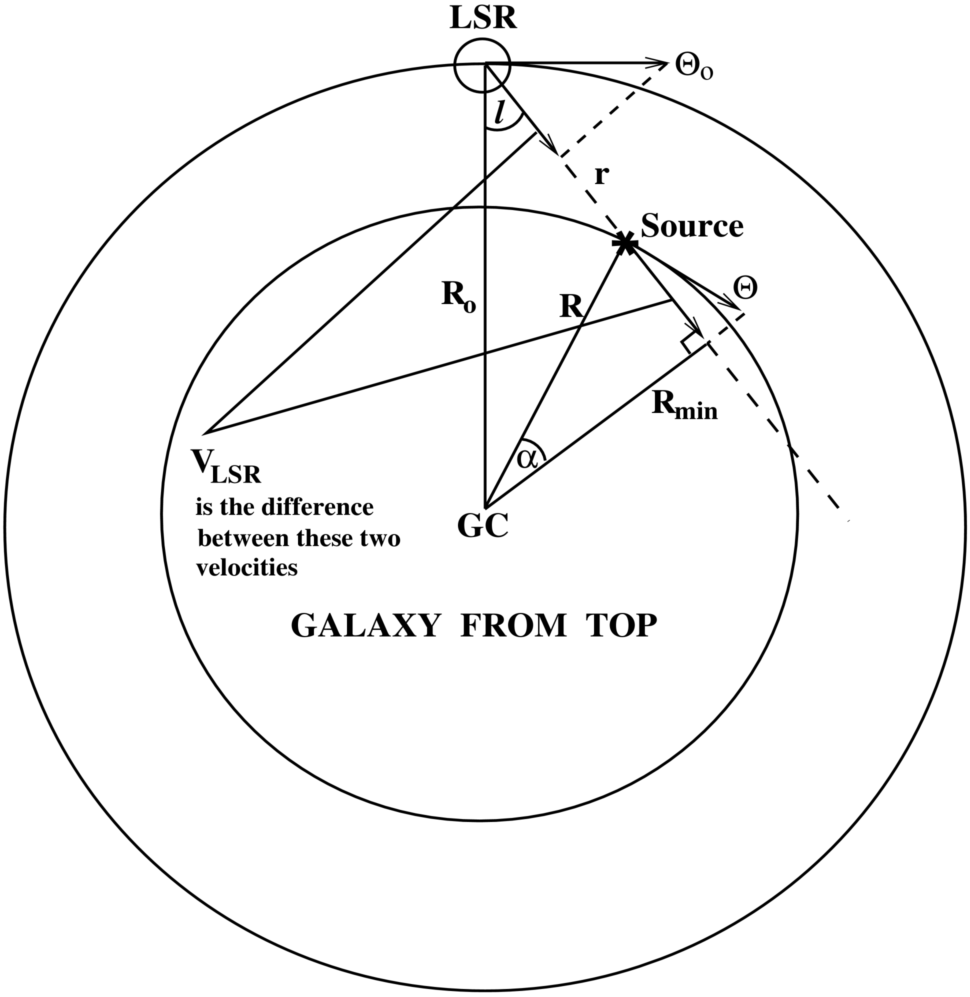

Fig 4-18: The basic idea of V_{LSR} for a source at a distance r and longitude l. R_o is the distance of the Solar system to the center of the Galaxy(~8.5kpc). The LSR frame(centered on sun) is moving at velocity Θ_o. The Source moves at velocity Θ. The V_{LSR} for the source is the difference of the projected motions of LSR and the source on the line of sight. This is quantified in the text. Since the geometries inside the solar system are tiny compared to the distance involved towards the source the telescope velocity in LSR can be simply projected on the line joining the Solar system with the source.

the source). The projection of V_{LSR} of the telescope towards a source is obtained by using the dopset program. Which takes into account the time, location on the earth, rotation of earth(0.5km/s), revolution of the earth(30km/s) around the sun and motion of sun(13.4km/s) w.r.t LSR. The LSR has its coordinates as U,V and W which are towards the Galactic center, the Galactic rotation direction and towards the Galactic north pole. The sun's velocities in these directions are 10.0 kms/s, 5.2 km/s and 7.2 km/s respectively. With this knowledge and converting the frequency axis of the observed spectral line to velocity by using Doppler principle one can deduce the V_{LSR} corresponding to that source(spectral line).

$$\Delta V = c\frac{\Delta \nu}{\nu_0}$$

where c is the velocity of light and ν_0 is the rest frequency of the spectral transition. Using the above relation the entire frequency scale of the observation band can be calibrated and expressed in velocity instead of frequency. Here 0 V_{LSR} refers to the rest frequency. Refering fig-18 we see that,

$$V_{LSR} = \Theta\cos\alpha - \Theta_0\sin l = R\omega\cos\alpha - R_0\omega_0\sin l$$

$$R\cos\alpha = R_0\sin l$$

$$V_{LSR} = (\omega - \omega_0)R_0\sin l \tag{4.9}$$

ω & ω_o being the respective angular velocities.

However this expression for V_{LSR} is in terms of the angular velocities of the LSR system and the source. When true observations are done the motion of earth and sun also have to be taken into account. This is done by the dopset program, which actually gives the velocity of the telescope(here termed E_{LSR}) along the line of sight. This information along with the observed frequency shift of the astronomical line from the rest frequency of the transition one can easily calibrate a velocity axis for the line.

$$\nu_{ch} = \nu_{ref} + \Delta\nu_{ch}(n_{ch} - n_{ref})$$

$$V_{LSR} = \left(\frac{\nu_0 - \nu_{ch}}{\nu_0}\right)c - E_{LSR} \tag{4.10}$$

These useful calibration expressions are given above (4.10), here nref and νref are the reference channel number and frequency which are known apriori, nch is arbitrary channel number for which the frequency is to be found. $\Delta\nu$ch is the band resolution, the other terms have been defined already.

4.5.6 First Line detection Using ORT-New digital backend

The first confirmed line detection using the NDB was made towards the position G36.5+0.0 on May08-2008. The LO frequencies selected were 297.54 & 297.24 which

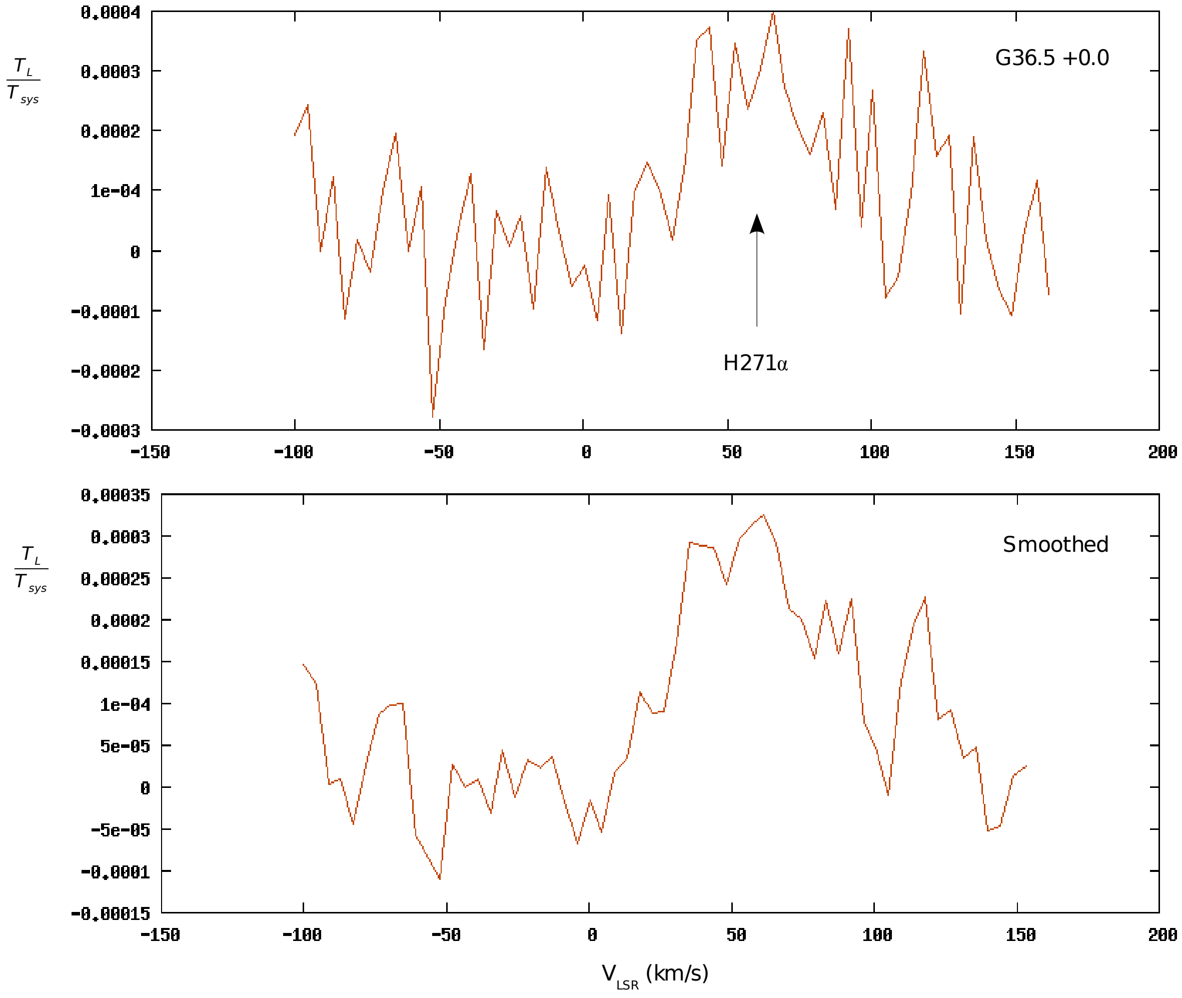

Fig 4-19: The first confirmed line detection using ORT-NDB towards the position G36.5 +0.0 in the Galactic plane. T_l/T_c *is in close agreement with previous observations. The lower plot is a smoothed version using a box of 3 channels.*

differed by 300kHz. The data was collected for 200x30 secs and amounted to ~48GB. After performing 512 point FFT to obtain 256 channel 1 sec spectrum this whole data reduced to a mere amount of ~180MB. A plot of this detection has been shown in the fig-19. T_l/T_c is of the order $\sim\tau_l$ as expected for ELDWIM. This position was observed multiple number of times to confirm its existance. Also observations at the same hour angle and declination but towards the cold sky(i.e at a different time) produced a blank region in the spectrum at the expected line position.

4.5.7 A survey of RRLs in the inner Galaxy.

The ORT was basically used to do a survey of the plane of the Galaxy. The range that was covered was galactic longitude $l=-30^o$ to $l=+78^o$ with latitude $b=-3^o$ to $+3^o$ in steps of 2^o (both l & b). The beam of ORT was approximately taken to be $2^o \times 2^o$. This was pointed towards the central points of the blocks shown in the fig-7. However the beam of the telescope would be spread along RA and declination. Each direction was observed on the average for about 2hrs. The total number of positions in the above patch are 165. A few positions were omitted due to non-availability of telescope time and are absent in the line map.

The results of observations towards different positions in the map shown in the fig-7 are displayed on the following pages(fig-20 to fig-25). In the Galactic plane majority of positions show hydrogen line along with an associated carbon line. The line features also exhibit multiple hydrogen components in a few positions. These could be explained as due to multiple clouds along the line of sight. Towards some positions(G28 +0) there seems to be a smearing of line amplitude. These features are consistent with observations using WSRT at a different frequency(1.4GHz) in almost all the bands of WSRT(refer chapter-3). The line amplitudes(T_l/T_c) are consistent with the typical optical depths($\sim10^{-3}$) for ELDWIM($n_e\sim10$ cm^{-3}). The typical line width in the Galactic plane seems to be around 30km/s. Considering pure doppler broadening the temperature of a model cloud with ionized hydrogen would be $\sim10^4$K. Which is the typical temperature of HII regions. However HII regions have larger electron densities $\sim10^4$ cm^{-3} . ELDWIM has been thought to be forming the envelopes(Anantharamaiah1984) of evolved HII regions with very low densities. Apart from Galactic plane hydrogen and carbon lines have also been detected along higher latitude regions. This indicates that ELDWIM has considerable Galactic scale height. There seems to be carbon line emission from some of the positions in higher latitude regions without an associated hydrogen line. Also the carbon line features towards some positions do not match in V_{LSR} with associated hydrogen lines indicating most probably a different region of origin.

The map had to be truncated towards lower longitude at l=-30° due to intense interference that was observed towards higher declination(>40°). A table of parameters extracted from each plot by gaussian fitting using leasqrdemo.m program of octave has been given in table-1 after the plots. Also these parameters have been displayed on longitude-velocity (lv) diagram for all the line detected positions following the plots. The observed positions have been marked on the continuum map at 1.4GHz with the projection of beam of ORT.

4.5.8 Scale height of ELDWIM from ORT data.

Numerous hydrogen line detections towards higher Galactic latitude indicated that ELDWIM has considerable scale height. From the line detections made here, the lower limit(meaning “atleast”, however ELDWIM can exist above this limit) for the scale height of ELDWIM has been estimated. The observed V_{LSR} of the lines could be used to estimate the height of the cloud above the Galactic plane by making a simple assumption that the gas in the higher latitudes follows the same rotation curve as in the plane and since the latitude is small, the height of the cloud would simply be $D_c\theta$. This has been pictured in fig-20. The rotation curve given by Burton & Gordon(1978) has been used to obtain the distance to the clouds from which line emission originates. Only near distances to the clouds have been considered favourable due to large beam dilution resulting in the ORT beam for larger distances. The distance D_c to the cloud from the solar system together with the Galactic latitude(3°) gives the height of the cloud above the plane of the Galaxy. A table of estimated height of the clouds for different line detected positions has been given in table-2. These estimates suggest that the distribution of ELDWIM can be as high as ~400pc across the Galactic plane. Due to non-availability of ORT data above the latitude of 3° the lower limit of ELDWIM can be thought to be of this order across the plane of the Galaxy. Also the ELDWIM seems to be “clumped” from the distribution of clouds with these variable heights.

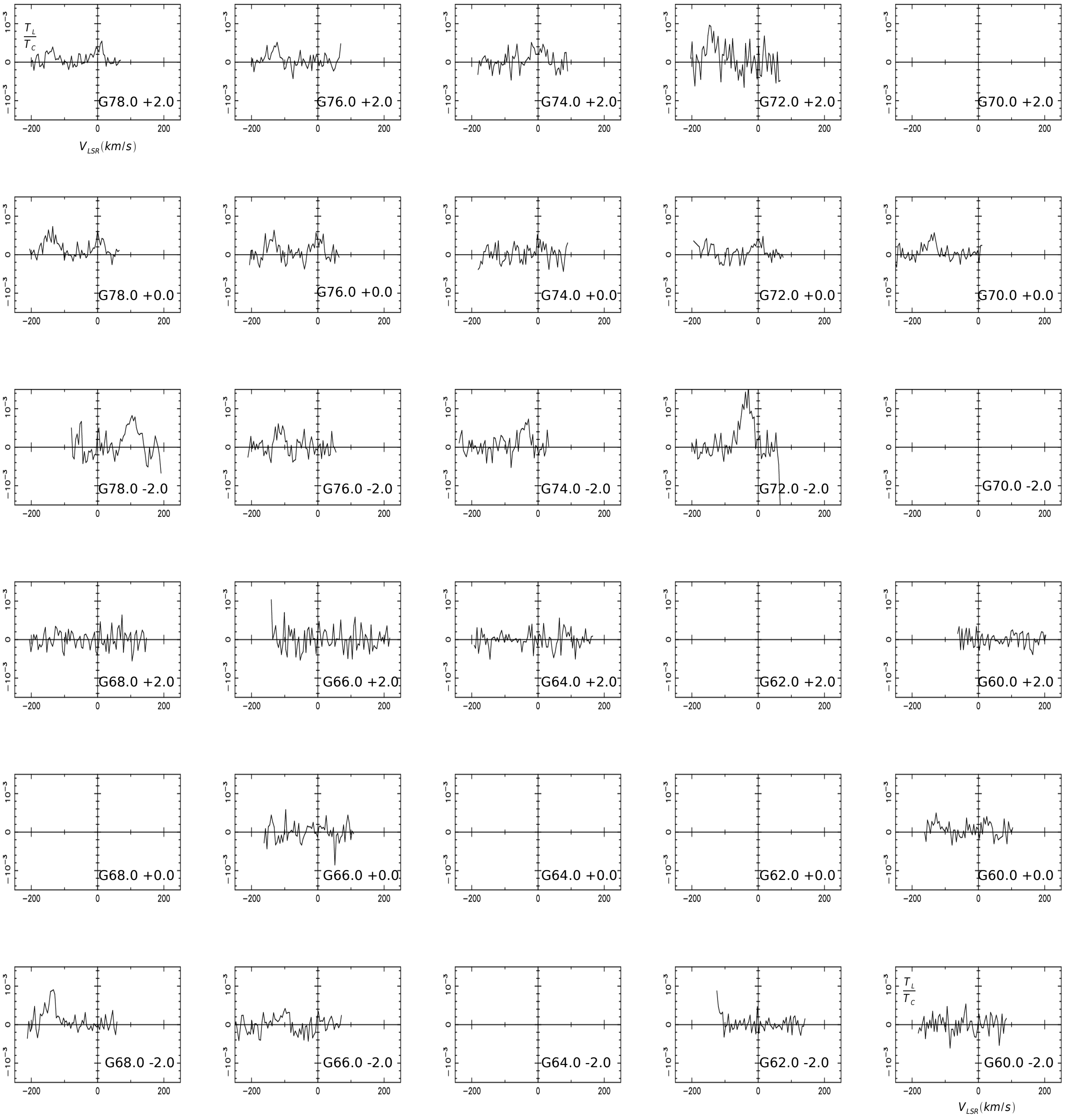

Fig 4-20: Line plots towards the Galactic positions G78±2 to G60±2. The abscissa is V_{LSR}(km/s) while the ordinate is T_l/T_c . The map runs horizontally from top left corner in longitude in steps of 2^o from 78 to 70 in the upper three rows which correspond to +2,0 and -2 Galactic latitude from top. While in the lower rows it goes from 68 to 60 with the similar latitudes. The scale of the two axis have been set equal in all the plots for the sake of comparison. The blank regions are those were observations were not possible. The abscissa runs from -250 km/s to +250 km/s. The gaussian fitted parameters are given in table-1.

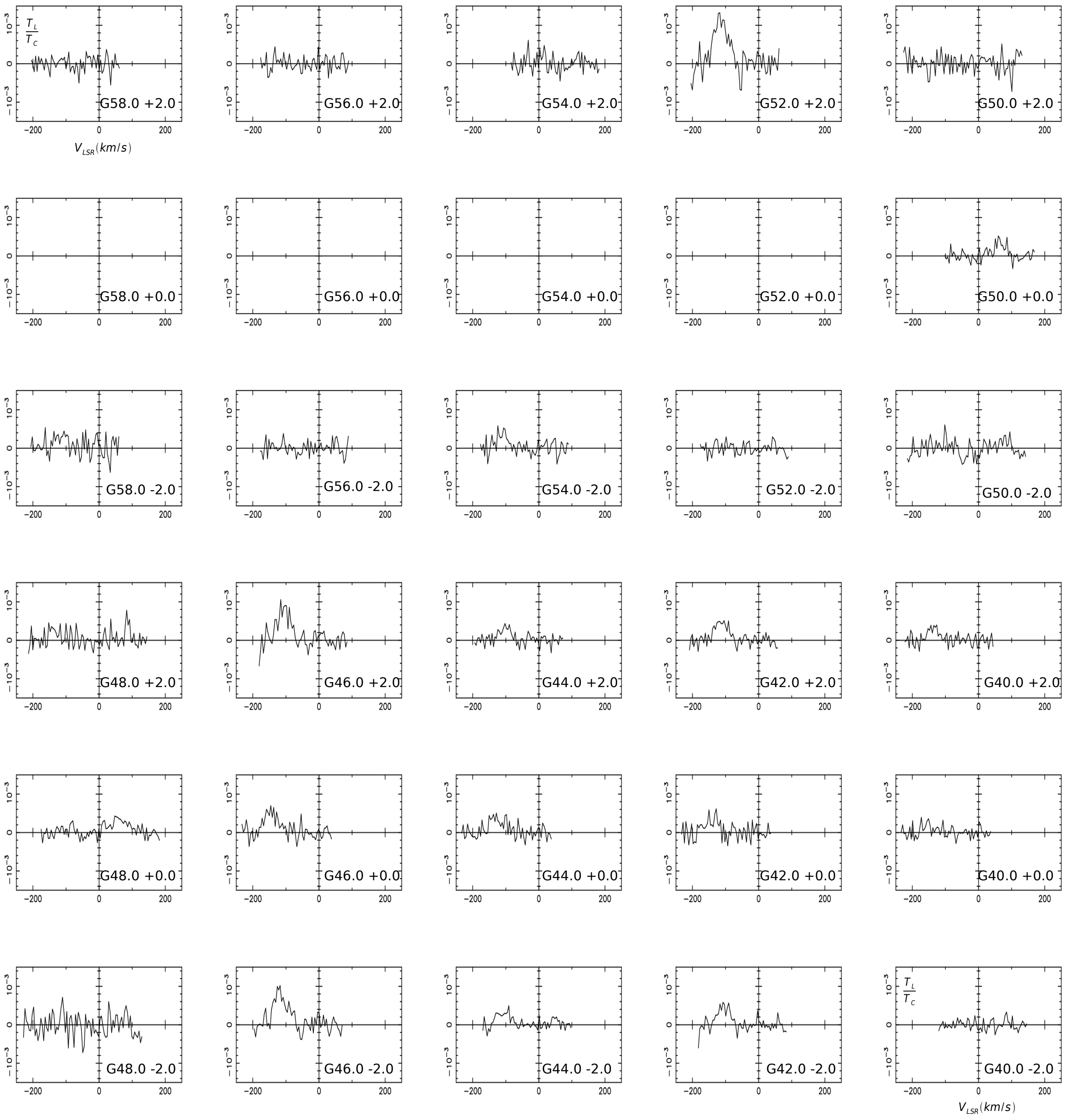

Fig 4-21: Line plots towards the Galactic positions G58±2 to G40±2. The abscissa is V_{LSR}(km/s) while the ordinate is T_l/T_c . The map runs horizontally from top left corner in longitude in steps of 2^o from 58 to 50 in the upper three rows which correspond to +2,0 and -2 Galactic latitude from top. While in the lower rows it goes from 48 to 40 with the similar latitudes. The scale of the two axis have been set equal in all the plots for the sake of comparison. The blank regions are those were observations were not possible. The abscissa runs from -250 km/s to +250 km/s. The gaussian fitted parameters are given in table-1.

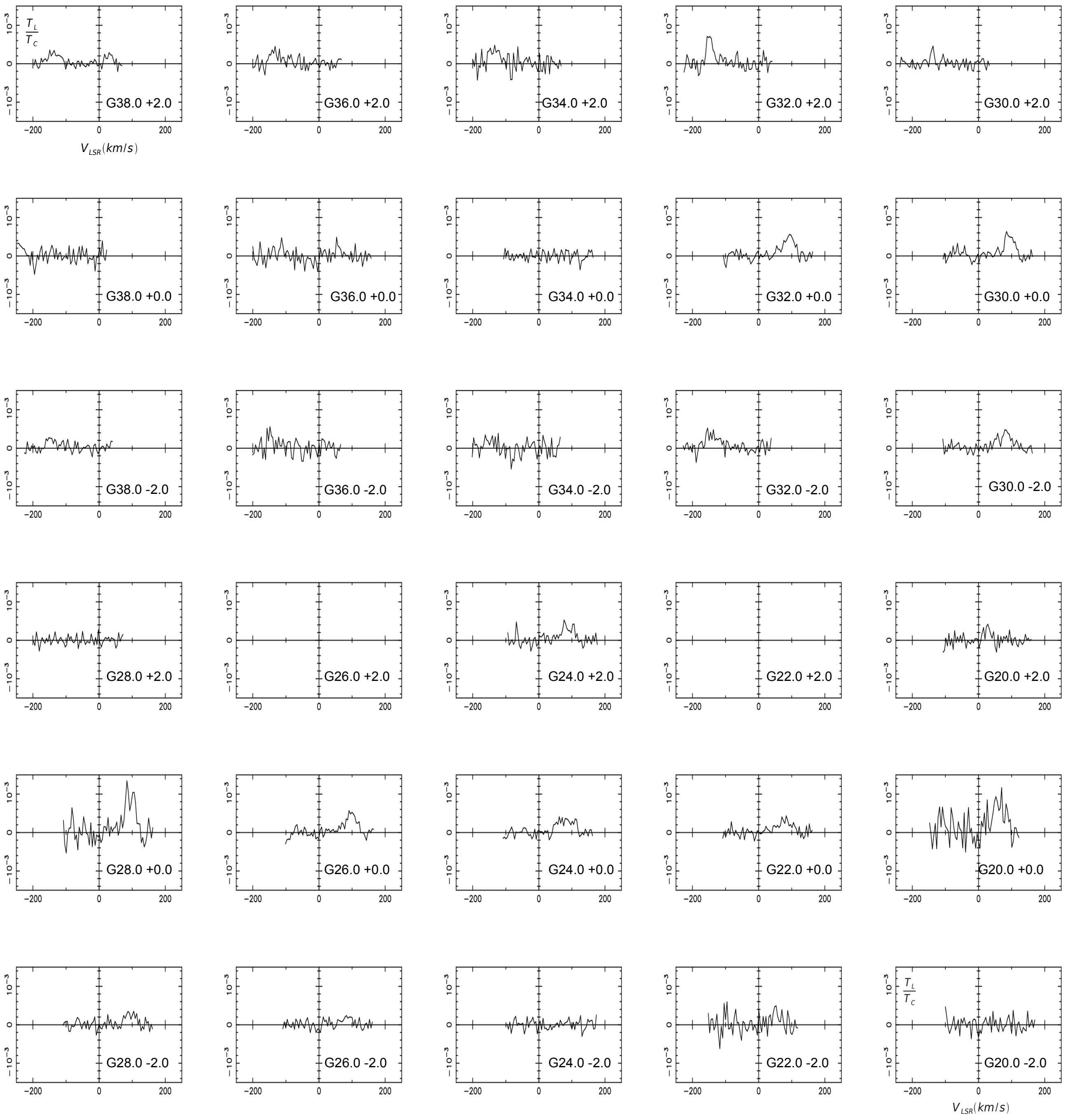

Fig 4-22: Line plots towards the Galactic positions G38±2 to G20±2. The abscissa is V_{LSR}(km/s) while the ordinate is T_l/T_c. The map runs horizontally from top left corner in longitude in steps of 2^o from 38 to 30 in the upper three rows which correspond to +2,0 and -2 Galactic latitude from top. While in the lower rows it goes from 28 to 20 with the similar latitudes. The scale of the two axis have been set equal in all the plots for the sake of comparison. The blank regions are those were observations were not possible. The abscissa runs from -250 km/s to +250 km/s. The gaussian fitted parameters are given in table-1.

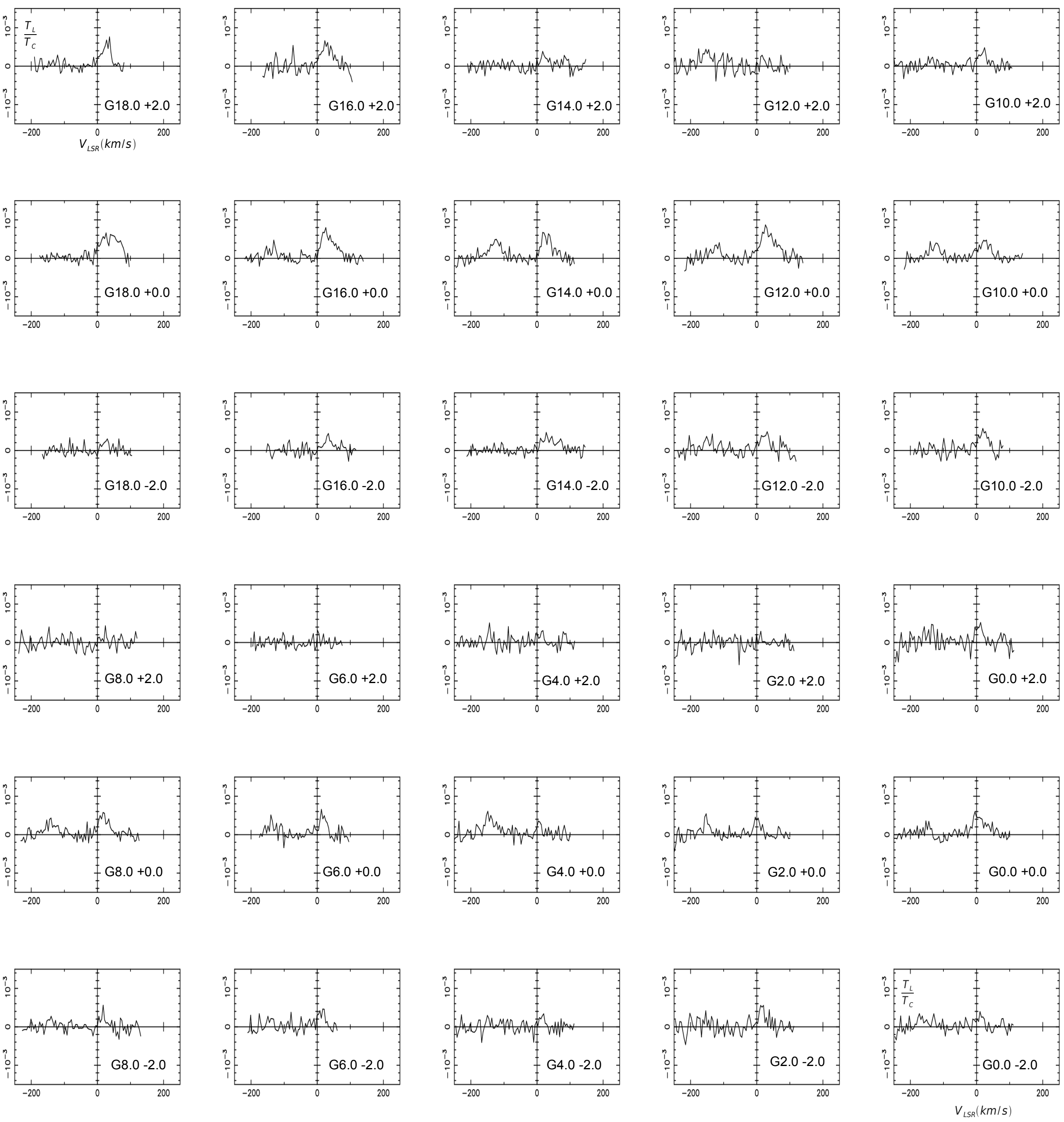

Fig 4-23: Line plots towards the Galactic positions G18±2 to G0±2. The abscissa is V_{LSR}(km/s) while the ordinate is T_l/T_c . The map runs horizontally from top left corner in longitude in steps of 2^o from 18 to 10 in the upper three rows which correspond to +2,0 and -2 Galactic latitude from top. While in the lower rows it goes from 8 to 0 with the similar latitudes. The scale of the two axis have been set equal in all the plots for the sake of comparison. The blank regions are those were observations were not possible. The abscissa runs from -250 km/s to +250 km/s. The gaussian fitted parameters are given in table-1.

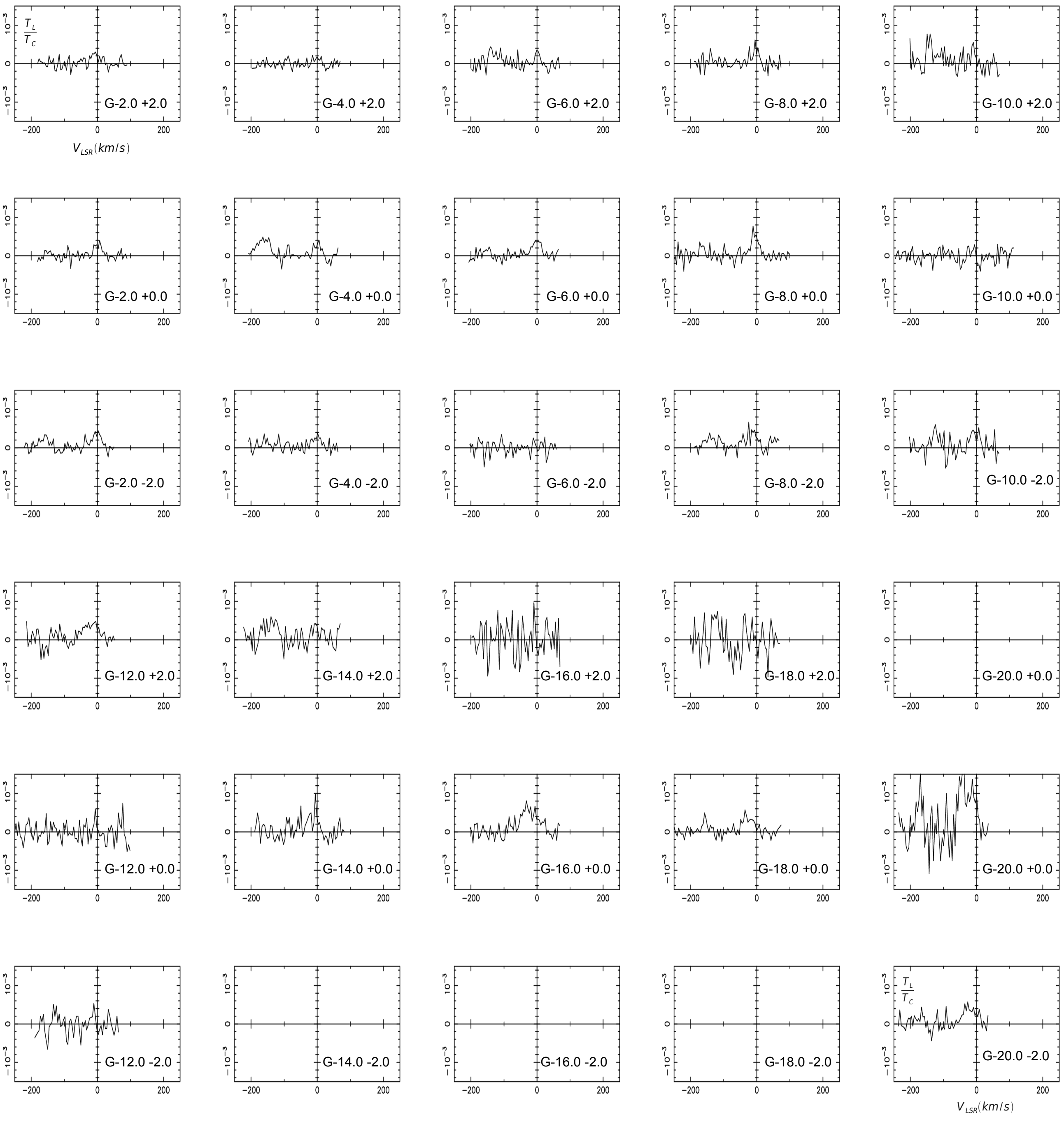

Fig 4-24: Line plots towards the Galactic positions G-2±2 to G-20±2. The abscissa is V_{LSR}(km/s) while the ordinate is T_l/T_c. The map runs horizontally from top left corner in longitude in steps of 2^o from -2 to -10 in the upper three rows which correspond to +2,0 and -2 Galactic latitude from top. While in the lower rows it goes from -12 to -20 with the similar latitudes. The scale of the two axis have been set equal in all the plots for the sake of comparison. The blank regions are those were observations were not possible. The abscissa runs from -250 km/s to +250 km/s. The gaussian fitted parameters are given in table-1.

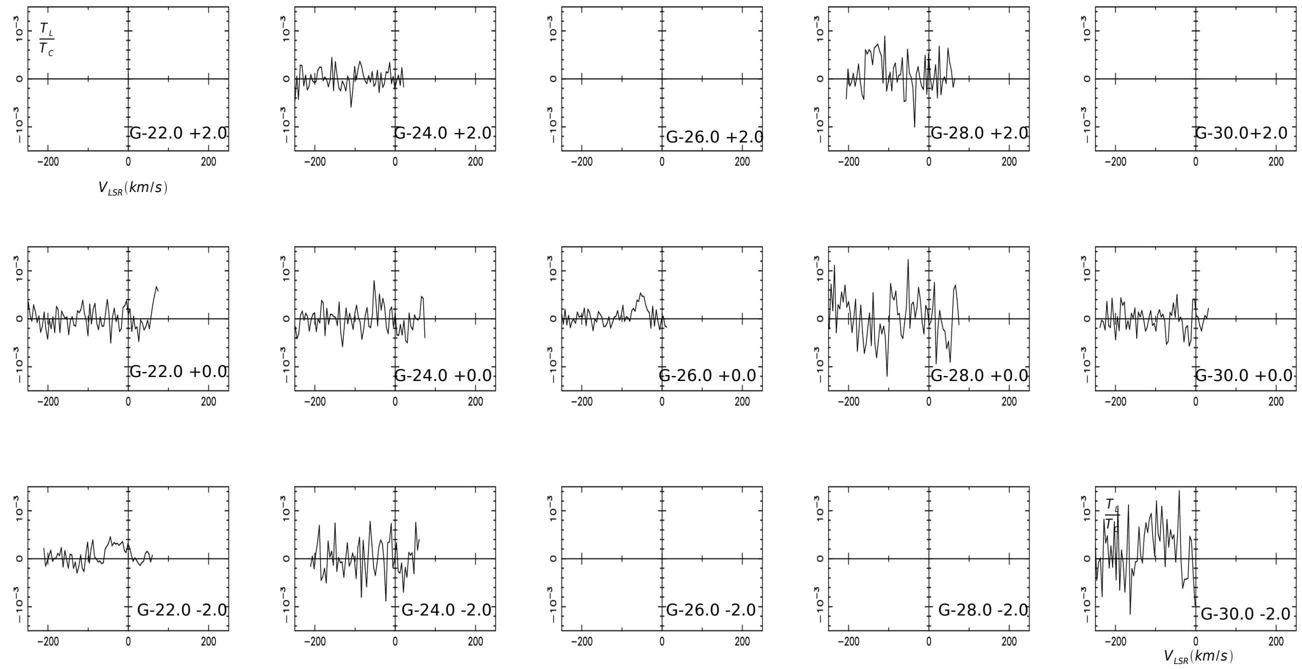

Fig 4-25: Line plots towards the Galactic positions G-22±2 to G-30±2.

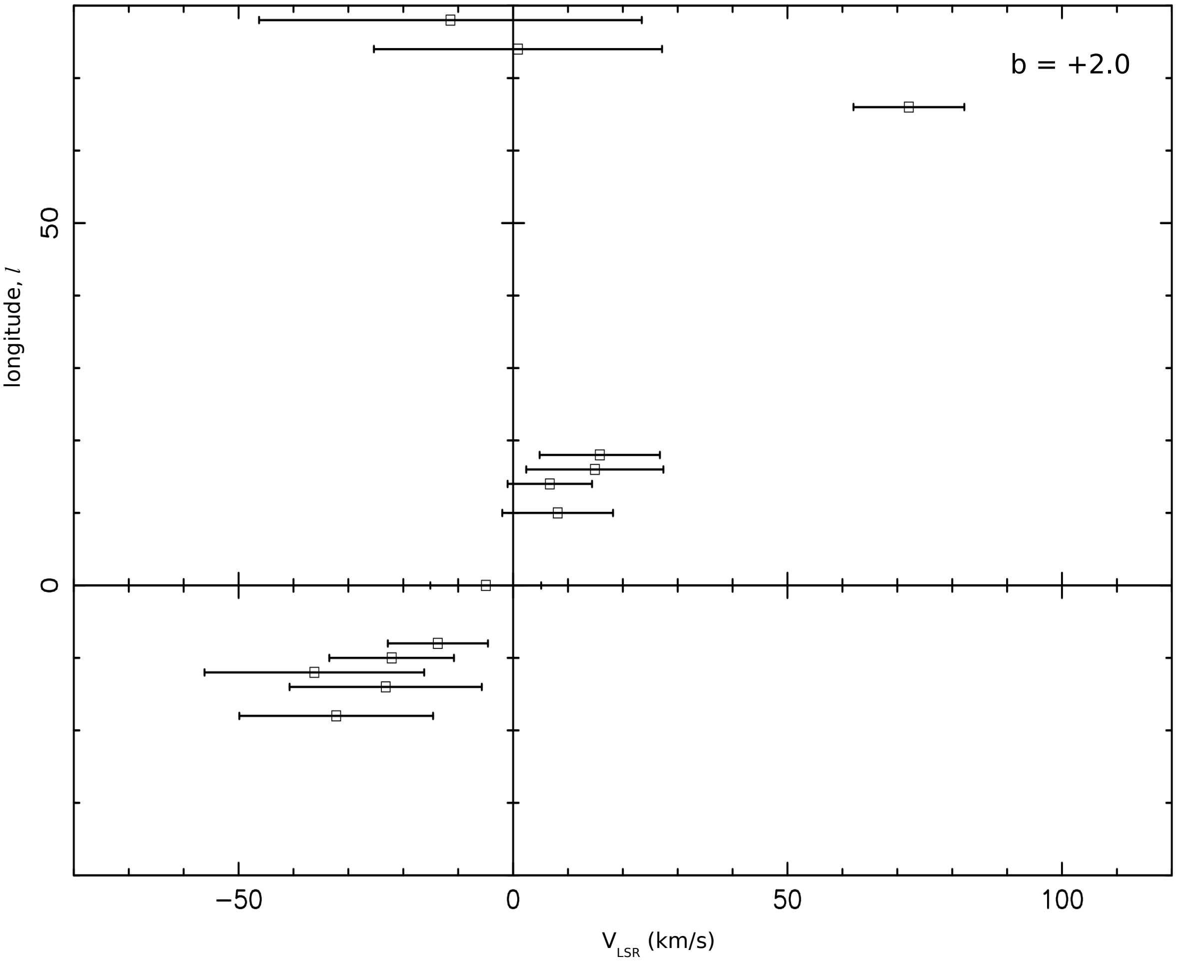

Fig 4-26 : lv-diagram marking the line detected positions with bars. The length of the bars indicates the line width of the line at longitude $l\,^{o}$, the central point of the bar gives the V_{LSR}(km/s) of the detected line.

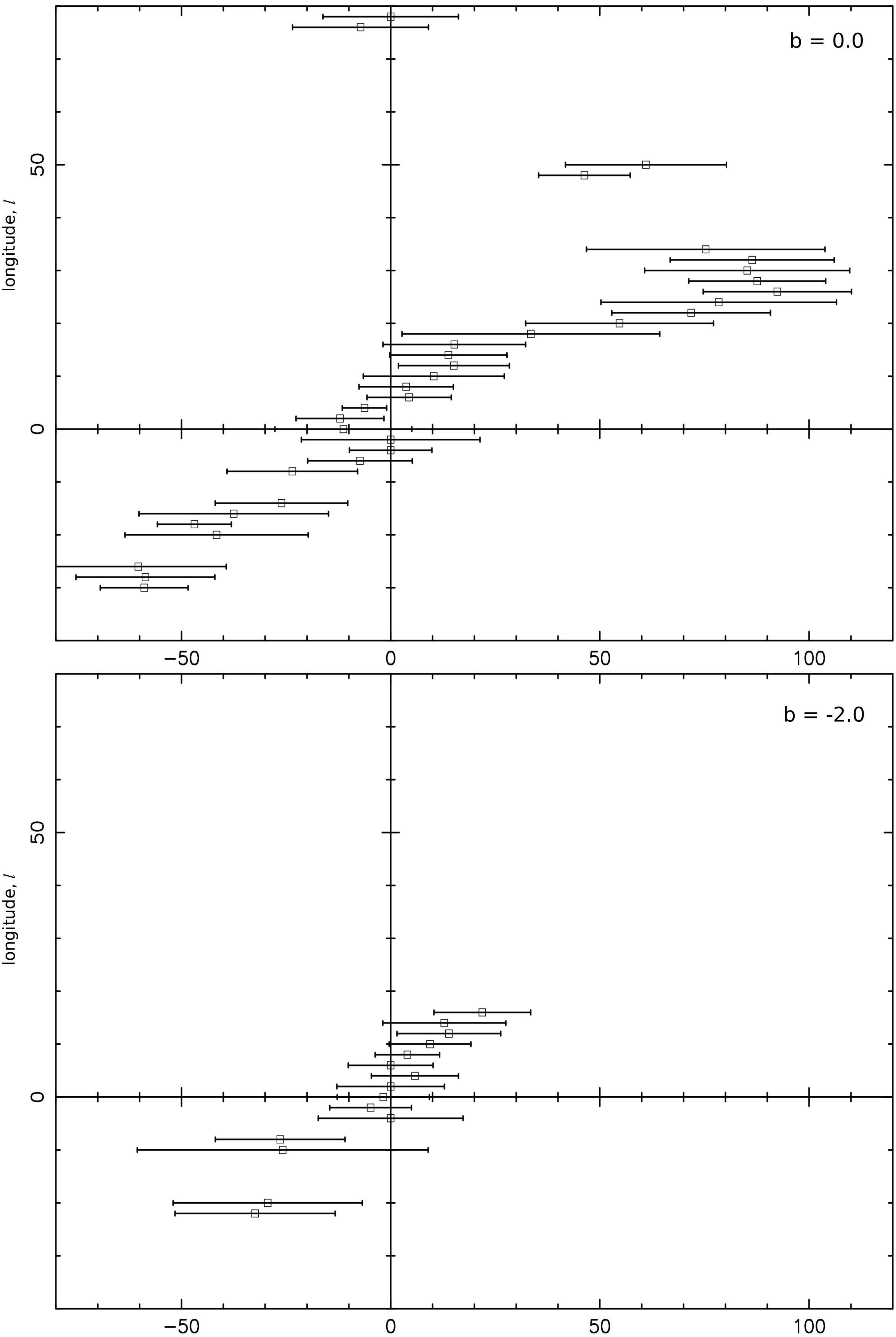

Fig 4-27 : lv-diagram marking the line detected positions with bars. The length of the bars indicates the line width of the line at longitude l^o, the central point of the bar gives the V_{LSR}(km/s) of the detected line.

l^o	b^o	T_l/T_c x 10^3	ΔV_{LSR} (km/s)	V_{LSR} (km/s)	T_c (K)	Comments[b]
78.0	2.0	0.41(0.06) 0.33(0.07)	33.7(5.8) 26.4(6.4)	3.1(2.5) -140.5(2.7)	297	H C
78.0	0.0	0.44(0.07) 0.52(0.06)	32.3(6.0) 46.9(6.1)	4.85(2.5) -141.2(2.6)	234	H C
78.0	-2.0	0.79(0.13)	38.5(7.2)	103.7(3.0)	104	H,pd
76.0	2.0	0.4(0.08)	31.7(7.0)	-129.7(3.0)	104	C
76.0	0.0	0.42(0.01) 0.45(0.01)	32.6(8.5) 30.5(7.8)	0.0 -137.5(3.3)	78	H C
76.0	-2.0	- 0.52(0.12)	- 26.3(6.8)	- -114.2(2.9)	66	C
74.0	2.0	0.35(0.085)	47.3(13.0)	0.3(5.5)	91	H
74.0	0.0	0.32(0.13)	24.0(11.0)	6.4(4.7)	140	H
74.0	-2.0	0.64(0.12)	28.8(6.0)	-38.0(2.6)	84	H
72.0	2.0	0.3(0.07)	36.3(11.3)	-143.6(4.8)	28	C
72.0	0.0	0.4(0.01)	32.5(10.0)	0.0(4.2)	84	H
72.0	-2.0	1.3(0.14)	39.6(5.0)	-35.3(2.1)	55	H
70.0	2.0	-	-	-	-	-
70.0	0.0	- 0.45(0.07)	- 33.0(6.1)	- -141.2(2.6)	72	- C
70.0	-2.0	-	-	-	18	-

68.0	2.0	-	-	-	91	-
68.0	0.0	-	-	-	140	
68.0	-2.0	0.8(0.09)	33.6(4.3)	-139.7(1.8)	163	C,pd
66.0	2.0	-	-	-	55	
66.0	0.0	-	-	-	111	
66.0	-2.0	0.38(0.1)	23.6(8.3)	-99.4(3.5)	111	C,pd
64.0	2.0	-	-	-	44	
64.0	0.0	-	-	-	72	
64.0	-2.0	-	-	-	60	
62.0	2.0	-	-	-	78	
62.0	0.0	-	-	-	72	
62.0	-2.0	-	-	-	72	
60.0	2.0	-	-	-	84	
60.0	0.0	0.33(0.1)	21.7(8.3)	25.2(3.5)	91	H
60.0	-2.0	-	-	-	55	
58.0	2.0	-	-	-	78	
58.0	0.0	-	-	-	91	
58.0	-2.0	0.35(0.1)	40.9(15.2)	-114.4(6.5)	49	C,pd
56.0	2.0	-	-	-	104	
56.0	0.0	-	-	-	118	
56.0	-2.0	-	-	-	78	

54.0	*2.0*	-	-	-	*140*	
54.0	*0.0*	-	-	-	*140*	
54.0	*-2.0*	- *0.42(0.09)*	- *34.9(8.4)*	- *-110.5(3.6)*	*84*	*C*
52.0	*2.0*	- *1.2(0.1)*	- *46.9(5.2)*	- *-114.8(2.2)*	*125*	*C,pd*
52.0	*0.0*	-	-	-	*188*	
52.0	*-2.0*	-	-	-	*97*	
50.0	*2.0*	-	-	-	*132*	
50.0	*0.0*	*0.38(0.06)*	*37.2(7.5)*	*64.3(3.2)*	*254*	*H*
50.0	*-2.0*	-	-	-	*206*	
48.0	*2.0*	*0.7(0.17)* *0.3(0.11)*	*12.3(3.5)* *30.7(12.3)*	*85.5(1.5)* *-138.2(5.2)*	*111*	*H* *C*
48.0	*0.0*	*0.24(0.04)*	*57.2(11.9)*	*67.5(5.1)*	*234*	*H*
48.0	*-2.0*	-	-	-	*38*	
46.0	*2.0*	- *0.86(0.1)*	- *42.9(5.5)*	- *-106.0*	*125*	*C*
46.0	*0.0*	- *0.37(0.09)*	- *42.9(12.0)*	- *-140.6(5.1)*	*275*	*C*
46.0	*-2.0*	- *0.85(0.08)*	- *48.0(5.4)*	- *-117.6(2.3)*	*188*	*C*
44.0	*2.0*	- *0.37(0.06)*	- *35.7(7.0)*	- *-101.0(3.0)*	*125*	*C*

44.0	0.0	- 0.38(0.06)	- 55.5(11.0)	- -126.4(4.7)	215	C
44.0	-2.0	0.22(0.08) 0.34(0.05)	17.6(7.5) 44.6(7.6)	48.3(3.2) -105.8(3.2)	132	H C
42.0	2.0	- 0.51(0.06)	- 43.8(5.6)	- -113.3(2.4)	197	C
42.0	0.0	- 0.37(0.09)	- 42.9(12.0)	- -140.6(5.1)	265	C
42.0	-2.0	- 0.52(0.07)	- 39.0(6.3)	- -105.6(2.7)	188	C
40.0	2.0	- 0.36(0.07)	- 34.8(7.7)	- -136.8(3.3)	308	C
40.0	0.0	-	-	-	344	
40.0	-2.0	-	-	-	234	
38.0	2.0	0.25(0.052) 0.29(0.04)	22.8(5.4) 41.0(6.4)	30.5(2.3) -136.7(2.7)	332	H C
38.0	0.0	-	-	-	482	
38.0	-2.0	- 0.27(0.06)	- 28.8(7.2)	- -145.8(3.0)	215	C,pd
36.0	2.0	- 0.34(0.07)	- 31.3(7.4)	- -133.5(3.2)	206	C,pd
36.0	0.0	-	-	-	320	
36.0	-2.0	- 0.48(0.15)	- 14.4(5.1)	- -148.2(2.2)	215	C,pd

34.0	*2.0*	*-* *0.39(0.09)*	*-* *37.0(10.3)*	*-* *-134.2(4.4)*	*197*	*C*
34.0	*0.0*	*-*	*-*	*-*	*452*	
34.0	*-2.0*	*-*	*-*	*-*	*188*	
32.0	*2.0*	*0.76(0.1)*	*20.9(3.0)*	*-148.1(1.3)*	*180*	*C*
32.0	*0.0*	*0.53(0.05)*	*38.7(4.3)*	*91.3(1.8)*	*344*	*H*
32.0	*-2.0*	*-* *0.36(0.06)*	*-* *45.5(8.1)*	*-* *-140.8(3.4)*	*357*	*C*
30.0	*2.0*	*-* *0.47(0.1)*	*-* *10.3(2.4)*	*-* *-139.2(1.0)*	*234*	*C,pd*
30.0	*0.0*	*0.58(0.06)* *0.15(0.06)*	*32.9(3.9)* *33.9(14.8)*	*92.9(1.6)* *-62.4(6.3)*	*452*	*H* *C*
30.0	*-2.0*	*0.3(0.08)* *0.44(0.06)*	*13.7(5.1)* *30.3(5.7)*	*54.2(2.1)* *85.2(2.2)*	*275*	*H* *H*
28.0	*2.0*	*-*	*-*	*-*	*297*	
28.0	*0.0*	*1.05(0.13)*	*35.9(5.05)*	*93.2(2.1)*	*423*	*H*
28.0	*-2.0*	*0.31(0.06)*	*34.8(7.6)*	*94.4(3.2)*	*308*	*H*
26.0	*2.0*	*-*	*-*	*-*	*308*	*H*
26.0	*0.0*	*0.51(0.05)*	*37.7(4.4)*	*96.6(1.9)*	*600*	*H*
26.0	*-2.0*	*0.21(0.5)*	*34.0(9.9)*	*85.6(4.2)*	*396*	*H*
24.0	*2.0*	*0.37(0.06)*	*43.2(7.6)*	*86.0(3.2)*	*382*	*H*
24.0	*0.0*	*0.36(0.04)*	*55.3(7.3)*	*81.0(3.1)*	*582*	*H*

24.0	-2.0	-	-	-	308	
22.0	2.0	-	-	-	344	
22.0	0.0	0.32(0.043)	50.1(7.8)	78.6(3.3)	618	H
22.0	-2.0	0.37(0.14) 0.43(0.21)	25.3(10.8) 10.7(6.1)	51.3(4.6) -99.0(2.6)	332	H C
20.0	2.0	0.35(0.09)	21.6(6.3)	26.8(2.7)	396	H
20.0	0.0	0.78(0.14) 0.53(0.22)	49.1(9.9) 18.3(8.9)	60.3(4.2) -111.5(3.8)	547	H C
20.0	-2.0	-	-	-	332	
18.0	2.0	0.6(0.06)	32.7(3.9)	26.9(1.7)	396	H
18.0	0.0	0.45(0.12) 0.56(0.06)	31.2(8.6) 42.9(11.2)	15.3(5.3) 52.9(6.0)	564	H H
18.0	-2.0	0.26(0.08)	20.9(7.2)	24.7(3.1)	320	H
16.0	2.0	0.54(0.08)	41.6(6.7)	28.5(2.9)	357	H
16.0	0.0	0.65(0.05) 0.24(0.06)	46.8(4.1) 36.8(9.8)	31.7(1.8) -136.3(4.2)	582	H C
16.0	-2.0	0.34(0.07)	28.9(6.8)	33.4(2.9)	382	H
14.0	2.0	0.3(0.07)	24.2(7.0)	21.3(3.0)	357	H
14.0	0.0	0.6(0.06) 0.44(0.05)	37.4(4.1) 42.6(5.9)	28.5(1.7) -125.2(2.5)	676	H C
14.0	-2.0	0.31(0.04)	60.2(8.5)	38.6(3.6)	357	H
12.0	2.0	- 0.35(0.08)	- 40.6(10.5)	- -153.7(4.5)	320	 C

12.0	0.0	0.69(0.05) 0.3(0.06)	55.4(4.8) 35.6(8.8)	32.9(2.0) -123.4(3.7)	564	H H
12.0	-2.0	0.43(0.08) 0.28(0.08)	32.1(6.6) 31.6(10.2)	24.0(2.8) -147(4.3)	396	H C
10.0	2.0	0.37(0.06) 0.17(0.07)	30.5(6.0) 25.0(11.7)	18.2(2.6) -137.1(5.0)	382	H C
10.0	0.0	0.42(0.04) 0.34(0.045)	45.9(5.2) 38.8(5.9)	22.7(2.2) -125.7(2.5)	656	H C
10.0	-2.0	0.5(0.07)	34.2(5.5)	19.5(2.4)	369	H
8.0	2.0	-	-	-	308	
8.0	0.0	0.51(0.06) 0.31(0.05)	34.5(4.7) 41.1(8.4)	18.3(2.0) -140.0(3.6)	618	H C
8.0	-2.0	0.35(0.09) 0.24(0.09)	17.6(5.0) 17.2(7.3)	16.3(2.1) -141.9(3.1)	396	H C
6.0	2.0	-	-	-	344	
6.0	0.0	0.54(0.085) 0.28(0.07)	24.1(4.4) 34.8(10.2)	17.1(1.9) -137.7(4.3)	738	H C
6.0	-2.0	0.41(0.085) 0.23(0.01)	27.1(6.6) 19.2(9..7)	12.2(2.8) -142.1(4.1)	369	H C
4.0	2.0	0.24(0.09) 0.52(0.16)	24.8(10.7) 7.3(2.5)	9.34(4.5) -144.2(1.2)	332	H C
4.0	0.0	0.37(0.11) 0.42(0.06)	14.0(4.7) 47.1(7.6)	6.3(2.0) -142.3(3.2)	637	H C
4.0	-2.0	0.3(0.1)	18.0(7.1)	15.5(3.0)	297	H

2.0	*2.0*	*-*	*-*	*-*	*482*	
2.0	*0.0*	*0.43(0.08)*	*21.5(4.5)*	*0.0(1.9)*	*656*	*H*
		0.46(0.09)	*17.1(3.8)*	*-152.3(1.6)*		*C*
2.0	*-2.0*	*0.56(0.12)*	*19.6(5.0)*	*15.3(2.1)*	*344*	*H*
0.0	*2.0*	*0.47(0.13)*	*23.3(7.1)*	*8.2(3.0)*	*437*	*H*
0.0	*0.0*	*0.45(0.05)*	*52.7(6.4)*	*7.6(2.7)*	*1150*	*H*
		0.27(0.08)	*18.8(6.3)*	*-147.8(2.7)*		*C*
0.0	*-2.0*	*0.3(0.08)*	*25.0(7.9)*	*10.0(3.4)*	*482*	*H*
		0.2(0.05)	*56.0(18.3)*	*-158.3(7.8)*		*C*
-2.0	*2.0*	*0.25(0.07)*	*28.8(8.6)*	*-7.5(3.7)*	*396*	*H*
-2.0	*0.0*	*0.31(0.06)*	*25.3(5.9)*	*0.0(2.5)*	*656*	*H*
		0.12(0.08)	*18.0(13.3)*	*-149.5(5.7)*		*C*
-2.0	*-2.0*	*0.41(0.06)*	*30.4(5.2)*	*0.0(2.2)*	*275*	*H*
		0.27(0.06)	*33.4(8.0)*	*-160.6(3.4)*		*C*
-4.0	*2.0*	*0.16(0.06)*	*22.5(10.5)*	*0.0(4.4)*	*357*	*H*
-4.0	*0.0*	*0.33(0.07)*	*23.1(5.7)*	*0.0(2.4)*	*514*	*H*
		0.45(0.05)	*44.0(5.9)*	*-163.3(2.4)*		*C*
-4.0	*-2.0*	*0.3(0.07)*	*31.0(8.3)*	*0.0(3.5)*	*332*	*H*
		0.24(0.09)	*19.8(8.2)*	*-157.3(3.5)*		*C*
-6.0	*2.0*	*0.37(0.12)*	*13.8(5.14)*	*1.4(2.2)*	*357*	*H*
		0.3(0.07)	*40.8(11.1)*	*-129.3(4.7)*		*C*
-6.0	*0.0*	*0.4(0.05)*	*30.4(4.8)*	*0.0(2.1)*	*467*	*H*
		0.19(0.07)	*19.2(8.3)*	*-150.3(3.5)*		*C*

-6.0	-2.0	-	-	-	188	
-8.0	2.0	0.43(0.11)	19.5(5.5)	0.0(2.35)	265	H
-8.0	0.0	0.6(0.08) 0.31(0.11)	25.1(4.0) 15.8(6.2)	-6.5(1.7) -166.4(2.6)	344	H C
-8.0	-2.0	-	-	-	215	
-10.0	2.0	-	-	-	215	
-10.0	0.0	-	-	-	344	
-10.0	-2.0	0.43(0.12) 0.46(0.13)	30.2(9.6) 24.2(8.0)	-6.1(4.1) -124.0(3.4)	254	H C
-12.0	2.0	0.43(0.08)	53.7(11.1)	-20.0(4.7)	180	H
-12.0	0.0	-	-	-	297	
-12.0	-2.0	-	-	-	234	
-14.0	2.0	0.34(0.12)	30.4(12.9)	0.0(0.12)	234	H
-14.0	0.0	-	-	-	320	
-14.0	-2.0	-	-	-	188	
-16.0	2.0	-	-	-	224	
-16.0	0.0	0.59(0.06)	62.8(7.4)	-24.8(3.2)	344	H
-16.0	-2.0	-	-	-	155	
-18.0	2.0	0.72(0.27)	19.1(8.4)	-124.6(3.6)	188	C,pd
-18.0	0.0	0.4(0.05) 0.46(0.1)	39.0(6.0) 11.7(2.8)	-27.5(2.5) -156.9(1.2)	332	H C
-18.0	-2.0	-	-	-	163	

-20.0	2.0	-	-	-	206	
-20.0	0.0	1.3(0.2) 1.13(0.34)	52.5(9.3) 18.0(6.14)	-30.8(4.0) -171.6(2.6)	320	H C
-20.0	-2.0	0.44(0.074)	46.0(8.9)	-21.2(3.8)	224	H
-22.0	2.0	-	-	-	171	
-22.0	0.0	-	-	-	369	
-22.0	-2.0	0.4(0.06)	47.8(9.4)	-29.3(4.0)	155	H
-24.0	2.0	-	-	-	140	
-24.0	0.0	-	-	-	254	
-24.0	-2.0	-	-	-	78	
-26.0	2.0	-	-	-	207	
-26.0	0.0	0.5(0.07)	27.0(4.6)	-52.6(2.0)	301	H
-26.0	-2.0	-	-	-	191	
-28.0	2.0	- 0.68(0.17)	- 36.6(10.5)	- -133.7(4.4)	125	C
-28.0	0.0	-	-	-	215	
-28.0	-2.0	-	-	-	147	
-30.0	2.0	-	-	-	125	
-30.0	0.0	-	-	-	225	
-30.0	-2.0	-	-	-	132	

Table 4-1: Parameters of line detections from ORT survey, the values in the paranthesis are errors on them.

[b] *H- hydrogen line , C- Carbon line, pd-probable detection*

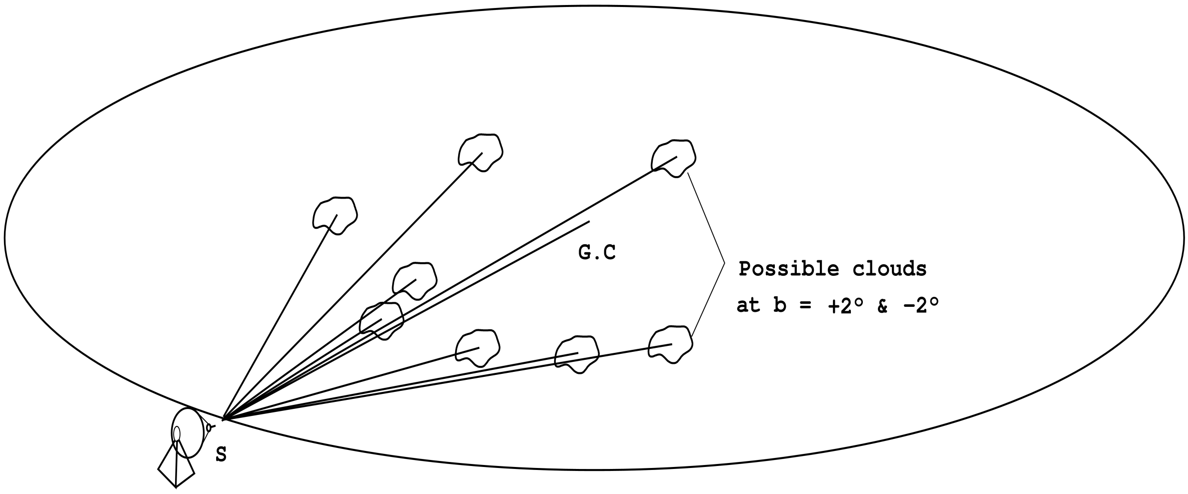

Fig 4-28: The figure shows the possible clouds at higher latitudes that give rise to the observed line intensities

Source	V_{LSR} ***(km/s)***	D_C ***(kpc)***	H_c ***(pc)***
G38.0 +2.0	*30.5*	*2.0*	*105*
G24.0 +2.0	*86.0*	*6.4*	*335*
G20.0 +2.0	*26.8*	*2.43*	*127*
G18.0 +2.0	*26.9*	*2.63*	*137*
G16.0 +2.0	*28.5*	*3.02*	*158*
G14.0 +2.0	*21.3*	*2.58*	*135*
G10.0 +2.0	*18.2*	*2.95*	*154*
G-2.0 +2.0	*-7.5*	*4.8*	*251*
G-4 +2.0	*0.0(4.4)*	*1.85*	*97*
G-6 +2.0	*1.4*	*0.24*	*12.6*
G-8 +2.0	*0.0(2.35)*	*0.53*	*27.8*
G-12.0 +2.0	*-20.0*	*2.76*	*144.5*

Table 4-2: Scale height (H_c) of clouds towards +ve latitude of +2 ^{o} together with their estimated near distances D_c . The values in the paranthesis are errors.

Source	V_{LSR} **(km/s)**	D_C **(kpc)**	H_c **(pc)**
G30.0 -2.0	*54.2, 85.2*	*3.8, 6.7*	*199,351*
G28.0 -2.0	*94.4*	*7.5*	*393*
G26.0 -2.0	*85.6*	*6.4*	*335*
G22.0 -2.0	*51.3*	*4.1*	*215*
G18.0 -2.0	*24.7*	*2.43*	*127*
G16.0 -2.0	*33.4*	*3.47*	*182*
G14.0 -2.0	*38.6*	*4.26*	*223*
G12.0 -2.0	*24.0*	*3.24*	*170*
G10.0 -2.0	*19.5*	*3.13*	*164*
G6.0 -2.0	*12.2*	*3.18*	*167*
G4.0 -2.0	*15.5*	*4.95*	*259*
G2.0 -2.0	*15.3*	*6.2*	*325*
G-2.0 -2.0	*0.0(2.2)*	*1.83*	*96*
G-4.0 -2.0	*0.0(3.5)*	*1.5*	*79*
G-10.0 -2.0	*-6.1*	*1.1*	*58*
G-20 -2.0	*-21.2*	*1.95*	*102*
G-22.0 -2.0	*-29.3*	*2.47*	*129*

Table 4-3: Estimated distances to the clouds (D_C) from the solar system and there heights (H_C) above the plane of the Galaxy. The values in the paranthesis are errors.

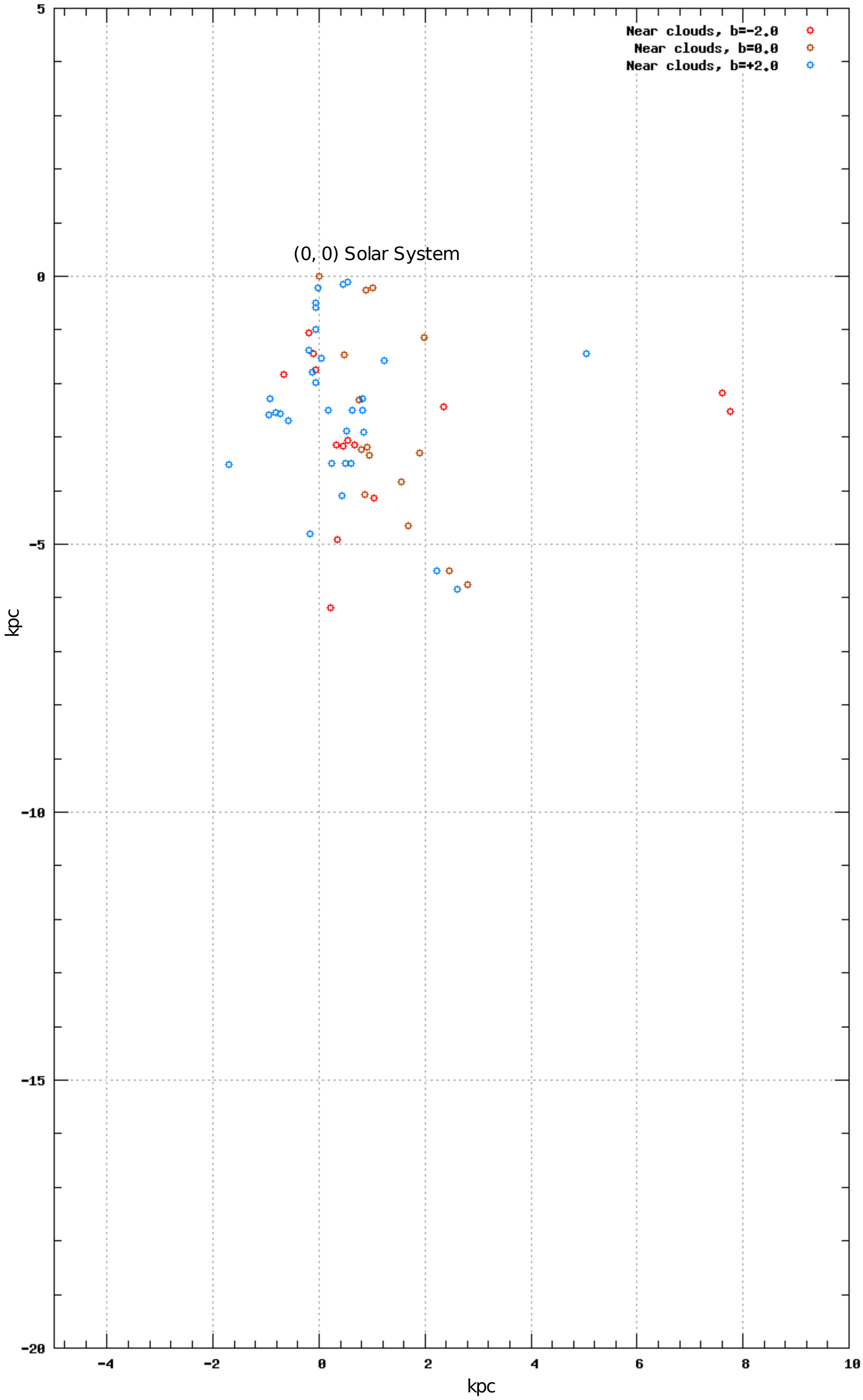

Fig 4-29: Distribution of near possible ELDWIM clouds in the Galaxy from ORT data. Distances obtained using Burton & Gordon(1978) Galactic rotation curve. Some of the b=0^{o} & b=-2^{o} location are not visible as they overlap with b=+2^{o} counter part.

Chapter 5

Discussion of observed RRLs

5.1 Dependence of Line intensity on physical parameters.

The observations towards different sources suggests us that a study of line intensity as function of different physical parameters like number density(n_e), electron temperature(T_e), background temperature incident on the source(T_{bg}), size of the source cloud or slab(s) and beam filling factor(Ω_B) is essential to understand the actual physical conditions existing in the line emitting sources(here ELDWIM). In this section the line temperature from hydrogen cloud corresponding to transitions H271α and H165α will be studied. The cloud model will be a simple one, which is a slab of thickness ' s ' (pc) as shown in the fig-1.

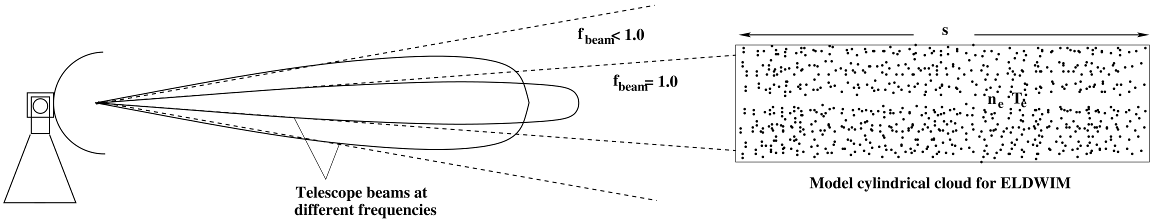

Fig 5-1: A slab or cylinder model for the line emitting region. The beams at different frequencies are different owing to their dependence on frequency and the dimensions of the telescope(diameter of the disc collecting radio waves). Due to the different beam sizes the source cloud may or may not fill the beam as can be seen in the figure above. In a fully beam filling cloud the emission measure($n_e^2 s$, which determines the optical depth) is primarily determined by the length of slab s.

The beam size of a telescope with a collecting dish of diameter d is of the order of λ/d. A cloud may or may not fill the beam depending on where it is placed along the line of sight. As the distance from the cloud increases the probability of catching a source within the beam increases as the beam becomes wider with distance. But due to increase in the distance the solid angle subtended by the source on the telescope decreases and this results in reduction of the observed line temperature. The observed line intensity from a cloud that subtends a solid angle of Ω_S at a telescope whose beam has a solid angle of Ω_B is given by the simple relation,

$$Tl_{obs} = Tl \frac{\Omega_S}{\Omega_B} \tag{5.1}$$

where Tl is the actual line strength from the source if the source had completely filled the beam. Multiple clouds along the line of sight can produce multiple components in observed spectrum. The separation between these components can give information about the location of these clouds along the line of sight by consideration of Galactic rotation. The widths of the lines tell about the distribution of gas in the region. The line from a region which is distributed along the line of sight would give rise to higher line widths owing to the spread in the velocity of the gas along the line of sight. This could be thought as a distribution of clouds along the Galactic arm intersecting with the telescope's line of sight. Each cloud produces its own line at a specific V_{LSR} . The following clouds produce their own lines whose V_{LSR} follow a certain gradient. Thus one can see broad lines towards certain regions. It is quiet common and also surely expected, to see multiple components appearing close by. It would be less probable in practical situations that one sees only one cloud along a given line of sight. This fact is supported by the observations made with WSRT towards several positions. Since the signal to noise ratio at 1.4 GHz is much better than at ~327 MHz(ORT) the line features can be identified more clearly. A two component fit is quiet common towards many positions. Some positions show more than two components, while a few also show smearing of line emission along the V_{LSR} axis. The manifestation of many components towards some positions has been displayed in the following figures. This has been analysed by fitting gaussians to these components. The removal of these fitted components from the actual data gives residual spectrum with noise of nearly zero mean. Indicating the validity of multiple components. From such a fit the main line emitting region can be thought of as a collection of clouds scattered about a mean position, determined by the mean V_{LSR} for the collection of lines. However pressure broadening cannot be completely neglected. Once the gaussian parameters have been fitted to these components individual clouds can be assigned to their origin. Further the widths of these lines tell about the temperatures of the clouds. At a high frequency like 1.4GHz the pressure brodening is quiet negligible(only when the density is small) and doppler broadening dominates. Assuming the observed width to be purely dopplerian originating from the maxwellian velocity distribution of emitting Rydberg atoms one can estimate the temperature of the clouds. In reality some contribution also comes from '*microturbulence*' which is the motion of the cells within the beam of the telescope with rest to the observer. This distribution is assumed to be dopplerian in behaviour.

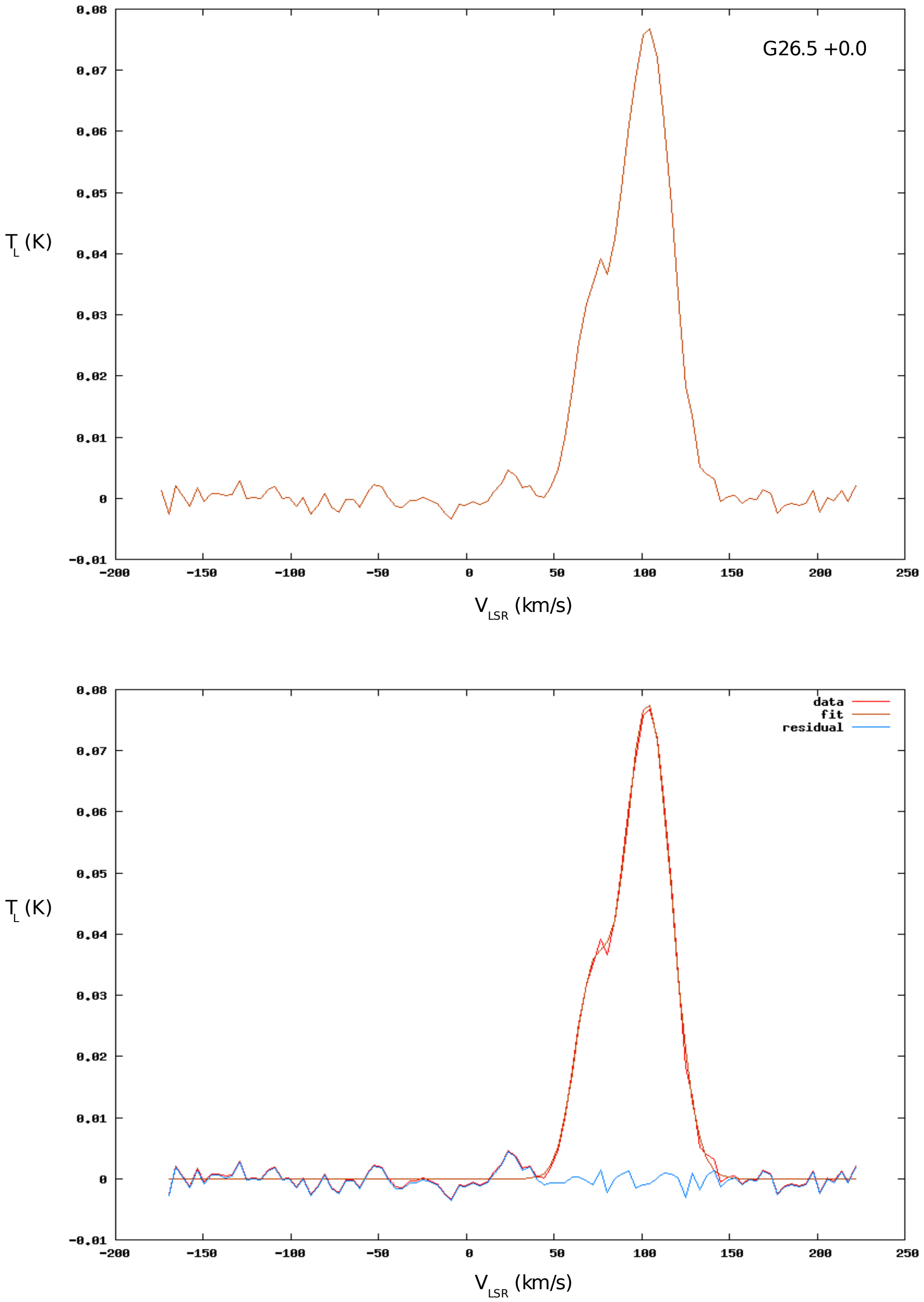

Fig 5-2: Observation towards the position G26.5 +0.0 which exhibits dual components. This is a weighted band averaged plot which has been fitted with gaussians(dual components) in the lower plot. The residual is noise with nearly zero mean expressing the validity of the fit.

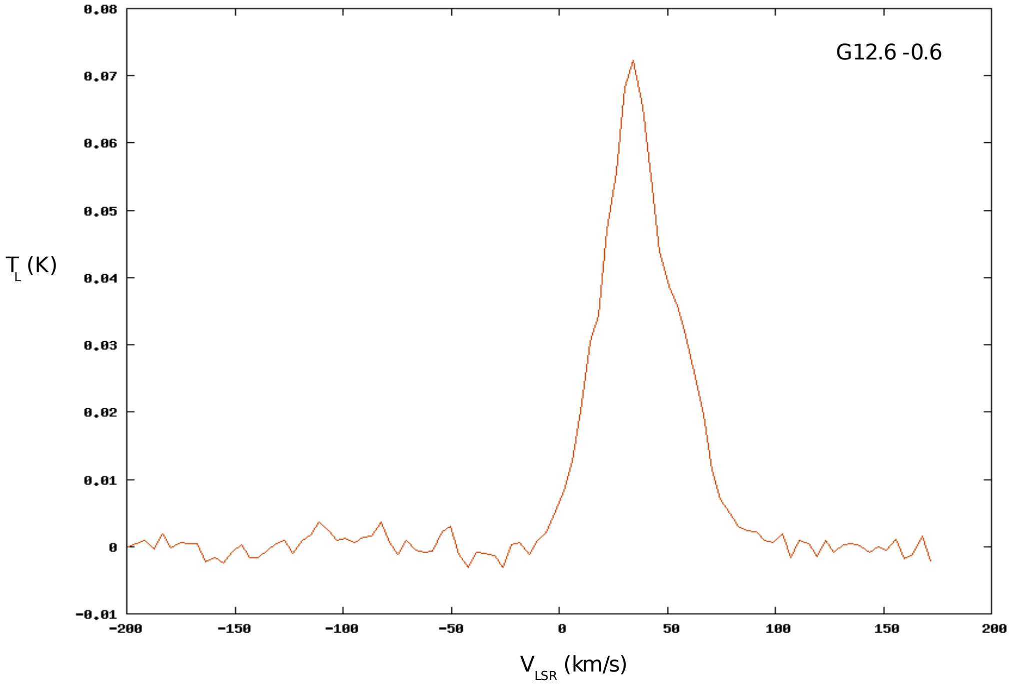

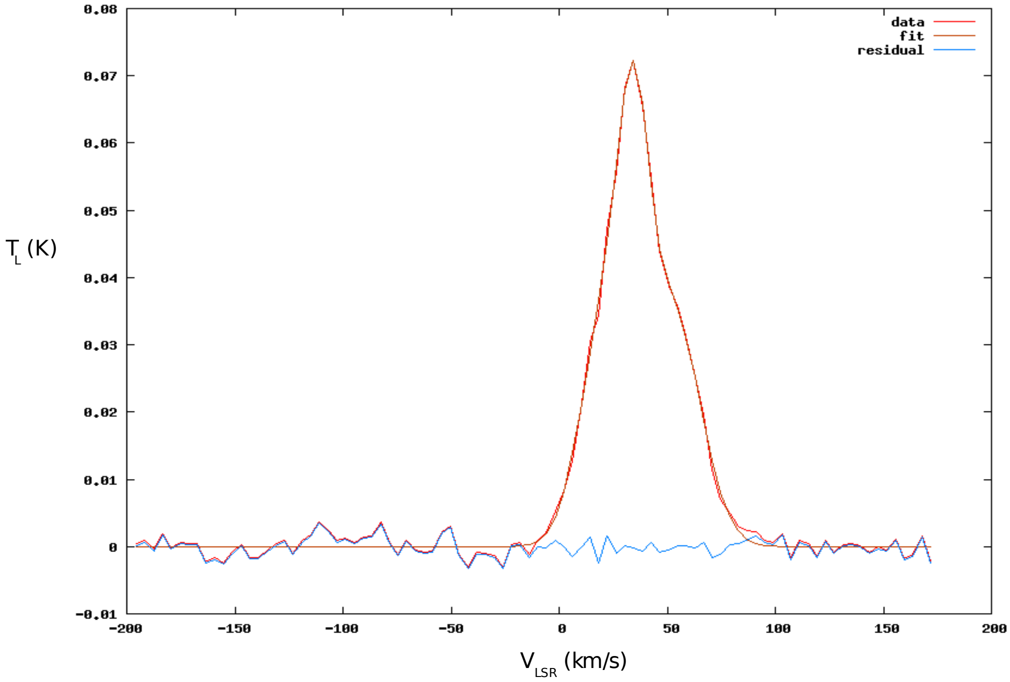

Fig 5-3: Observations towards the position G12.6+1.8 which exhibits triple components. A gaussian fit to the components(lower plot) results in a residual that is pure noise with nearly zero mean. Indicating the validity of triple component fitting.

This is normally taken to be ~20 km/s. The parameters fitted to these components suggest that the temperature of these clouds are on the order of 10^3 to 10^4 K.

$$T \approx \frac{\Delta V_D^2}{8\ln 2}\frac{M}{k} \qquad (5.2)$$

$$\Delta V_D^2 = \Delta V_{obs}^2 - \Delta V_T^2 \qquad (5.3)$$

Where ΔV_D is the observed line width, M is the mass of hydrogen atoms and k is the Boltzmann's constant. Assuming an average width of V_{obs} = 30 km/s one sees that the temperature comes out to be ~10000K where ΔV_T = 20 km/s as mentioned earlier. Interestingly some positions have exhibited quadruple components and some have smearing of line emission as displayed in fig-5.

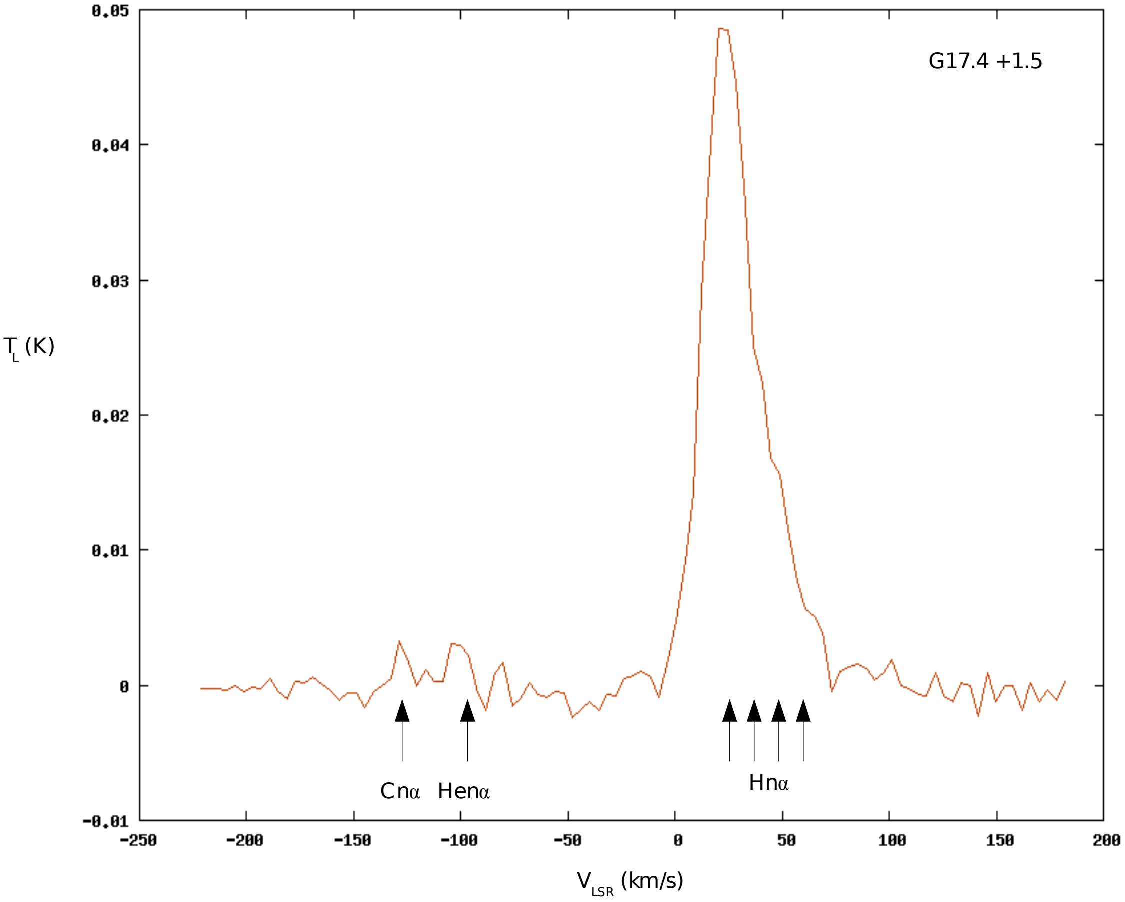

Fig 5-4 : Band average of observations made towards G17.4+1.5. The abscisssa is V_{LSR} (km/s) and ordinate is T_L (K). The hydrogen line features exhibit as many as 5 components when inspected carefully. The main component which has the highest amplitude(V_{LSR} ~ 22 km/s) seems to have an associated helium and carbon component at ~ -100 km/s and -125 km/s respectively. These features are not strong but are clearly distinguishable w.r.t to the noise else where in the band.

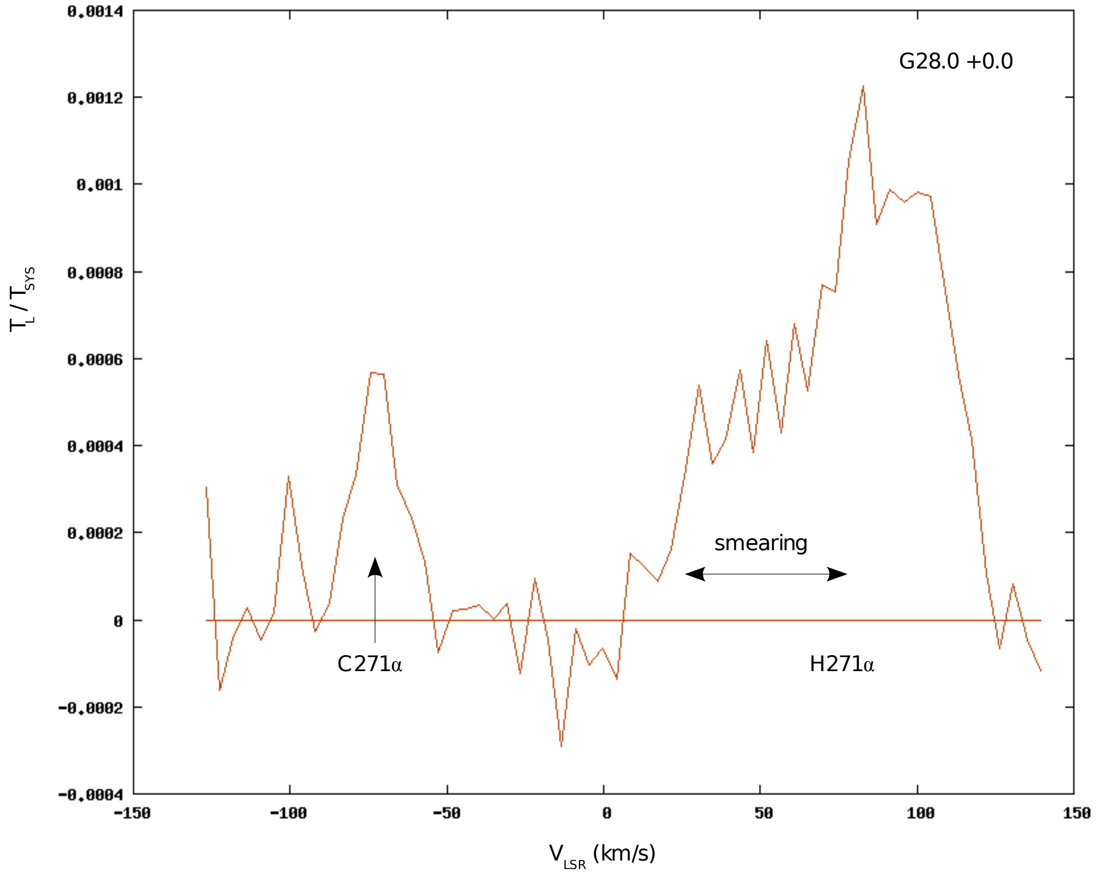

Fig 5-5: ORT observation of G28+0.0 which exhibits smeared line emission between V_{LSR} *= 10 km/s to 75 km/s. This is also visible in the associated carbon line around ~-70 km/s, which seems to have atleast 3-components.*

The mathematical formulation for the strength of observed line temperature has already been discussed in chapter 2. Here practical calculations for the model shown in fig-1 have been given. Assuming a fixed path length of s=10 pc as was concluded from modelling results in chapter 3 the expected line strength(ΔT_L) as a function of number density n_e has been given. The model can be formulated as

$$\Delta T_L = T_0\left[e^{-\tau_C}\left(e^{-\tau_L}-1\right)\right] + T_e\left[\left(\frac{b_n \tau_L^* + \tau_C}{\tau_L + \tau_C}\right)\left(1-e^{-(\tau_L+\tau_C)}\right) - \left(1-e^{-\tau_C}\right)\right] + T_{nc}\left[\frac{1-e^{-(\tau_L+\tau_C)}}{(\tau_L+\tau_C)} - \frac{1-e^{-\tau_C}}{\tau_C}\right] \tag{5.4}$$

where T_0 is the incident background temperature on the slab. T_e is the electron temperature in the slab and T_{nc} represents the non-thermal continuum distribution within the cloud. These have been taken to be

$$T_0 = T_c(1 - \frac{D_c}{D_G}); \quad T_{nc} = \frac{T_c s}{D_G}; \tag{5.5}$$

with D_c = 3.0 kpc and D_G = 15 kpc. Plots of LTE optical depth τ_l^*, departure coefficients b_n and β_n have also been displayed for two frequencies for comparision.

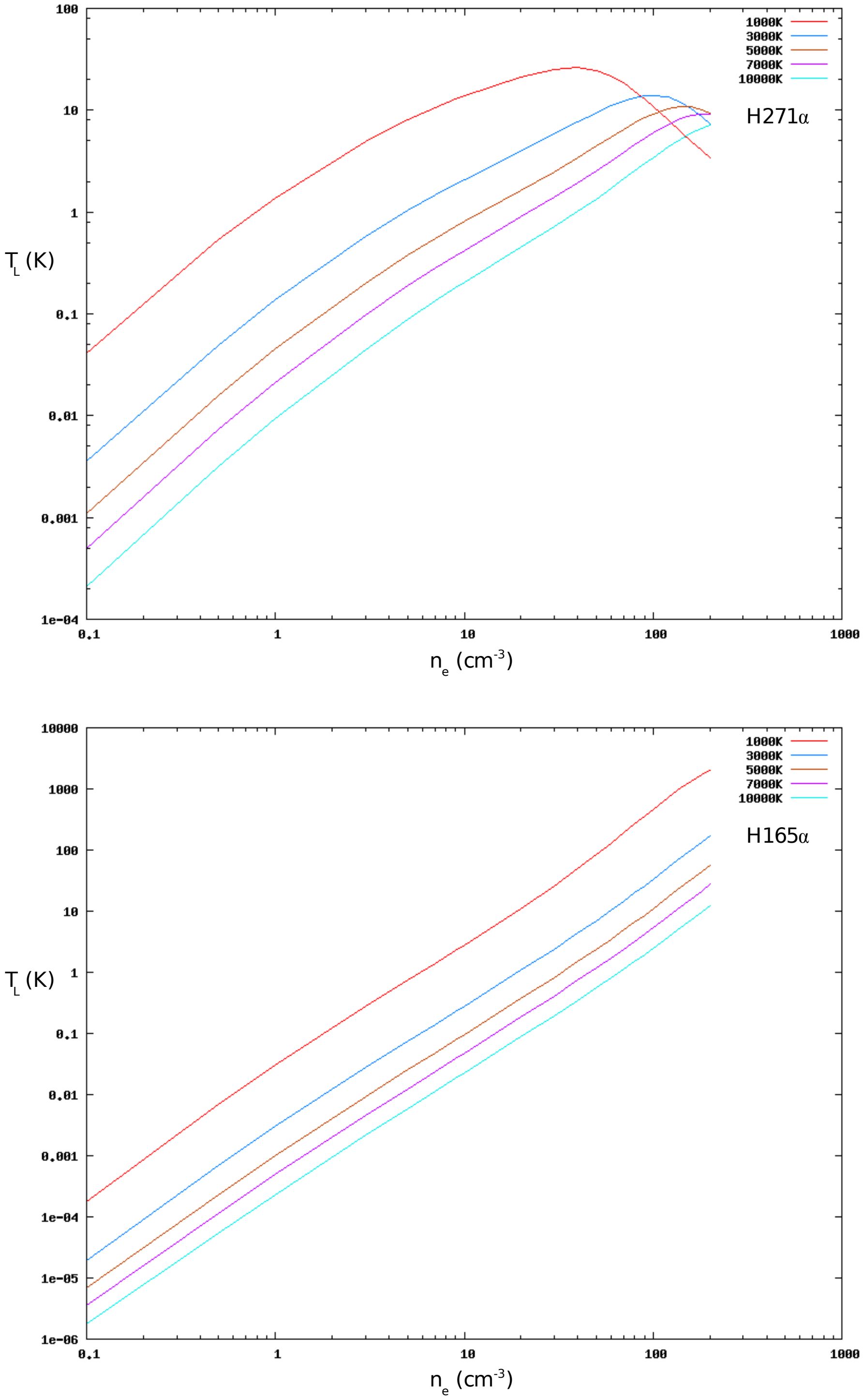

Fig 5-6: non-LTE line temperature for the model described in the text.

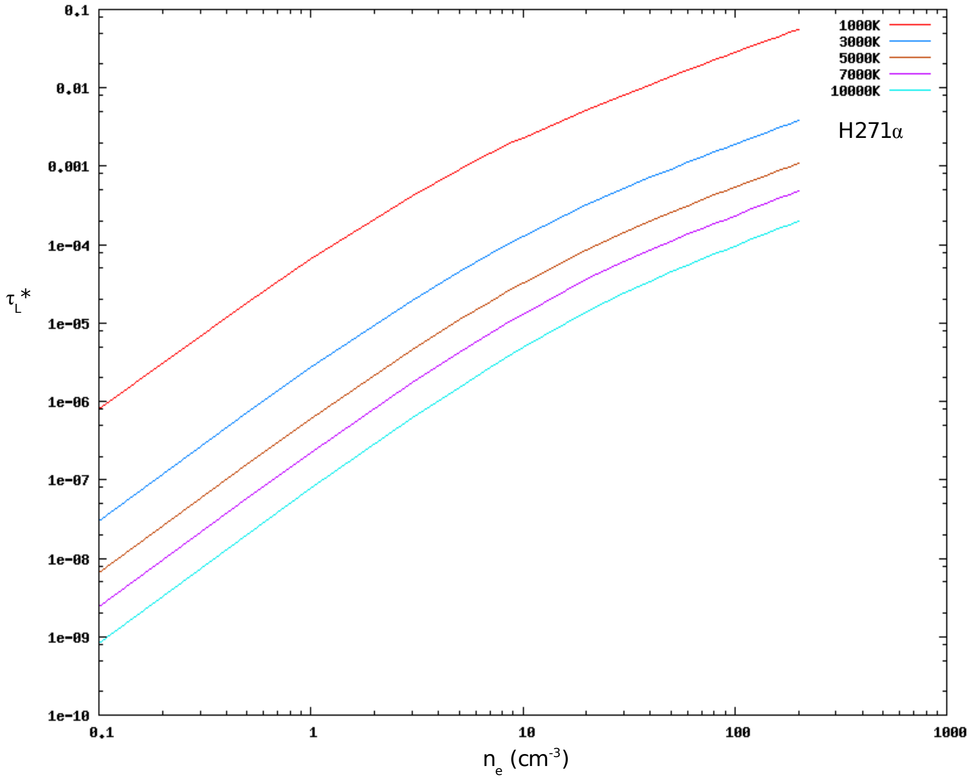

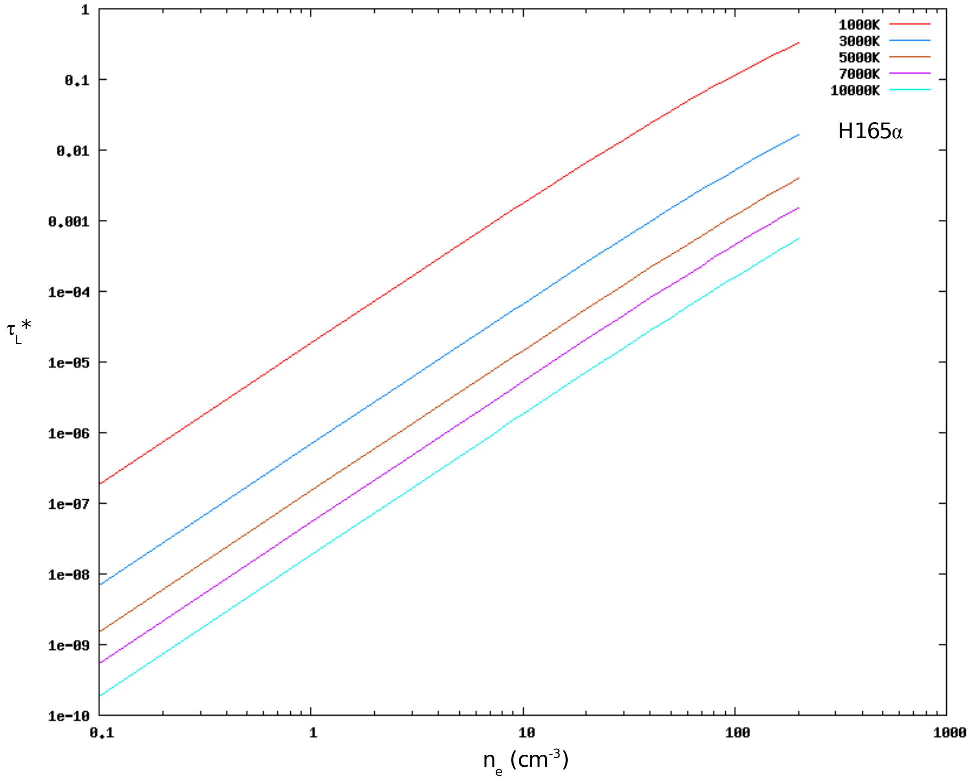

Fig 5-7: Plots of LTE line optical depth as function of electron number densities. The labels in the top right corner indicate the corresponding electron temperatures.

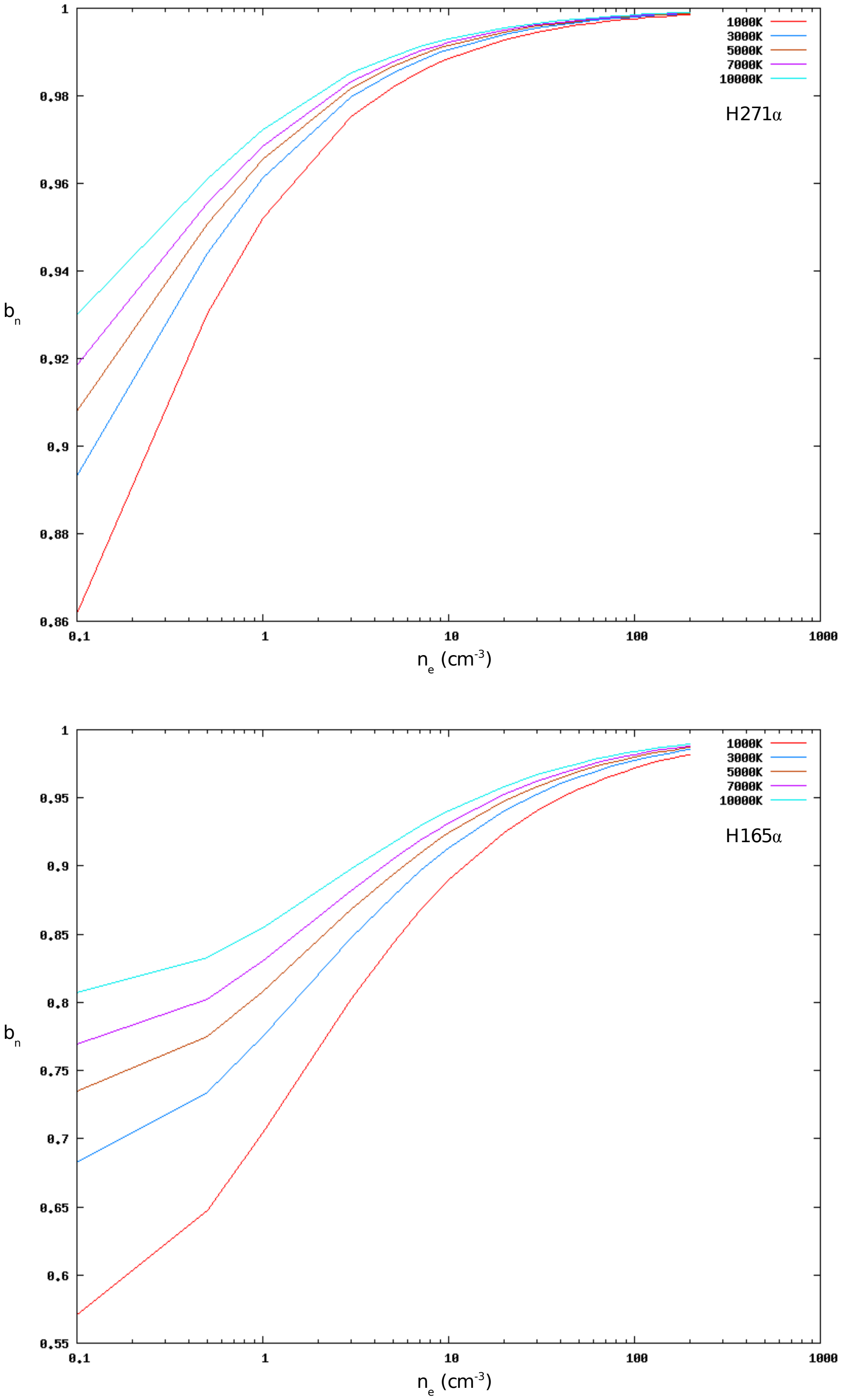

Fig 5-8: bn values as a function of electron number density and temperature. The upper plot corresponds to H271α while the lower to H165α .

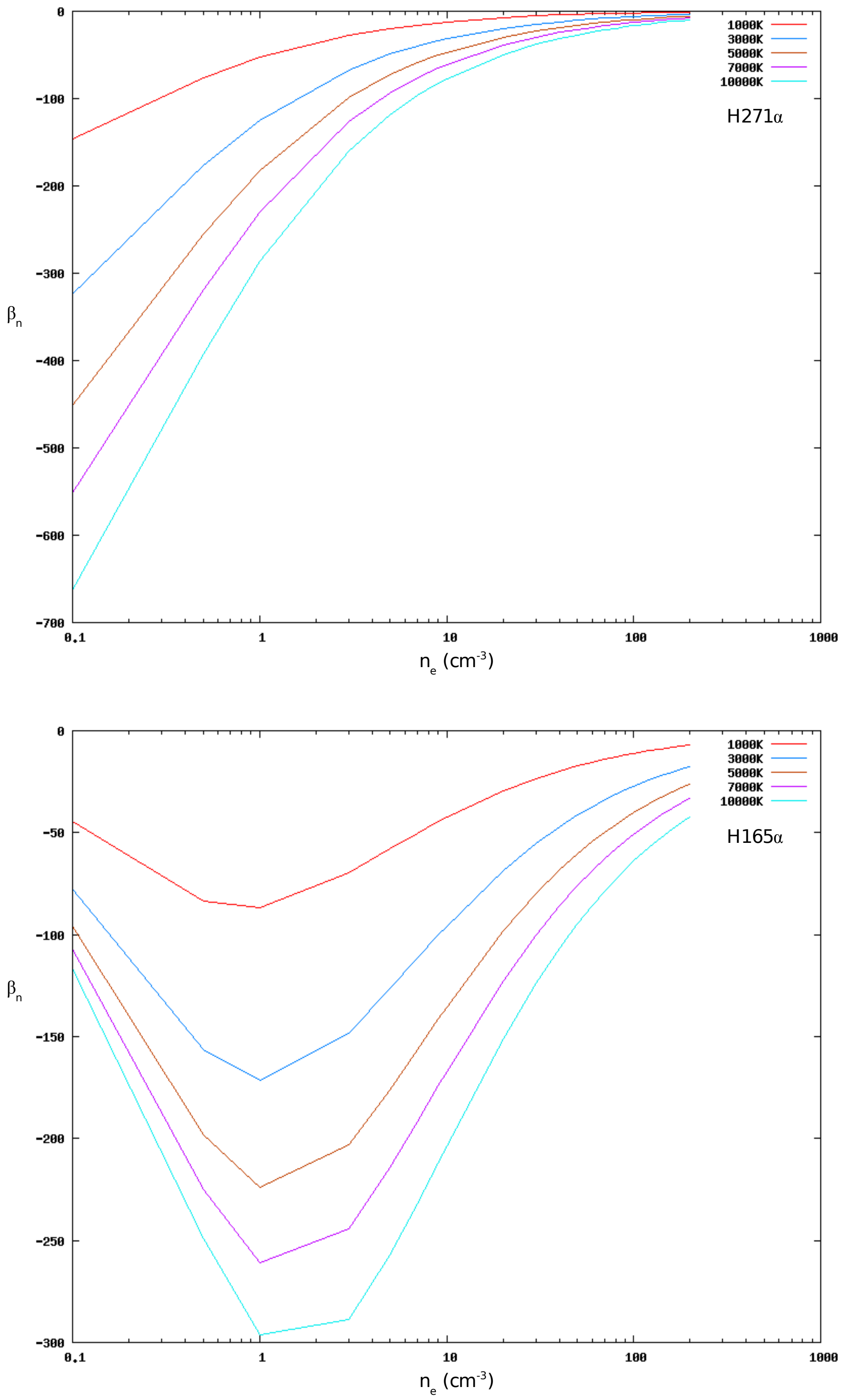

Fig 5-9: β_n values as a function of electron number density and temperature. The upper plot corresponds to H271α while lower to H165α.

The line emission characteristics from a model cloud can be understood in simple terms as follows. With the increase in the number density n_e firstly the continuum optical depth τ_c increases. If one were to consider the continuum emission alone which can be formulated as

$$T_c = T_e(1 - e^{-\tau_c}) \qquad (5.6)$$

where T_c would be the observed continuum temperature from the cloud with electron temperature T_e. This equation suggests that the continuum radiation would continuously increase with increase in τ_c. It would approach a black body with temperature of T_e when the optical depth would become infinite as one would expect. The increase in continuum radiation within the cloud is favourable for the stimulated emission as its probability will also increase with the increase in the intensity of stimulating radiation. Thus one would expect an increase in line emission temperature with increase in number density from a certain point. It should be noted that the line temperature is a pure manifestation of radiation from atomic transitions. The extra bump ΔT_L is to be attributed to atomic transitions. However the stimulated emission also depends on the number of atoms available in the excited state. As can be seen from the b_n curves with respect to principle qauntum number the departure from LTE provides population inversion. Which is that, the atoms in the higher quantum number state are more in number than the lower quantum number state. However with the increase in density thermalization begins which brings down this inversion towards LTE situation. This is seen with the b_n values approaching unity with increasing density. The increase in density also increases the LTE line optical depth τ_l* monotonically. b_n is also a monotonic increasing function of n_e, as can be seen in the plots. However β_n that appears as a factor for the non-LTE line optical depth τ_l goes as the derivative of logarithm of b_n. Which as we see is non-monotonic and acheives a maxima. This is also reflected in τ_l. The increase in the line intensity from that of the LTE situation is characterised by the β_{ne}-amplification factor as has already been discussed in chapter-2. The existence of a maxima for β_{ne} can be understood as a situation optimized for stimulated emission. When background radiation is present it can be seen from the first term in the above equation that an amplification of this occurs due to the stimulated atomic transitions along its path through the cloud. In the present model the plots corresponding to the line temperature contributions from the first(background radiation incident on the cloud) and the last term(non-thermal distribution within the cloud) have been given below.

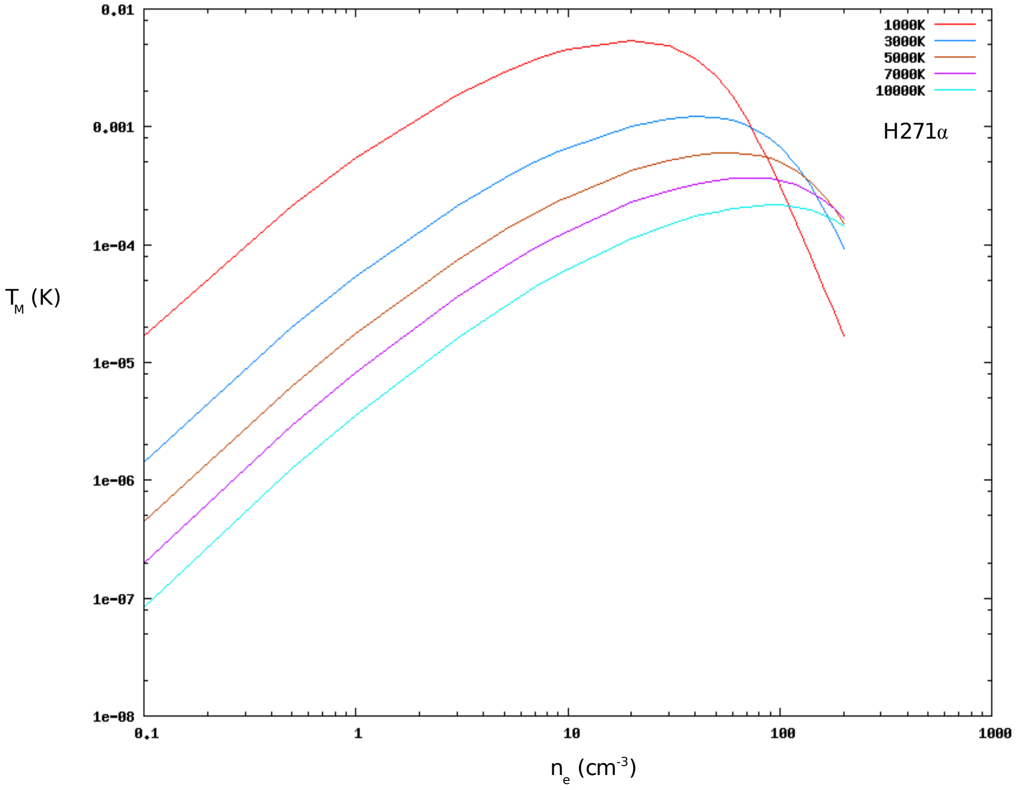

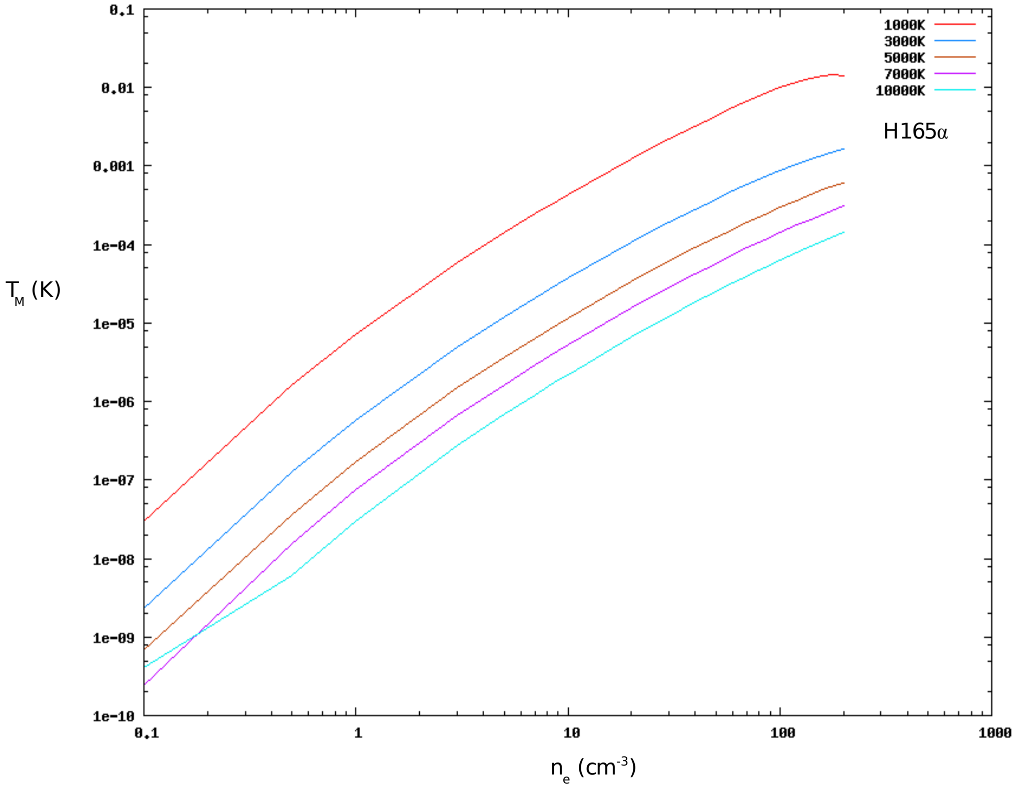

Fig 5-10: The line radiation contribution from the non-thermal radiation distributed within the cloud.

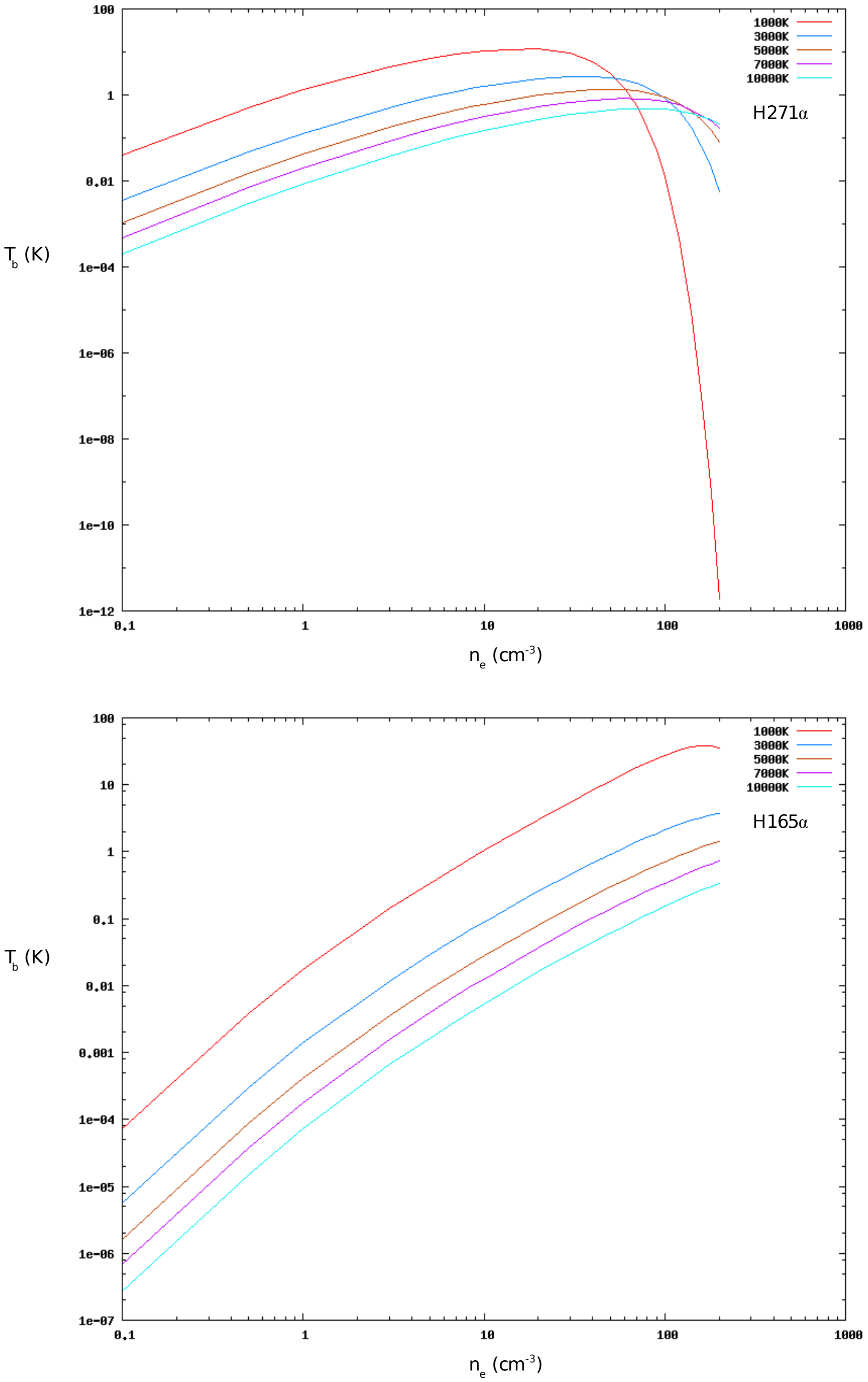

Fig 5-11: The line radiation contribution due to background radiation field on the cloud, which has been taken to be 10^4*K at 100 MHz and scaled to other frequencies using a spectral index of -2.7.*

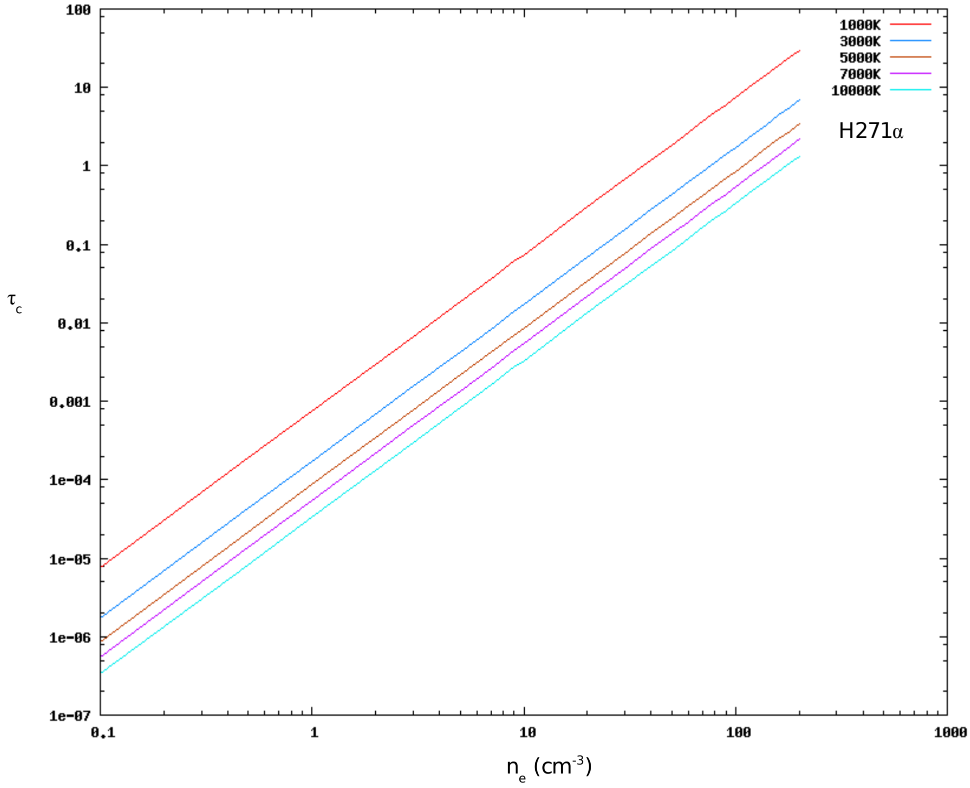

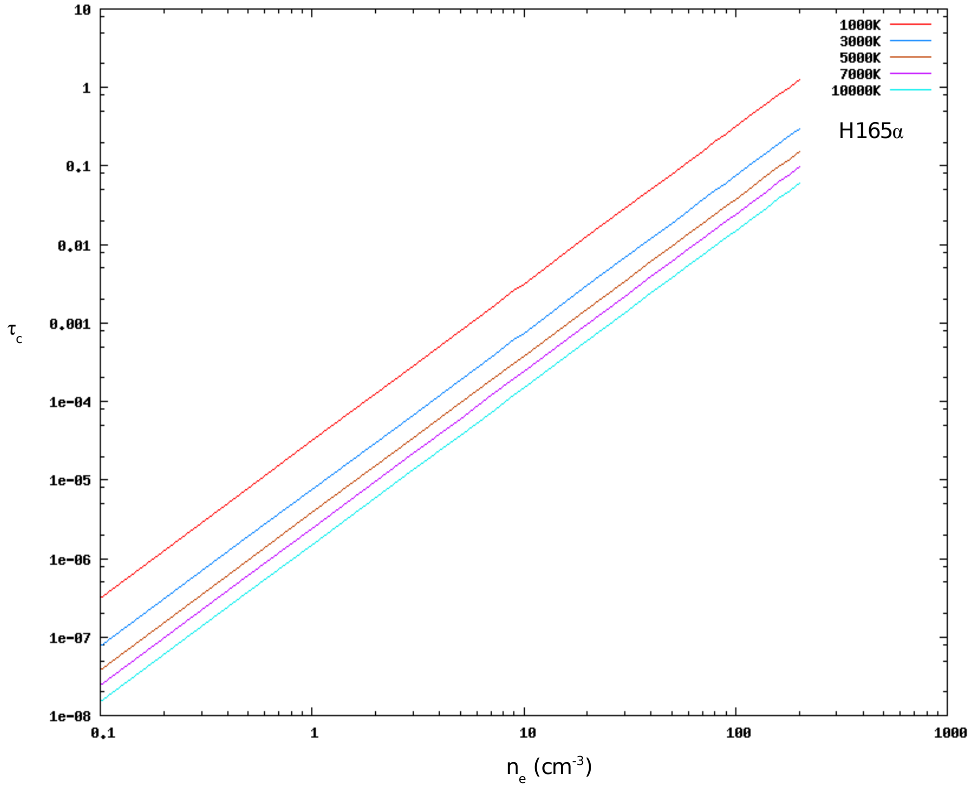

Fig 5-12:Continuum optical depth as a function of electron number density n_e for the two frequencies.

5.2 Line Emission from a spherical cloud.

In the last section line emission from a slab of cloud completely filling the beam of the telescope was studied. In this section the derivation of line intensity if the cloud were a sphere of uniform density has been considered.

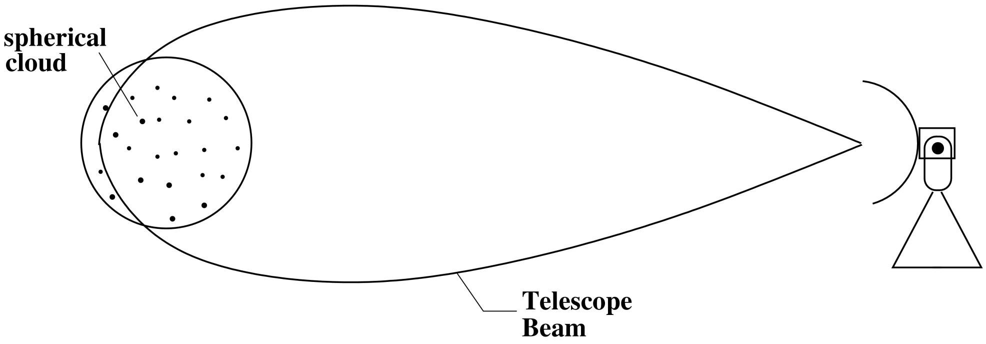

Fig 5-13: Observing a spherical cloud of uniform density with a telescope.

Unlike the slab the spherical cloud parially fills the beam of the telescope. The gross line temperature observed by the telescope from such a spherical cloud can be derived by using the equation given below.

$$T_L = \frac{\int_{A_s} T(s)\ dA}{A_B} \tag{5.7}$$

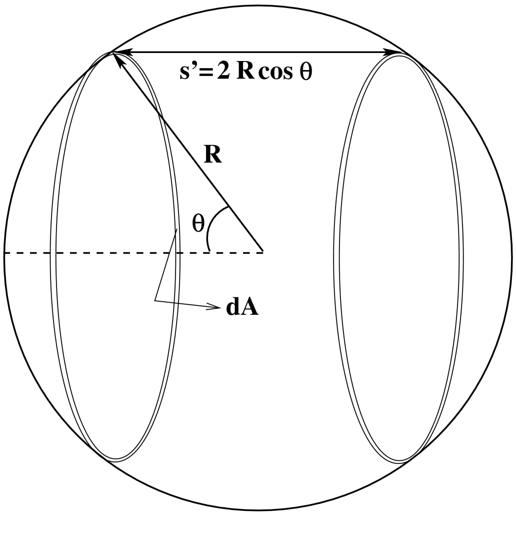

Fig 5-14: Spherical cloud of uniform density.

where T(s) is the line temperature from a cylinder of path length s if it were completely filling the beam. A_s is the projected area of the source. dA is the projected differential area of the cylindrical sheet which has the path length s' as shown in the fig-14. Since the distance to the source is extremely large and the beam width of the telescope is normally quiet small the beam is assumed to be a circular patch of area A_B w.r.t to the cloud. At angle θ, dA is given by

$$dA \;=\; 2\pi\, R \sin\theta\, R\, d\theta \cos\theta \tag{5.8}$$

Now the line temperature depends on the optical depth which in turn depends on the path length s' = 2Rcosθ. The normal optical depth now will be replaced for s' accordingly. For a spherical cloud the differential area dA as well as the path length s' are both functions of θ. As per equation 5.4 it is the exponential term alone that gets effected in the spherical case. Thus one need to know only the integrals ,

$$\begin{aligned} \int_0^{\frac{\pi}{2}} 2\,e^{-t\cos\theta}\sin\theta\cos\theta\, d\theta \;&=\; 2\frac{1\;-\;(1\;+\;t)e^{-t}}{t^2} \\ \int_0^{\frac{\pi}{2}} 2\,e^{t\cos\theta}\sin\theta\cos\theta\, d\theta \;&=\; 2\frac{1\;+\;(-1\;+\;t)e^{t}}{t^2} \end{aligned} \tag{5.9}$$

which arise in equation 5.7 for a spherical cloud. To transform from a completely beam filling slab cloud of path length s to a partially beam filling spherical cloud of diameter s one has to simply apply the following changes to the exponential terms.

$$\begin{aligned} e^{-t} \;--> \;& \frac{2e^{-t}(-1-t+e^{t})}{t^2} \\ e^{t} \;--> \;& \frac{2\,e^{t}(-1+t+e^{-t})}{t^2} \end{aligned} \tag{5.10}$$

The resulting T_L has to be multiplied by the beam filling factor $\frac{\Omega_S}{\Omega_B} = \frac{A_S}{A_B}$. These changes do no apply beyond the point where the dimensions of the cloud exceed the beam width of the telescope. In such a case the integral should not be carried out upto $\pi/2$ but upto an angle that touches the edge of the beam. So the above transformations do not apply in such a case. A plot of comparision between the completely filling slab model and the partially filling spherical model has been given below. As is expected the line temperature corresponding to spherical cloud is less compared to the slab cloud. The clouds are pictured in fig-16.

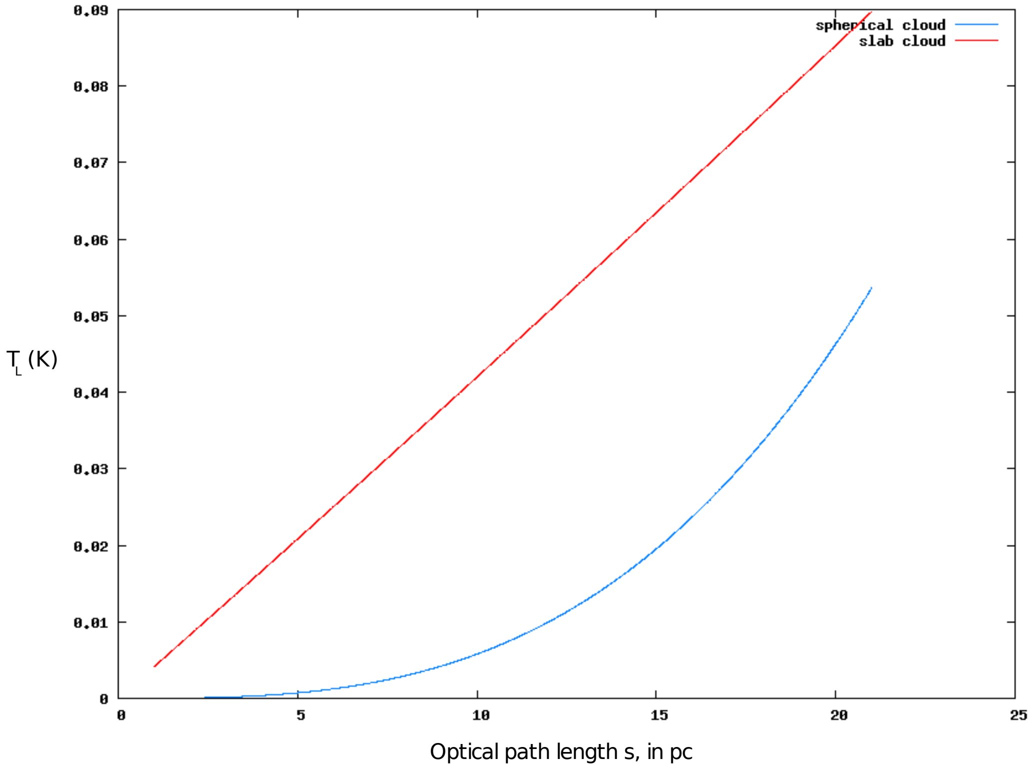

Fig 5-15: Comparision of line emission between a spherical cloud(He, 0.1N_H) and a completely beam filling slab cloud of same path length and diameter s. Here the telescope beam of 0.5^o has been considered for a cloud at a distance of 2.5 kpc. The density(N_H) of the cloud is 50 cm^{-3} .

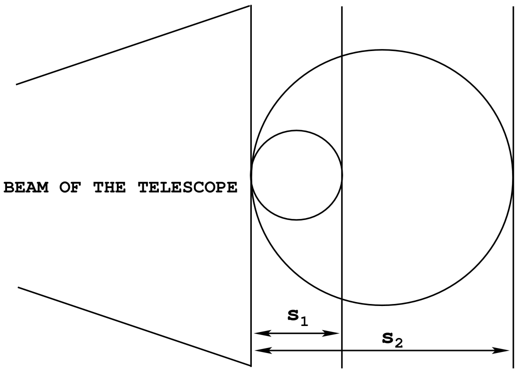

Fig 5-16: The slab cloud and the spherical cloud. The slab cloud always completely fills the beam while the spherical cloud depending on the size partially fills the beam. s determines the thicness for the slab while its diameter for spherical.

It should be noted that for very small values of |t| as is quiet often the case with the line and continuum optical depths($<10^{-3}$) the following approximation applies,

$$\int_0^{\frac{\pi}{2}} 2e^{t\cos\theta}\sin\theta\cos\theta\, d\theta \;=\; 2\int_0^{\pi/2}(1+t\cos\theta)\sin\theta\cos\theta\, d\theta$$
$$= 1 + \frac{2t}{3} \qquad (5.11)$$

else eqn - 5.10 should be used.

5.3 Helium Line towards G18.0+1.8

The parameters fitted to the helium and hydrogen lines detected towards the position G18.0+1.8 for one of the bands are as follows,

	T_L (mK)	***ΔV_{LSR} (km/s)***	***V_{LSR} (km/s)***
He	*7.1(0.9)*	*32.6(4.7)*	*-97.3(2.0)*
H	*129.4(1.0)*	*27.0(0.2)*	*27.4(0.1)*

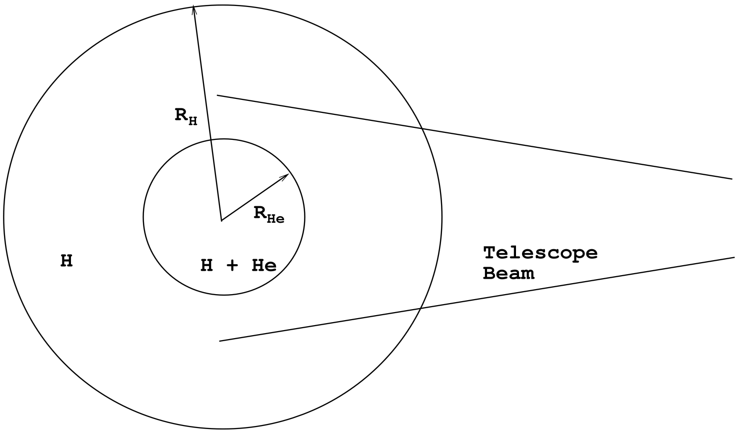

Fig 5-17: The stromgren spheres of Hydrogen and Helium within which the ionization of atoms by the star's radiation is balanced by the recombination of ions and electrons.

The feasible spherical models of Hydrogen and Helium for different electron density n_e and temperature $T_e = 10^4$ K are given in table-1.

n_e (cm^{-3})	s_{He} (pc)	s_H (pc)	s_{He}/s_H	T* (K)
20.0	21.0	25.0	0.83	32700
30.0	16.12	18.17	0.83	
40.0	13.36	14.9	0.84	
50.0	11.55	12.72	0.84	
60.0	10.25	11.3	0.84	
70.0	9.26	10.16	0.85	
100.0	7.22	7.95	0.86	
200.0	4.6	4.92	0.86	
300.0	3.5	3.71	0.87	
500.0	2.5	2.62	0.88	
1000.0	1.57	1.65	0.89	34700

Table 5-1: Table giving the diameters of stromgren spheres(H & He) and their ratios. T are from fig 5-19, blank entries correspond to inbetween values.*

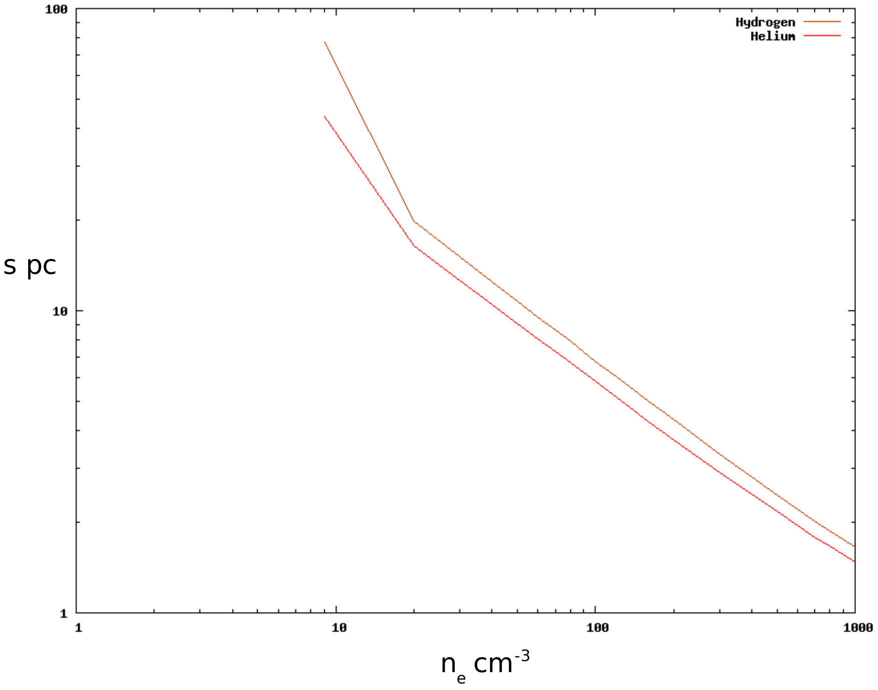

Fig 5-18: A plot of stromgren diameters for the Hydrogen & Helium spherical clouds corresponding to table-1.

As per the V_{LSR} of the lines the nearer distance to the cloud turns out to be ~2.5 kpc using the Galactic rotation curve given by Burton & Gordon(1978). The WSRT telescope at ~1.4GHz has a beam width of 0.5°. At 2.5 kpc this corresponds to an arc of ~21.8 pc. A cloud that exceeds the dimensions of the beam can produce slightly different temperature depending upon the portion of the cloud within the beam. As the cylindrical sheets have different optical depths and hence different temperatures. However if the cloud is sufficiently large the portion of the cloud within the beam can be taken to be nearly flat and the line temperature to be equal to that of the slab cloud with the path length equal to the diameter of the spherical cloud. A plot of ratio of radius of Helium zone to Hydrogen zone as a function of stellar temperature T* is given in fig-18 using eqn (5-15).

5.4 Basic discussion of photoionization around a star.

The material around a star(most of which is just hydrogen) gets ionized by the star's photons with energy in excess of the ionization potential of the atoms.

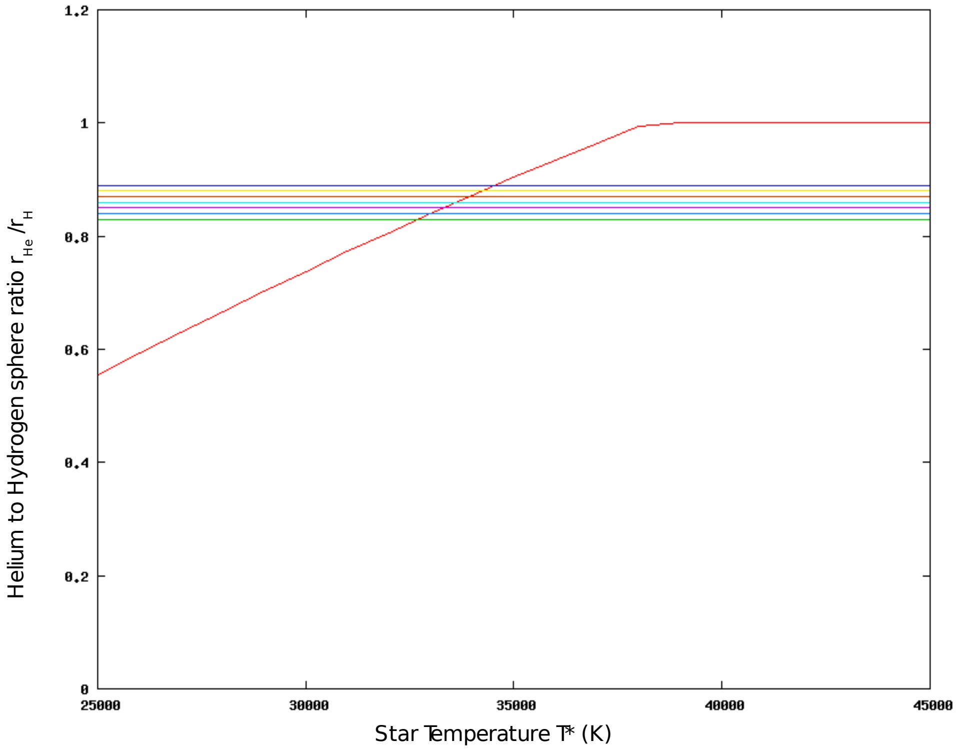

Fig 5-19: A plot of ratio of stromgren spheres of He and H as a function of star temperature at the center, $N_{He}/N_H = 0.1$ *. The horizontal lines mark the ratios* s_{He}/s_H *in table 1.*

Hydrogen which is the most abundant in the universe has a ionization potential of 13.6 eV. The second most abundant is Helium which has two ionization potentials due to two electron in it, of 24.6 eV(He+) and 54.4 eV(He++). Other species of atoms also exist but in far smaller amounts compared to H. The ionization spectrum starting from the star is rich in high energy photons and the material surrounding the star is almost ionized. The radiation as it propagates away from the star is depleted of high energy photons due to their consumption in photoionization. As such the probability of ionization of atoms with higher ionization potential decreases. So as one goes away from the star it is reasonable to believe that the ionization zones are of the species with lower and lower ionization potentials. The atom with higher ionization potential tends to have lower radius of ionization. This is the reason the He-stromgren radius is normally smaller than the H-stromgren radius. However it can happen if the spectrum from the star is hot enough then the helium and hydrogen radii can almost overlap. It is seen in the simplified uniform density modelling of the practically observed He-H radio spectral lines that the He radius is always smaller than the H radius. The ions

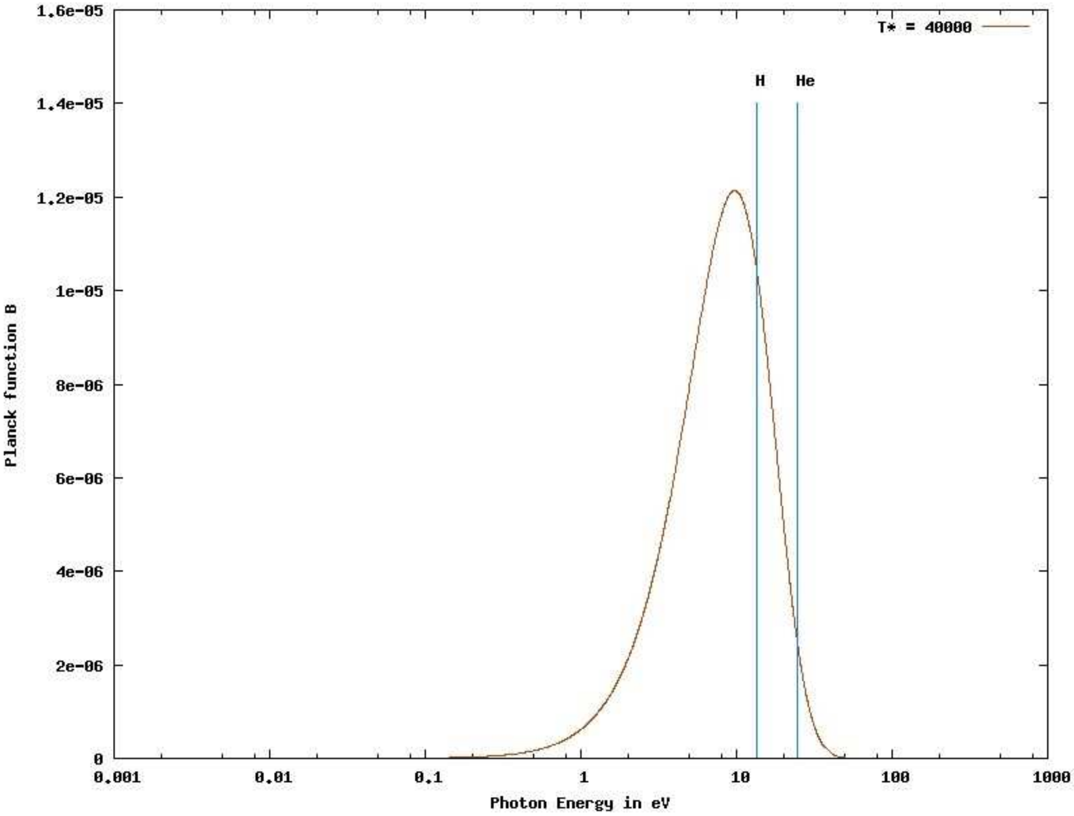

Fig 5-20: Planck function B(ν,T) for a star with effective temperature T = 40000K. The vertical lines mark the threshold photon energies of H and He. Photons above the first mark can ionize Hydrogen while those after second mark can also ionize Helium. It can be seen that they form a small fraction compared to those that can ionize Hydrogen.*

and electrons recombine to form neutral atoms. The freshly formed atom after recombination is in one of the excited states of the atom. It cascades down to lower states by radiating excess energy as photons. The photon spectrum from the star also decides the ionization condition in the surrounding gas. According to the star's effective temperature the photon spectrum peaks at certain frequency. This decides the photons available to ionize atoms with higher ionization potential. If the photon spectrum peaks just near the vicinity of 13.6eV then it can be seen by plotting the Planck function that the photons having energy in excess of 24.6 eV form a small fraction compared to those that can ionize hydrogen. A plot of photon spectrum from a star of effective temperature T*=40000 K has been shown in fig-20.

The ionization potential of helium is much higher than hydrogen. It is possible that the photons emitted by bound-bound transitions within helium can ionize hydrogen but not helium. Calculations(Osterbrock 1989) indicate that a good fraction of recombinations to excited levels result in production of such ionizing photons that are absorbed immediately. Even at electron densities far in excess of critical density, where the collisional transitions compete with the radiative transitions, this fraction is greater than 60%. However at much lower densities this fraction is almost 100%. Hence it is justified to assume that the absorption of photons by helium does not effect the ionization of hydrogen seriously. With this assumption one can decouple the ionizing photon spectra of hydrogen and helium and estimate the order of magnitude of the sizes of hydrogen and helium zones as follows.

The total number of photons available for the ionization of Helium & Hydrogen can be written as,

$$Q(He^o) = \int_{\nu_{He}}^{\infty} \frac{L_\nu}{h\nu} d\nu \quad ; \quad Q(H^o) = \int_{\nu_H}^{\infty} \frac{L_\nu}{h\nu} d\nu . \tag{5.12}$$

where ν_{He} and ν_H are the threshold ionizing frequencies for Helium and Hydrogen respectively. L_ν is the luminosity of the star. Further for the equilibrium condition these photons should balance out the recombinations within a certain volume containing the star such that,

$$Q(H^o) = \frac{4\pi}{3} r_H^3 N_{H^+} N_e^H \alpha_B(H^o) \tag{5.13}$$

$$Q(He^o) = \frac{4\pi}{3} r_{He}^3 N_{He^+} N_e^{H+He} \alpha_B(He^o) \tag{5.14}$$

where $\alpha_B(H^o)$ & $\alpha_B(He^o)$ are the recombination coefficient which accounts for all the recombinations occuring to levels n>1.

$$\alpha_B = \sum_{i=2}^{\infty} \alpha_i$$

Since the recombination(H) occuring to n=1 always satisfies $h\nu$ > 13.6 eV it is quickly reabsorbed due to large absorption coefficient for it. So the photoionizations due to the photons from the star can be thought to be balanced by the net recombinations occuring to levels >1. The recombinations to level n=1 do not take part in this balance as the photons from them always quickly create one more electron-ion pair replacing them. Most of the gas is in ionized condition due to large photoionization rate and relatively low recombination rate(by rate here is meant the time scales involved). This can be understood by considering the enormous amout of gas around the star. The number of atoms far out numbers the photons emitted by the central star. A small fraction of this ionized gas undergoes recombination to produce excited neutral atoms. It is this small fraction that the star's photons re-ionize or in simple words photoionization takes much less time after recombination than recombination after photoionizaton. The ion and electron densities can be directly replaced by the density of the respective materials. With this the ratio of radii of Helium zone to the Hydrogen zone ($r_{He} < r_H$)can be written as,

$$\left(\frac{r_{He}}{r_H}\right) = \left(\frac{Q(He^o)}{Q(H^o)} \frac{N_H}{N_{He}} \frac{1}{\left(1+N_{He}/N_H\right)} \frac{\alpha_B(H^o)}{\alpha_B(He^o)}\right)^{1/3} \tag{5.15}$$

A plot using this equation has been displayed in fig-19. The helium to hydrogen abundance N_{He}/N_H has been taken to be 0.1.

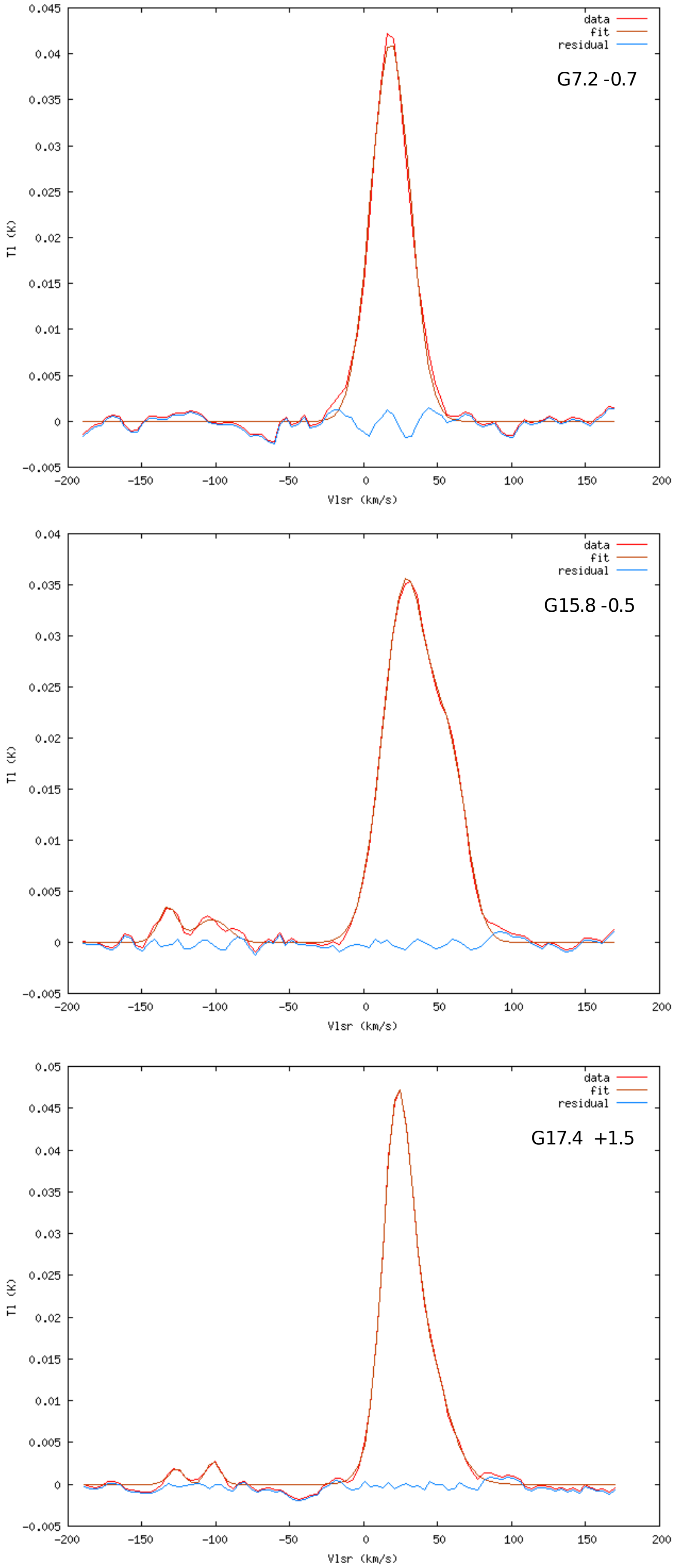

Fig 5-21: Smoothed plots with a 3 channel boxcar function corresponding to weighted average of 1-2-4-5-6-7 bands.

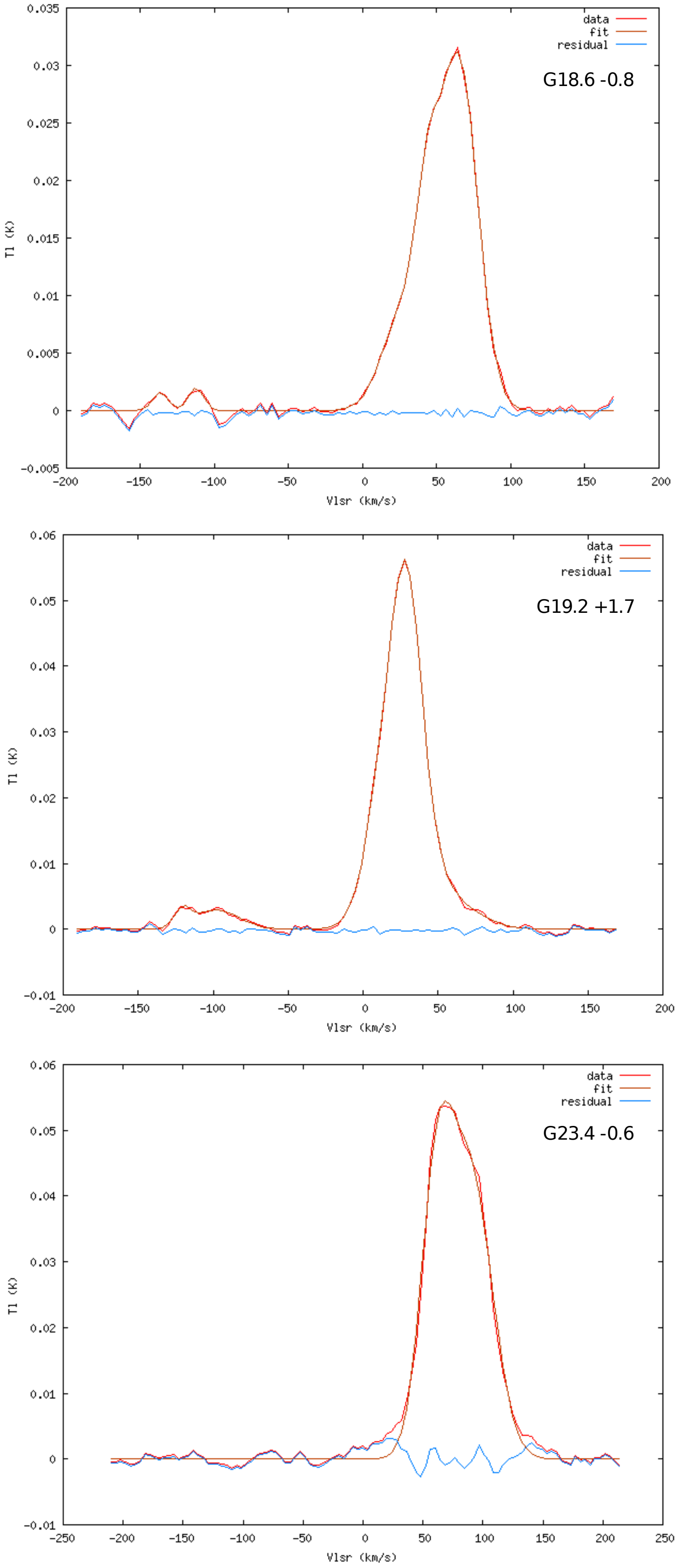

Fig 5-22: Smoothed plots with a 3 channel boxcar function corresponding to weighted average of 1-2-4-5-6-7 bands.

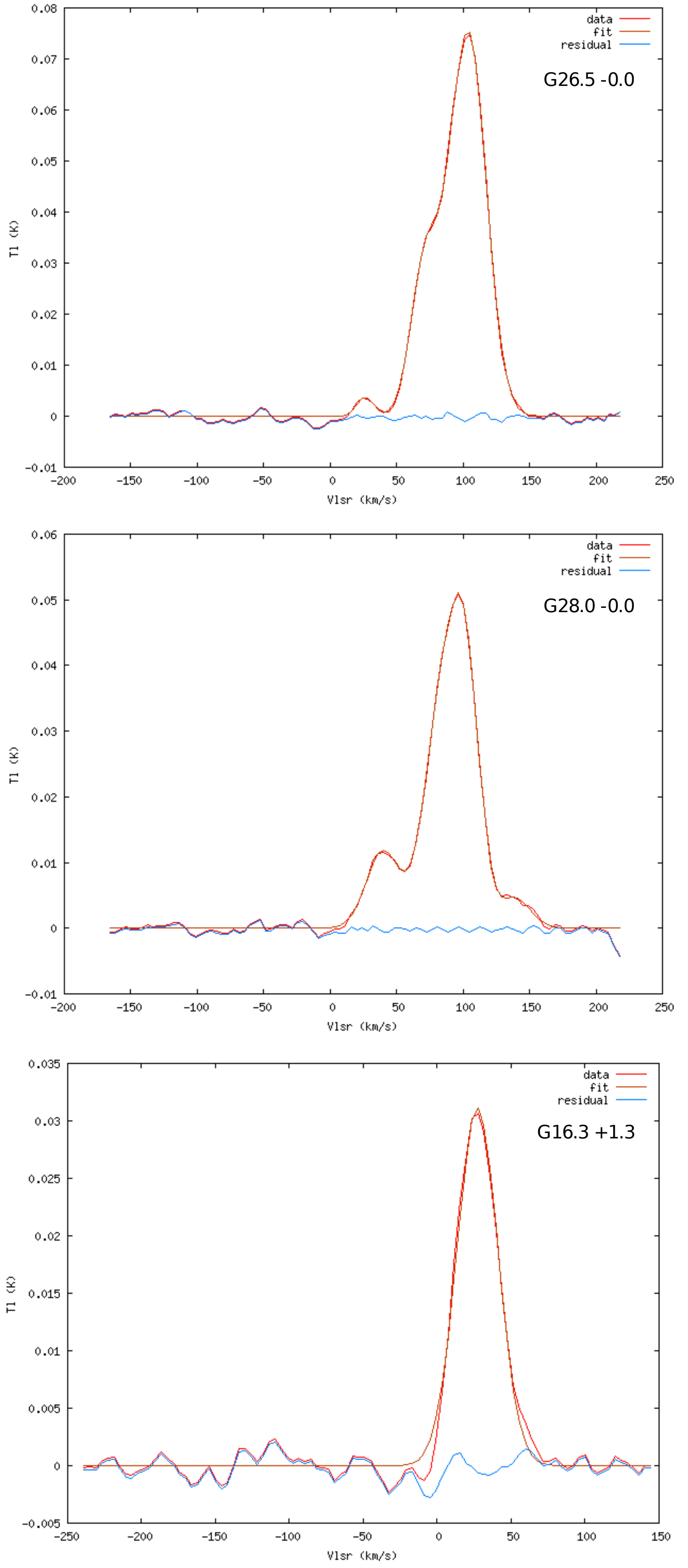

Fig 5-23: Smoothed plots with a 3 channel boxcar function corresponding to weighted average of 1-2-4-5-6-7 bands.

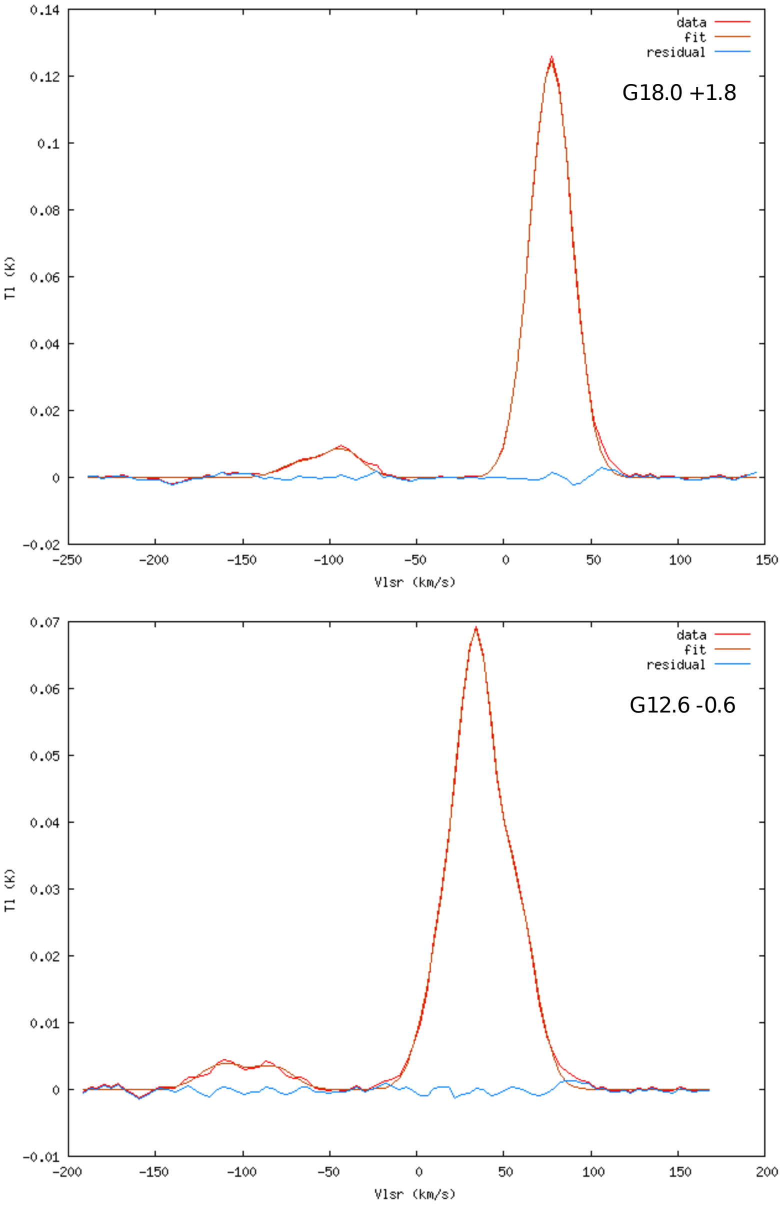

Fig 5-24: Smoothed plots with a 3 channel boxcar function corresponding to weighted average of 1-2-4-5-6-7 bands.

5.5 Helium line limits towards other positions at ~1.4 GHz

Observations with WSRT were carried out towards 15 positions with the intension of detecting Helium line. For this purpose the positions that exhibited sufficiently strong hydrogen lines(>50 mK) were chosen from a survey of previously observed directions(Heiles 1996, Lockman 1976,1989). For a typical line strength of 50mK for hydrogen the expected line temperature of helium as per the then estimated mean N_{He+}/N_{H+} (Heiles 1996, which would be the ratio of line strengths when the regions overlap) ratio of 0.025 was 1.25mK. The band averaged spectra towards all the hydrogen line detected positions have been shown in fig:21-24. Many of these positions do exhibit a significant helium line. As such an attempt has been made to smooth these spectra with a 3-boxcar function to acheive better signal to noise ratio for the He-line. An estimate of upper limit on the ratio N_{He+}/N_{H+} towards all the positions with H-line detection alone has also been tabulated in table-2.

The smoothed spectra seem to be interestingly rich in features. In some spectra there is a likelihood of appearance of lines in many places along the spectrum. Probably multiple clouds lying along the line of sight give rise to low intensity hydrogen lines at different positions in the spectrum. The clouds could be either small or lying far away relative to the solar system. As these low intensity features appear considerably far away from the main feature(s) they definitely come from distinct clouds separated from the main cloud. The features towards the smaller V_{LSR} from the main component correspond to nearer distances whereas those towards the higher V_{LSR} correspond to farther distances from the main cloud, if one were to consider the lines to be coming from the nearest possible clouds as per the Galactic rotation curve. The nearer clouds would have a better chance of detection than farther ones. In many spectra there is a distinct feature, even though low in strength associated with the largest hydrogen line component corresponding to the Helium line position. In some spectra this is quiet clear and believable while in others they are a bit ambigious. It is unlikely that these scattered features could be systematics sitting in the spectrum as some of the spectra are quiet clean and do not exhibit such features at all, like the ones towards G18.0+1.8. However the feature at -50 km/s seems to be interference. The projected velocity of the telescope in the V_{LSR} frame towards all the positions is of the order of ~km/s less than the resolution of the spectra . A locally originating radio signal would more or less appear constant in the band under such a situation. It is narrow and appears towards all the positions which again justifies its local origin. Surprisingly it seems to also appear in all the bands appearing clearly in the band averaged spectrum.

The parameters fitted to the band averaged spectra have been displayed in table-2. To get the ratio of He line towards non He-line detections the upper limit on He-line amplitude has been taken to be the standard deviation across the spectrum. If at all the He-line exists then its amplitude is lesser than the σ in the averaged

Source		**T_L (mK)**		**V_{LSR} (km/s)**		**ΔV_{LSR} (km/s)**		**σ (mK)**	**N_{He+}/N_{H+}**
l^o	**b^o**	**H**	**He**	**H**	**He**	**H**	**He**		
7.2	-0.7	41.2(0.5)	-	18.0(0.2)	-	31.0(0.4)	-	0.74	0.018
15.8	-0.5	35.2(0.4)	2.25(0.3)	28.4(0.5)	-102.8(2.0)	36.3(0.8)	25.2(5.0)	0.41	0.064(0.01)
		15.4(0.8)		59.0(0.8)		27.1(1.2)			
17.4	+1.5	33.4(2.2)	2.73(0.6)	21.9(0.2)	-102.0(1.2)	21.7(0.9)	11.2(2.8)	0.66	0.082(0.02)
		18.7(1.6)		35.7(1.7)		40.8(1.4)			
18.6	-0.8	9.1(1.8)	-	29.3(6.1)	-	34.8(6.7)	-	0.69	
		10.3(3.8)		43.7(0.8)		17.7(2.8)			
		30.4(0.1)		64.5(0.7)		30.5(1.0)			0.023
19.2	+1.7	41.8(6.2)	2.9(0.2)	24.1(1.5)	-98.2(2.6)	34.6(1.1)	35.7(5.4)	0.41	0.069(0.015)
		14.8(3.5)		30.4(0.4)		18.8(1.8)			
		4.2(2.1)		55.4(18.8)		48.6(18.6)			
23.4	-0.6	40.0(5.4)	-	61.4(1.5)	-	32.1(1.7)	-	0.7	
		41.4(2.8)		90.3(2.6)		42.3(3.1)			0.017
26.5	0.0	3.8(0.6)	-	26.1(1.2)	-	14.9(2.9)	-	0.78	
		29.3(0.7)		71.6(0.47)		25.2(0.85)			
		75.4(0.5)		103.4(0.2)		32.3(0.44)			0.01
28.0	0.0	11.7(0.5)	-	39.4(1.1)	-	29.0(2.3)	-	0.55	
		39.0(12.0)		87.5(7.6)		34.5(8.2)			
		24.1(24.4)		103.7(1.7)		22.8(5.4)			
		45.5(0.6)		138.7(2.7)		28.0(5.1)			0.012

16.3	+1.3	31.1(0.5)	-	27.1(0.25)	-	32.6(0.6)	-	0.92	0.03
18.0	+1.8	124.5(0.5)	8.4(1.2)	27.4(0.06)	-92.8(3.5)	28.4(0.1)	26.0(5.2)	0.75	0.067(0.01)
12.6	-0.6	56.1(13.0)	3.2(0.7)	34.2(1.0)	-81.5(4.2)	22.9(2.2)	25.5(6.9)	0.46	0.057(0.026)
		22.7(8.0)		16.9(5.5)		27.6(4.7)			
		28.8(2.5)		56.2(1.9)		27.9(2.1)			

Table 5-2: Gaussian parameters fitted to smoothed spectra. The values in the paranthesis are errors. Multiple entries correspond to multiple components.

spectrum. A ratio of this σ to the H-line amplitude has been tabulated. The highest ratio is towards G17.4+1.5(with He-line detection) with a value of 0.082, which is still less than 0.1. But this value comes from the assumption that the Helium and Hydrogen zones overlap. However if this were not so and the He^+- zone size were less than the H^+- zone this ratio would be still larger, as the ratio would get divided by the beam filling factor(<1.0) of He^+- zone. Many smoothed spectra also exhibit significant pressure broadening, clearly visible with the hydrogen component having extended wings at the edge of the profile. Especially the spectra to be mentioned are G23.4 -0.6 and G19.2 +1.7.

5.6 An attempt to detect He-line with previous ORT-data.

An attempt to detect Helium line at the frequency of ~327 MHz was taken up using a previous data set(Roshi & Anatharamaiah 2000) obtained from ORT observations. This set consisted of observations made towards several positions(>50). Only 41 positions showed a hydrogen line detection. Obviously He-line was not distinguishable in any of these 41 spectra. The spectra towards positions without H-line detection were discarded. The probability of existance of He-line in the absence of H-line would be unreasonable. Each of these spectra was an average of line detections due to 4-transitions $H270\alpha$ - $H273\alpha$. All of these positions lie within the Galactic plane(b=0) with longitude ranging from 332.1° to 88.6°. The spectra were at different resolutions but were multiples of basic resolution of 0.69 km/s. In order to detect the He-line if at all it existed in the spectra, the 41 spectra were averaged by resampling and fourier shifting them to align the H-line with respect to one reference spectrum. This was carried out as has been described in Chapter-3 with WSRT data. The spectra were brought to a common resolution of 1.383 km/s by fourier resampling, i.e 2 times the basic resolution. The spectrum with the resolution of 0.69 km/s was brought to a common resolution by convolving it with a 3 element boxcar function and picking up the alternate values. To make the best of the data 2 types of weighted average were carried out as given by (5.16) & (5.17).

$$S_i = \frac{\sum_i W_{ij} S_{ij}}{\sum_j W_{ij}} \tag{5.16}$$

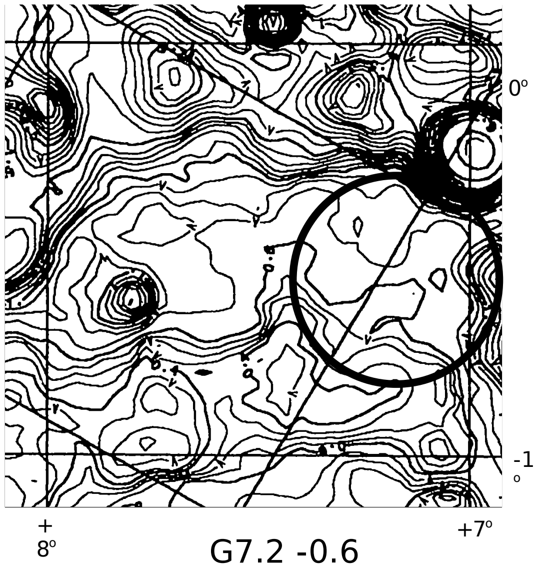

G7.2 -0.6

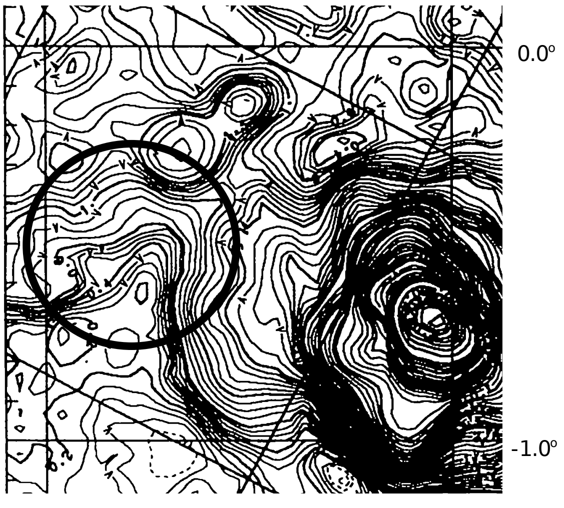

G15.8 -0.5

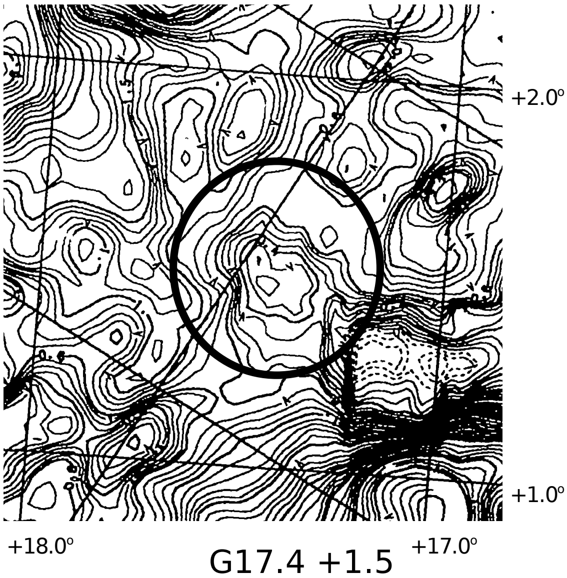

G17.4 +1.5

G18.6 -0.8

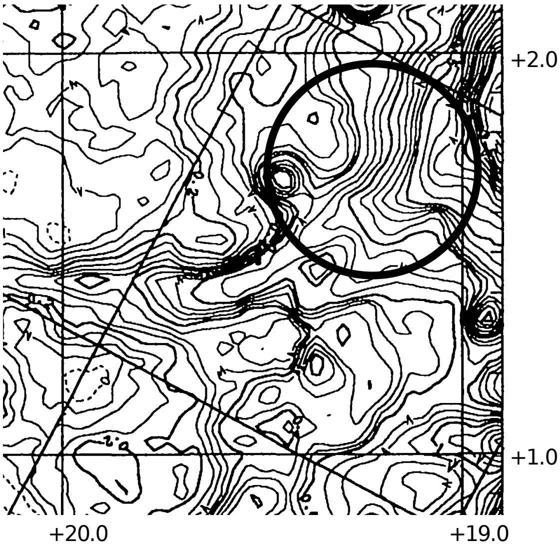

G19.2 +1.7

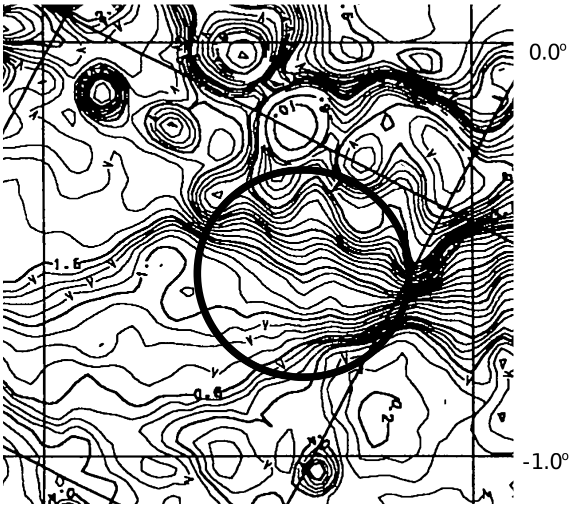

G23.4 -0.6

Fig 5-25: The beam of WSRT ~0.5° has been shown on the 11cm Effelsberg map(Reich et.al 1990). The beam contains no strong HII regions, The map has been marked with Galactic coordinates l-abscissa, b-ordinate.

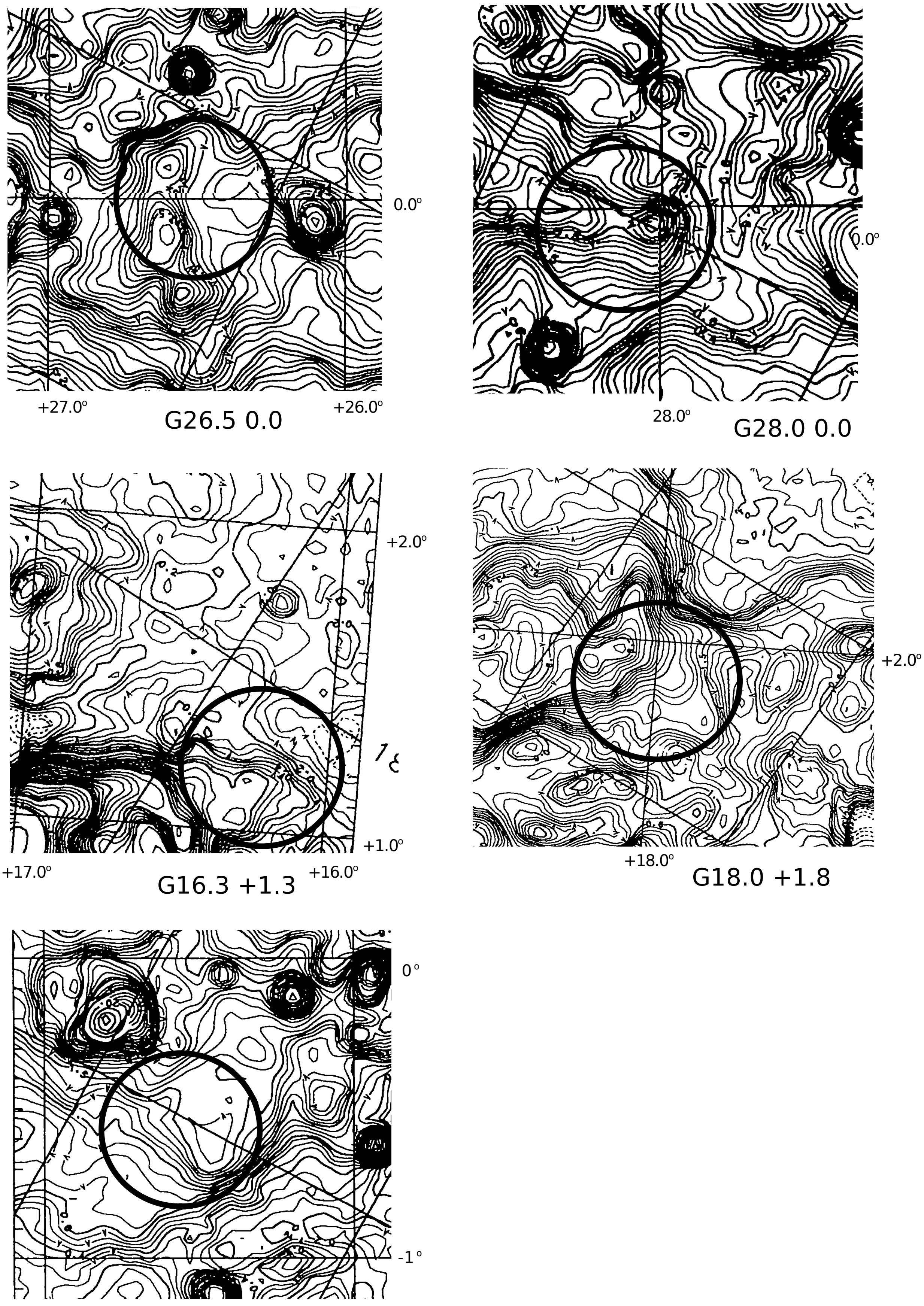

G26.5 0.0

G28.0 0.0

G16.3 +1.3

G18.0 +1.8

G12.6 -0.6

Fig 5- 26: The beam of WSRT ~0.5^o has been shown on the 11cm Effelsberg map(Reich et.al 1990). The beam contains no strong HII regions, The map has been marked with Galactic coordinates l-abscissa, b-ordinate.

$$S_i^{'} = \frac{\sum_i T_j \frac{S_{ij}}{\sigma_j^2}}{\sum_j \frac{T_j}{\sigma_j^2}} \qquad (5.17)$$

where S_i is the average spectrum with i being the channel number, j is the spectrum number. A second order baseline was removed from each of the average spectrum by selecting data values in signal free regions of the average spectrum. The average spectra obtained in this manner have been displayed in the fig-27.

The parameters fitted to the average spectra are given in table-3.

	T_L (mK)		ΔV_{LSR} (km/s)		Weighting
	327 MHz	1.4 GHz	327 MHz	1.4 GHz	
H	251.7	44.0	37.1	33.3	(5.16)
	281.9		37.1		(5.17)
He	11.5		-		(5.16)
C	100.0		23.2		(5.16)

Table 5-3: Parameters fitted to the previous ORT data(Roshi & Anantharamaiah 2000). The weighting is relevant to the 327 MHz data alone. The plots have been displayed in fig-27.

A simple ratio of line intensities which corresponds to N_{He+}/N_{H+} when the He and H regions overlap turns out to be 0.046 . Which can be taken to be an average value for ELDWIM as per this investigation.

A similar set of data towards 26 positions in the Galactic plane at a frequency of 1.4 GHz was again taken from previous observations(Roshi & Anantharamaiah 2000) to model(EM Vs n_e) with the 327 MHz ORT observations. This type of modelling has already been described in Chapter-3. The parameters which were already available towards all these positions were averaged similarly to obtain an over all average. These parameters have been tabulated in table 5-3, adjacent to 327MHz parameters.

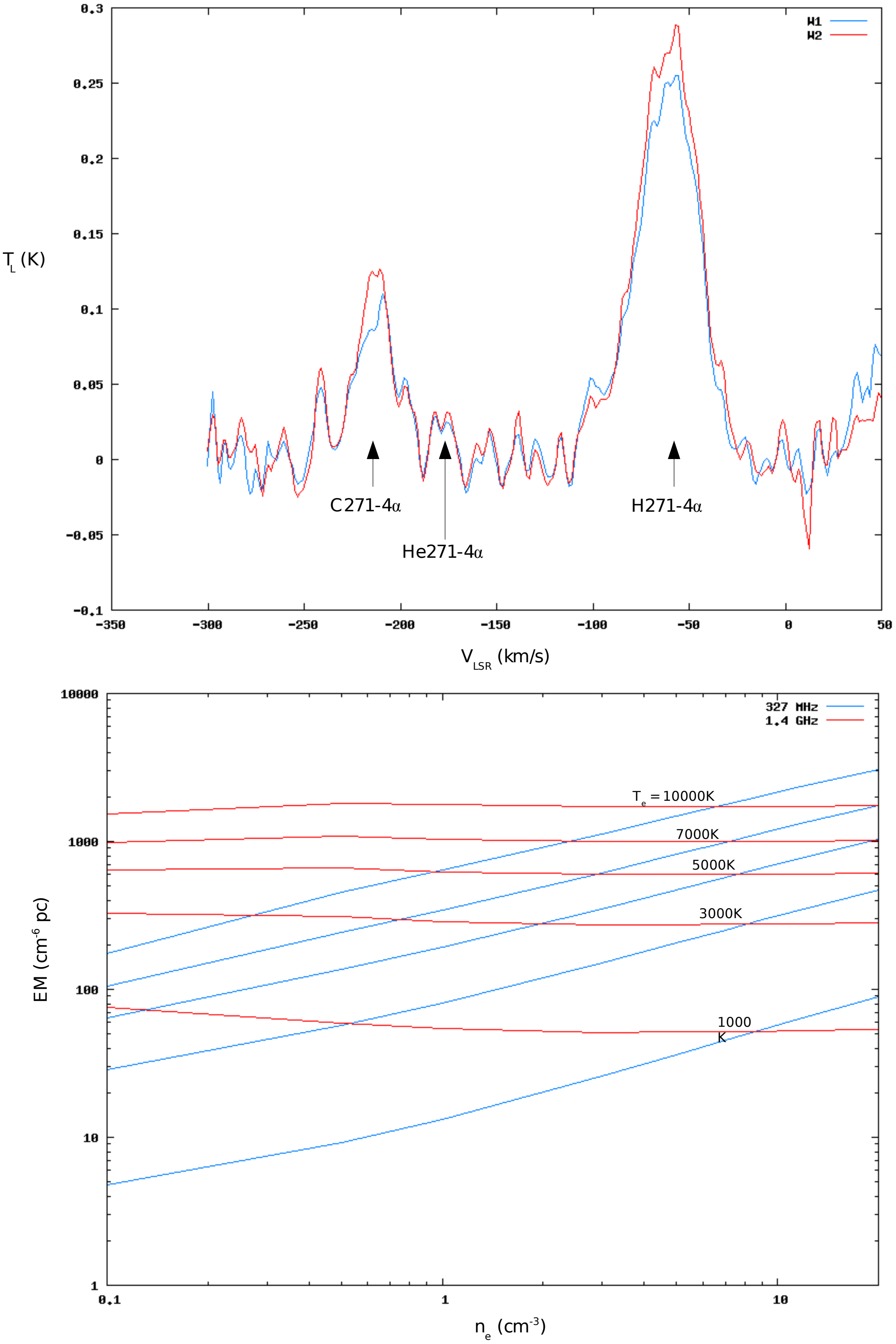

Fig 5-27: The averge spectra(top) of ORT data(Roshi & Anatharamaiah 2000) with the two types of weighting W1 & W2 corresponding to equations (5.16) and (5.17) respectively. Here V_{LSR} *has no meaning only relative* V_{LSR} *between different lines is meaning full. The actual spectra towards different positions were an average of four spectra from the transitions H271- 4α . The lower figure shows the modelling results.*

5.7 Discussion and Interpretation of Helium line intensities.

5.7.1 Line profiles and their implications.

The parameters fitted towards different positions for the hydrogen and helium line profiles have been tabulated along with the N_{He+}/N_{H+} ratio in table 5-2. The non-detection or lower intensity than expected for He-line implies that Helium is not ionized or is partially ionized in ELDWIM. It is most likely that ELDWIM originates from the outer envelopes of HII regions. The gas that is driven away from HII regions wanders between HII regions in ISM manifesting itself as ELDWIM. Almost all the positions selected in this investigation seem to lie near to some HII region. Density bounded HII regions can act as a source of hot ionizing photons. The escaping photons

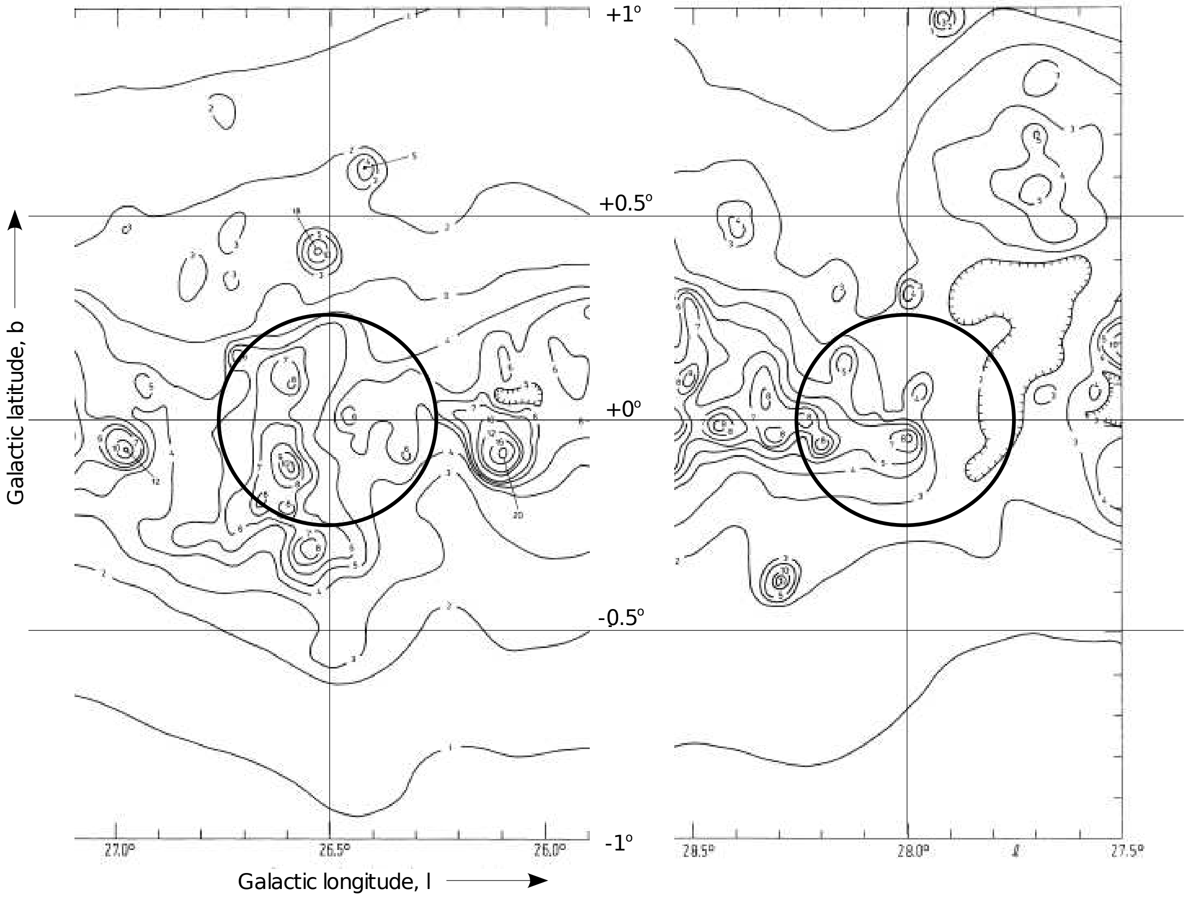

Fig 5-28: WSRT beam position towards the positions G26.5 +0.0 & G28.0 +0.0 showing no helium lines. Interestingly these regions seem to be having numerous HII regions. The map has been taken from Altenhoff's 4.9GHz continuum survey (Altenhoff et.al 1979).

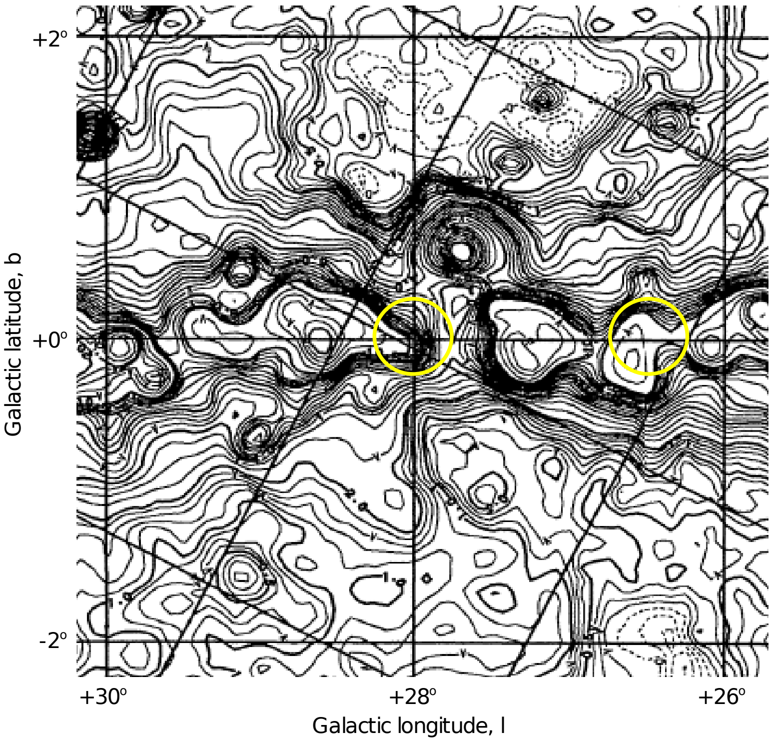

Fig 5-29: WSRT beam positions(yellow circles) for G28.0 +0.0 & G26.5 +0.0 marked in the 2.7GHz continuum map of Reich et.al 1990. These regions seem to be surrounded by HII regions, however V_{LSR} information about the lines from these HII regions would give better information about their positions in relation to these directions.

will ionize ELDWIM in the vicinity. However the photon spectrum will be drastically modified by the gas surrounding the HII regions. Since any photon that can ionize helium can also ionize hydrogen only those higher energy photons that escape hydrogen, which is much more abundant than helium, can ionize helium in the ELDWIM. As has already been discussed in sec-5.4 from the black body spectrum it can be seen that only a small fraction of photons is available for helium ionization compared to the photons that can ionize hydrogen. The escaping ionizing spectrum from HII regions is thus much cooler than that originating from the stars.

This investigation has revealed some new results in terms of N_{He+}/N_{H+} ratio. A high value of 0.082 has been seen towards the position G17.4 +1.5. This is near to the accepted cosmic abundance of ~ 0.1, but however less. There are also interesting positions like G28.0 and G26.5 in Galactic plane(b = 0°) which even though appear to be surrounded by HII regions show a lack of He line. More observations or a further study of observations towards these and surrounding regions can tell more about the ionization of ELDWIM in these directions. Especially it is important to have a good idea of the positions of existing HII regions towards these directions. This indicates that either helium is under abundant or is not ionized within these regions. The observation of helium line can also be reverted back to the morphology and ionization spectrum originating from the HII regions. Lack of He-line indicates that the photons leaking from the surrounding HII regions have a cooler spectrum whereas directions towards which He-line is seen have a stronger ionizing spectrum. This investigation has produced five positions towards which distinct He-line profiles have been observed. Out of these 5 positions(table 5-2), 3 (G15.8 -0.5, G17.4 +1.5 and G12.6 -0.6) are clear regions which do not have any noticeable HII regions within the beam. Indicating clearly the presence of diffuse ionized helium. RRL detections towards the nearby HII regions by earlier observers(Heiles et.al 1996b) match closely with the V_{LSR} of the current observed lines. These RRLs are much stronger than the values obtained here, as expected. The line widths of the hydrogen and helium lines are another interesting aspect. Towards some regions like G17.4 +1.5 and G15.8 -0.5 the line width of He is nearly half of H width as should be in the case of pure doppler broadening. In general the width of He line is smaller than H towards all the positions

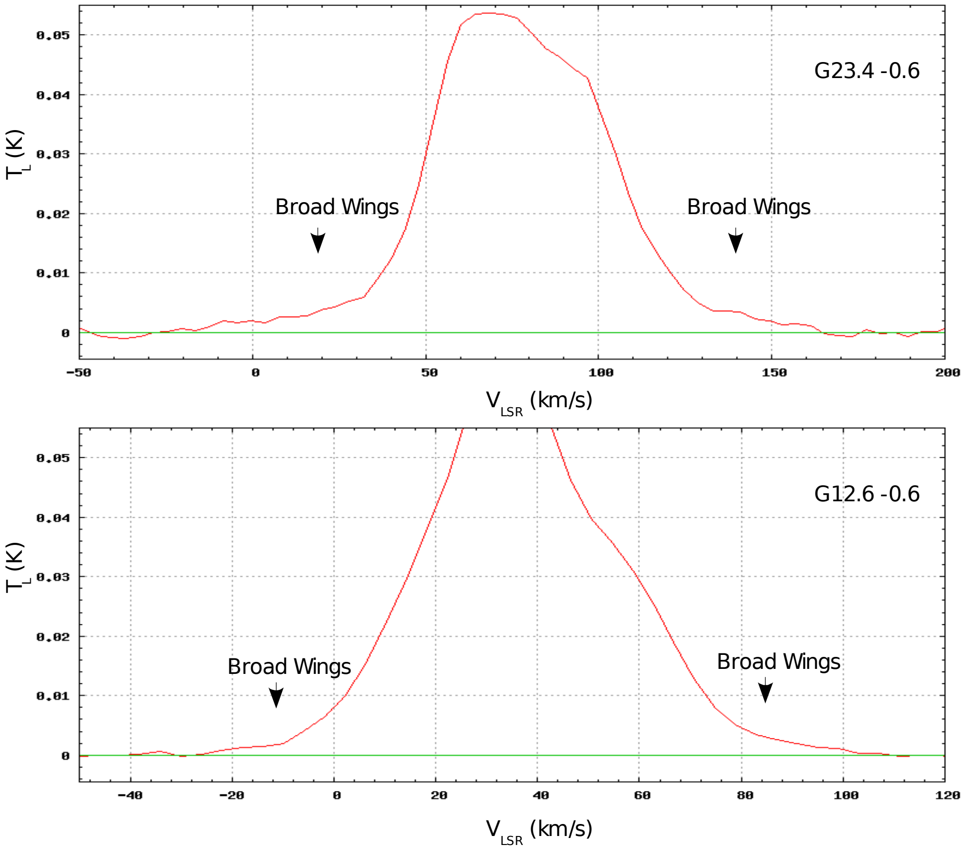

Fig 5-30: Characteristic extended wings of pressure broadening.

within the error bars. The width agreement between He and H is a criterion to hold the two lines to be originating from the same region. In the case where the He line width is simply half of the H line width it suggests that the lines originate in a low density medium with negligible pressure broadening. Pressure broadening could contribute to the width of the He line in denser regions and make it larger than the thermal width. There seems to be small amount of pressure broadening towards positions like, G18.0 +1.8 and G12.6 -0.6 which have a small extended wing towards the edge of the line feature. Towards some regions like G23.4 -0.6 and G19.2 +1.7 it is quiet significant. The worst case is that of the later which also exhibits slightly more broader wings than the former.

Another deduction from the simple non-agreement of He and H line widths is that they can originate from different regions. If the width of He line is larger than the hydrogen it means under the assumption of same pressure broadening for He and H that He line radiation is mainly coming from a denser or a hotter region. Further the constraint of observed V_{LSR} difference(~122.2 km/s) between H and He suggests that the region of origin moves at the same velocity along the line of sight. And based on differential Galactic rotation is the same cloud or very near by clouds. One more remark that should be made is, it has been assumed during gaussian fitting to obtain the parameters for the He line that the He line is mainly associated with the strongest hydrogen component. This seems to be true towards the positions G17.4 +1.5, G19.2 +1.7 and G18.0 +1.8 where the V_{LSR} for He and H are in good agreement within the error bars. But again consistently towards other detection positions where the hydrogen has significant multiple components the helium line widths are broader. Completely consistent with this argument is the position G12.6 -0.6. Further from the obtained V_{LSR} for He and H lines we see that for this position as expected the V_{LSR} of He line moves inwards towards the main H line and is slightly short(~6.5 km/s) of the required difference of 122.2 km/s from the H line. This can be explained as due to the amalgam of multiple He lines associated with the multiple H components. With this line of argument the interesting positions are G18.0 +1.8 and G19.2 +1.7 where a complete agreement of V_{LSR} between He and H is seen but the widths do not agree in dopplerian sense. For example for the position G18.0 +1.8 with the overall errors taken into account there is a disagreement of 4.7 km/s in the expected width of He line. A close inspection of this region on the continuum map suggests that this region does incorporate a HII region within the beam even though this is near the edge, but is well within the beam. This is also true for G19.2 +1.7. The broader width of He line indicates its origin to be in the denser and hotter regions within the beam, near to the core of the HII region. Interestingly the profiles of both He and H in the later show similar extended wings at the edge.

Another interesting region in the list is G18.6 -0.8 which exhibits mulitple hydrogen line components. Even though small line like features have been seen towards the -ve V_{LSR} of the spectra the fitted parameters are not consistent with the velocity difference between He and H lines to be originating from the same region. However the left edge of the hydrogen feature complex covers the expected H line in relation to this He line very well. It does'nt seem to be difficult to think of an associated H line with 2 times the width (~25 km/s) centered at around ~10 km/s. Also by assuming the feature at -112 km/s to be that of He the expected maximum H

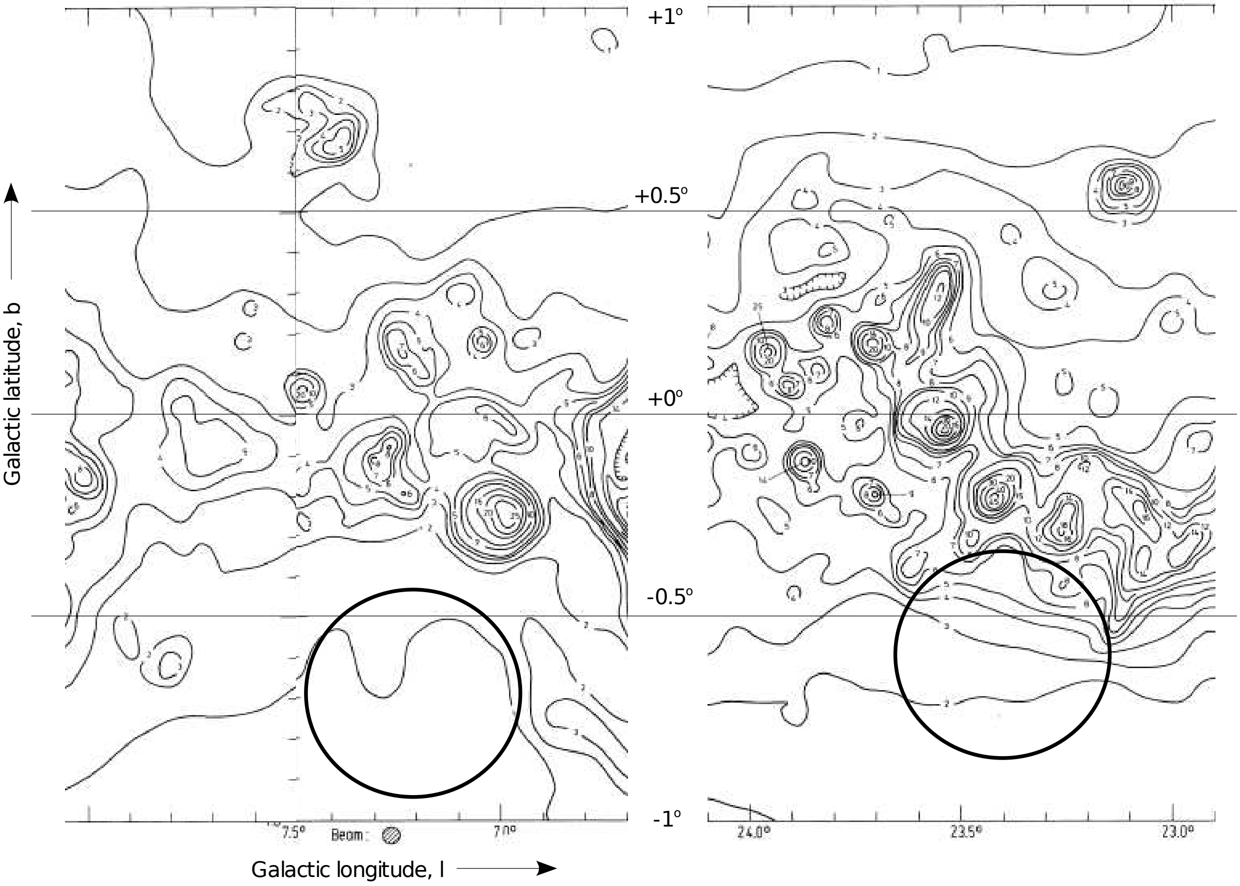

Fig 5-31: WSRT beam position towards the positions G7.2 -0.7 & G23.4 -0.6 showing no helium lines. The map has been taken from Altenhoff's 4.9GHz continuum survey (Altenhoff et.al 1979).

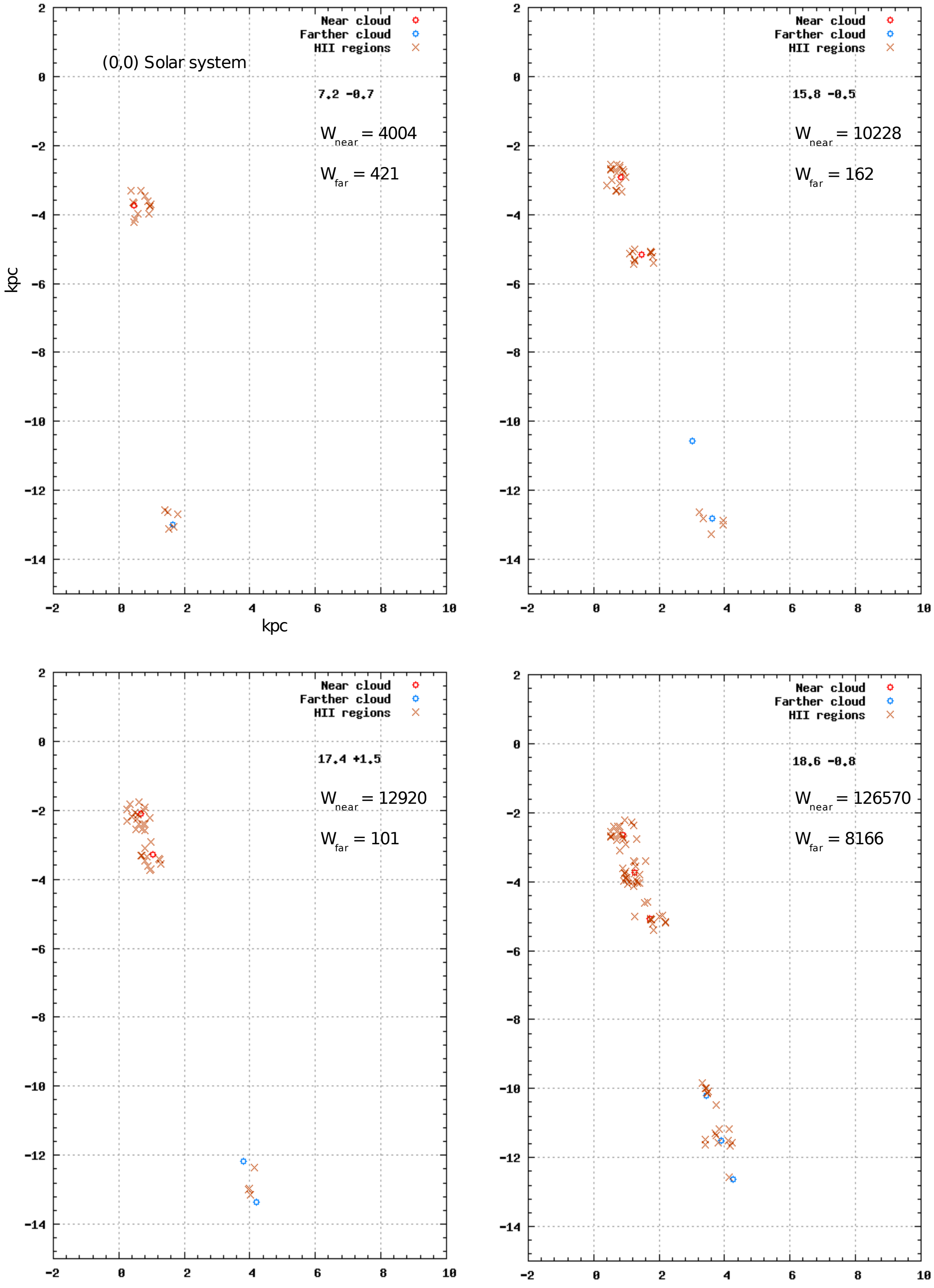

Fig 5-32: The HII regions from Paladini et.al 2003 catalogue have been marked along with line originating clouds. The distances to the HII regions and the clouds were obtained from Burton & Gordon 1978 Galactic rotation curve. The HII regions are within a distance of 500 pc from the clouds.

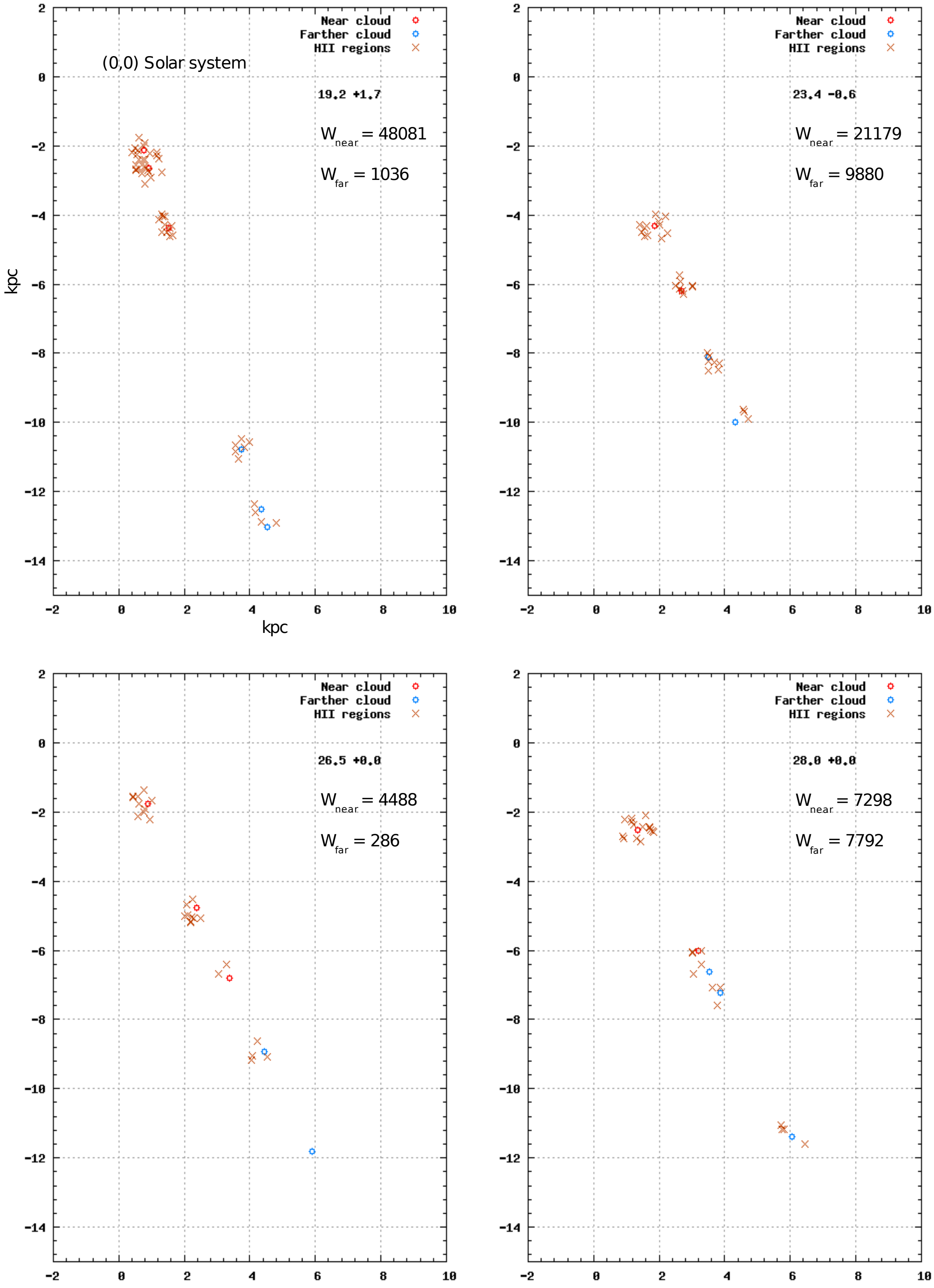

Fig 5-33: The HII regions from Paladini et.al 2003 have been marked along with line originating clouds. The HII regions are within a distance of 500 pc from the clouds. It should be noted however that none of the HII regions in all these plots lie within the beam of the telescope except for G26.5 +0.0 and G28.0 +0.0.

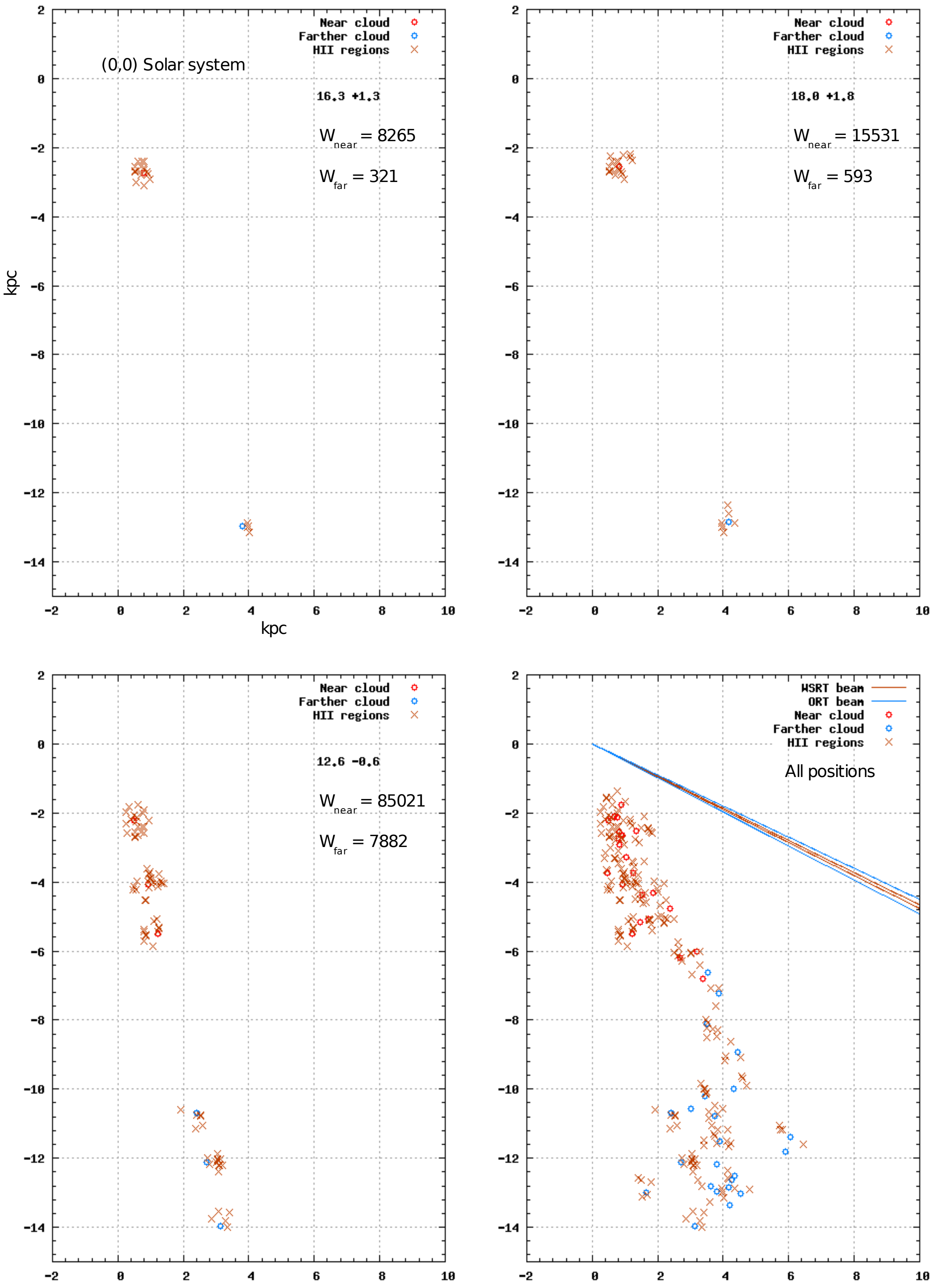

Fig 5-34: The HII regions from Paladini et.al 2003 have been marked along with line originating clouds. The HII regions are within a distance of 500 pc from the clouds. The last corner plot shows all the positions and the HII regions together, along with the beams of ORT and WSRT telescopes.

line strength is about 100mK which is not difficult to visualize in the hydrogen feature complex. But due to beam dilution this could be considerably less. This position does cover an HII region at the edge within the beam. Another observation from the spectrum that can be stated is the broad wing like profile near the left edge which perhaps is manifestation of pressure broadening giving a Lorentzian profile to the line feature. If this is true then indeed a hydrogen line is associated with the -112 km/s He feature which originates from denser regions near to the HII region. The gross HII region weightage for this position has a maximum value. Most likely the He feature comes from a different region.

The set of positions with no detection of He line are G7.2 -0.7, G23.4 -0.6, G26.5 0.0, G28.0 0.0 and G16.3 +1.3. The position G7.2 -0.7 lies close to a HII region but the beam does not include it. This region shows a strong H line but has no associated He line which is expected from the parameters fitted to H line at -102 km/s. As can be seen from the spectra in fig-21 this region has no noticeable feature representing He line. However this position is a good candidate for inspecting ELDWIM and its ionization. G23.4 -0.6 is another good candidate for ELDWIM. This region is well separated from HII regions and is a true representative of diffuse ELDWIM as can be checked with the 4.9GHz map in fig-31. Interestingly the H line feature shows significant pressure broadening indicating contribution from denser regions as well. The most interesting cases of non-detection are G28.0 +0.0 and G26.5 +0.0 which inspite of being surrounded by numerous HII regions and being in the plane of the Galaxy do not show any He line. These two regions should be further investigated to understand the ionization of ELDWIM. The non-detection of He line is a sure indicator of cold ionization spectrum for ELDWIM or under abundance of helium itself. G16.3 +1.3 is another good representative of clean ELDWIM which shows a single hydrogen line component. However due to poor signal to noise ratio w.r.t to He line much cannot be said regarding the failure of its detection.

The possible kinematical distances of the clouds due to V_{LSR} of the lines from all the 11 positions in tabel 5-2 have been marked in fig 5:32-34. The identified HII regions distributed in Galactic longitude and latitude within a distance of 500pc from the line originating positions have also been marked on the same plot to give an idea of the their relative location to these ELDWIM clouds.

5.7.2 N_{He+}/N_{H+} ratio and the ELDWIM ionization spectrum.

The obtained values of N_{He+}/N_{H+} ratio for different positions has been tabulated in table 5-2. This ratio with the normal accepted abundance of hydrogen to helium is expected to be 0.1. However in most of the cases it has turned out to be much smaller than this. When helium RRL are observed in HII regions this depression in the ratio is attributed to the smallness of the ionized He zone compared to the H zone which engulfs the former, as has already been discussed in sec-5.4. However in the case of ELDWIM, gas is ionized externally where a situation like that in HII regions is difficult to realize between He and H. In a diffuse extended gas it is expected that He and H are ionized similarly with no morphological difference between He and H ionization, whatsoever. Under such a situation the ratio N_{He+}/N_{H+} should reveal the abundance ratio between the two elements assuming complete ionization. However in ELDWIM this is not seen. This ratio is less than the expected abundance ratio. This implies either He is under abundant or the radiation ionizing the extended diffuse gas is not strong enough to ionize helium which has a much higher ionization potential then hydrogen. The higher ionization potential of helium seems to be a good reason to believe its non-ionization condition. It seems from the listing of HII regions around the line originating positions that this ratio is higher were there is a crowding and larger number of HII regions. HII regions for positions where He line is not detected lie noticebly away and are less in number, like G7.2 -0.7, G23.4 -0.6, G26.5 +0.0 and G28.0 +0.0. The position G16.3 +1.3 shows significant crowding of HII regions but unfortunately the signal-to-noise(snr) ratio for its spectrum is poor regarding He line detection. The apparent conclusion from this observation is straight forward, the regions in the middle of more number of HII regions show a He line which is an indication of hot ionization spectrum where as the regions having less number of HII regions or in the case they lie farther apart do not show a He line indicating a colder ionization spectrum. So insufficient number of photons to ionize He. This argument with HII regions has been quantified as a weight associated to each region given as under,

$$W = N_{HII}\left(\frac{1}{D^2_{1\mathrm{HII}}} + \frac{1}{D^2_{2\mathrm{HII}}} + \frac{1}{D^2_{3\mathrm{HII}}} + \ldots \frac{1}{D^2_{NHII}}\right) \qquad (5.18)$$

The weightage has been considered to be proportional to the inverse square of the distance to the HII region, as the flux from a source goes as inverse square of the distance. Since every HII region may not be a source of ionizing photons the weightage has been taken to be proportional to number of HII regions as well. This weightage scheme produces figures consistent with the arguments given here in the last paragraph. The net weights obtained using (5.18) have been displayed within the plots, individually for near clouds and farther clouds.

General considerations of overall ionization of Galactic hydrogen constrains the ionization spectrum of ELDWIM through star formation. Order of magnitude calculations(Heiles et.al 1996) indicate that with this requirement satisfied one must definitely expect the helium to be completely ionized under this condition. However alternative possibilities to explain the anamoly of helium being not ionized with hydrogen completely ionized have been sought after. Possibilites of excess emission of photons that can ionize hydrogen but not helium from certain types of stars(B-stars) has also been considered. Sciama(1990) has proposed the decay of dark matter into photons that have energy sufficient (~14eV) to ionize hydrogen but not helium. Such a process can explain the ionization situation between H and He but has been found to contradict with other facts of observations. Investigators have assessed such propositions, but have found them unsatisfactory. The current observations indicate that the diffuse ionization spectrum concerning ELDWIM has varying strengths towards different positions and leaks out from near by HII regions. The current observational fact of the correlation between non-detection of He line and the lack of near by HII regions(either less in number or farther apart, understood as a weight) implies the dependence of ionization of He upon HII regions. This in turn means the photons responsible to ionize helium come from the surrounding HII regions. Further observations towards similar positions to strengthen/check this fact would assist to resolve the He non-ionization problem and help in understanding the ionization situation between hydrogen and helium in ELDWIM.

The ionization flux due to the obtained values of N_{He+}/N_{H+} towards each position have been calculated under the assumption of complete ionization of hydrogen/partial ionization of helium and tabulated in table 5-4. The effective temperature of the black body which would result in such a spectrum of ionization for H and He has also been tabulated to give a feel for its strength. The assumption of complete ionization of H in the concerned medium is justified by the fact that radiation characteristic of blackbody temperature ~3200K can produce 99% ionization of hydrogen with a typical density of 10 cm^{-3}. A simple analysis of ionization and recombination in a volume element indicates that the expected effective temperature of the radiation is ~6000K to produce the observed fractional ionization of He. This temperature is nearly twice quoted earlier, validating the complete ionization of hydrogen.

In a volume element where the photoionization of He is balanced by the recombinations we have for the equilibrium as,

$$(1 - x_{He}) N_{He} \int_{\nu_{He}}^{\infty} \frac{4\pi}{h\nu} \sigma_{He}(\nu)\ B_{\nu}\ d\nu = \alpha_{He} n_e x_{He} N_{He} \tag{5.19}$$

where $x_{He} = N_{He+}/N_{He}$ is the ionization fraction of He, N_{He} is the number of He atoms per unit volume. σ_{He} is the ionization cross-section of He which is function of frequency ν. B_ν is the black body planck function, α_{He} is the recombination coefficient of helium, which is a function of electron temperature(T_e) and n_e is the electron density. The intensity of the radiation all over the cloud is assumed to be constant for the sake of simplicity, so $4\pi\ B_\nu/h\nu$ is the number of photons between ν and $\nu+d\nu$. Only those photons that can ionize helium count in, so we have a lower limiting threshold frequency ν_{He}.

For a Black body,

$$B_{\nu} = \frac{2h\nu^3}{c^2} \frac{1}{e^{h\nu/kT} - 1} = \frac{2h\nu^3}{c^2}\ e^{-h\nu/kT} \tag{5.20}$$

For a typical cloud temperature of 10^4 K, the ratio $h\nu/kT$ is quiet large than 1 for $\nu > \nu_{He} = 5.94 \times 10^{15}$ Hz the threshold frequency for helium. Which means unity in the denominator can be neglected. With this approximation the equilibrium condition (5.19) is written as,

$$\frac{8\pi}{c^2} \int_{\nu_{He}}^{\infty} \nu^2 \sigma_{He}(\nu) e^{-h\nu/kT} d\nu = \frac{n_e \alpha_{He} x_{He} N_{He}}{(1 - x_{He})} \tag{5.21}$$

The photoionization cross-section σ_{He} has been approximated(Osterbrock 1989) as,

$$\sigma_{He}(\nu) = \sigma_{THe}\left(\beta\left(\frac{\nu}{\nu_{He}}\right)^{-s}+(1-\beta)\left(\frac{\nu}{\nu_{He}}\right)^{-s-1}\right) \tag{5.22}$$

where $\sigma_{THe} = 7.83 \times 10^{-18}$ cm^2 , $\beta = 1.66$, $s = 2.0$. With the introduction of this cross-section in (5.21) we can write this expression as,

$$2.69\times10^{5}\ T e^{-h\nu_{He}/kT} + 3.02\times10^{10}\ expIEi(-\frac{h\nu_{He}}{kT}) = n_e\alpha_{He}\left(\frac{x_{He}}{1-x_{He}}\right) \tag{5.23}$$

This equation can be solved numerically to obtain a value for the radiation temperature T, for a given n_e and x_{He} . x_{He} and n_e can be obtained from observation. Assuming the cosmic abundance of He w.r.t H to be 0.1, $x_{He} = N_{He+}/(0.1\ N_{H+})$. Having a good idea of n_e(~10cm^{-3}) for ELDWIM from constraints drawn in chapter-3, T has been determined numerically. These values of T and the resulting flux have been tabulated for different positions in table 5-4.

The flux at a temperature T is given by,

$$\begin{aligned} F\nu_{He} &\approx \frac{8\pi}{c^2}\int_{\nu_{He}}^{\infty}\nu^2\ e^{-h\nu/kT}\ d\nu \\ &\approx \frac{8\pi kT}{hc^2}\left(\nu_{He}{}^2 + \frac{2kT\nu_{He}}{h}\right)e^{-h\nu_{He}/kT} \end{aligned} \tag{5.24}$$

The counter part of (5.23) for hydrogen is,

$$\begin{aligned} -2.12\times10^{13}\ T e^{-h\nu_H/kT} - \left(8.35\times10^{13} + \frac{3.34\times10^{18}}{T}\right)\ expIEi(-\frac{h\nu_H}{kT}) \\ = y = n_e\alpha_H\left(\frac{x_H}{1-x_H}\right) \end{aligned} \tag{5.25}$$

y is just a function of temperature alone, expIEi is the exponential integral function. For a given temperature x_H can be obtained by rearranging (5.25) as given under,

$$x_H = 1 - \frac{1}{1 + \frac{y}{n_e \alpha_H}} \qquad (5.26)$$

It can be seen from this equation that for a temperature like 3200K and n_e = 10cm^{-3} hydrogen is almost fully ionized, i.e x_H ~ 1.0.

Source (Galactic Coordinates)	***Flux*** (Log$_{10}$ [F photons/cm^2])		***Temperature*** (K)	
		Errors		***Errors***
G7.2 -0.7	*9.1*	- -	*5896*	- -
G15.8 -0.5	*10.0*	*-0.2* *+0.2*	*6156*	*-54* *+62*
G17.4 +1.5	*10.4*	*-0.5* *+1.3*	*6281*	*-136* *+446*
G18.6 -0.8	*9.2*	- -	*5933*	- -
G19.2 +1.7	*10.1*	*-0.3* *+0.4*	*6186*	*-83* *+115*
G23.4 -0.6	*9.1*	- -	*5888*	- -
G26.5 +0.0	*8.8*	- -	*5816*	- -
G28.0 +0.0	*8.9*	- -	*5840*	- -
G16.3 +1.3	*9.4*	- -	*5977*	- -
G18.0 +1.8	*10.1*	*-0.2* *+0.2*	*6174*	*-55* *+66*
G12.6 -0.6	*9.9*	*-0.5* *+0.6*	*6119*	*-136* *+172*

Table 5-4: Table of flux and corresponding effective temperature derived from the observed N_{He+}/N_{H+} ratio and the constrained average number density.